AFRL-VS-HA-TR-1998-0105, Pt. 2

INFRARED EMISSIONS MODELING

Part 2

B.D. Green
W.T. Rawlins
L.G. Piper
G.E. Caledonia
M.E. Fraser
K.W. Holzclaw
B.L. Upschulte
P.A. Mulhall
J.F. Cronin
R.H. Krech
D.B. Oakes

Physical Sciences, Inc.
20 New England Business Center
Andover, MA 01810

September 1998

Final Report

APPROVED FOR PUBLIC RELEASE; DISTRIBUTION IS UNLIMITED.

AIR FORCE RESEARCH LABORATORY
Space Vehicles Directorate
29 Randolph Rd
AIR FORCE MATERIEL COMMAND
Hanscom AFB, MA 01731-3010

"This technical report has been reviewed and is approved for publication."

Dean F. Kimball
DEAN F. KIMBALL
Contract Manager
Background Clutter Mitigation Branch

Harold A. B. Gardiner
HAROLD A. GARDINER
Acting Branch Chief
Background Clutter Mitigation Branch

This report has been reviewed by the ESC Public Affairs Office (PA) and is releasable to the National Technical Information Service (NTIS).

Qualified requestors may obtain additional copies from the Defense Technical Information Center (DTIC). All others should apply to the National Technical Information Service (NTIS).

If your address has changed, if you wish to be removed from the mailing list, or if the addressee is no longer employed by your organization, please notify AFRL/VSIM, 29 Randolph Road, Hanscom AFB, MA 01731-3010. This will assist us in maintaining a current mailing list.

Do not return copies of this report unless contractual obligations or notices on a specific document require that it be returned.

REPORT DOCUMENTATION PAGE	*Form Approved* *OMB No. 0704-0188*

1. AGENCY USE ONLY *(Leave blank)*	**2. REPORT DATE** September 1998	**3. REPORT TYPE AND DATES COVERED** Scientific,Final, Sep 1993-Aug 1998

4. TITLE AND SUBTITLE Infrared Emissions Modeling Part 2 of 2	**5. FUNDING NUMBERS** Contract F19628-93-C-0046 PR S322 TA GD WU AB
6. AUTHOR(S) B.D. Green, W.T. Rawlins, L.G. Piper, G.E. Caledonia, M.E. Fraser, K.W. Holzclaw, B.L. Upschulte, P.A. Mulhall, J.F. Cronin, R.H. Krech, and D.B. Oakes	
7. PERFORMING ORGANIZATION NAME(S) AND ADDRESS(ES) Physical Sciences, Inc. 20 New England Business Center Andover, MA 01810	**8. PERFORMING ORGANIZATION REPORT NUMBER** PSI-1179/TR-1580
9. SPONSORING/MONITORING AGENCY NAME(S) AND ADDRESS(ES) Air Force Research Laboratory/VSBM 29 Randolph Rd Hanscom AFB, MA 01731-3010 Contract Manager: Dean Kimball	**10. SPONSORING/MONITORING AGENCY REPORT NUMBER** AFRL-VS-HA-TR-98-0105
11. SUPPLEMENTARY NOTES	
12a. DISTRIBUTION AVAILABILITY STATEMENT Approved for Public Release; Distribution Unlimited	**12b. DISTRIBUTION CODE**

13. ABSTRACT *(Maximum 200 words)*

This report summarizes a multi-year program to analyze upper atmospheric radiance data to deduce product distributions, extract the operative kinetic mechanisms, and quantitatively determine local conditions in the emission volume. Spectral and kinetic models were used to analyze emissions from several molecules including NO, NO+, ozone, and excited nitrogen. Radiances rom the mesosphere both under equilibrium and non-equilibrium conditions were analyzed. The radiance changes produced by non-equilibrium excitation mechanisms such as electrons, kinetic energy from fast atoms, and solar-induced transients at terminator were all addressed by multiple analyses during this program.

14. SUBJECT TERMS Infrared emission Electron excitation Mesospheric chemistry Nitric oxide Ozone Nitrogen	**15. NUMBER OF PAGES** **16. PRICE CODE**

17. SECURITY CLASSIFICATION OF REPORT UNCLASSIFIED	**18. SECURITY CLASSIFICATION OF THIS PAGE** UNCLASSIFIED	**19. SECURITY CLASSIFICATION OF ABSTRACT** UNCLASSIFIED	**20. LIMITATION OF ABSTRACT** UNL

APPENDIX 10

Analysis of CIRRIS 1A $O_3(V)$ Spectra in the 9.6 μm Region

Analysis of CIRRIS1A $O_3(v)$ Spectra in the 9.6 μm Region

B.D. Green and W.T. Rawlins
Physical Sciences Inc.

J.R. Lowell, S.J. Lipson, P.S. Armstrong, and W.A.M.Blumberg
Phillips Laboratory

J.A. Dodd
Stewart Radiance Laboratory

Presented at the
IAGA Symposium GA202
21st General Assembly of the International Union of Geodesy and Geophysics
Boulder, CO

10 July 1995

Sponsored by the Ballistic Missile Defense Organization

Data Analysis Approach

95-645

- Screen CIRRIS1A data for filters and tangent heights of interest
- Visually review to eliminate “bad” spectral (32%)
- Spectrally fit to determine $O_3(v_1, v_2, v_3)$ excited state populations
  - — selected high resolution spectra
  - — day and night to determine CO_2 radiances
  - — develop best procedures to determine internal distribution of states
  - — 1-quanta (scalable to total ozone)
  - — 3-quanta (scalable to atomic oxygen)
- Integrate ozone spectral database in several (9) bandpasses
- Terminator series at several altitudes
- Global variability

Air Parcel Variations: 96 km, Night

95-646

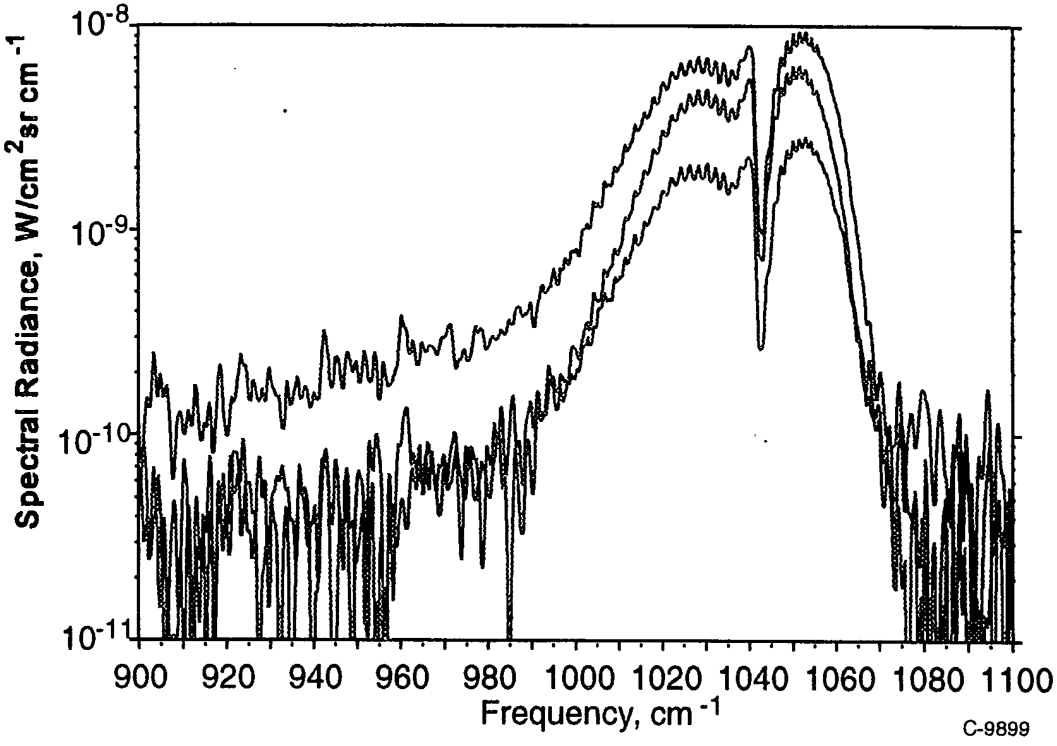

CIRRIS1A O_3 Fluorescence: Night

T-23984

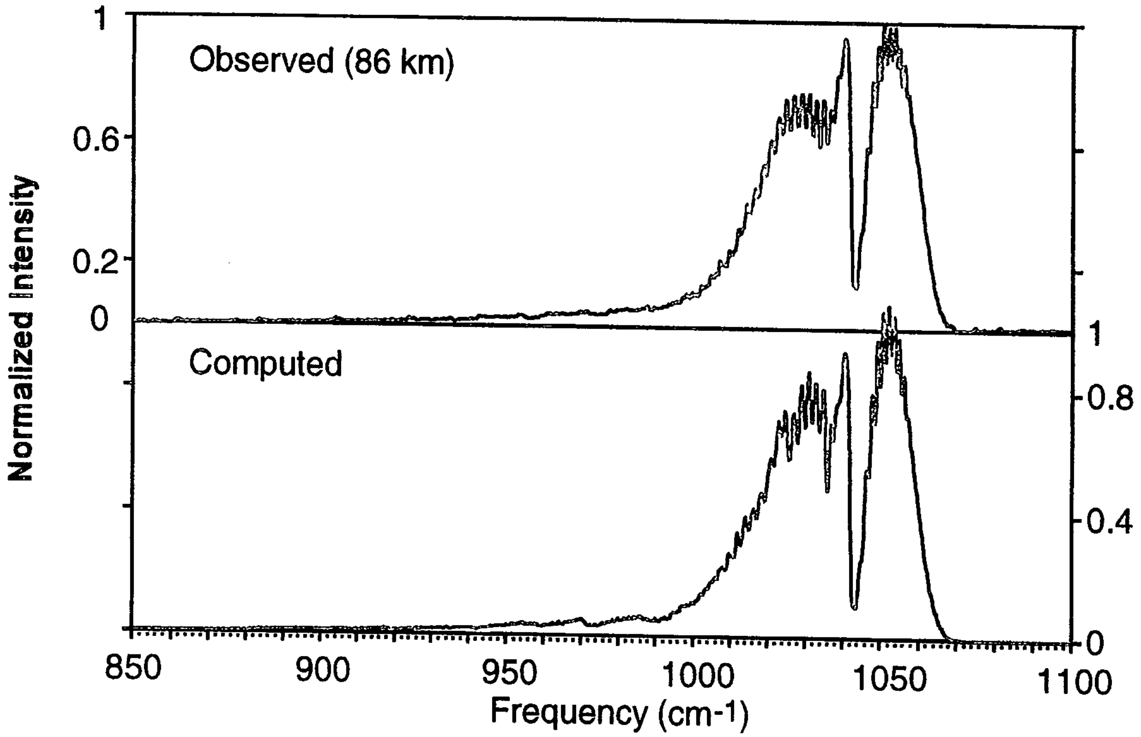

CIRRIS1A O_3, CO_2 Fluorescence: Day

T-23985

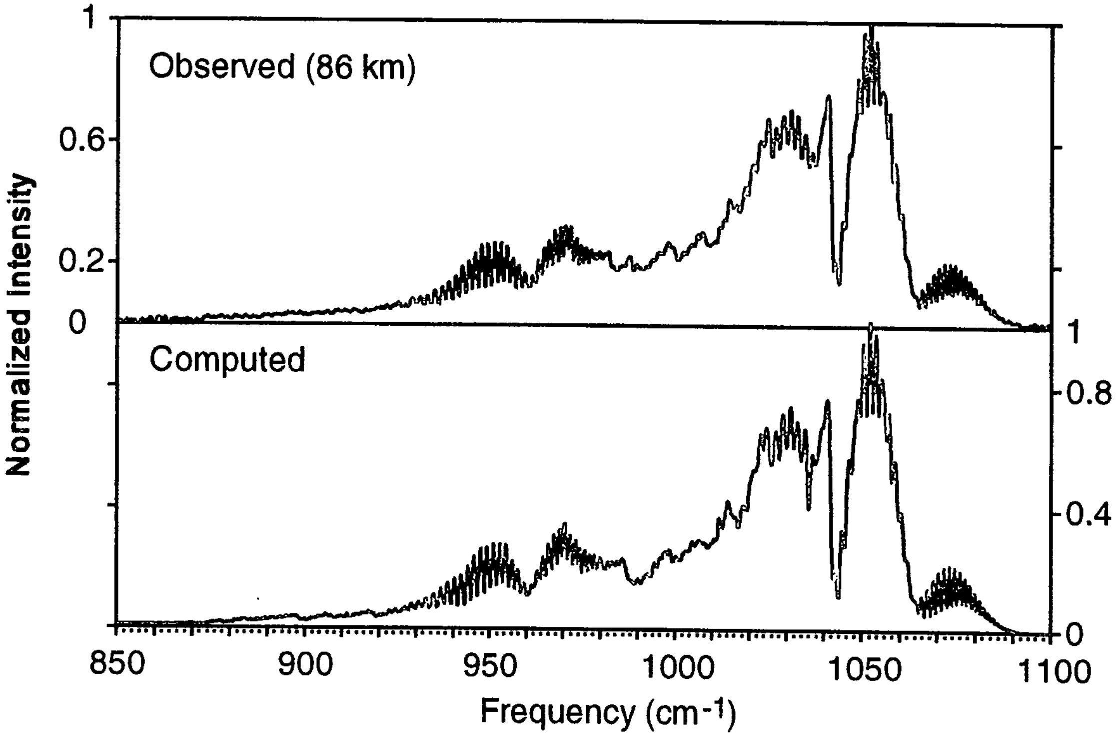

Comparison of CIRRIS with Photochemical Model : Night (Allen et al., 1984)

95-647

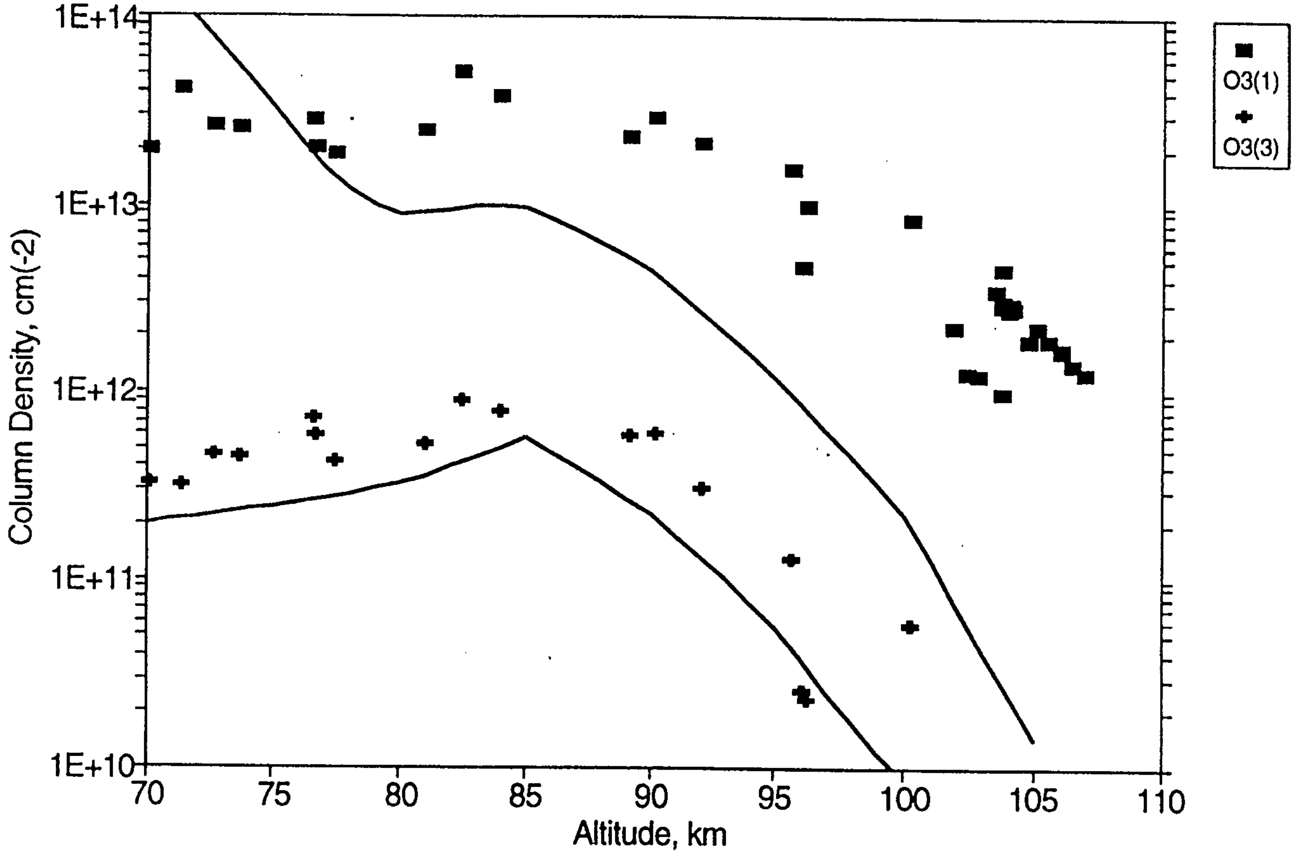

Comparison of CIRRIS with Photochemical Model: Day (Allen et al., 1984)

95-648

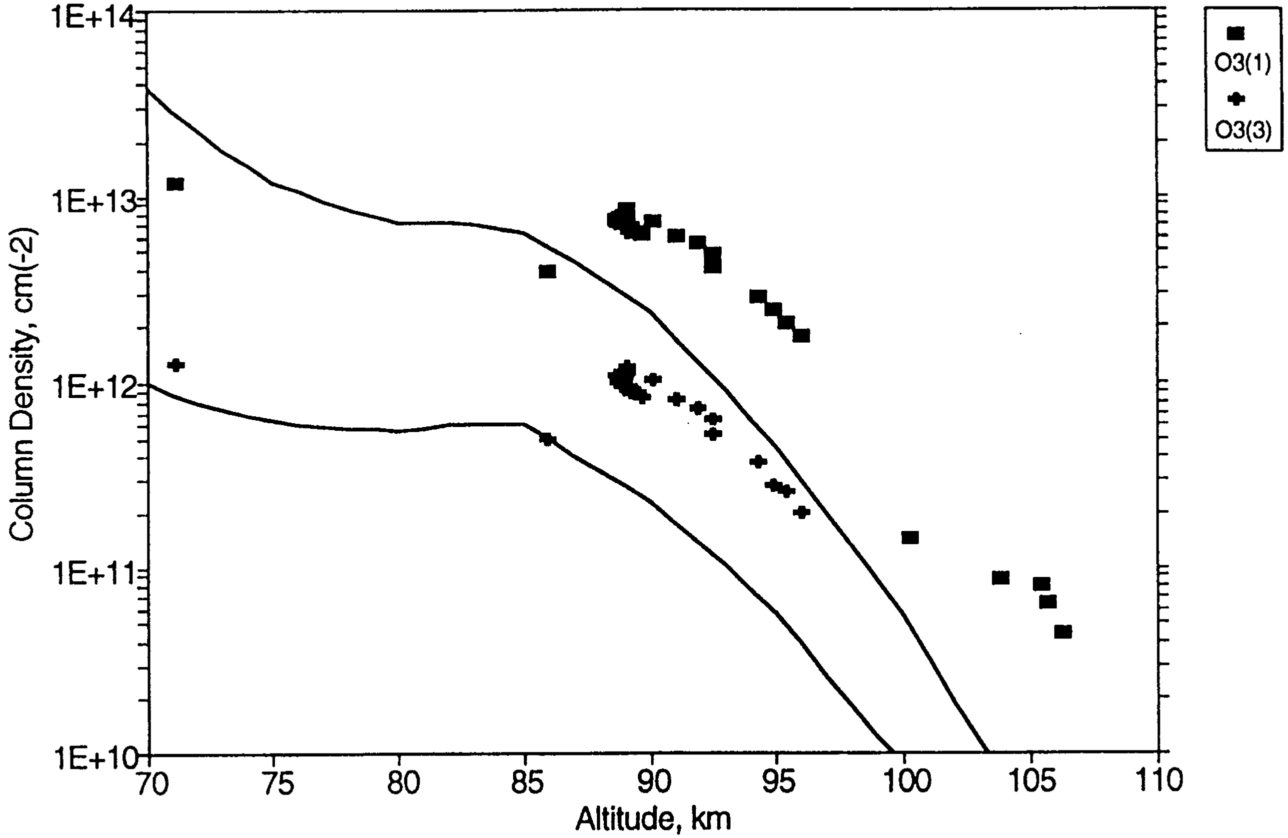

Comparison of CIRRIS with EXCEDE Column Densities

95-649

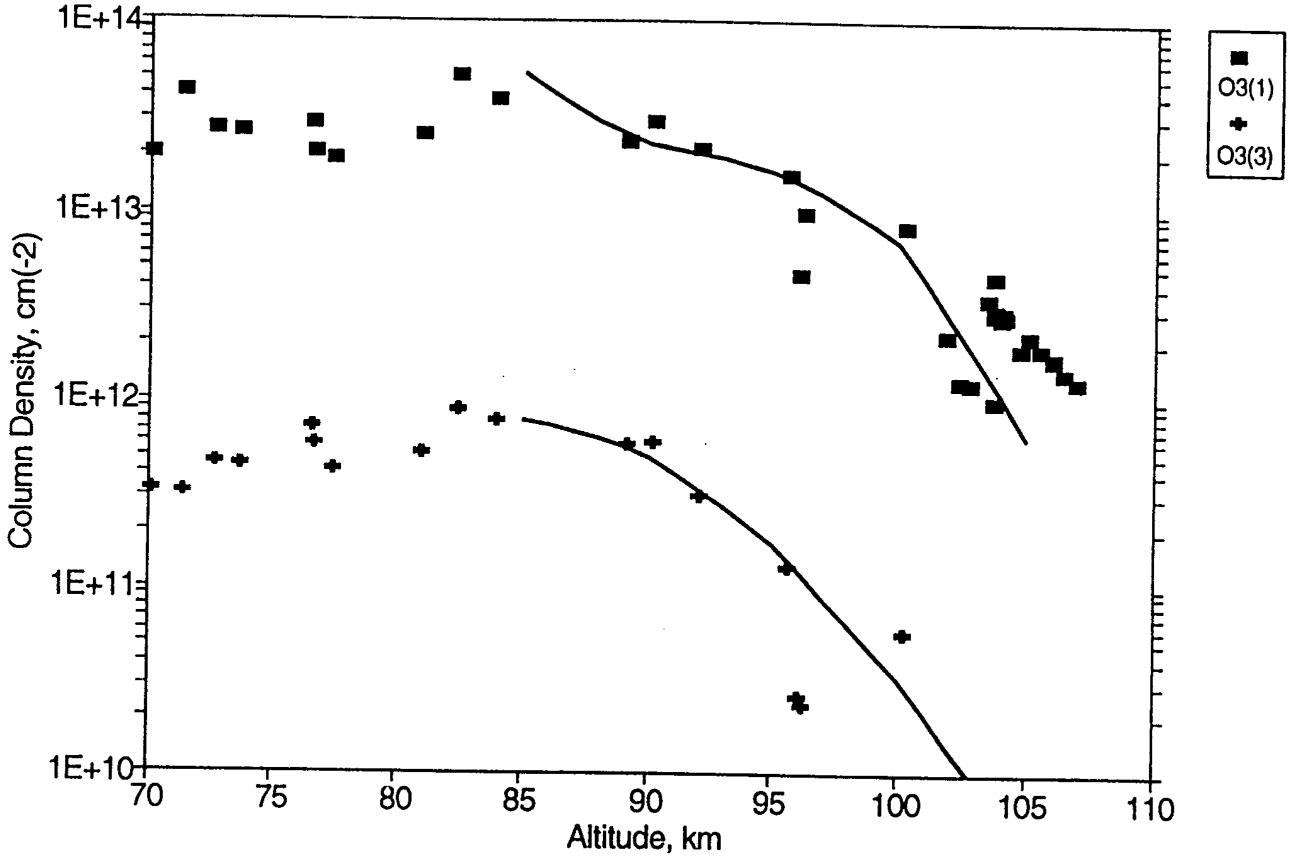

Nighttime Ozone (001) Radiance

95-650

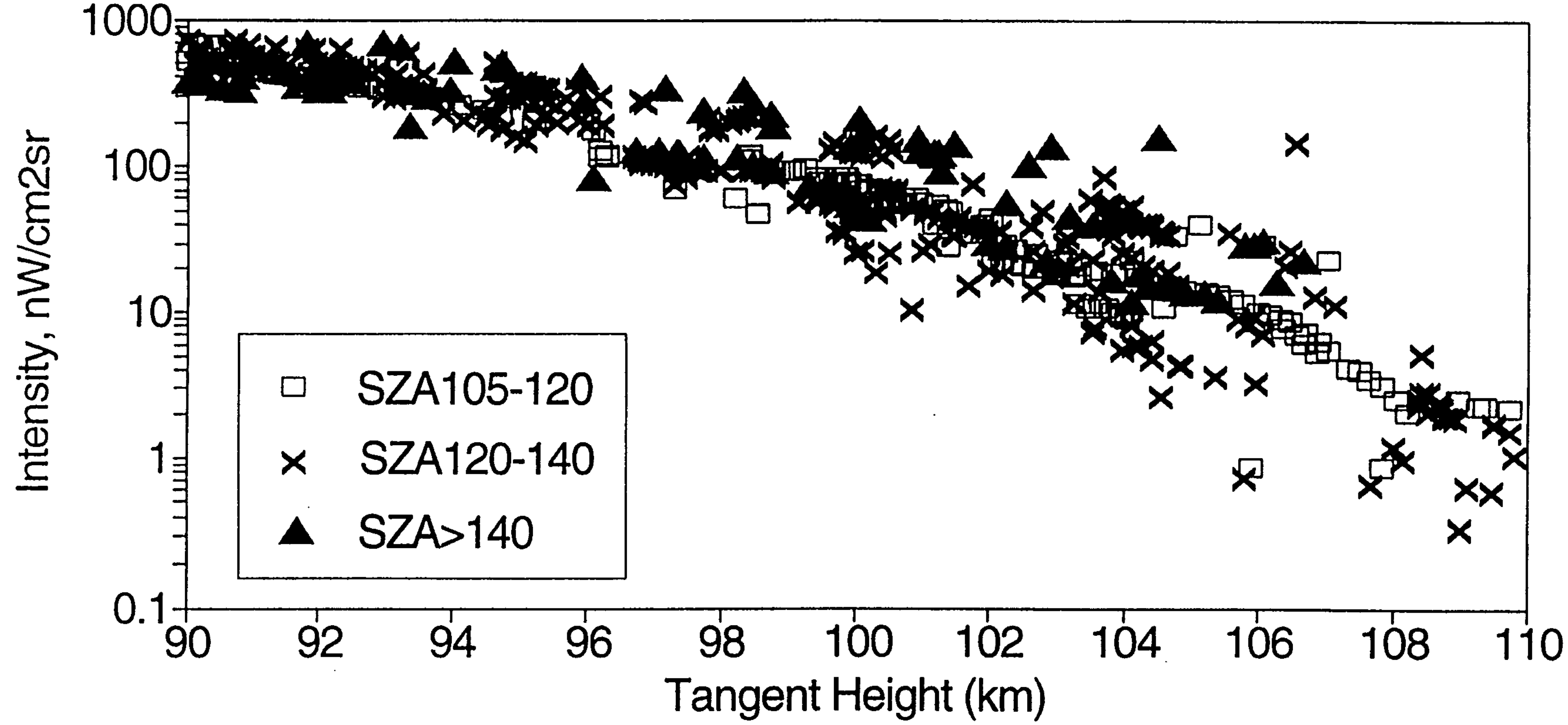

Sunrise Terminator Series 71.8 km Tangent Height

95-651

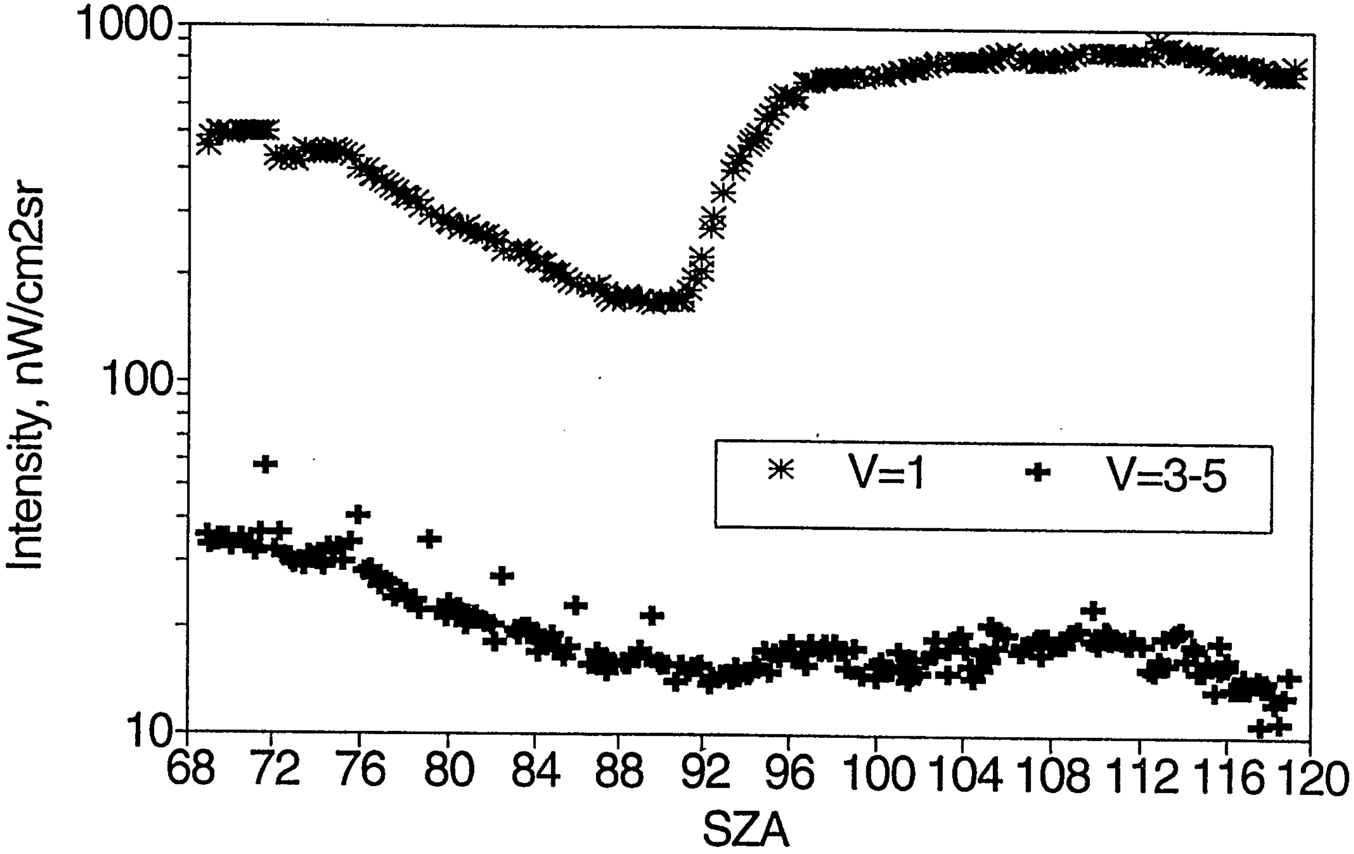

- Instantaneous O_3 photolysis
- 10 hr chemical production time dayside

Modeled Terminator Transient

Sunrise 72 km

95-652

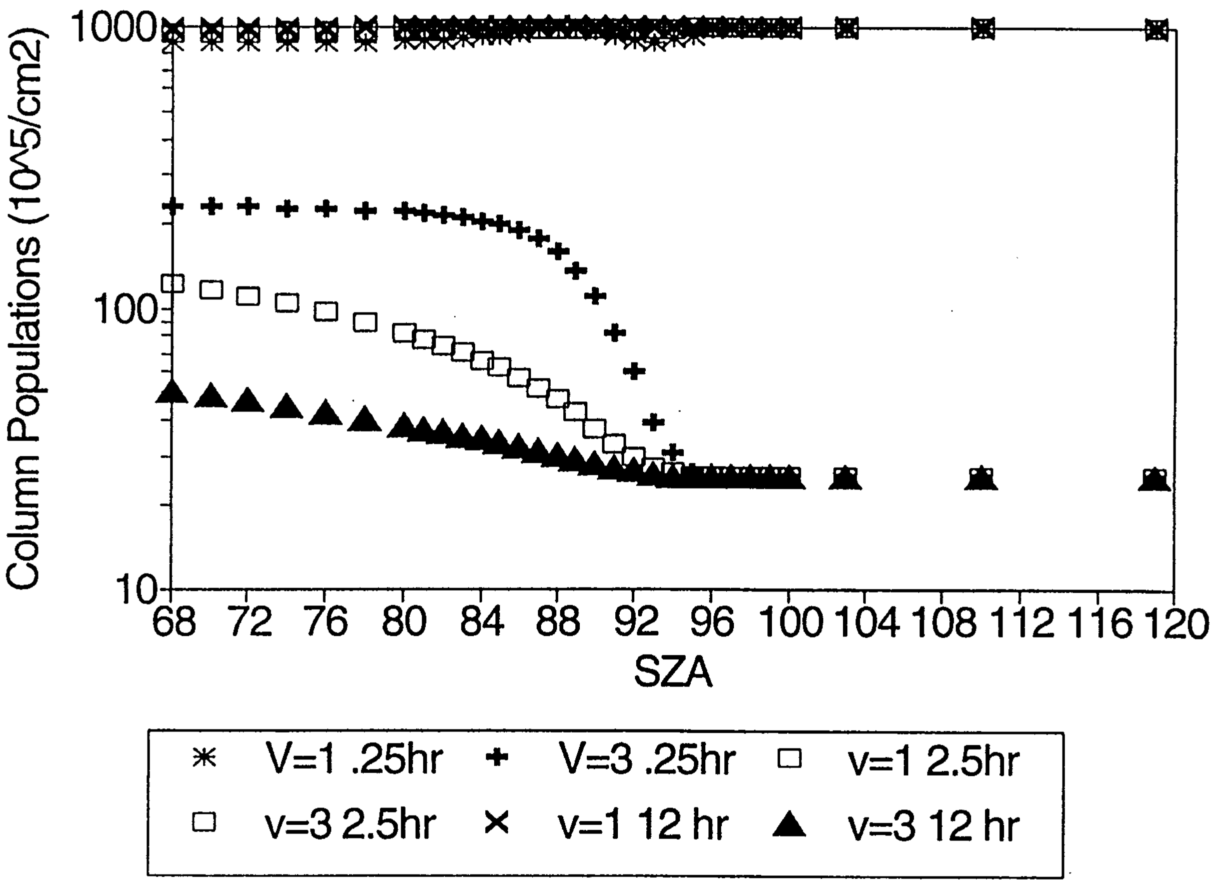

Sunset Terminator Series 104.5 km Tangent Height

95-653

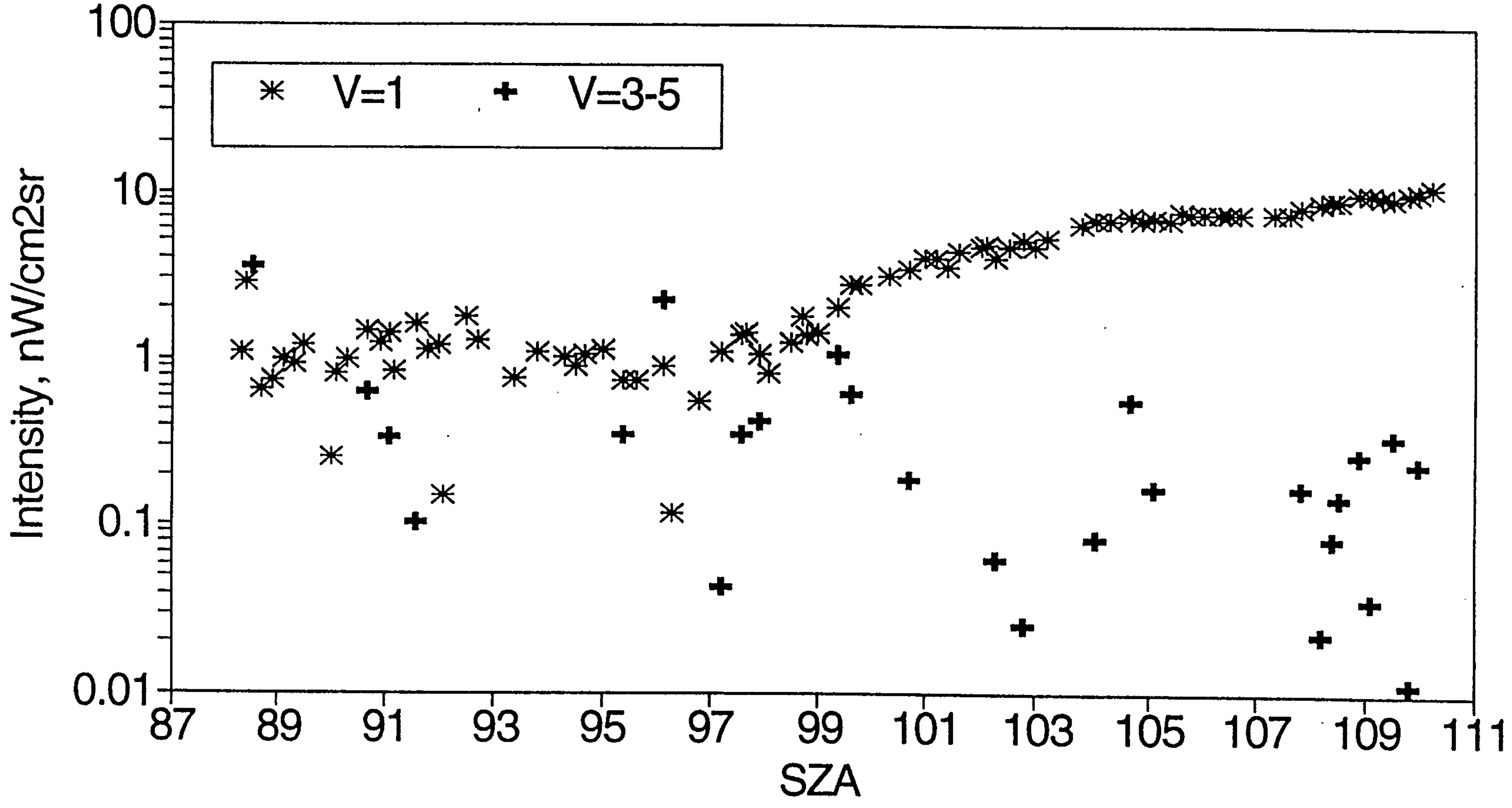

CIRRIS1A Ozone v=1 Latitude Variation with Altitude

95-654

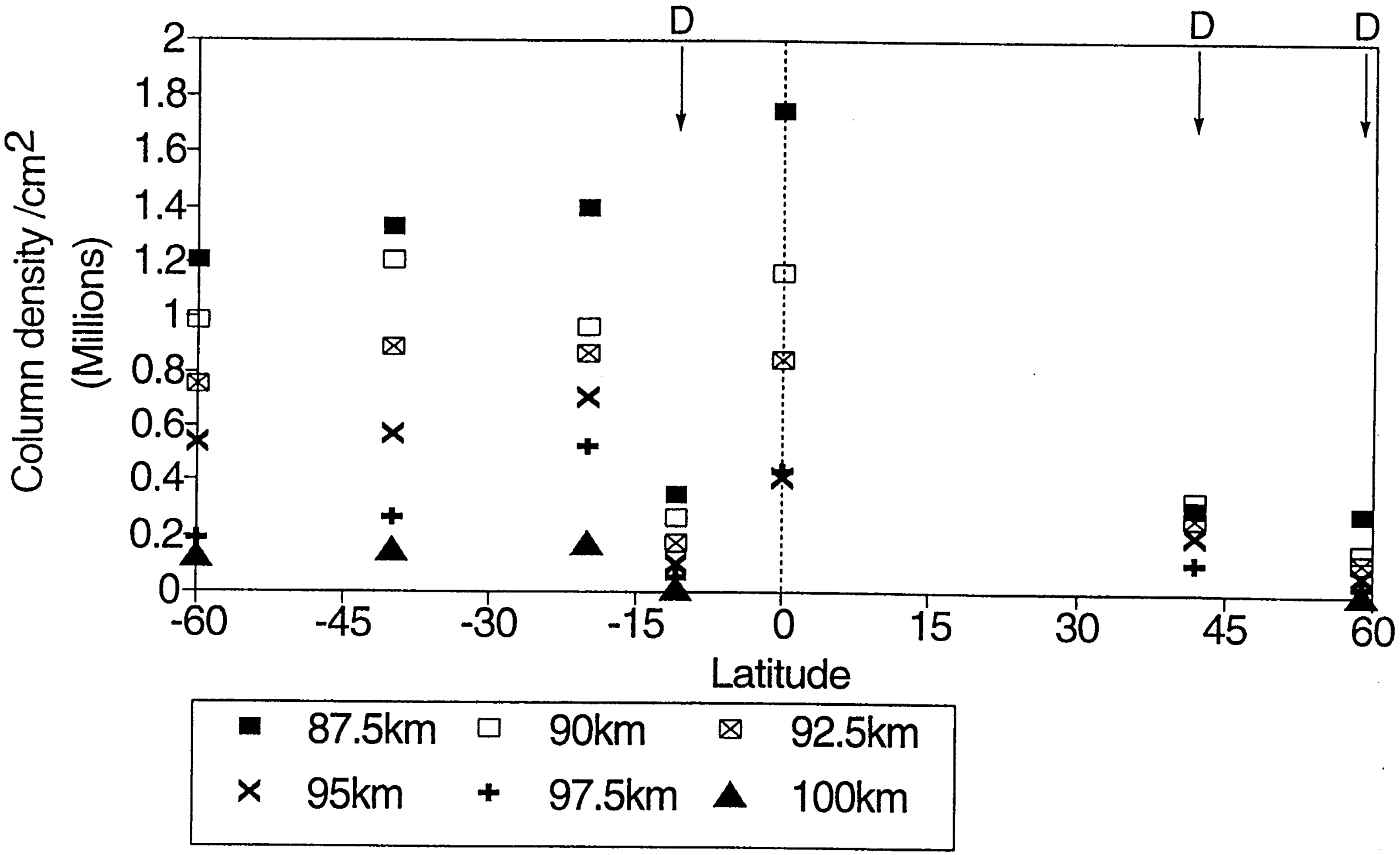

CIRRIS1A Ozone v=3 Latitude Variation

95-655

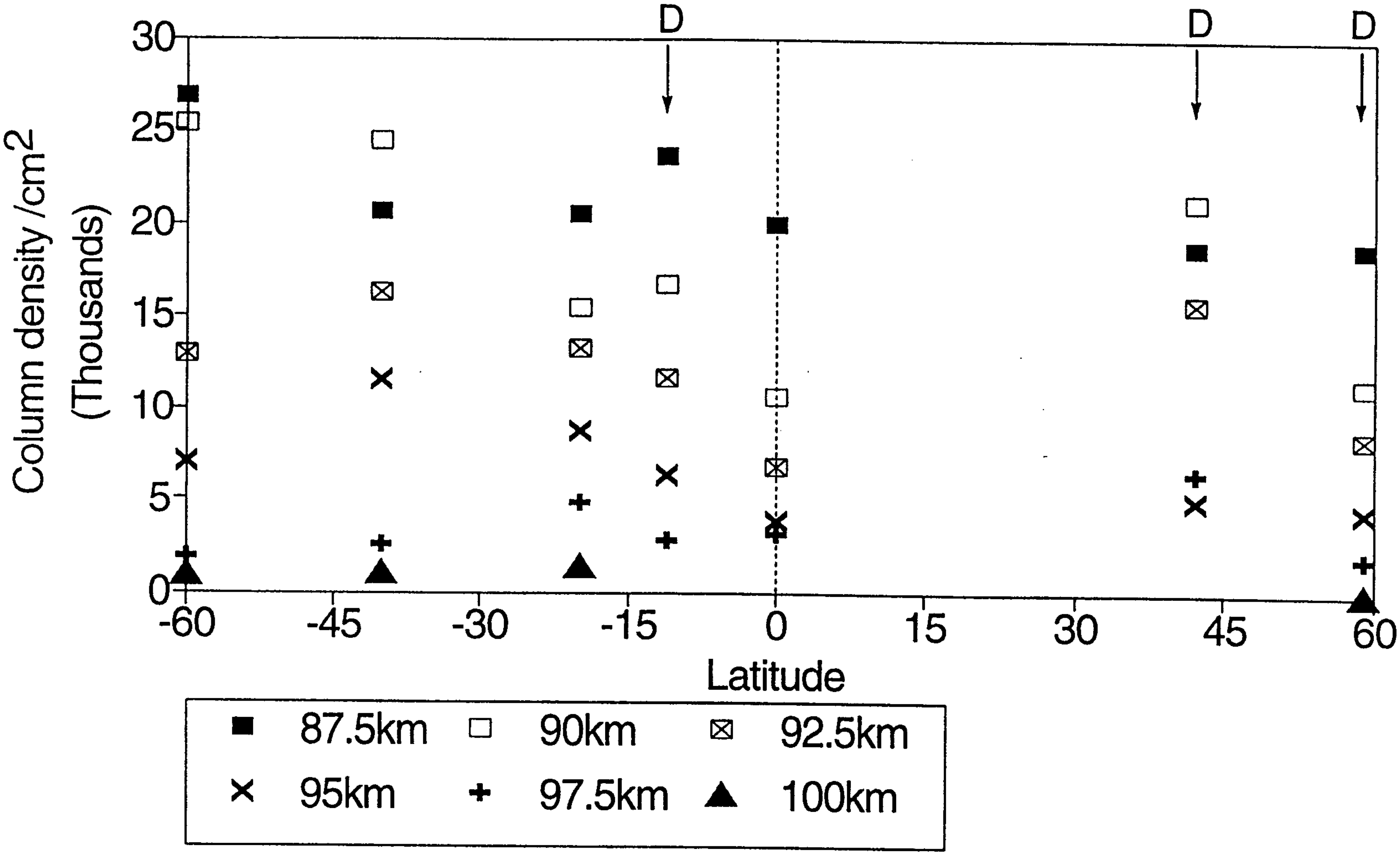

Daytime Ozone/CO_2 Ratio

95-656

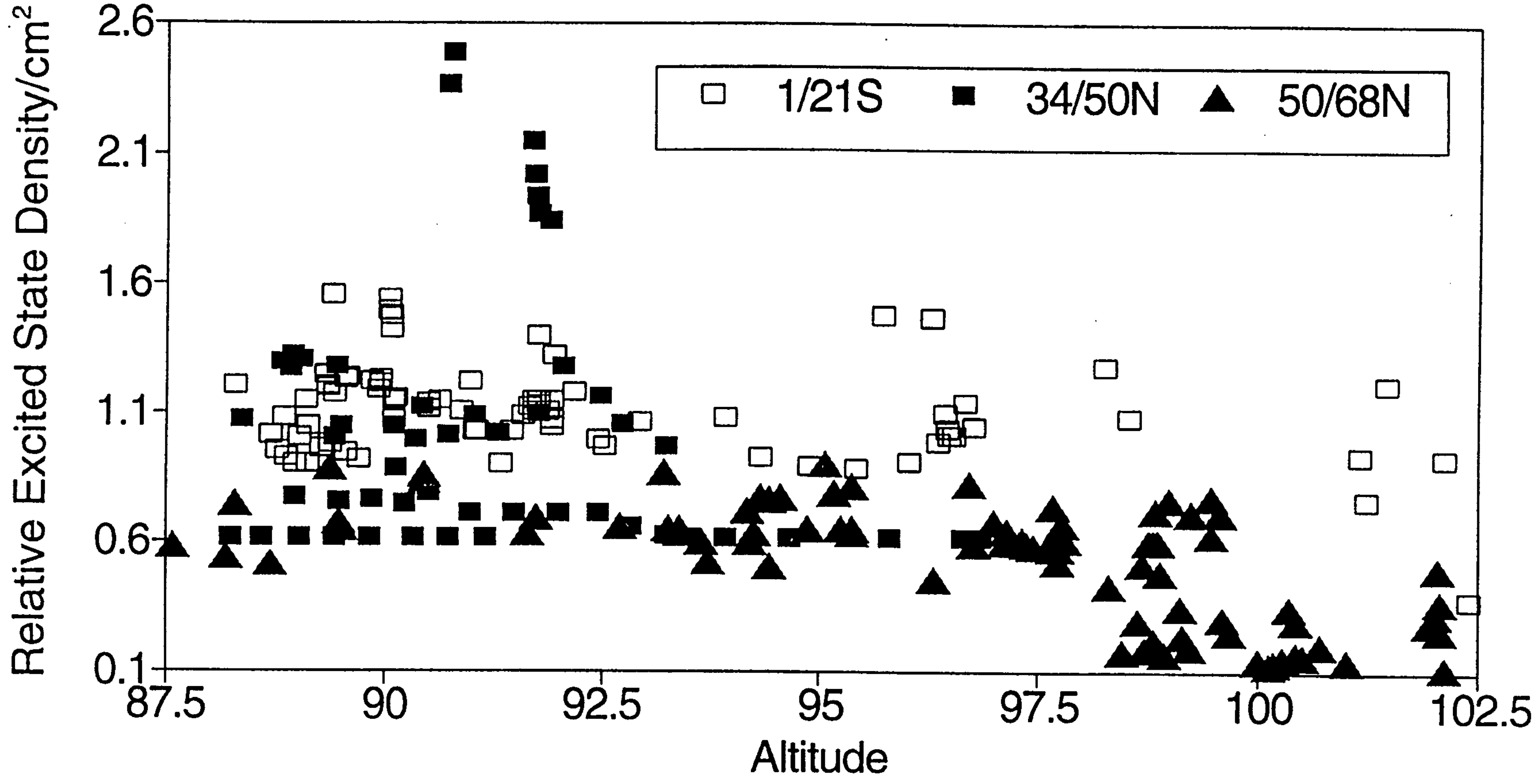

CIRRIS1A Ozone v=1 Altitude Variation

Night, 30 to 50 S

95-657

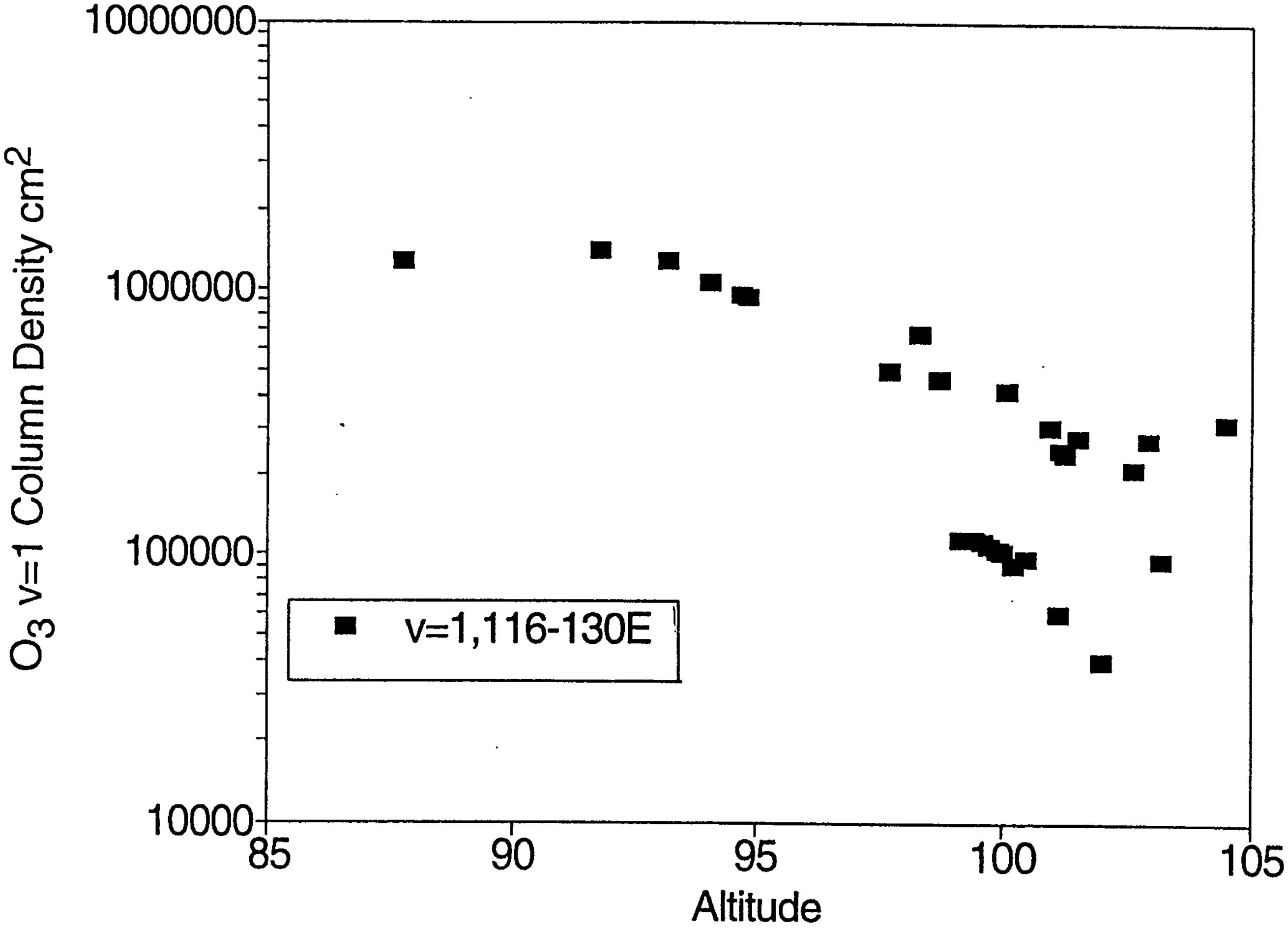

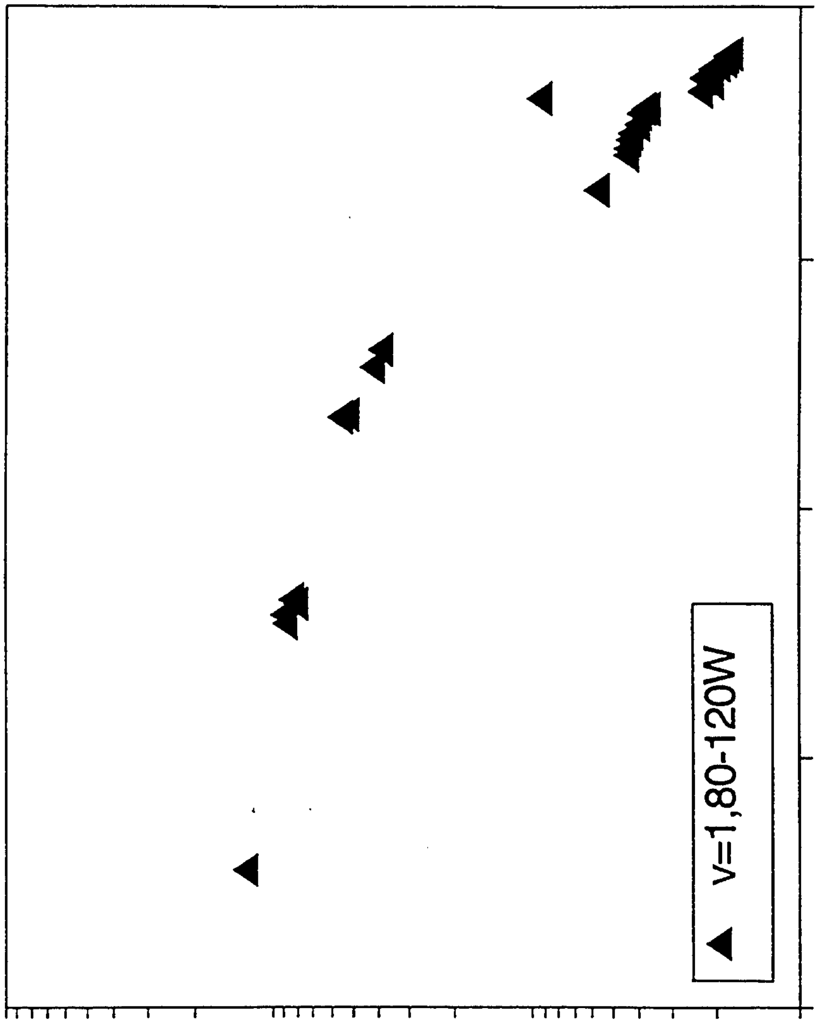
▲ v=1,80-120W

CIRRIS1A Ozone v=3, Altitude Variation

Night, 30 to 50 S

95-658

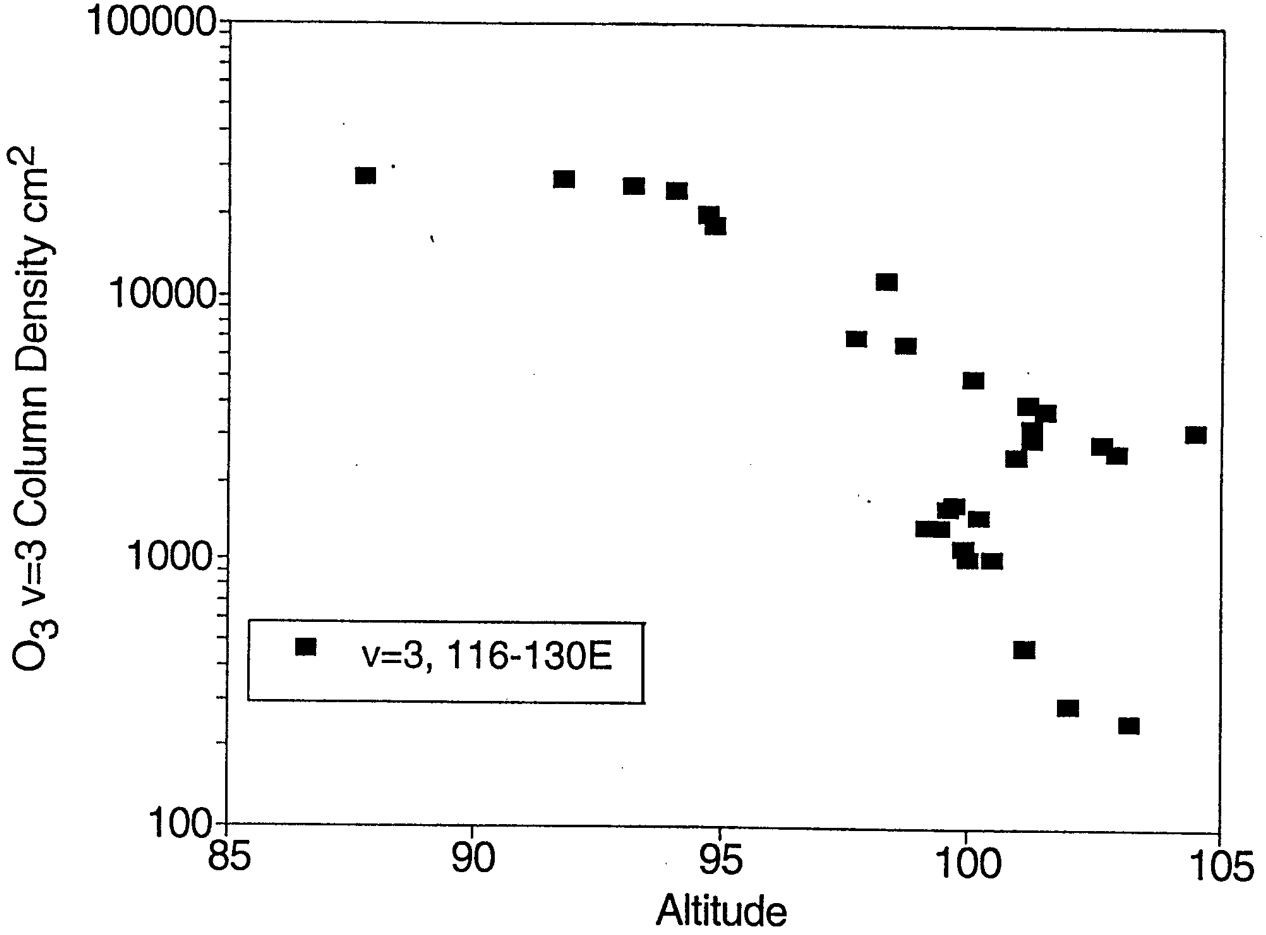

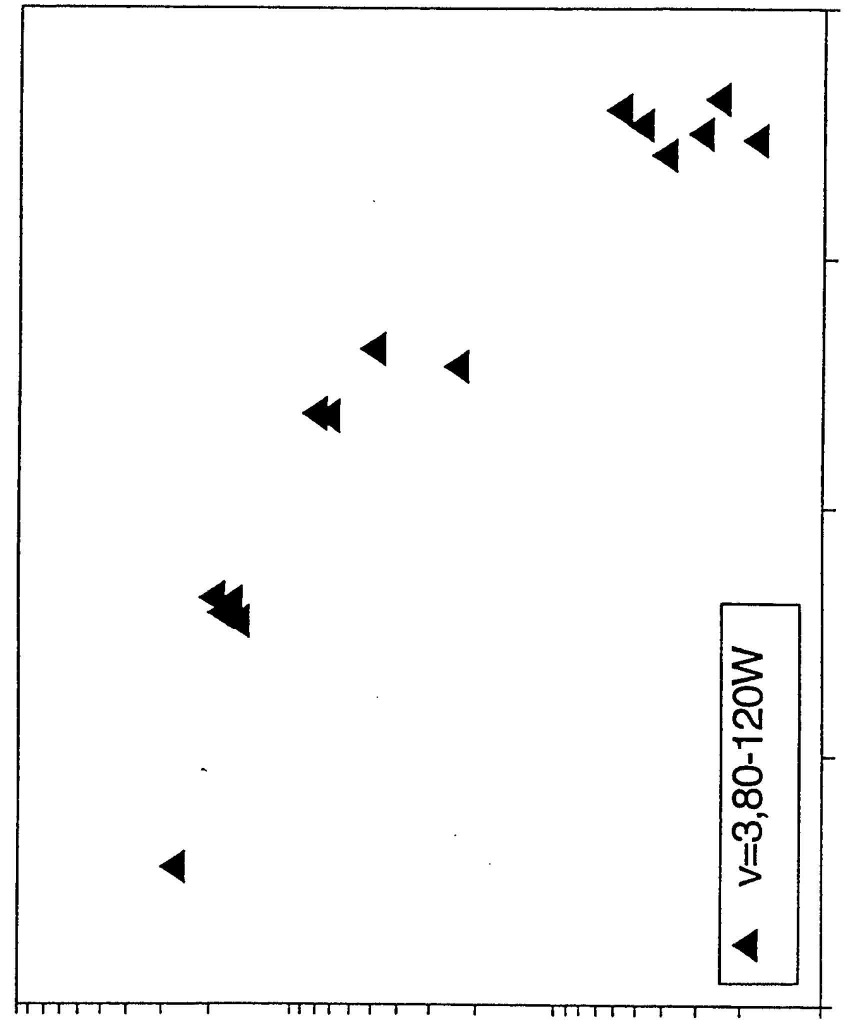
v=3,80-120W

CIRRIS1A Ozone v=1 Geomagnetic Scaling

Night, 30 to 50 S Latitude

95-659

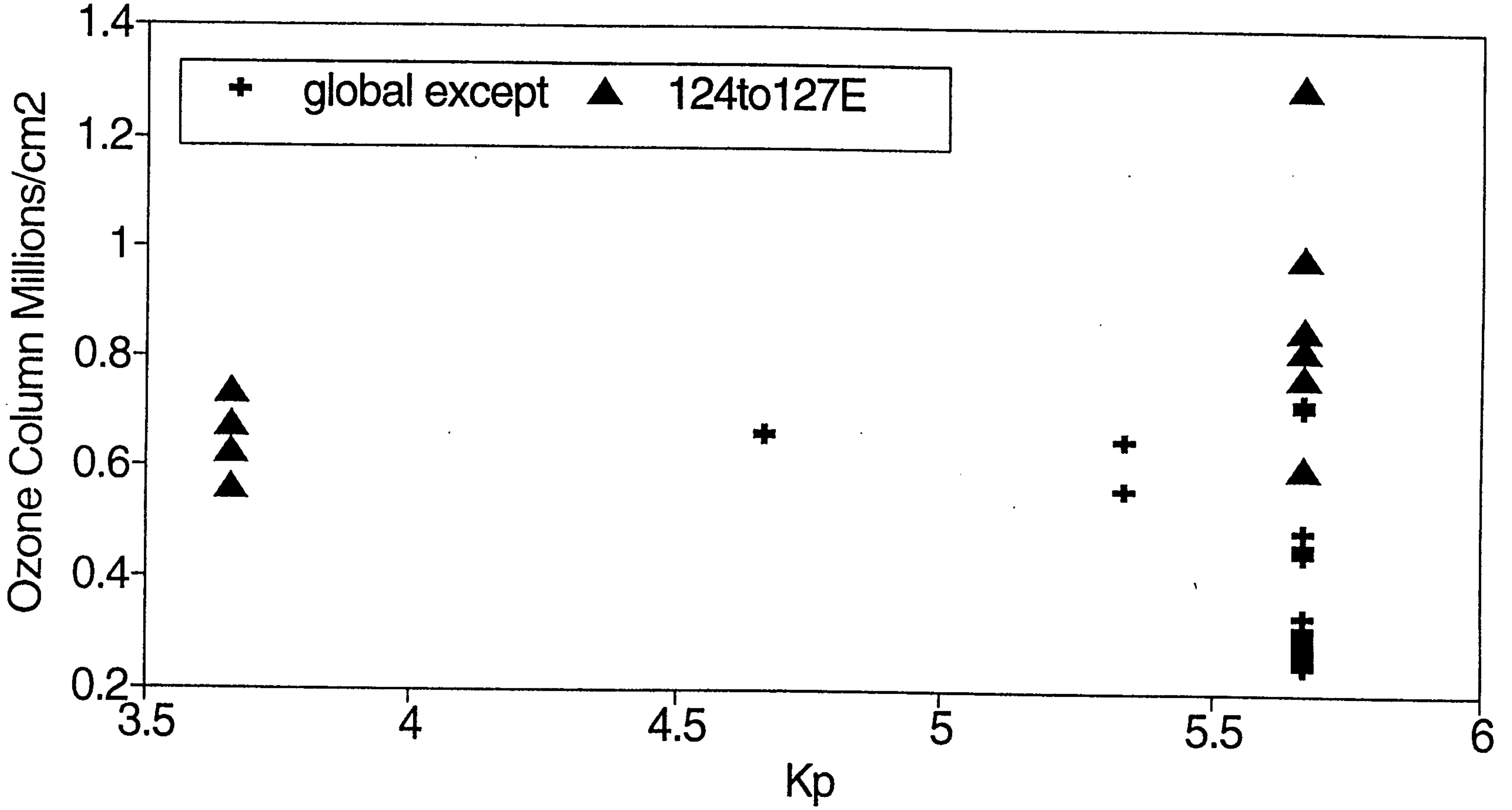

CIRRIS1A Ozone/CO_2 Ratio Geomagnetic Scaling

Night, 30 to 50 S

95-660

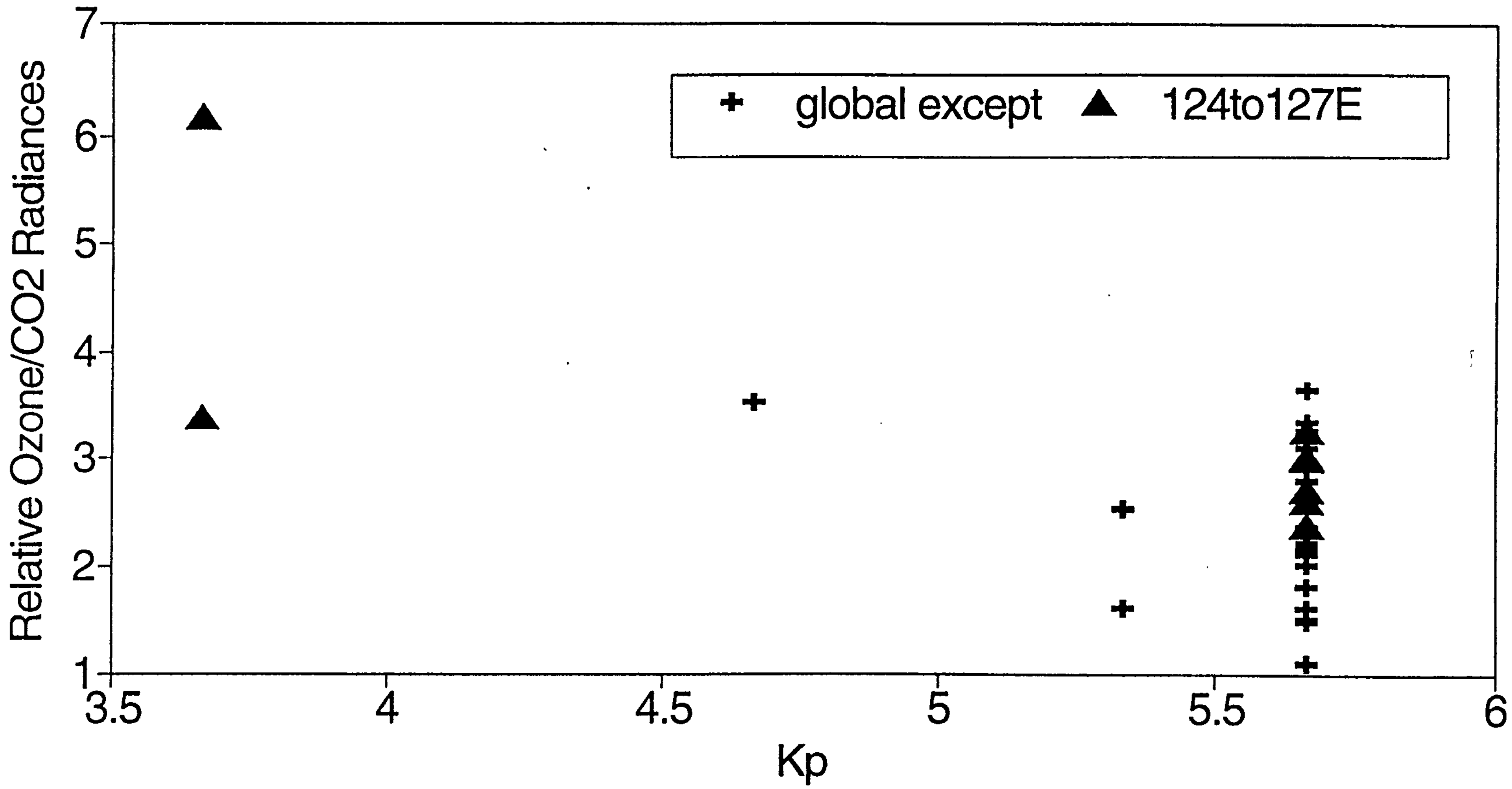

Conclusions

95-661

- Review and analyze 4000 interferometric spectra
- Internal state distribution consistent with three-body recombination
- Ozone > order of magnitude spatial variability above mesopause
- Diurnal variability magnitude (O, O_3) as expected
- Variabilities not due to kinetic uncertainties
  — dynamics (or additional processes)?
- Evidence of enhanced equatorward transport of ozone from auroral zone

APPENDIX 11

Ozone Variability Near the Mesopause from the CIRRIS 1A data

Ozone Variability Near the Mesopause from the CIRRIS 1A Data

B.D. Green and W.T. Rawlins
Physical Sciences Inc. Andover MA

and

S.J. Lipson, P.S. Armstrong, W.A.M. Blumberg
Air Force Research Laboratory Hanscom AFB MA

1. INTRODUCTION

The CIRRIS 1A mission (Ahmadjian et al., 1990) acquired the first global infrared atmospheric emissions data base during a several day mission in 1991. They successfully obtained over thirty hours of observation time of emissions from the daytime and nighttime, quiescent and aurorally disturbed mesosphere and thermosphere using a cryogenically-cooled, telescoped interferometer and radiometers.

Detailed fitting was performed of selected representative spectra to determine emitting states and to determine whether the high quality radiance data from the upper atmosphere can extend the laboratory data on the ozone formed by the three-body reaction of O with O_2. We performed analyses to extract: new spectroscopic constants for very highly vibrationally excited states with energies near the dissociation limit; the chemiluminescent vibrational distribution produced in the thermosphere; and the level-dependent quenching of the excited states as a function of altitude.

Based on this information, we next quantified variability in ozone and atomic oxygen over the entire global database using bandpass radiances for insolated and nighttime conditions as a function of altitude. Transients upon terminator crossings were analyzed for several tangent point altitudes. Comparison to photochemical models indicates that ozone variability increases with altitude and can not be due to transport alone.

2. CIRRIS 1A MISSION AND OZONE DATA

The primary optical instrument was a cryogenically cooled Michelson interferometer of the flex pivot design and a co-aligned radiometer array. The entire optical system operated at cryogenic temperatures to permit detection of faint atmospheric emissions with the detectors cooled to 12 K by close thermal linkage to a liquid helium reservoir. The cryogen was replenished as close as possible to Shuttle launch. The 0.3 m diameter gimbaled, telescoped optical system was carefully designed to permit accurate observation of the faint emission from the tenuous upper atmosphere with good rejection of the emission from lower altitudes and the hard earth. The primary mirror had an active area of 1065 cm^2. The focal plane array consisted of five detectors. All were located nearly on-axis within the central fringe and possessed comparable resolution. They were sized to provide tangent point altitude footprints of 2.2, 2.9, 6.7, and 14 km, with somewhat larger horizontal spatial extent. We selected data from detector 4 for these analyses due to its superior noise performance and its 2.2 km vertical and 7 km horizontal footprint that is smaller than the atmospheric scale height.

A filter wheel was located at the aperture stop. These constrained the radiances to fixed bandpasses to decrease the photon noise on the detectors from bright out-of-band emitters (such as CO_2 emission at 15 μm). Faint emissions present in atmospheric window regions could be observed and accurate spectrally resolved data obtained using the high throughput interferometer. In this analysis we used the 11 to 13 μm , 8 to 13 μm, and 4.7 to 13 μm bandpass filters. The interferometer scan rate was fixed, but the scan length was selected to provide data with spectral resolutions of 1, 3.3, and 8 cm^{-1}.

The CIRRIS 1A experiment was manifested on the STS-39 Shuttle Mission and launched on 28 April 1991 into a nearly circular 260 km altitude 57 deg inclination orbit. Cover opening and first data observations occurred 20 hours after launch. Data acquisition continued frequently over the next 43 hours until cryogen depletion and focal plane array warming terminated data acquisition. Because thruster firings were expected to produce bright near-field interfering radiances, thrusters firings were minimized by decreasing the pointing accuracy requirement to a value corresponding to 5 km drift at the tangent point. This drift and pointing were recorded and the data assigned to its actual line-of-sight tangent point. A series of preprogrammed data collection sequences were used to target specific mission objectives. These included auroral and airglow signatures and structure, Variability and spatial structure near the mesopause were the specific target of many experimental sequences and a good global spatial sampling was obtained.

The use of database screening tools permitted rapid review and retrieval of selected data within the calibrated CIRRIS-1A radiance and pointing data set. We selected for analysis the LWIR ozone data “scans” at all three spectral resolutions for all observations with tangent point altitudes from 70 to 110 km. Over 4000 spectra comprised this initial data set.

Initial batch processing of the data sets was performed to produce radiance altitude profiles. These profiles did not follow a smooth altitude scaling. The profiles exhibited wide scatter, with radiances from many scans orders-of-magnitude larger than expected. Upon visual inspection, LWIR spectra in the 9 to 12 μm region of the outlying radiances were observed to be not ozone, nor even resemble molecular emission. We performed the arduous task of visually reviewing each of 4000 spectra in the initial data set to identify and remove spectral scans containing artifacts. These artifacts are likely arise from either interferometer scanning anomalies or from shuttle environmental perturbations affecting the ability to observe the far-field atmospheric signature. Over 32% of the spectra were eliminated via this screening process. The spectra removed had the wrong spectral shape, periodic high or low frequency oscillations running across the spectra, baseline offsets, or other clear indications that the spectra were corrupted and not representative of remote mesospheric emissions. The appear to arise from the detected radiance changing magnitude within an interferometer scan. Due to the regular occurrence and periodicity of the “noisy” spectra, we feel these are contaminated radiance from the shuttle thrusters rather than interferometer scan anomalies. In earlier work we quantified the optical contamination of CIRRIS data by near field particles and high-velocity gas phase interactions (Green et al., 1997a; Green et al., 1997b; Ahmadjian et al., 1992).

The scrubbed data set was then applied to extract upper atmospheric ozone production distributions through a detailed spectroscopic analysis.

3. DETAILED SPECTRAL ANALYSIS

Data from four observations exhibiting the highest quality signal to noise levels at 1 cm^{-1} resolution were thoroughly analyzed to identify ozone vibrational states contributing to the observed emission signatures. These limb emission spectra were from four tangent point altitudes of 71, 74, 86, and 98 km, selected to span the altitude regions that are optically thin. All data selected was from high northern latitudes. The spectrum observed from a tangent point of 86 km at high latitude during daytime is shown in Figure 1. Note the logarithmic intensity scale displaying the excellent dynamic range in the data. The noise level is well below the 10^{-10} W/cm-sr level. The bright ozone ν_3,v=1 feature dominates the spectrum from 1020 to 1060 cm^{-1}. The slowly decreasing radiances from 1020 toward 800 cm^{-1} are in the region of more highly vibrationally excited states. The feature between 920 and 990 cm^{-1} arises from the solar excited CO_2 ν_3->2ν_2 transition. Less apparent, but significantly contributing is the CO_2 ν_3->ν_1 feature between 1040 and 1090 cm^{-1}. The small scale spectral structure seems to be reproducible in all the spectra, indicating that the radiances may be attributable to molecular emissions, not noise.

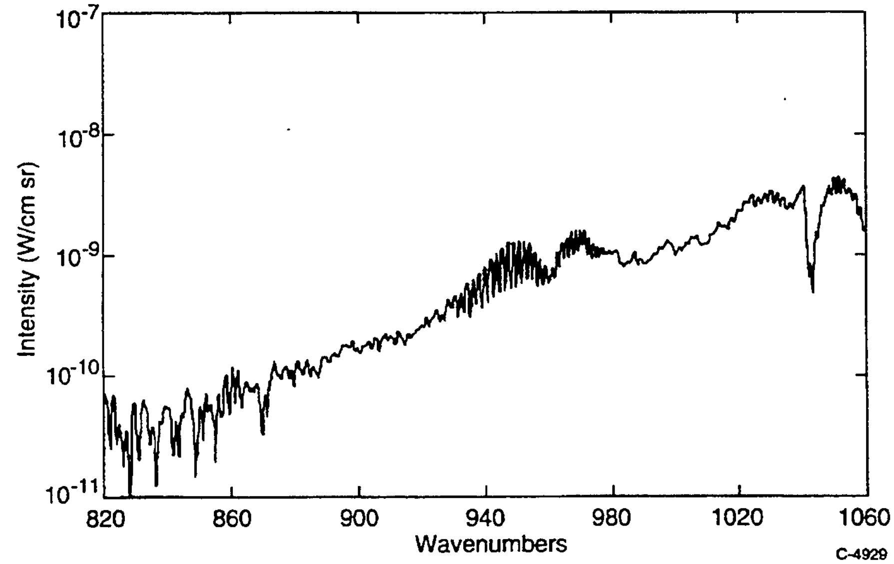

Figure 1. CIRRIS 1A SCAN 11E0250, 86 km tangent height, 61 deg North, 65 deg solar zenith angle.

To discriminate ozone from CO_2 emissions and to identify states contributing to the observed fluorescence, the four atmospheric spectra were subjected to a detailed comparison with theoretically predicted ozone emission from each vibrational level using experimentally determined spectroscopic constants and radiative lifetimes (Rawlins et al., 1987a,b; Upschulte et al., 1994). Both spectral smoothing and baseline corrections were applied before spectral fitting. In this process, the populations of the ozone states are adjusted to minimize the squares of the differences between the experimental data and theoretical spectral distribution at all wavelengths. The emissions from different vibrational states have considerable spectral overlap. The least-squares fitting process permits accurate population determination even under these severely overlapped conditions (Fraser et al., 1988). We considered the entire 820 to 1060 cm^{-1} spectral region for ozone population determination using three approaches: including seven excited states with only ν_3 quanta excited; including ν_1,ν_3 coupled dyads (101,002; 102,003;...) with up to seven energy quanta; and including ν_1,ν_3 and ν_2,ν_3 coupled dyad states (101,002; 012,111; ...) with up to twelve quanta in the analysis. These vibrational states have energies up to 6700 cm^{-1}, corresponding to over 75% of the ozone bond energy. Spectral contributions from states up to these energies are clearly are detected in the atmospheric radiances, filling the entire 9.4 to 12 μm spectral region.

We determined that the spectral signature was well described by including the ν_1,ν_3 and ν_2,ν_3 dyads in the spectral fitting. Emission from the computed best match to the observed daytime radiance at 86 km is displayed in Figure 2 on a linear intensity scale. The corresponding comparison at 86 km during the nighttime is shown in Figure 3. The vibrational state populations producing the best match to the observed radiance spectrum is shown in Figure 4. Hot band emission and spectral structure from ozone excited states was detected out to beyond 12 μm, demonstrating the excellent quality of the data base.

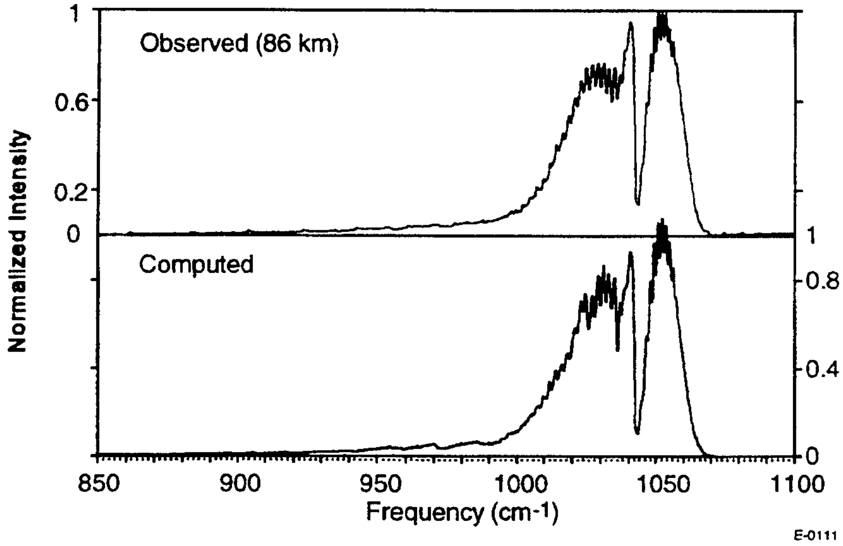

Figure 2. CIRRIS 1A fluorescence: night

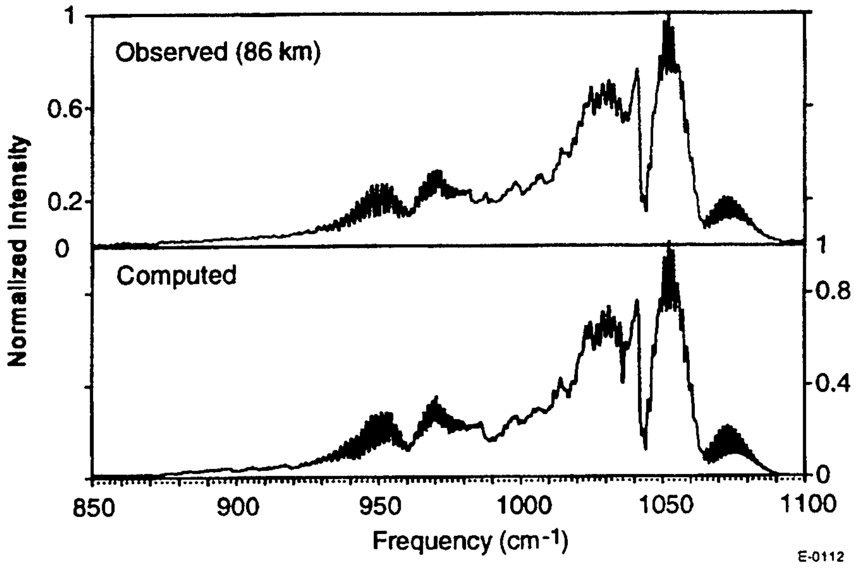

Figure 3. CIRRIS 1A O_3, CO_2 fluorescence: day.

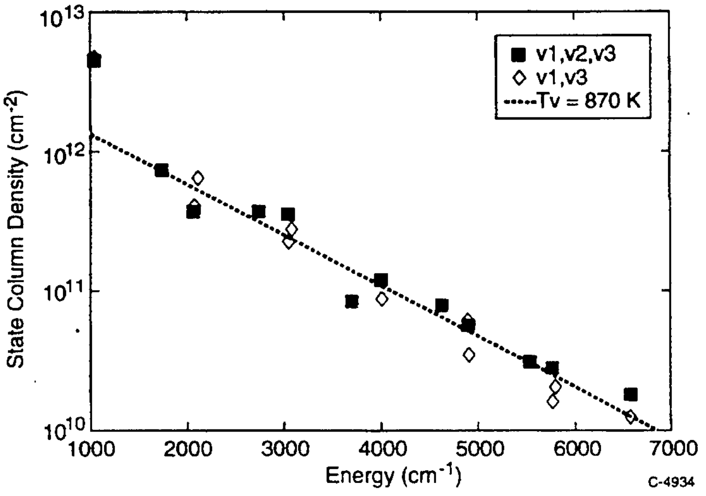

Figure 4. CIRRIS 1A ozone nighttime vibrational distribution (86 km).

The distribution derived from the 86 km data is very highly excited, decreasing only slowly with energy. Although the distribution is not expected to be described by a Boltzmann temperature, the excited state populations do fall off with energy in the same manner as a distribution with a 870 K temperature as shown in Figure 4. Similar analyses of radiances from other altitudes produce excited state distributions with up to 6700 cm^{-1} of vibrational energy.

The excited vibrational state distribution does change with altitude in response to level dependent vibrational relaxation. The distribution observed at 98 km, as shown in Figure 5, should be nearly free of relaxation, and thus reflect the radiatively-relaxed nascent distribution produced upon recombination. The distribution at this altitude is roughly described by a temperature of 1800 K. Rawlins (1985) has modeled the expected distribution based upon laboratory measurements of distribution $O + O_2 + M$ at low temperature and pressure and upon experimentally supported theoretical Einstein coefficients. The distribution predicted by this model for 100 km altitude is also plotted in Figure 5. The model agrees closely with the absolute excited state column density, but decreases with vibrational energy more somewhat more rapidly than the CIRRIS 1A data.

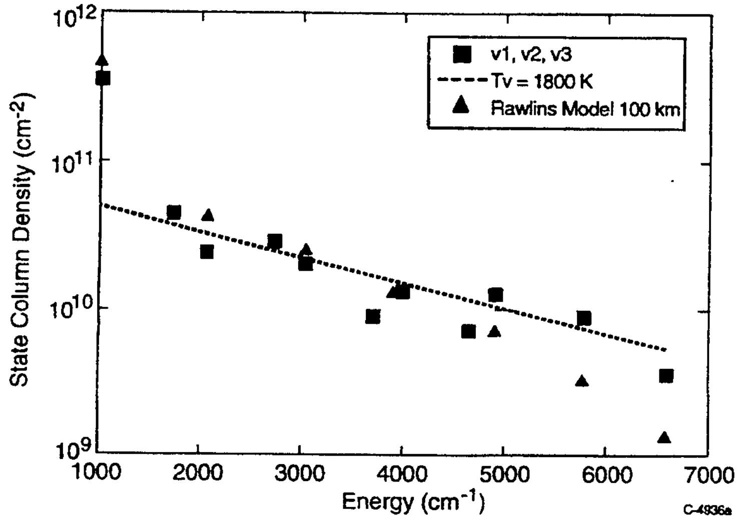

Figure 5. CIRRIS 1A O_3 nighttime vibrational distribution (98 km).

The variation of the observed distribution with altitude permits the relaxation rate of the vibrationally excited states to be estimated. Relaxation rate coefficients were derived from the population distributions at several altitudes assuming single quantum relaxation and atmospheric concentrations calculated using MSIS86. The resulting values with error bars are displayed in Figure 6 for ozone states with two through seven quanta of vibrational relaxation. The estimated rate coefficients are quite slow, increase rapidly with vibrational level, but are all much less than 1% of gas kinetic and follow a v^2 or e^v scaling. The values derived by careful laboratory experiments (also assuming single quantum relaxation) are plotted in Figure 6 (Upschulte et al., 1994). The values for 2 and 3 quanta are lower than the CIRRIS-1A aeronomic values, but overlap at the limits of their error bars. Also shown for comparison are rate coefficients derived from spectrally resolved CVF spectrometer data as part of the SPIRE mission also observing the northern high latitude mesospause region near terminator (Green et al., 1986). The rates for 4 through 6 quanta states derived from the SPIRE data are less than the CIRRIS 1A values by 5×10^{-13} cm^3s, but exhibit a similar trend with vibrational level.

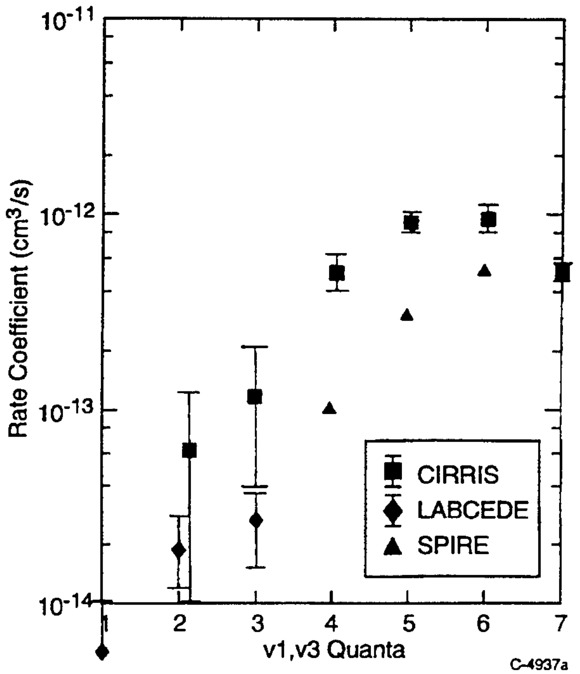

Figure 6. Relaxation of ozone excited vibrational levels.

Evidence for emission from (ν_1,ν_3) and ν_3 states with up to seven quanta were clearly observed due to the excellent dynamic range of the CIRRIS 1A data. However, emission did not extend to levels above those observed in the laboratory chemiluminescence experiments. Thus no new spectroscopic information on ozone highly excited vibrational states could be derived. The observed distributions are consistent with three-body recombination as the exclusive source of nighttime ozone chemiluminescence. Thus the ν_3,v>1 emission is produced by recombination and is proportional to atomic oxygen. The ν_3,v=1 emission is dominated by collisional and earthshine pumping of ground state ozone, and thus proportional to its density. The emission from these states may be independently used to remotely monitor local O and O_3 densities (Rawlins, 1985).

4. OZONE VARIABILITY

Armed with knowledge of the ozone excited states contributing to the observed radiant signatures, we next undertook an analysis of the entire CIRRIS 1A ozone data set to extract variabilities due to spatial, latitudinal, and solar effects.

The 2740 uncorrupted spectra were too numerous to permit detailed spectral fitting at the level described in Section 3. To characterize the large data base, we integrated the spectra over ten bandpasses within the ozone feature to permit trends in ν_3,v=1, hotband, and CO_2 radiances to be extracted. The bandpass wavelengths were selected based on our spectral fitting analysis isolate the ozone v=1 R branch (scalable to total ozone) , v=3 (scalable to atomic oxygen density), and other ozone hotbands emissions, while carefully accounting for baseline intensity changes and the spectral interference from mesospheric CO_2 emission under sunlit conditions. The bandpass integrals were correlated with ozone excited state densities and employed to observe trends within and between data collection sequences as a function of altitude, latitude, solar zenith angle, and longitude.

The background corrected radiances in bandpasses containing ozone v=1 and v=3-5 emissions were sorted into bins centered at 5 km intervals to observe the altitude scaling. Figure 7 displays the ozone v=1 radiances as a function of solar zenith angle (SZA) for altitudes between 80 and 110 km. Note the logarithmic intensity scale. A clear change in magnitude is observed at terminator (SZA 93 to 97 degrees) at 80 to 90 km, but the transition becomes more gradual, but of larger magnitude, at 95 km and above. The radiances are from several data collection events with different geographic coordinates. Note that the 80, 90, 95, and 100 km data are each offset by *10 for clarity. Variation within data at comparable altitudes is about a factor of 2 at 80 and 90 km, but becomes a factor of 5 at 95 km and above. The noise level in this bandpass is about 10^{-9} W cm^{-2} sr^{-1}. Ozone emission above the noise level is observed up to 110 km altitude. There appears to a marked change in ozone behavior above 90 km. Ozone appears to remain constant during the night at lower altitudes, and rise during the night at higher altitudes.

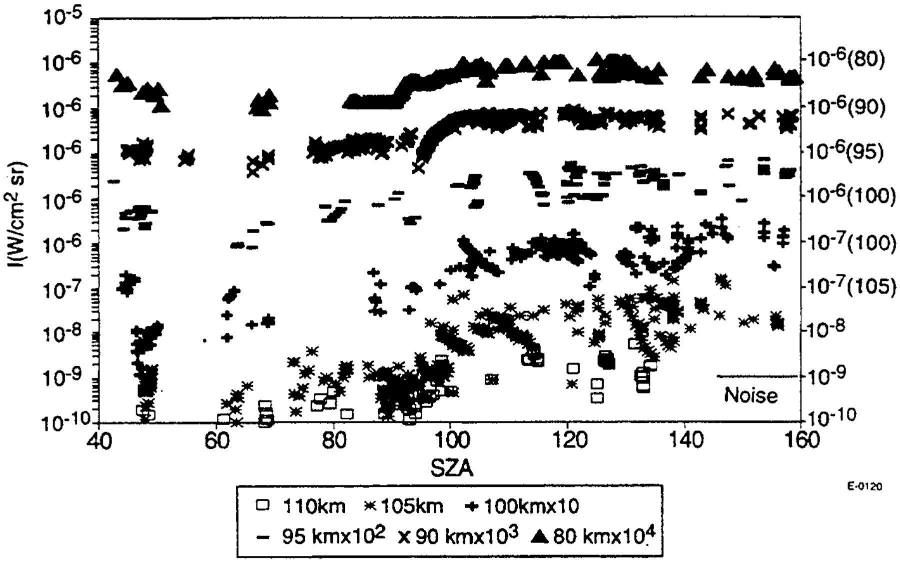

Figure 7. Ozone v_3 v=1 radiances as a function of SZA for several altitudes (offset for clarity).

The comparable radiance plot for the more vibrationally excited states of ozone (v=3 to 5) is presented in Figure 8, again with data from the lower altitudes offset for clarity. The radiances from these states are about 100 times less intense than the v=1 emission. Scatter between the data from different atmospheric parcels is <50% for 70 and 80 km altitudes, increasing to a factor of 2 at 85 km, a factor of 5 at 90 km and an order of magnitude as radiances fall into the noise above 100 km. In contrast to the v=1 radiances, the change at terminator is less pronounced for these states that are tracers for atmospheric atomic oxygen. Atomic oxygen is relatively invariant over the diurnal cycle at altitudes above 80 km. Note the factor of 3 increase in radiances at 70 km during the daytime.

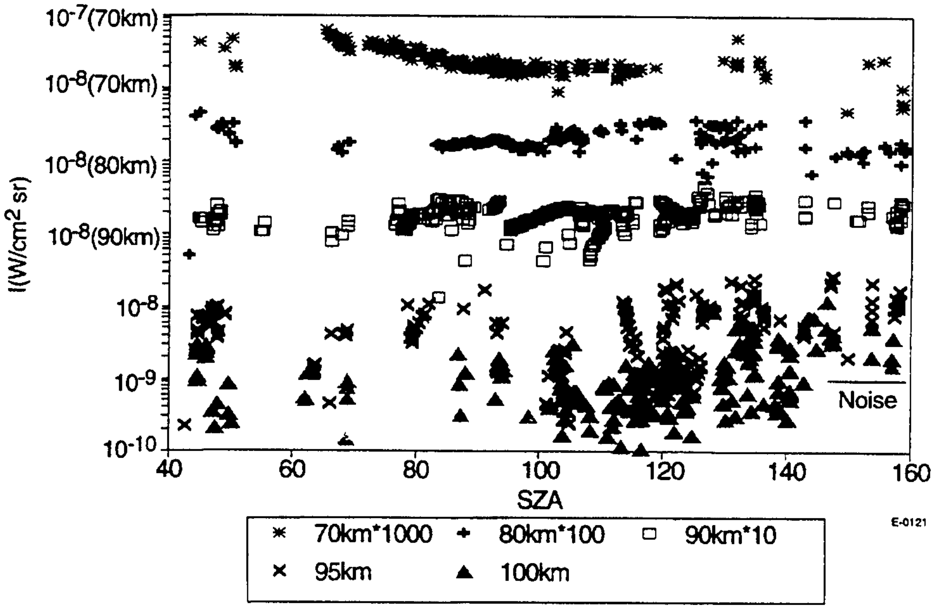

Figure 8. Ozone ν_3 v=3-5 radiances as a function of SZA for several altitudes (offset for clarity).

These radiances are the sum of the atmospheric ozone volumetric emissions along the line-of-sight path. Although strongly weighted to emission from the tangent point altitude for exponentially decreasing atmospheres, the ozone radiance altitude profile has a maximum between 80 and 85 km (Green et al., 1986; Rawlins et al., 1985) altering this weighting. Atmospheric column path inversion to create volumetric radiances will be undertaken in a future effort, and we emphasize column emissions above 85 km in this paper.

The CIRRIS 1A column radiances from v=1 for altitudes of 90 ± 2.5 km and 100 ± 2.5 km are displayed again in Figure 9. The variability is much greater at 100 km and is not attributable to noise as indicated. Rodrigo (et al., 1991) have modeled the variation of ozone over the daily cycle using a 1 dimensional photochemical model. We converted their predicted local densities to column radiances using the method of Green et al., 1986 and Einstein coefficients of Upschulte et al., 1994, assuming a v=1 vibrational temperature of 225 K during the nighttime, and 240 K during the day as appropriate during the CIRRIS 1A observation period (Zhou et al., 1998). The ozone v=1 radiances at 90 and 100 km based on this scaling of the Rodrigo model are also presented in Figure 9. Curves for both dawn and dusk terminator are indicated. Agreement with the CIRRIS 1A data for 90 km at night is quite good, but the daytime radiances(ozone concentrations) are under predicted by about a factor of three. The 100 km data lies an order of magnitude above the predicted radiances scaled from the model both day and night. Even the variability in the data does not encompass the model except for values near its noise level. We interpret this to mean that ozone above the 85 km layer is enhanced during the CIRRIS 1A mission period.

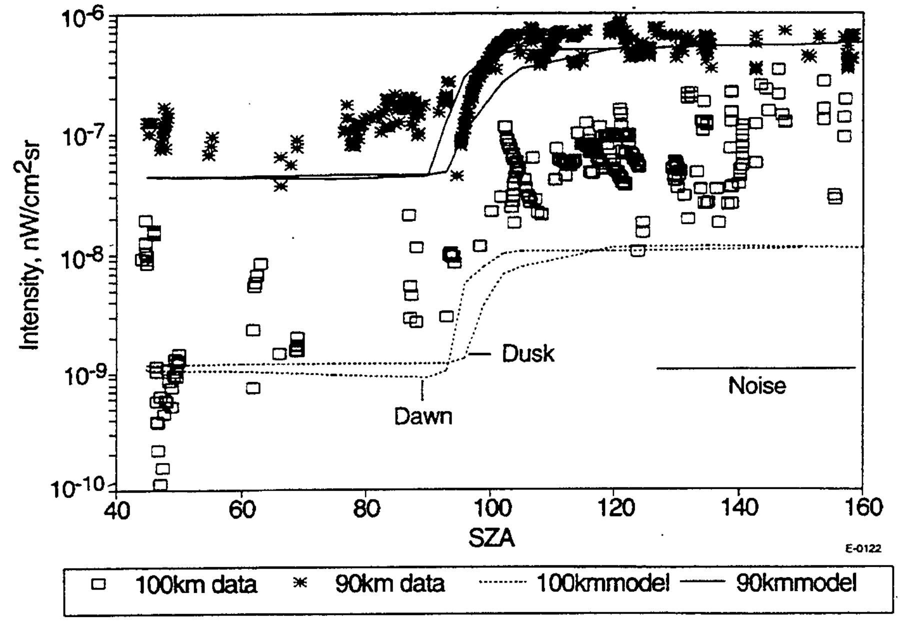

Figure 9. Ozone ν_3 v=1 radiances as a function of SZA for 90 and 100 km compared to model.

The ozone ν_3 v=1 nighttime radiances when plotted as a function of altitude display this variability more clearly as shown in Figure 10. Data collected during a single observation of the mesopause region follow a smooth trend with altitude. Different observational sequences have different magnitudes. The data in Figure 10 are grouped by SZA. The data near terminator seem to exhibit less variation than that at larger solar zenith angles.

Mid-latitude CIRRIS 1A ozone radiances from a mid-latitude observational sequence was converted to column radiances and compared to another observation and models as shown in Figure 11. The EXCEDE III suborbital mid-latitude mission (Rawlins et al, 1998) observed ozone with an interferometer with similar resolution. The upward looking radiances from atmospheric observations were converted to limb column densities and plotted on Figure 11. The agreement with the CIRRIS 1A data for both v=1 and v=3-5 is quite good, matching the altitude scaling and average values. Few data points differ from the EXCEDE trend by more than

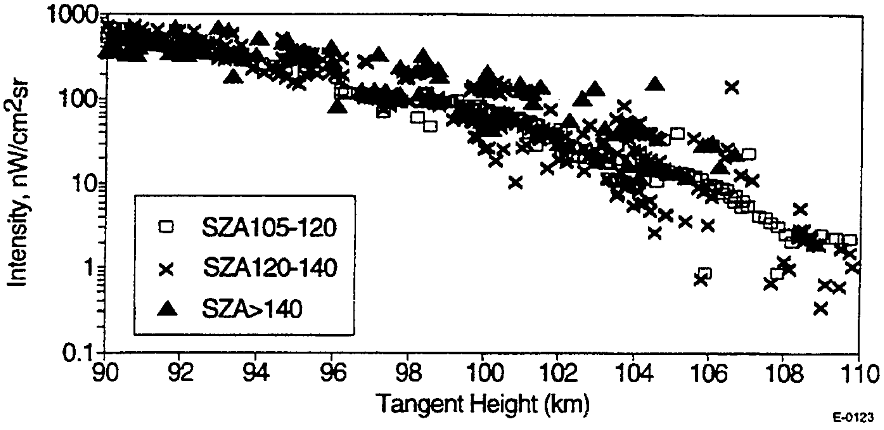

Figure 10. Nighttime ozone ν_3, v=1 radiances.

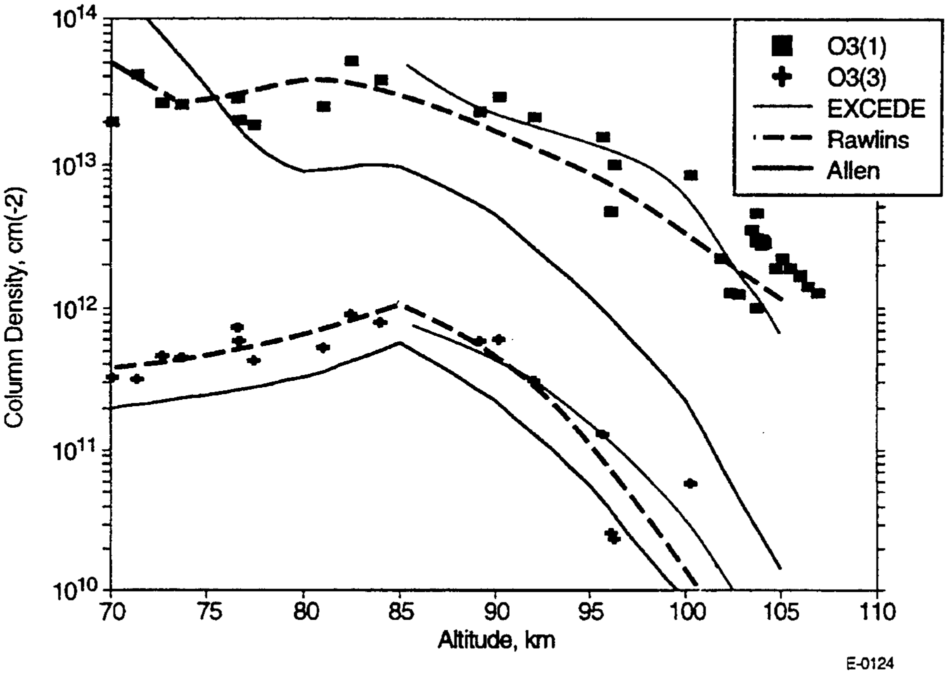

Figure 11. Comparison of nighttime CIRRIS data with EXCEDE data and models.

a factor of three. Also shown in Figure 11 are the 2D model predictions of Allen et al., 1984, and 1D kinetic model predictions of Rawlins (1985). The results of Rawlins, drawing on previous observational and laboratory data sets, exhibit excellent agreement with the EXCEDE and CIRRIS 1A column densities for both v=1 and v=3-5 over the full altitude range of the data. The model of Allen exhibits a much steeper decay of ozone with altitude than exhibited by the data.

A comparison of the model predictions with daytime mid-latitude CIRRIS 1A data is presented in Figure 12. The model by Rawlins falls uniformly a factor of 4 below both the v=1 and v=3-5 data except at the lowest altitudes. The Allen predicts even lower column densities and again falls off more steeply with altitude. Thus all three models (Allen, Rawlins and Rodrigo, Figure 9) predict 3-5 times less ozone than is observed during daytime conditions. Comparison of the CIRRIS 1A ozone data to the SHARC3 2D photochemical model has reported that the model under predicts the daytime ozone densities in this altitude region (Zhou et al., 1998). We conclude that additional processes must be considered in the models.

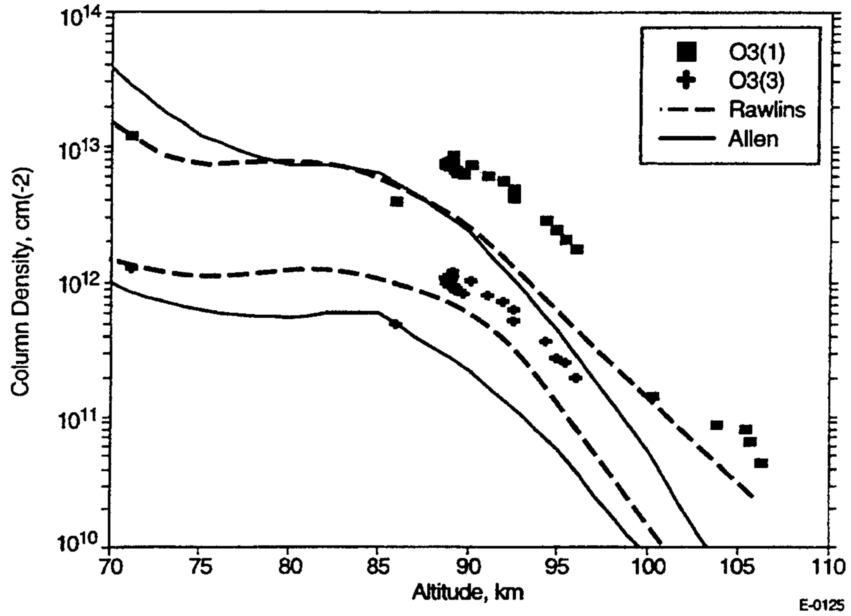

Figure 12. Comparison of daytime CIRRIS data with models.

As part of the CIRRIS 1A mission specific data collections were made with the goal of observing the transition of the atmosphere at terminator. The shuttle and telescope system were aligned along the direction of constant local time direction and fixed tangent point as closely as possible. The shuttle orbital motion moved the observation volume through terminator. A sequence of scans from an observation of the evening (dusk) terminator with 87.3 km tangent point altitude (15S to 39S latitude, 93W to 60W longitude) is shown in Figure 13. The excellent quality of the CIRRIS 1A data is evident through the small (<10%) scatter present within the data. There is a sharp order of magnitude increase in ozone v=1. Note that the ozone v=3-5 intensities (proportional to atomic oxygen) rise 50% then drop back to the levels at terminator. Predictions based on the model of Rodrigo (1991) are also displayed. The model prediction shown is for 87 km altitude and is based on our interpolation between their 85 and 90 km curves and assumes a 225 K v=1 vibrational temperature. The model agrees well with the magnitude of the observed data, and describes the terminator transient quite well. The data indicates that ozone recombination occurs more rapidly than predicted by the model, reflecting larger O concentrations than included in Rodrigo. This would correspond to [O] densities in excess of 10^{12} cm^{-3} at 87 km.

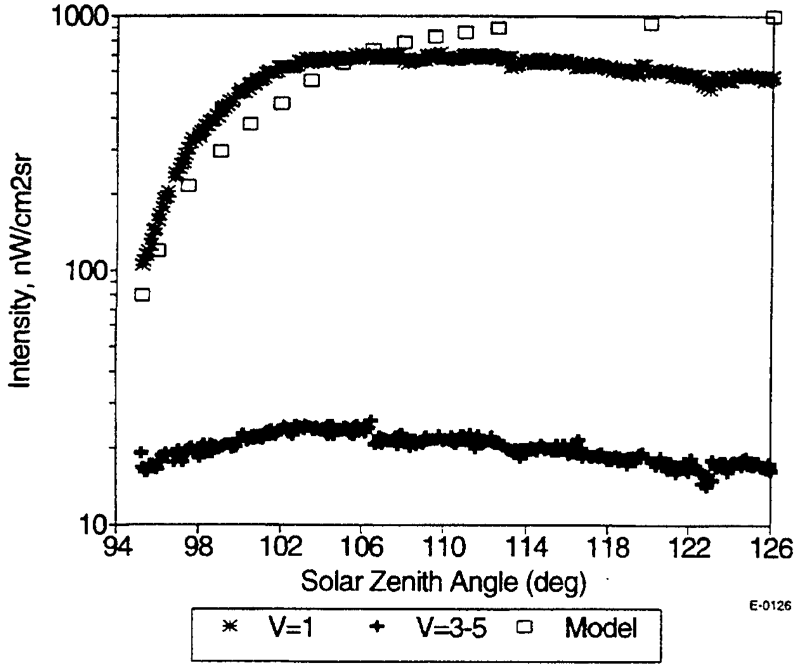

Figure 13. Mid-latitude dusk terminator radiances at 87.3 km from CIRRIS 1A and model prediction.

A pair of separate observation sequences at 105 km of the dawn and dusk terminators are shown in Figures 14 and 15. The dawn terminator sequence (6S to 18N latitude, 145E to 160E longitude) at 104.9 km tangent point altitude displays the quality of the data even at the limit of ozone detection. The Rodrigo model prediction at 100 km scaled to the CIRRIS geometry and radiances is also displayed. The transient at sunrise exhibits the same behavior as the data. The data are from 5 km higher altitude than the model and are thus expected to be less intense. Instead the day data match the model and the night data exceed the model by a factor of 4. The dusk terminator series (15S to 34S latitude, 98W to 79W longitude) compares very well with the 100 km model both night and day. The transient upon sunset is well described temporally, but the model prediction is offset from the data by about 2 degrees of solar zenith angle. This offset is well outside the emphemeres of the CIRRIS 1A pointing. Taken together, Figures 14 and 15 clearly demonstrate that ozone variations above 90 km are significant. The dawn radiances are a factor of 4 brighter than the dusk values as compared to model, yet the scatter within each data set is much less than this. We conclude that significant air parcel variations lead to the "scatter" of the data observed in Figures 7, 8, and 10.

A dawn terminator sequence at 71.8 km (8S to 37N latitude, 160E to 160W longitude) is shown in Figure 16. The ozone v=1 radiances decrease by a factor of 5 upon sunrise, but then slowly rise again during the day (with a two hour characteristic time) until nearly reaching nighttime levels. The v=3-5 states increase in intensity reflecting the rise in atmospheric atomic oxygen at these altitudes during the day. The daytime increases of v=1 and v=3-5 are both proportional to [O], and both exhibit the same slope of this logarithmic intensity plot.

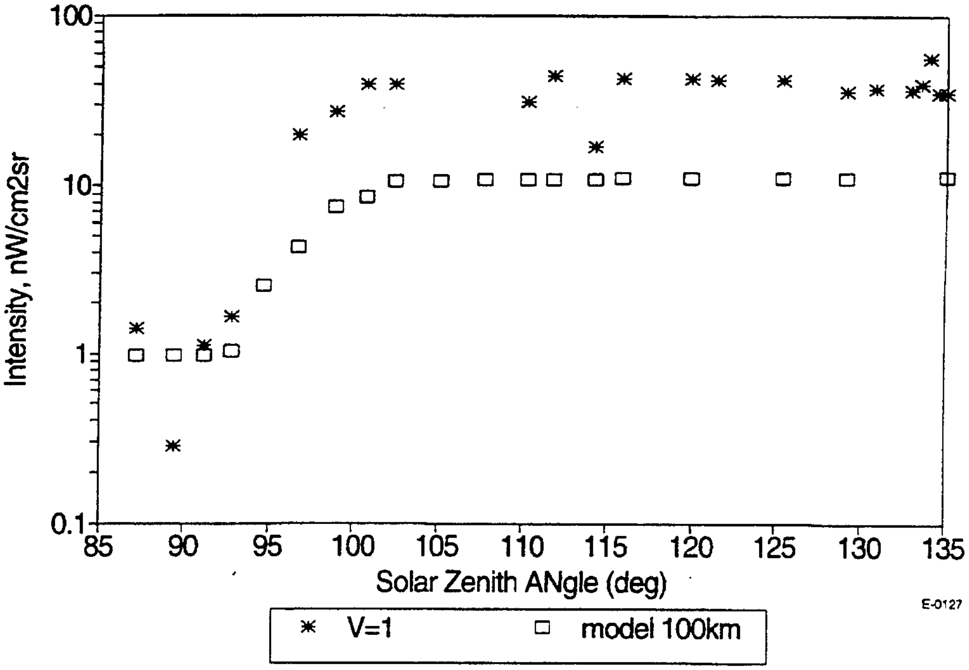

Figure 14. Dawn terminator radiances at 104.9 km from CIRRIS and model prediction.

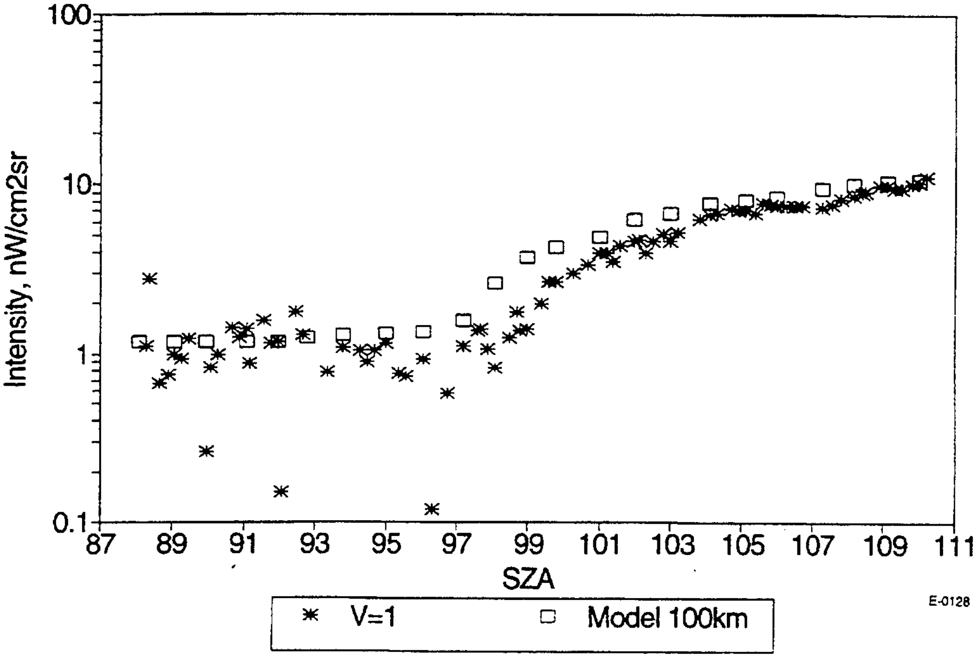

Figure 15. Dusk terminator radiances at 104.5 km from CIRRIS and model prediction.

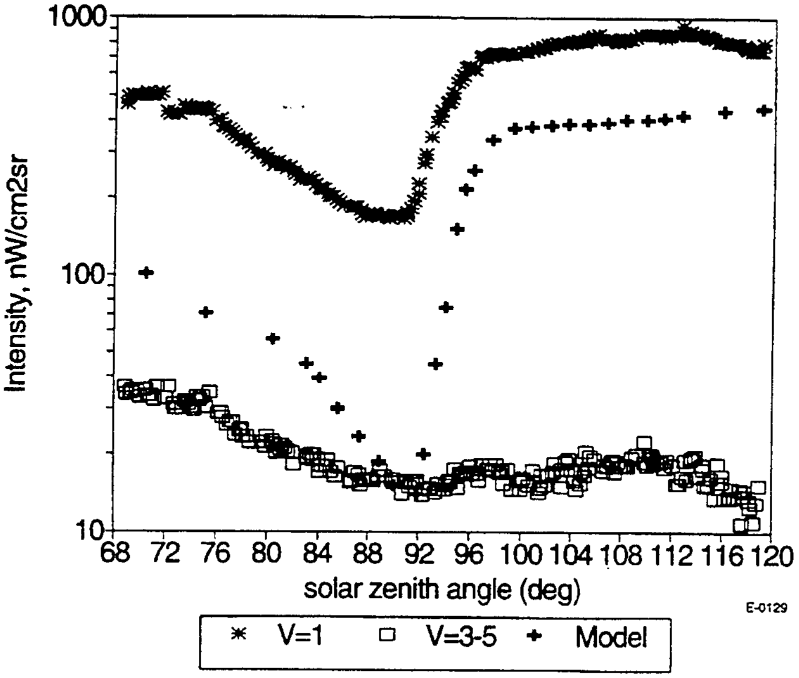

Figure 16. Dawn terminator radiances at 71.8 km from CIRRIS and model prediction.

The model of Rodrigo, scaled to this altitude, is shown for illustration. The model under predicts the observed ozone magnitude by a factor of 2 at night and a factor of 6 during the day, but accurately predicts the magnitude of daytime ozone restoration. For this paper, we have assumed that the radiance is dominated by the local emission at the tangent point - we have not treated the limb inversion problem properly. Emissions from tangent points below the ozone 80 to 85 km altitude peak will have significant contributions from higher altitudes along the column path. Preliminary modeling of the contributions from higher altitudes to the observed signature at 72 km indicates that increases the magnitude of the predictions but not sufficiently to match the CIRRIS 1A radiance data.

The altitude profiles of ozone ν_3,v=1 radiances for several latitude regions is shown in Figure 17. Although there is air parcel variations within each data set, consistent trends with latitude are observed. The temperate (34 to 50N) zone data consistently has greater magnitude (about a factor of three) than high latitude (50 to 68N) data, with the equatorial (1 to 21 S) data intermediate. This radiance variation could either correspond enhanced ozone production in the 40N zone relative to the 60 N zone, or to a 35 K hotter vibrational temperature (i.e., 235 K vs 200 K).

The nighttime radiance data was sorted into 20 degree latitude zones as a function of altitude, and transformed into excited column densities for v=1 (Figure 18) and v=3-5 (Figure 19). Nighttime data acquisitions were mainly in the southern hemisphere during the austral early fall (April 29,30 1991). There is no clear latitude trend in the v=1 data. The lowest

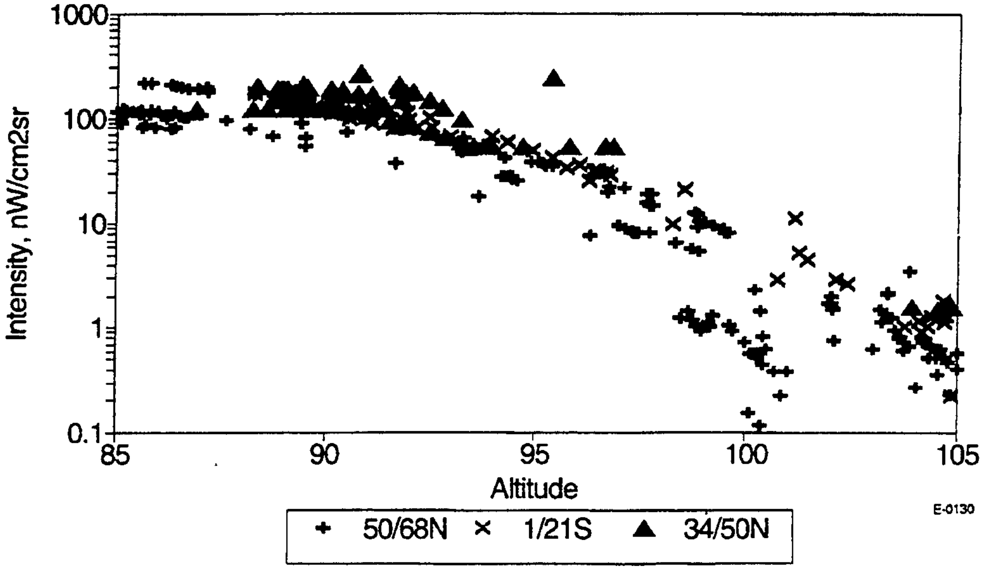

Figure 17. Altitude profiles for ozone v=1 radiances during the day for several latitudes.

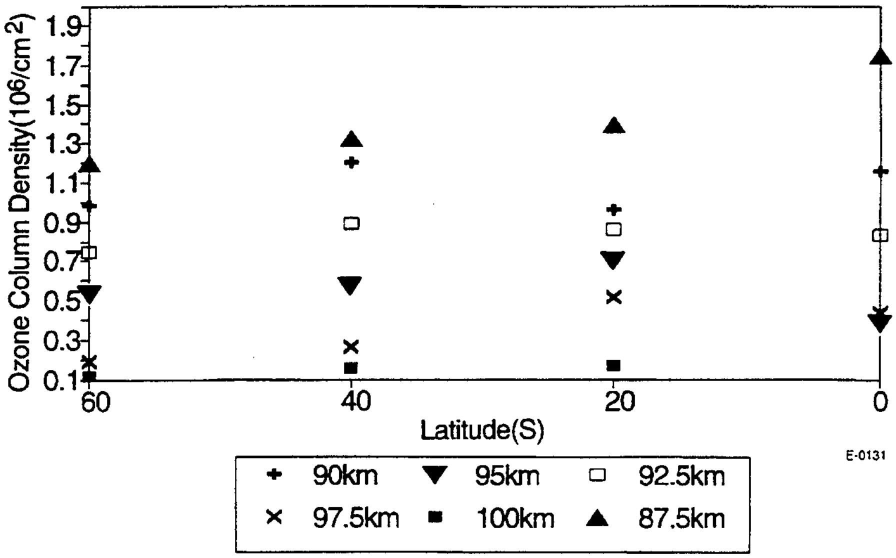

Figure 18. Zonally averaged nighttime ozone v=1 column densities as a function of altitude.

and highest altitudes seem to have ozone v=1 densities that increase toward the equator, indicating either enhanced ozone or vibrational temperatures near the equator during this time period.

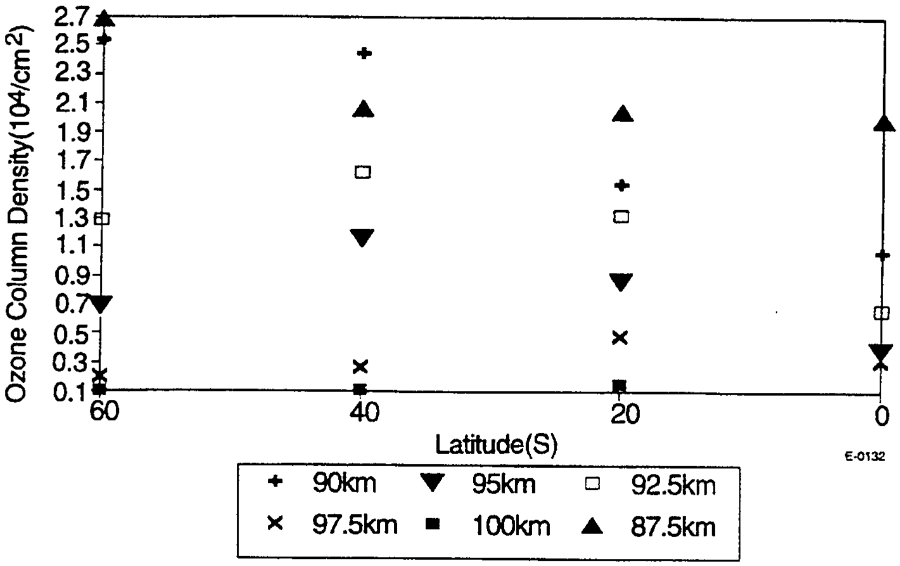

Figure 19. Zonally averaged nighttime ozone v=3-5 column densities as a function of altitude.

The v=3 column density (proportional to atomic oxygen) exhibits a 40 +/-10 S peak at all altitudes with a decrease toward the equator and poles. The v=3 column densities at 87 and 90 km have a peak in the high latitude bin. There was significant geomagnetic activity during the CIRRIS mission with K_p values in excess of 5.5 reported. Ozone data collected at high latitudes was observed to have great variability during high K_p periods. A very significant local enhancement in ozone v=1 and v=3-5 radiances was observed later in time and equatorward of an intense auroral arc, suggesting large scale atmospheric air parcel transport. We suggest that auroral processes may alter the ozone altitude profile at high latitudes depleting ozone in the deposition regions, enhancing production at lower altitudes.

We observed no significant variation in ozone radiances with longitude. The scatter within a data collection sequence is greater than the differences between sets collected at different longitudes. There are also spectrally resolved CO_2 emission features within these filtered data sets. While we have removed the CO_2 radiances for our analysis, this high quality data set will be subject of future analyses to understand atmospheric variability and to complement our ongoing ozone variability analyses.

5. SUMMARY

We presented here our spectral analysis of the ozone interferometric data acquired during the CIRRIS 1A mission. We determined that the observed vibrational distribution was consistent with that formed upon three-body recombination of O + O_2 +M as measured in the laboratory.

The upper atmospheric data was not able to extend our knowledge of ozone vibrational spectroscopic constants to more highly excited levels. Ozone above the mesopause exhibits large (order of magnitude) spatial variability. Our review of this data base indicates that the global variability is large compared to the local variability. Over an order-of-magnitude variability was observed in the ozone ν_3,v=1 radiances (column densities) at altitudes above 100 km even after background correction. Ozone fundamental band radiance was observable above the noise for tangent point altitudes up to 109 km. We feel that the variabilities are not arising from kinetic uncertainties, but must arise from dynamics or additional formation mechanisms.

The CIRRIS observations indicate ozone column densities in excess of model predictions. Another mechanism for increasing vibrationally excited ozone production during the daytime is required to explain the upper atmospheric data. The transients observed upon dawn and dusk terminators agree reasonably well with transients predicted by the diurnal model of Rodrigo, but again column densities are under predicted. We believe the CIRRIS 1A emphasizes the need for improved mesospheric/thermospheric ozone photochemical models.

ACKNOWLEDGMENTS

The authors acknowledge the assistance of Jay Lowell and Jim Dodd in developing database manipulation tools and many useful technical discussions. We express appreciation of the entire CIRRIS 1A team led by Dick Nadile of Air Force Research Laboratory, Hanscom for their tireless efforts to make the CIRRIS 1A mission a success. This effort was sponsored by Ballistic Missile Defense Organization and the Air Force Office of Scientific Research.

REFERENCES

Ahmadjian, M., D.E. Jennings, M.J. Mumma, B.D.Green, B.D. Dix, and R.Russell,"Infrared Spectral Measurement of the Space Shuttle Glow," J. Spacecraft Rockets **29**(1), 102 (1992).

Ahmadjian, M., J. Wise, R. Nadile, and B. Bartschi, "CIRRIS-1A Space Shuttle Experiment," J. Spacecraft and Rockets **27** (6), 669 (1990).

Allen, M., J.L. Lunine, and Y.L. Yung,"The Vertical Distribution of Ozone in the Mesosphere and Lower Thermosphere," J. Geophysical Research **89**, 484 (1984).

Green, B.D., W.T. Rawlins, and R.M. Nadile,"Diurnal variability of vibrationally excited mesospheric ozone as observed during the SPIRE mission," J. Geophys. Res. **91**,311 (1986).

Green, B.D., P.A. Mulhall, W.T. Rawlins, and O.M. Uy,"Optical Signatures of Particles in Space," Optical Engineering **36**(1),56-72 (1997a).

Green, B.D. and M. Ahmadjian,"The Variable Particle Environment Around the Shuttle," Applied Optics **36**(6), 1399-1406 (1997b).

Rawlins, W.T.,"Chemistry of Vibrationally Excited Ozone in the Upper Atmosphere," J.Geophysical Research **90**, 12,283-12,292 (1985).

Rawlins, W.T. and R. Armstrong, "Dynamics of vibrationally excited ozone formed by three-body recombination, I Spectroscopy," J. Chem. Phys. **87**, 5202 (1987a).

Rawlins, W.T., G.E. Caledonia, and R. Armstrong," Dynamics of vibrationally excited ozone formed by three-body recombination, II. Kinetics and mechanism," J. Chem. Phys.**87**, 5209 (1987b).

Rawlins, W.T., M.E. Fraser, K.W. Holtzclaw, W.J. Marinelli, H.C. Murphy, and L.G. Piper," Ultrasensitive Infrared Chemiluminescence Detection," PL-TR-93-2266, PSI-TR-1277

Rawlins, W.T., Green, B.D., D.E.Paulsen, W.A.M. Blumberg, and R.E. Murphy,"Excitation of $O_3(v_3)$ by Electron Bombardment in the EXCEDE III Rocket Experiment" J.Geophysics Research accepted 1998.

Rodrigo, R., M.J. Lopez-Gonzalez, and J.J. Lopez-Moreno,"Variability of the Neutral Mesospheric and Lower Thermospheric Composition in the Diurnal Cycle," Planetary Space Sciences **39**(6), 803-820 (1991).

Upschulte, B.L., B.D. Green, W.A.M. Blumberg, and S.J. Lipson,"Vibrational Relaxation and Radiative Rates of Ozone", J. Chemical Physics **98**, 2328-2336 (1994).

Zhou, D. K., M.G.Mlynczak, G.E.Bingham, J.O.Wise, and R.M. Nadile,"CIRRIS-1A limb spectral measurements of mesospheric 9.6-μm airglow and ozone," Geophysics Research Letters **25**(5), 643-646 (1998).

APPENDIX 12

Molecular Excitation in Sprites

GEOPHYSICAL RESEARCH LETTERS, VOL. 23, NO. 16, PAGES 2161-2164, AUGUST 1, 1996

Molecular excitation in Sprites

B.D. Green, M.E. Fraser, W.T. Rawlins, L. Jeong, W.A.M. Blumberg, S.B. Mende,
G.R. Swenson, D.L. Hampton, E.M. Wescott, and D.D. Sentman

Abstract. We have determined the molecular internal energy distribution in the N_2 $B^3\Pi_g$ state from the fluorescence measured during the observations of sprites during 1995. Spectrally resolved data from two different instruments and three different sprites are compared with theoretical spectra to obtain excited state vibrational distributions. Energy dependent electron excitation cross-sections and laboratory data were used to estimate the energies of electrons producing the red sprite radiance. Implications for chemical production in the mesosphere and critical future measurements are discussed.

Introduction

Red sprites and blue jets are middle-atmospheric electric discharges linked to lightning. Sprites have been reported episodically for many years, but systematic investigation has begun only recently [Lyons, 1994; Sentman & Wescott, 1993; Sentman et al., 1996]. We present an analysis of the spectral data from observations of the visually red portion of the sprite column at altitudes near 70 km. Two groups have reported spectra obtained from ground based instruments. Hampton et al. [1996] used a TV slit spectrograph with the slit positioned horizontally so that emission from a single altitude was observed. Sprites were observed from Mt. Evans, CO in June 1995 with this instrument operated at two different spectral resolutions. Mende et al. [1995] used a bore sighted intensified CCD video system with a slit and transmission grating positioned vertically observing from Yucca Ridge, CO in July 1995. Details of these instruments and observations are contained in their respective papers. Both groups identified emissions from N_2 First Positive ($B^3\Pi_g \rightarrow A\,^3\Sigma_u^+$) as the only significant emission within their instrumental bandpass. Vibrational levels in the B-state up to at least v=6 [Mende et al. (1995)] and 10 [Hampton et al. (1995)] were identified.

We present a spectral analysis to extract upper-state vibrational distributions from the observational data. Energy-dependent electron excitation cross-sections for N_2 electronic states were used to bound the electron energy distribution responsible for the excited-state vibrational populations. This stratospheric/mesospheric discharge process appears to be highly variable. The analysis below draws conclusions based on the first spectral data of the red sprite column. Insight and spectra of the other facets of sprites await future measurement campaigns.

Spectral Analysis

We have presented details of our spectral analysis code previously (Fraser et al., 1988) as applied to extract detailed excitation mechanisms in the aurorally disturbed upper atmosphere and in chemical flow reactors. The line strengths and positions for all transitions in the $N_2(B^3\Pi_g\text{-}A^3\Sigma_u^+)$ (1PG) for v'=2-12 and $N_2^+(A^2\Pi_u\text{-}X^2\Sigma_g^+)$ (Meinel) for v'=2-5 were included in the comparisons. The spectral fitting technique was employed first to determine the actual spectral resolutions and then to determine the presence and vibrational extent of the nitrogen 1PG and Meinel emissions. The Mende et al.[1995] data were best reproduced with a triangular slit function of 5 nm resolution. The Hampton et al. [1996] high and low resolution data were best reproduced with slit functions of 2 and 6 nm.

The molecular rotational levels were modeled to be in thermal equilibrium at a temperature of 220 K. The spectral resolution in the data does not permit accurate rotational temperature determination. Fits with temperatures as high as 300 K were also consistent with the data. The theoretical spectra were calculated at high resolution, and then convolved with the slit function. Although the data from both instruments was spectrally response corrected, atmospheric attenuation by the O_2 (b-X) system around 762 nm, and the rapid decrease in detector response beyond 750 nm, make the 1PG $\Delta v=2$ and Meinel $\Delta v=2$ sequence data in this region less accurate.

The experimental data were corrected for atmospheric transmittance using MODTRAN predictions [Anderson et al., 1993]. The transmittance was calculated assuming a 400 km atmospheric path length from a 10,000 ft ground point to 45 and 85 km altitudes. The resulting transmittance data were convolved with a slit of equivalent resolution and applied to the experimental data. Because atmospheric absorption of the N_2 1PG transitions occurs over Voigt lineshapes, this treatment is not exact. However, because the atmospheric column density profiles in the wake of the thunderstorm are not accurately known, a more exact treatment was not warranted in this analysis. The effects of errors in the instrumental radiance response were minimized by determining the vibrational populations in each spectral sequence separately.

The population in each vibrational level is not set by a "temperature" but rather determined by the linear solution vector that minimizes the least-squares difference between the computed and observed spectra. To achieve spectral alignment, the data from both instruments had to be spectrally shifted by less than the resolution to best match the theoretical spectra. The spectrum of a red sprite at 2 nm resolution (Hampton et al. [1996]) is presented in Figure 1a. The sprite emission originates from an altitude estimated to be about 70 km [Sentman et al., 1996]. The synthetic spectrum resulting from the best fit to the data is also shown. Both N_2(B-A) and N_2^+(A-X) transitions are included in the theoretical spectrum, however, only 1PG features up to v'=8 are definitely observed. Meinel emission from v'=2 would be most prominent at 780 nm, v'=3 at 810 nm, and v'=4 at 700 nm. The observed radiance in these regions is at the noise level, thus N_2^+(A) populations can only be set as upper bounds. The derived populations are plotted in Figure 2 as the AK-HI points. The

Paper number 96GL02071
0094-8534/96/96GL-02071$05.00

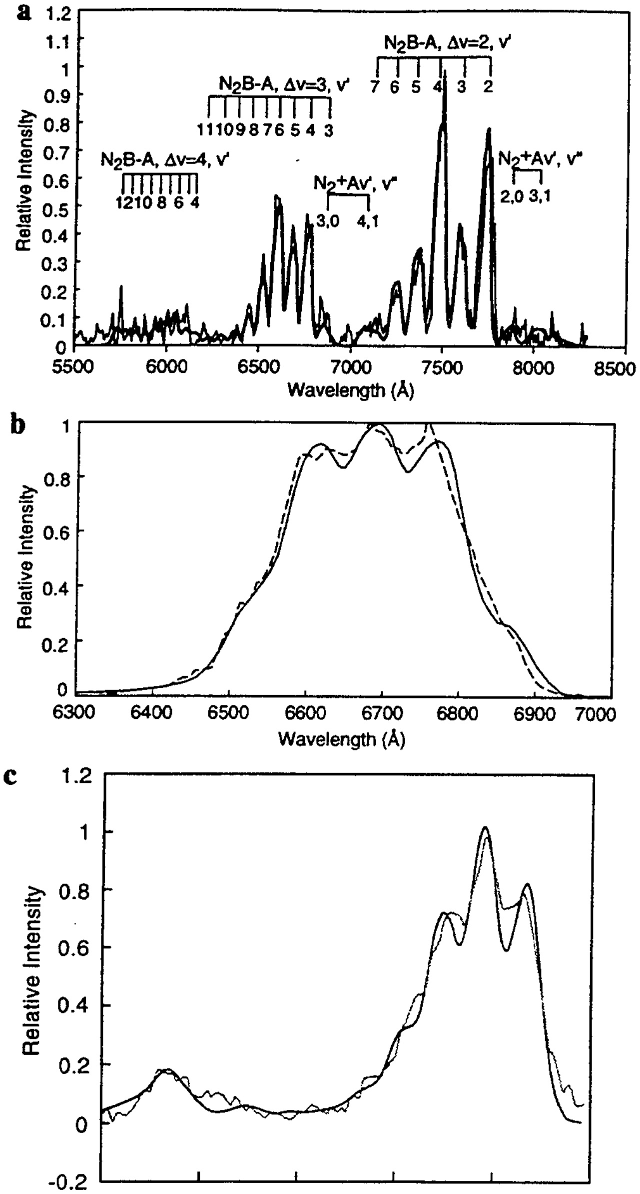

Figure 1. Comparison of synthetic spectra of N_2 B-A and N_2^+ A-X emissions (bold, smoother lines) with response corrected spectra from sprites (lighter/broken lines). Features are labeled in Figure 1A. (a) Hampton et al. at 2 nm res. (AK-HI); (b) Hampton et al. at 6 nm res. (AK-LO); (c) Mende et al. at 5 nm res. (MENDE).

uncertainties for B,v=9-11 as indicated are ±0.0012 based on the fitting errors and noise levels.

The lower resolution (6 nm) spectrum of a different sprite by Hampton et al. [1995] is presented in Figure 1b. A dramatic improvement in signal to noise ratio results at this decreased resolution, permitting more detailed analysis. N_2(B) vibrational levels up to v=11 are present above the noise level. The Meinel transitions are not detectable above the noise level. An upper bound on their population is based on the small noise levels present in the spectrum. The populations determined from fitting are presented as the points labeled AK-LO in Figure 2.

The spectrum obtained by Mende et al.(1995) is presented in Figure 1c. It contains emission from a range of altitudes, but emission from about 70 km is felt to dominate. Although this spectrum has greater noise than the data of Figures 1a and 1b, a good comparison to the theoretical spectrum is obtained. The calculated distribution decreases more rapidly with v. This may be due to inexact baseline correction, variability between different sprites, or the inclusion of emission from lower altitudes by the vertical slit orientation. N_2(B) v ≤ 8 are present above the noise level. Vibrational populations derived from the three sprite spectra are plotted in Figure 2.

At these altitudes, collisional quenching competes with radiative decay from the allowed electronic transitions. Consequently, comparison of sprite data to other atmospheric emissions, such as observed during auroral events at higher altitudes, is not straightforward. The Meinel transitions will be severely quenched [Piper et al., 1985]. Comparison with laboratory data acquired in electron irradiated nitrogen and air mixtures at pressures representative of 70 km altitudes permits the vibrational distributions and ion/neutral relative populations to be compared against expectations based on electron excitation cross-sections and molecular quenching. These data were acquired with the LABCEDE Facility at the Phillips Lab Geophysics Directorate [Green et al., 1988]. A monoenergetic beam of 4 keV electrons was introduced into a 0.9 m diameter chamber containing a well-mixed nitrogen/oxygen gas mixture.

The N_2 B-state and N_2^+ A-state vibrational distributions from collisional quenching of N_2^* produced by keV energy electron excitation as measured in this facility at pressures corresponding to 70 km altitudes is also shown in Figure 2. Levels B, v=8-10 are produced more abundantly by keV electrons than in the sprite distributions. Laboratory N_2^+ A-state populations are comparable to the upper bounds of the Mende and Hampton high resolution data. However, the lab data are significantly greater than the N_2^+A population bounds on the Hampton et al. low resolution data. Future campaigns should target accurate measurement of the Meinel bands as a critical indicator of the electron energy causing the excitation.

The relative B-state populations in levels 2,4-7 are similar in all three sprite observations and the laboratory data. The (3-0) feature is relatively weak and dominated by the experimental noise level. The (3-1) transition is severely attenuated in the atmospheric path. Incomplete correction for this attenuation results in an inexact determination of the v'=3 population.

The higher B-state levels have the smallest radiances. To minimize the contribution from noise, we subtracted a baseline from the data. The populations for v'≥ 9 are most significantly affected. The low resolution data from Hampton et al. [1995] has the best signal levels, exhibits a monotonic decrease with increasing v, and provides the most accurate high v population determination. Emission from states up to v'=11 is observed.

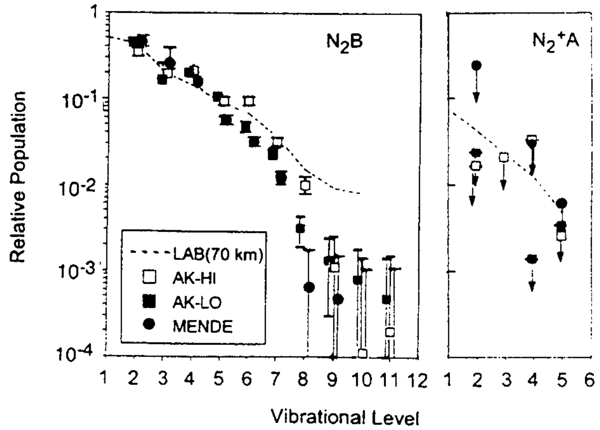

Figure 2. Vibrational distributions deduced from Figure 1 and laboratory observations (---); AK-HI (*); AK-LO (■); MENDE (●). Baseline subtraction applied.

This state lies at an energy near the dissociation limit for nitrogen, and only a few eV below the ionization threshold. Atoms and ions created in the sprite may act as precursors to initiate chemical reactions affecting the atmospheric odd nitrogen (NO) and oxygen (O,O_3) budgets.

To provide further insight, we undertook simple modeling of the electron-impact excitation processes that could produce the observed sprite distributions. The excitation cross sections of each vibrational level in the N_2 B and C and N_2^+ A states as a function of energy have been measured by Stanton and St. John [1969]. The excitation spectrum is quite structured, peaking in the 10 eV region for low v′ and increasing with v′. Cascade from the C-state peaks for 14 eV electrons and is a significant contribution to the total B-state excitation for the lower levels. We calculated the excitation of each vibrational level in each electronic state for all electron energies between 6 and 100 eV at 0.25 eV intervals. The distribution in the B-state changes significantly for electron energies in the 8 to 14 eV range. Ion A-state emission is a sensitive indicator of the presence of high energy electrons, with a peak in the excitation cross-section near 100 eV and a threshold above 15 eV.

At 70 km altitudes both the B- and ionic A-states are quenched. Using measured lifetimes [Piper et al., 1989] and quenching rate coefficients for the B-state [Piper et al., 1992] and the A-state [Piper et al., 1985], the expected radiance levels and vibrational distributions at 70 km altitude were modeled as a function of electron energy. Quenching of the A-state is severe with only 5 to 7% of the excitation escaping as fluorescence. The ionic B-state (with prominent emissions at 391.4 and 427.8 nm) is less sensitive to quenching, but is severely attenuated due to atmospheric scattering. MODTRAN calculations showed this attenuation to be one to two orders of magnitude at 427.8 nm, being a very sensitive function of aerosol loading and look angle. Intensities of tens of kR of 427.8 nm emission from red sprites have been observed using a ground-based radiometer [Armstrong, 1995].

The observations are compared to predictions based on both mono-energetic electron excitation, and electrons with a Boltzmann approximation for the distribution of energies. Mono-energetic electrons at 100 eV match the shape of both B and ion A-state distributions observed in LABCEDE. The LABCEDE ion A-state populations are higher as expected for the higher energy 4 keV source [Green et al., 1988].

The energies of electrons producing the sprites can be bounded through model comparison with the deduced B- and ion A-state populations. The derived population distribution based on the low resolution spectrum from Hampton et al. [1995] is shown in Figure 3 in comparison with the predicted distributions for several characteristic Boltzmann electron temperatures. The B-state distribution is best matched using a 1 eV Boltzmann electron distribution. A Druyvesteyn distribution with a suppressed high-energy tail may be more realistic. Thus 1 eV represents a lower bound to the characteristic electron temperature. The mono-energetic predictions reveal that electrons with energies above 9.25 eV must be present to excite $N_2(B,v' \geq 8)$. The population distributions from the Mende et al. data and the Hampton et al. high resolution data agree best with Boltzmann electron temperatures of 0.4 and 2 eV respectively, and require mono-energetic electrons of 8.8 and 9.5 eV to be present. These differences appear to be statistically significant and may represent variability in the electron distributions producing these different sprites.

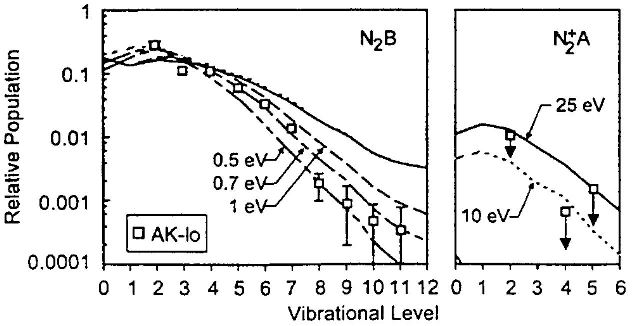

Figure 3. Populations derived from AK-LO data compared with population distribution produced by Boltzmann electron temperature of 0.5, 0.7, 1, 10 , and 25 eV.

The ion A-state populations are not well determined by this analysis. The data points represent upper bounds. The values as plotted indicate that a Boltzmann electron distribution of 10 to 25 eV would be required to produce the populations at the upper bound levels. Electrons above these energies cannot be present at any significant concentration. The B-state provides a more accurate estimation of the electron energy distribution. We cannot distinguish the effects of noise levels in the individual spectra from true variability of the sprite phenomena with such a sparse data set. The population distributions and electron energies may vary for different sprite events.

The implications of these distributions can be addressed through numerical solutions of the Boltzmann transport equation, that incorporates detailed inelastic energy transfer cross-sections to solve for the electron energy distribution as a function of the parameter E/N. E/N is the ratio of the electric field per unit length to the total number density. Convolution of the electron energy distributions with species excitation cross-sections gives rate coefficients for the key excitation processes as functions of E/N. The electron energy distributions that match the sprite distributions suggest E/N on the order of 10^{-15} V cm^2 and 100 to 200 V/m electric fields at 70 km. Qualitative comparison to spectra observed in laboratory microwave discharges for E/N spanning the (0.9 to 20) x 10^{-15} V cm^2 range [L.G. Piper, private communication] lead to similar conclusions. These values are consistent with theoretical predictions based on lightning-induced electromagnetic pulses (Milikh et al, 1995) and heating by quasi-electrostatic thundercloud fields (Pasko et al, 1995), but not with values required for runaway electron mechanisms (Chang and Price, 1995). However, the absence of obvious $N_2^+(A \rightarrow X)$ transitions in sprite spectra does not by itself preclude E/N values in excess of the runaway electron threshold. Our excitation modeling of N_2^+ B-state production indicates that atmospheric regions having (order of 10^{-15} V cm^2) could produce ionization and tens of kR radiances as observed by Armstrong et al. [1995].

Low-energy discharges of this type generate sufficient electronic excitation, dissociation, and ionization to initiate atomic and excited-state chemical reactions such as the formation of NO, N_2O, and O_3, perturbing the local photochemical balances of odd-nitrogen and odd-oxygen in the stratosphere and mesosphere. A simple mechanism (based on Rawlins et al., 1989) for sprite-induced NO production near 70 km is electron dissociation of N_2 followed by atomic excitation to $N(^2D, ^2P)$, followed by reaction with O_2 to form NO. The dissociation and excitation rate coefficients are strongly dependent on E/N (through their sensitivities to the electron energy distribution). For the conditions of 2 x 10^{-15} Volt cm^2 and 10^3 electrons/cm^3, the local NO production rate for a 10 ms sprite at 70 km is $\approx 10^2$ molecules $cm^{-3}s^{-1}$, which is comparable to the background photochemical NO production rate. However, this rate is extremely sensitive to E/N and to the square of the sprite's electron number density, resulting in many orders of magnitude uncertainty. For fixed electron number density, the computed NO production rate increases almost two orders of magnitude upon doubling E/N, and decreases by over three orders of magnitude upon halving E/N. Thus factor of two uncertainty in E/N encompasses 5 to 6 orders of magnitude in the local NO production rate. Discharge intensities, durations, and frequency of occurrence are highly variable, further complicating assessment of local and regional chemical production rates. Clearly, reliable estimates of E/N for a large range of sprite-related phenomena and altitudes are required to evaluate their atmospheric chemical impacts. This can be accomplished through analysis of emission spectra giving neutral and ionic excited-state population distributions as demonstrated here. If NO production is indeed significant, it may be possible to observe infrared fluorescence from NO(v). Atmospheric aerosol and molecular scattering are reduced in the infrared spectral region, possibly permitting observation of NO(v) and N_2^* emissions that will provide increased insight into the sprite electron excitation energies and mechanisms.

Conclusions

Spectrally resolved emissions from different sprites taken by two different instruments have been analyzed to extract the transient vibrational distributions resulting from the excitation process(es). Nitrogen First Positive (B-A) transitions dominated all the observations in this wavelength range. While low signal levels and atmospheric transmission compromise the accuracy of the data and analysis, spectral fitting permitted accurate excited state population determination. The relative B-state populations in levels 2,4-7 are similar in all three sprite observations. The low resolution spectrum from Hampton et al. (1996) has the best signal levels, and exhibits a distribution monotonically decreasing with increasing v. The distributions are consistent with excitation by electrons with a Boltzmann temperature of 1 eV (range 0.4 to 2 eV). The variations may be due to different electron distributions present in the different sprite observations.

The sprite electrons appear to be of energy sufficient to dissociate and ionize N_2. The magnitude of this dissociation and ionization and its effect on stratospheric and mesospheric odd-N and odd-O budgets remain key unknowns. There is no clear evidence for the presence of MeV energy electrons as required for runaway breakdown in the red sprite data.

Future data are needed to clearly identify and quantify the ion emissions either from the A-state in the near infrared or the B-state in the UV. Spectra of the precursor high altitude blue flash ("elve") would be useful in establishing local conditions at the onset of the sprite. Measurements of the electric field and electron densities at the 20 to 40 km altitudes are critical for assessing the onset of sprite-produced chemical reactions. Direct measurements of sprite-produced radiances in the infrared will aid in the assessment of the electron energy distributions in the sprite and the impact on atmospheric chemistry.

Acknowledgments. We acknowledge useful discussions with R.A. Armstrong of MRC. L.G.Piper of PSI provided insight in the spectral analysis. R. Rairden provided assistance in the calibration of the Lockheed data.

References

Anderson, G.P., et al., MODTRAN 2: Suitability for remote sensing, SPIE International Symposium on Optical Engineering and Photonics in Aerospace and Remote Sensing, April 1993.

Armstrong, R.A., private communication, 1995.

Chang, B. and C. Price, Can gamma radiation be produced in the electrical environment above thunderstorms?, *Geophys. Res. Lett.*, *22*, 1117, 1995.

Fraser, M.E., W.T. Rawlins, and S.M. Miller, Infrared (2 to 8 μm) fluorescence of the $W^3\Delta_u \rightarrow B^3\Pi_g$ and $w^1\Delta_u \rightarrow a^1\Pi_g$ systems of nitrogen, *J. Chem. Phys*, *88*, 538, 1988.

Green, B.D, et al. LABCEDE fluorescence investigations, *AFGL-TR-88-0186*, 1988 (available upon request).

Hampton, D.L., M.J. Heavner, E.M. Wescott, D.D. Sentman, Optical spectral characteristics of sprites, *Geophys. Res. Lett*, *23*, 89, 1996.

Lyons, W.A., Characteristics of luminous structures in the stratosphere above thunderstorms as imaged by low-light video, *Geophys. Res. Lett.*, *21*, 875, 1994.

Mende, S.B., R.L. Rairden, G.R. Swenson, W.A. Lyons, Sprite spectra; N_2 1PG band identification, *Geophys. Res. Lett.*, *22*, 2633, 1995.

Milikh, G.M., K. Papadopoulos, and C.L. Chang, On the physics of high altitude lightning, *Geophys. Res. Lett.*, *22*, 22, 85, 1995.

Pasko, V.P., U.S. Inan, Y.N. Taranenko, and T.F. Bell, Heating, ionization and upward discharges in the mesosphere due to intense quasi-electrostatic thundercloud fields, *Geophys. Res. Lett.*, *22*, 365, 1995.

Piper, L.G., B.D.Green, W.A.M. Blumberg, S.J. Wolnik, N_2^+ Meinel band quenching, *J. Chem. Phys.*, *82*, 3139, 1985.

Piper, L.G., K.W. Holtzclaw, B.D. Green, W.A.M. Blumberg, Experimental determination of the Einstein coefficients for the N_2(B-A) transition, *J. Chem. Phys.*, *90*, 5337, 1989.

Piper, L.G., Energy transfer studies on N_2(X,v) and N_2(B), *J. Chem. Phys.*, *97*, 270, 1992.

Rawlins, W.T., M.E. Fraser, and S.M. Miller, Rovibrational excitation of nitric oxide in the reaction of O_2 with metastable atomic nitrogen, *J. Chem. Phys.*, *93*, 1097, 1989.

Sentman, D.D. and E.M. Wescott, Observations of upper atmospheric optical flashes recorded from an aircraft, *Geophys. Res. Lett.*,*20*, 2857, 1993.

Sentman, D.D. and Westcott, E.M., Red sprites and blue jets: high altitude optical emissions linked to lightning, *EOS 77*, 1, 1996.

Stanton, P.N. and R.M. St. John, Electron excitation of the first positive bands of N_2 and of the first negative and Meinel bands of N_2^+, *J. Optical Soc. Amer.*,*59*, 252, 1969.

B.D. Green, M.E. Fraser, W.T. Rawlins, Physical Sciences Inc., 20 New England Business Center, Andover, MA (e:green@psicorp.com).

L. Jeong and W.A.M. Blumberg, Phillips Laboratory, Hanscom AFB, MA 01731 (jeong@plh.af.mil)

S.B. Mende, Space Sciences Laboratory, U. California. Berkeley, CA 94720 (mende@ssl.berkeley.edu).

G.R. Swenson , Lockheed Martin Palo Alto Research Lab., 3251 Hanover St., Palo Alto, CA 94304 (swenson@sag.space.lockheed.com).

D.L. Hampton, E.M. Wescott,and D.D. Sentman, Geophysical Institute, 903 Koyukuk Dr. Fairbanks, AK 99775 (dsentmann@guiaf.gi.alaska.edu).

(Received date - Dec. 21, 1995; revised date - June 24, 1996; accepted date - July 2, 1996)

APPENDIX 13

Molecular Excitation from Sprite Emission Spectra

Molecular Excitation from Sprite Emission Spectra

B.D. Green, W.T. Rawlins, M.E. Fraser
Physical Sciences Inc.

L. Jeong and W.A.M. Blumberg
Phillips Laboratory Geophysics Directorate

D.L. Hampton, E. Wescott, D. Sentman, M.J. Heavner
University of Alaska

Presented at 1996 AGU Fall Meeting
Paper A11A-20

Supported by Sprites Program at Phillips Laboratory/AFOSR

Abstract

We have determined the internal vibrational and electronic state energy distributions based on a spectral analysis of the large spectrometric observation data base acquired by the University of Alaska group during the summer of 1995 campaign. Knowledge of the energy dependent electron excitation cross-sections and the molecular excited state quenching data permits estimation of the energy distribution of the electrons producing the observed excitation levels as ≈ eV energy. Only small variations are observed in the spectral distribution from several different sprites.

Sprite Spectra: Log Scale

96-4020

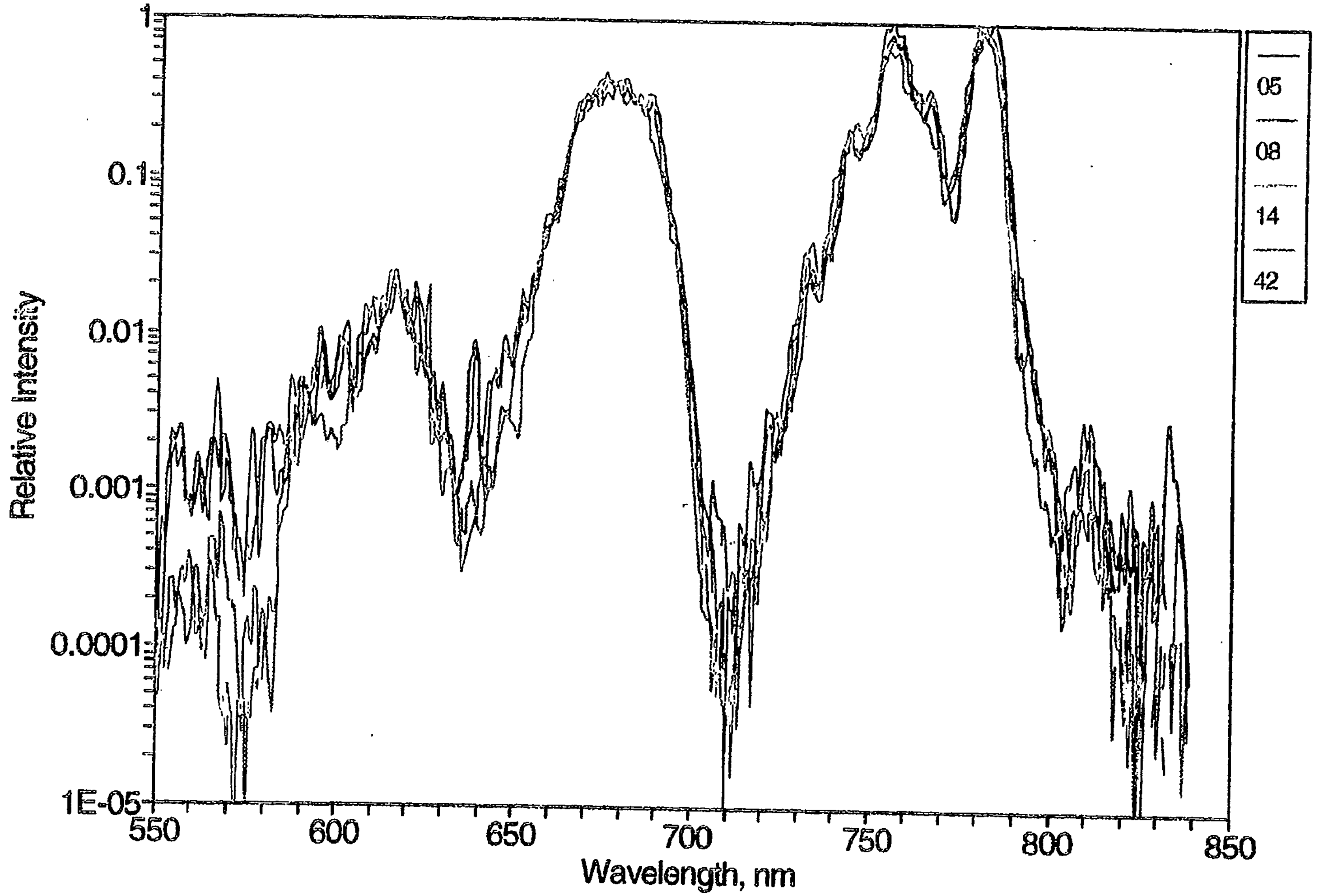

○ Large dynamic range in sprite data

○ Very reproducible, little variability between sprite spectral distributions

Atmospheric Transmission through Slant Path to Sprite

96-4019

Source 70 km, Obs 3 km, Range 500 km
No Tropospheric Aerosols

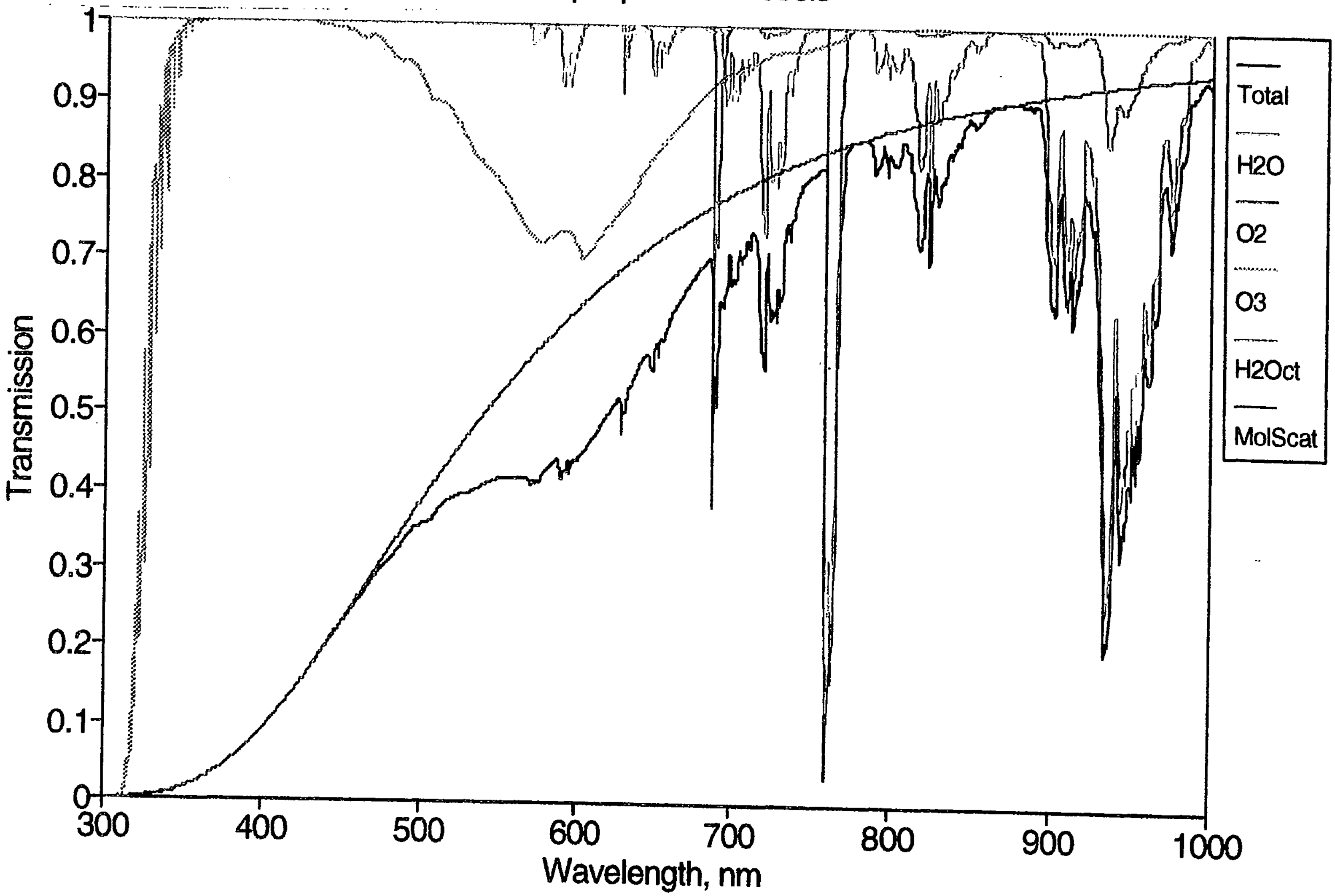

Spectral Fitting Procedure

96-4021

- Generate spectral basis functions: 250 K, 60 Å
- Flat response, fit dv=2 for wavelength correction
- Atm transmission correction:
  - — MODTRAN, US Std Atm, minimum aerosols
  - — slant path parameters: 3→70 km @ 500 km
  - — pass 60 Å slit function
- Fit dv=2 for v′=2,4-7 populations
- Fit dv=3 for v′=3-10 populations
- Combine populations to determine $N_v/\mathrm{Sum}(N_v)$

Potential Energy Curves for N_2 and N_2^+

96-4018

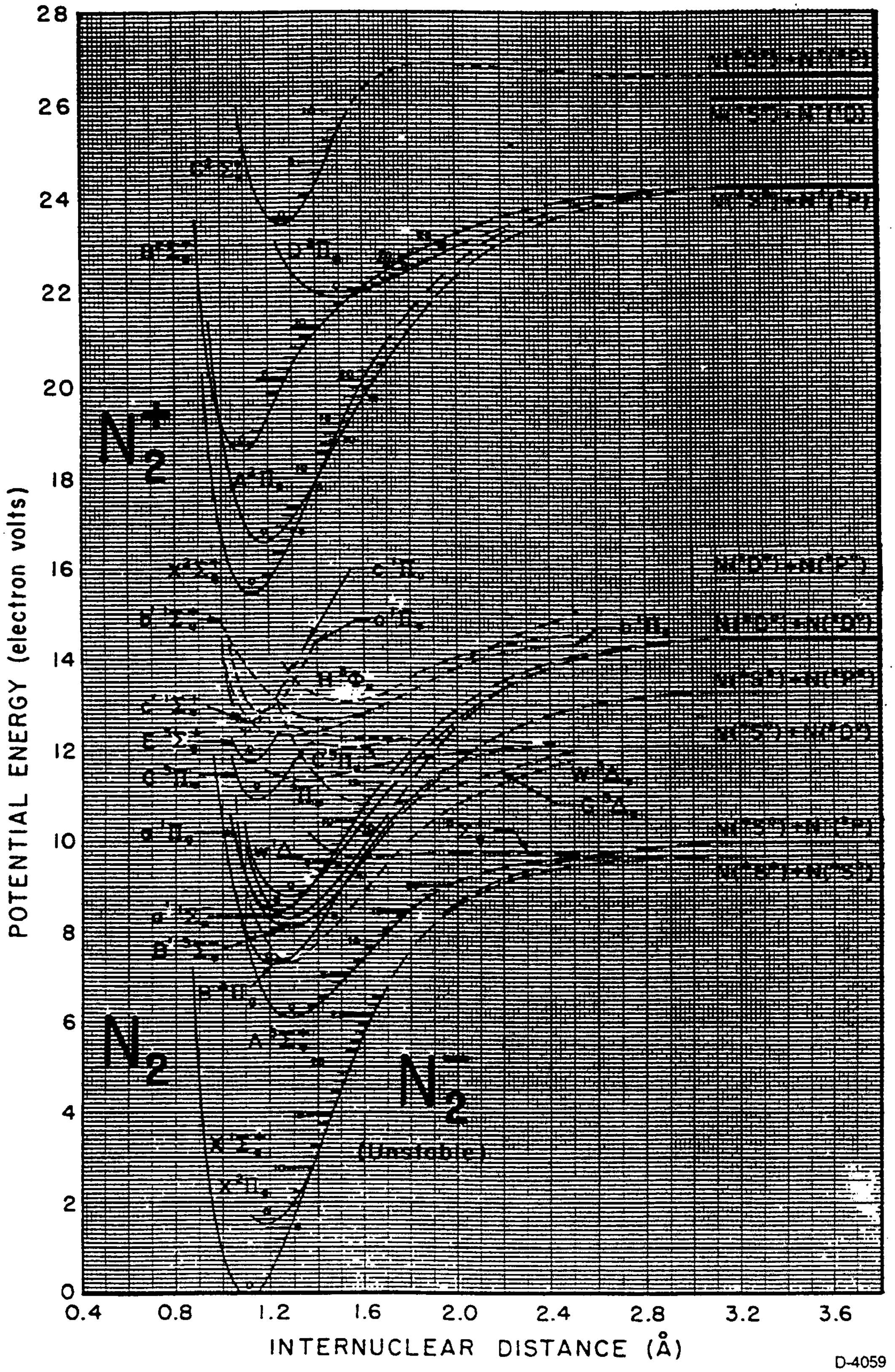

D-4059

Hampton et al. at 2 nm Resolution (AK-HI)

96-294a

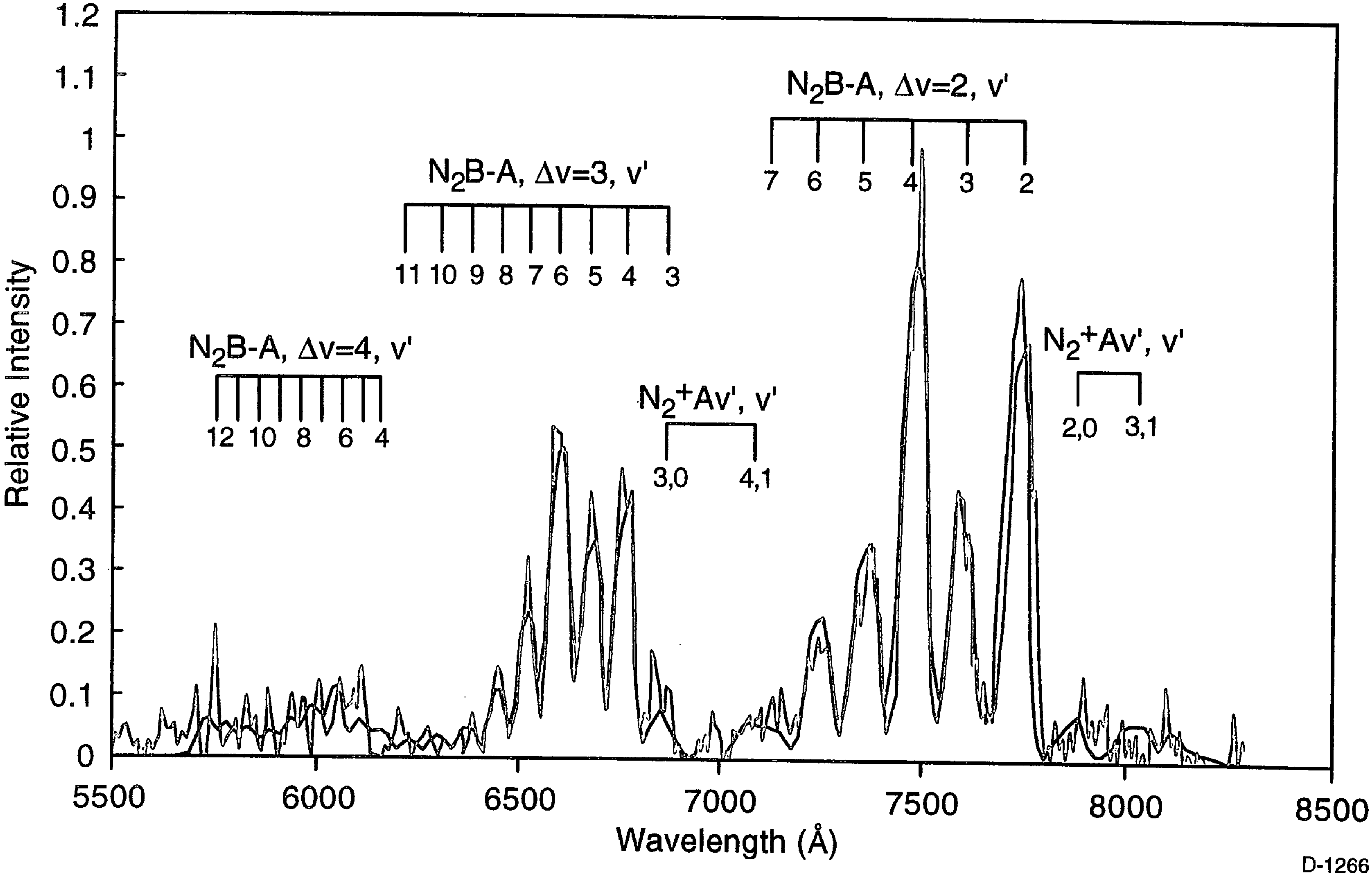

D-1266

Nitrogen B-State Vibrational Population Distributions

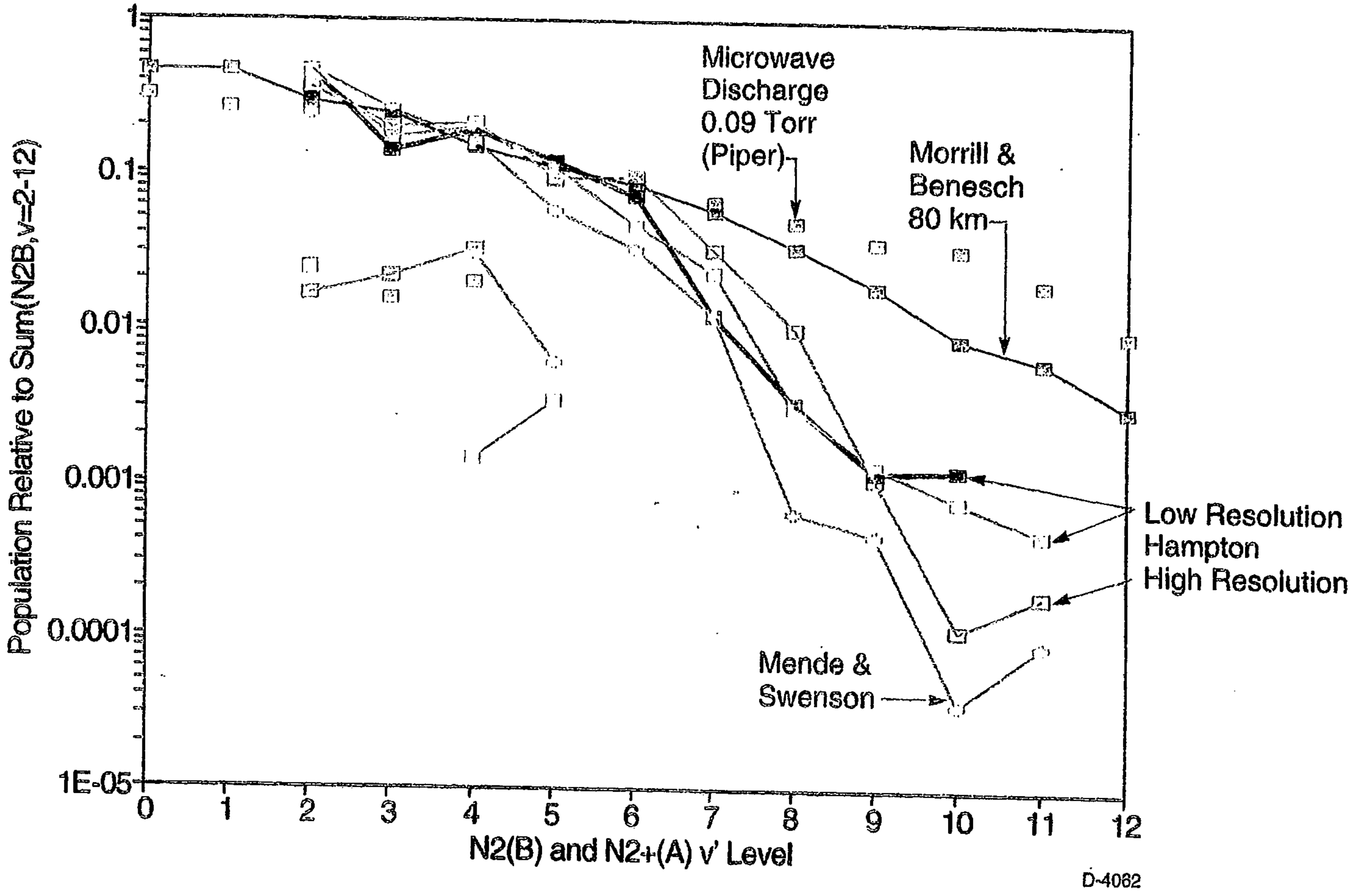

- Distributions similar (within error bars)
- Instrumental baseline signals and atmospheric transmission
- Derived populations clearly “colder” than auroral-like (MB) and microwave discharge (P) distributions

Vibrational Distributions

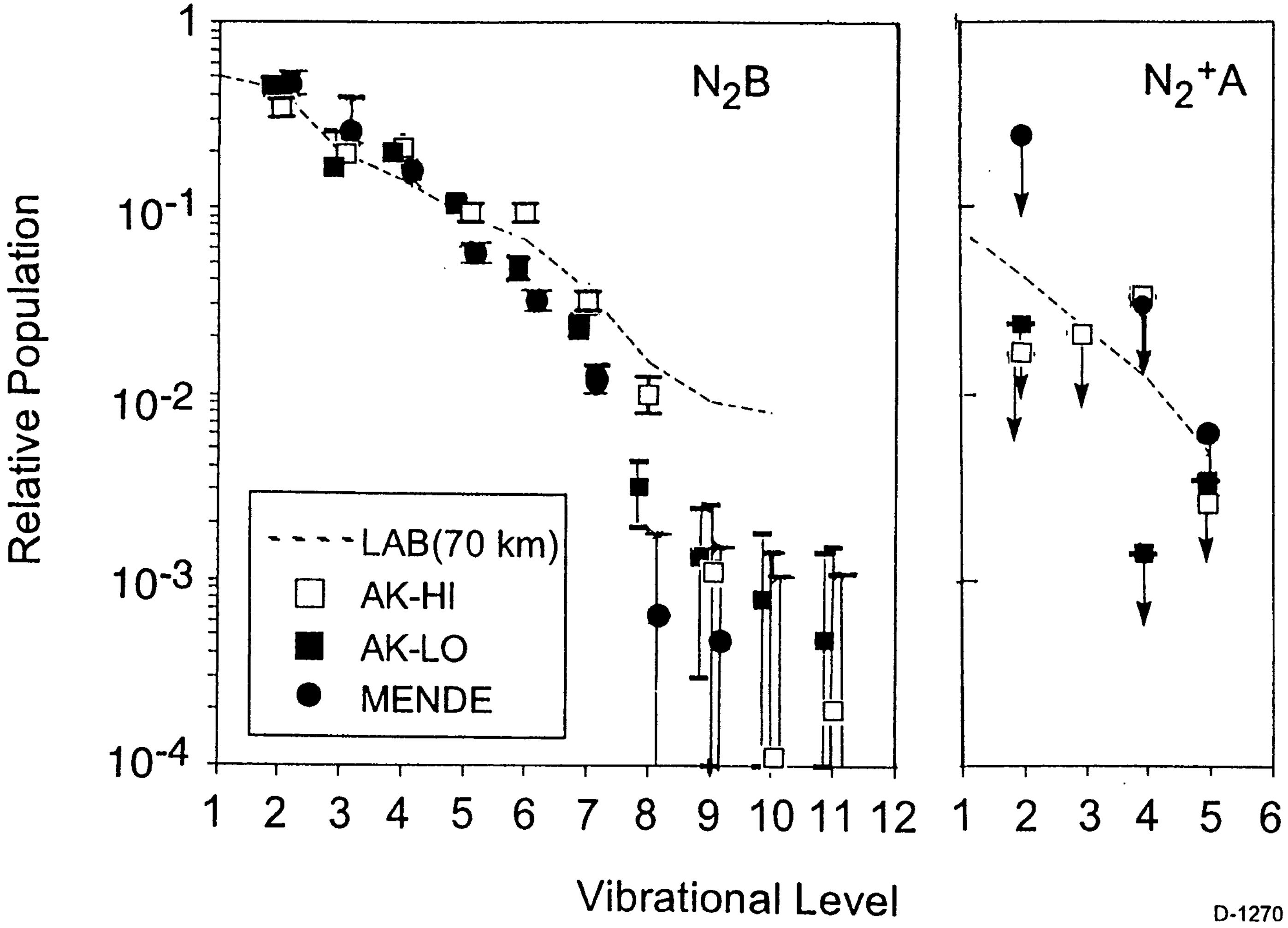

- From GRL 23(16), 2161 (1996).

What Happened to $N_2(B,v'>6)$?

- Transmission (response) function <7000 Å
  - — ozone
  - — aerosols
- Quenching or W↔B intersystem collisional transfer (ICT)
  - — quenching unlikely
  - — ICT has only subtle effect on v distribution
- High v′ not produced: not enough electrons > 10 eV

Boltzmann Electron Model

96-300a

- Boltzmann electron energy distribution
  - convolve with excitation cross sections
  - correct for quenching
  - integrate over energy distribution to create rate coefficient
  - compare predicted and observed population distributions
- Best match: 1 eV electron "temperature"
  - lower bound
  - Druyvesteyn <E> probably 2 to 3 eV
  - $T_e > 10$ eV required to produce observable $N_2^+(A)$
- Monoenergetic electron model
  - 9 to 10 eV electrons must be present (N_2B, $v \geq 8$)
  - > 23 eV electrons not present (no $N_2^+(A)$)

Boltzmann Electron Model

96-298a

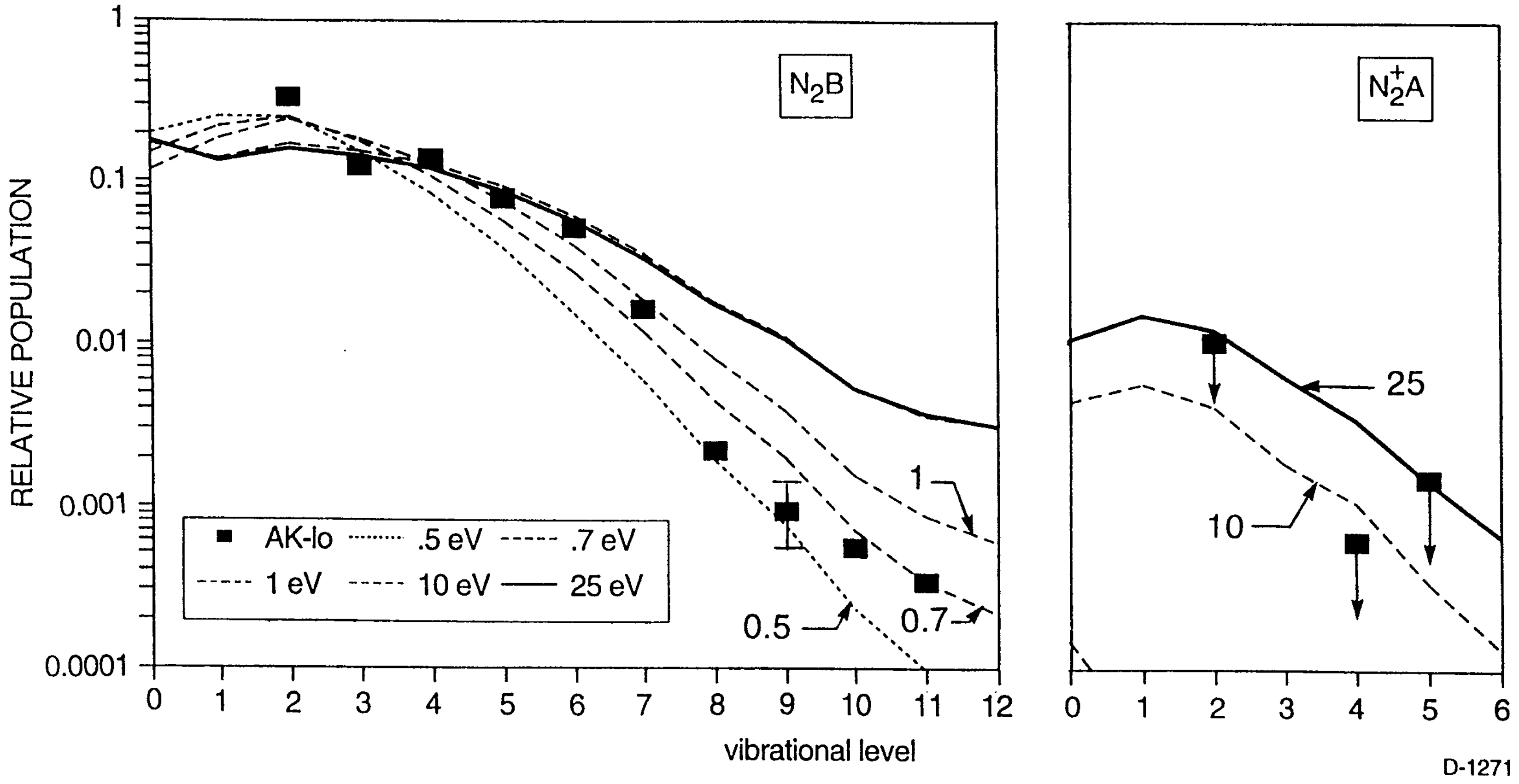

Monoenergetic Electron Model

96-299a

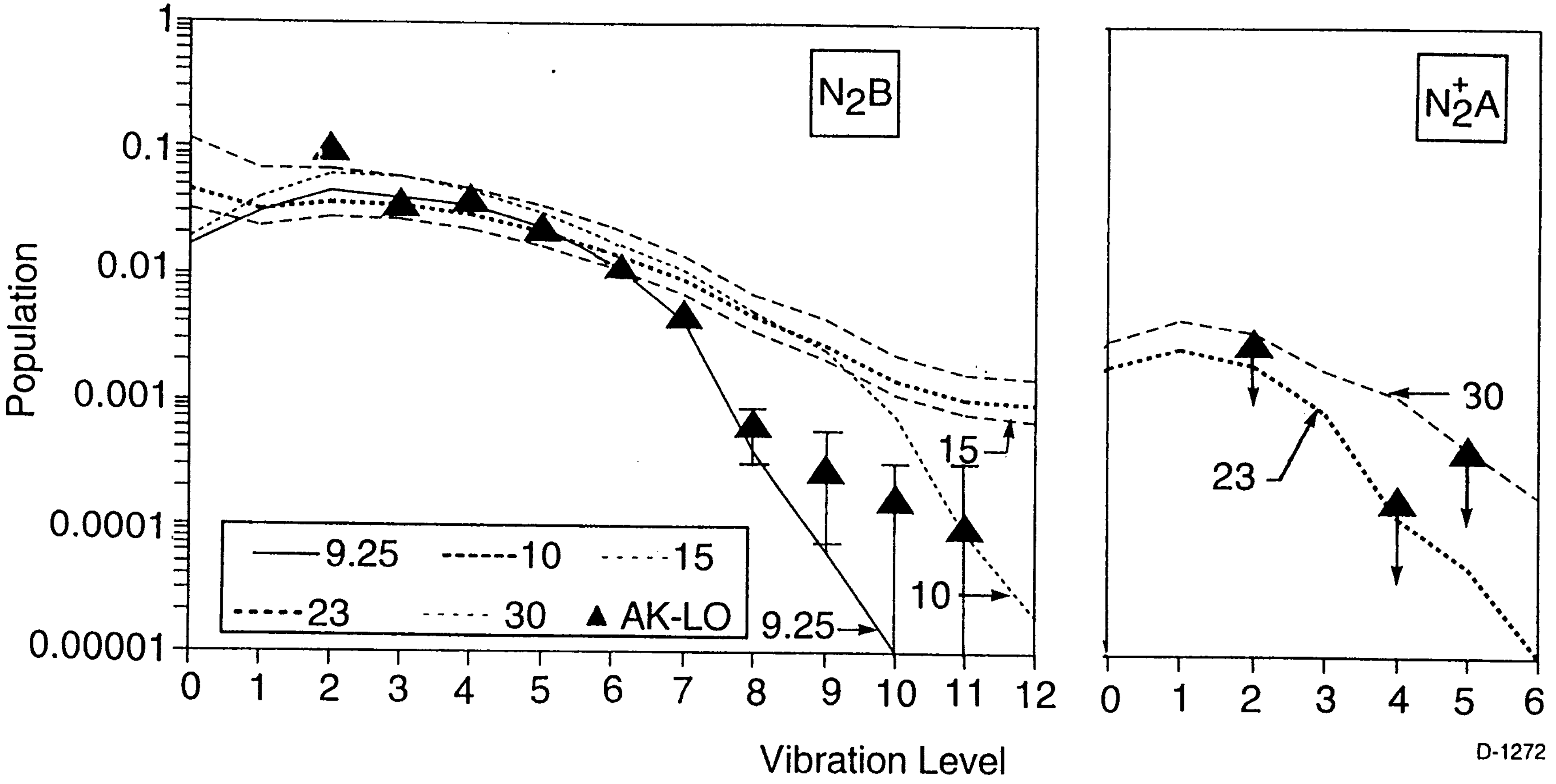

Characteristic Electron Energies
Pure N_2 Discharge

96-4022

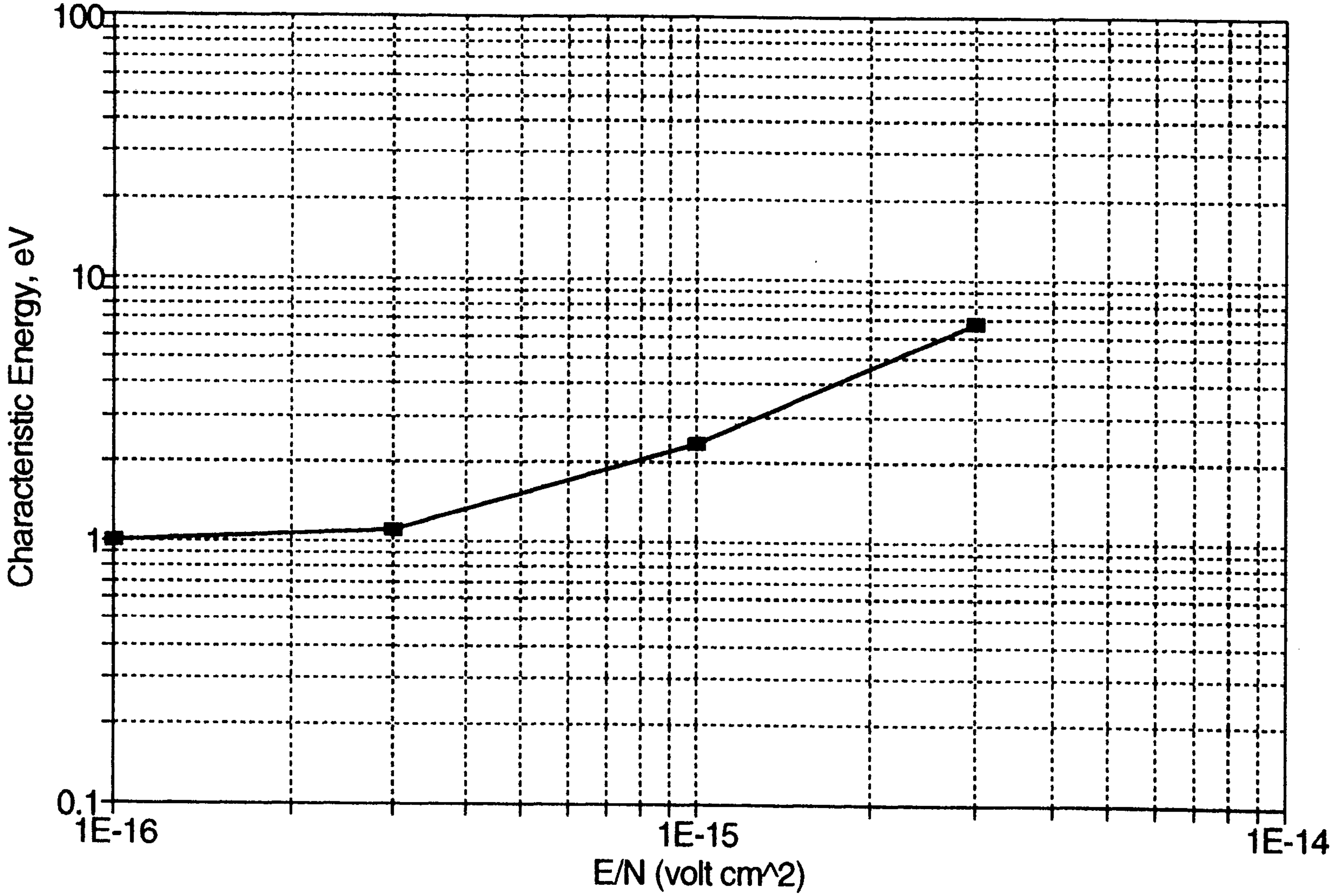

Laboratory Microwave Discharge - Pure N_2

96-4023

Typical E = 30 V/cm

Typical [e] = 10^{11} to 10^{12} cm^{-3}

Druyvesteyn electron energy distribution

P (Torr)	"Altitude" (km)	E/N (V cm^2)	<E> (eV)
0.09	70	2×10^{-14}	> 10 (?)
1.0	55	2×10^{-15}	4
2.0	45	9×10^{-16}	2

Laboratory 40 W Microwave Discharge Emission Spectra at 1 Torr (Piper)

N_2(B-A): v=0-12; N_2(A-X): v=2-5; 600 K

96-4024

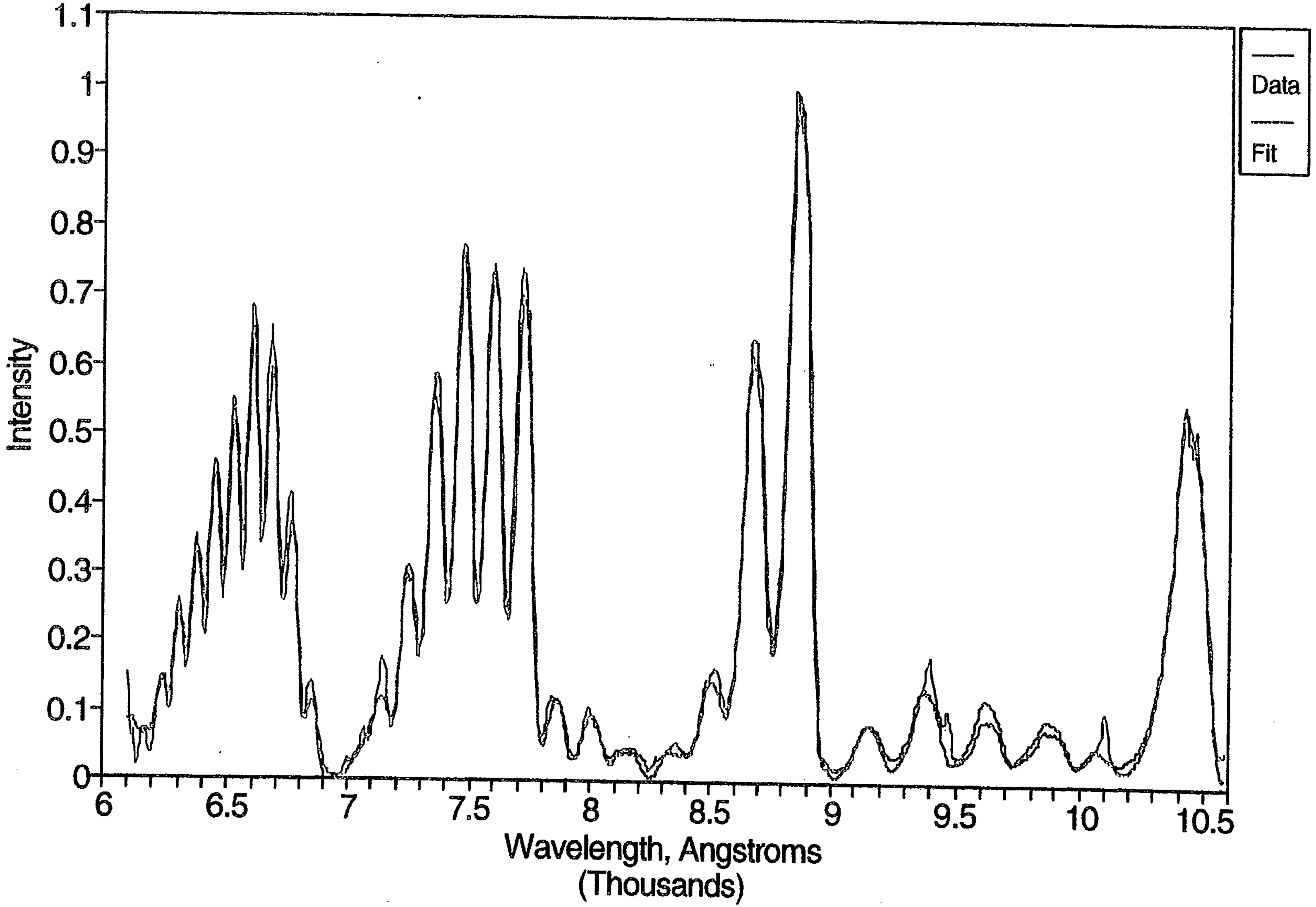

Vibrational Populations Derived from Microwave Discharge Data

N_2(B-A) and N_2^+(A-X): 600 K, 3 nm

96-4025

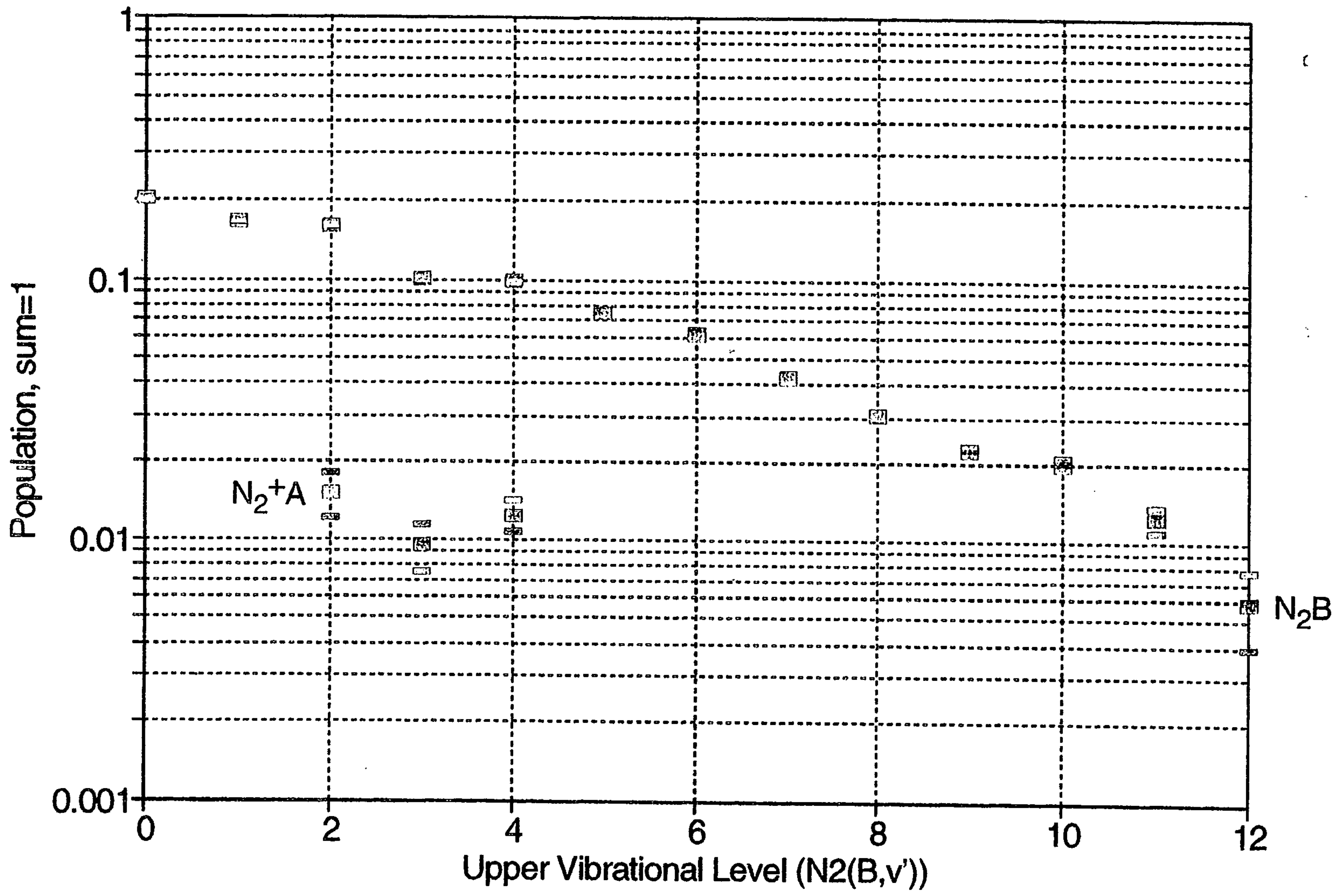

Normalized B-State Vibrational Distribution

96-4026

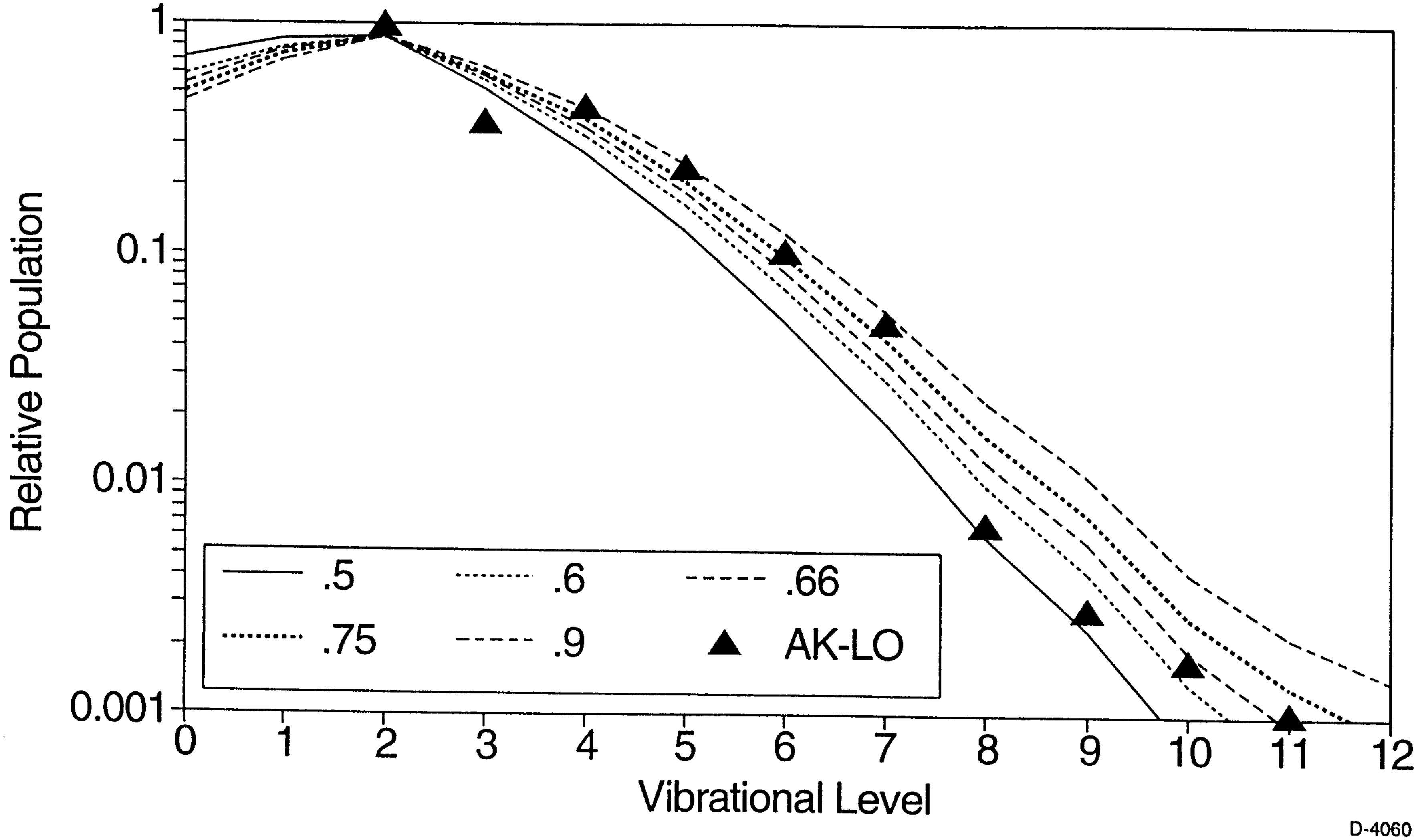

D-4060

Normalized Vibrational Distribution

96-4027

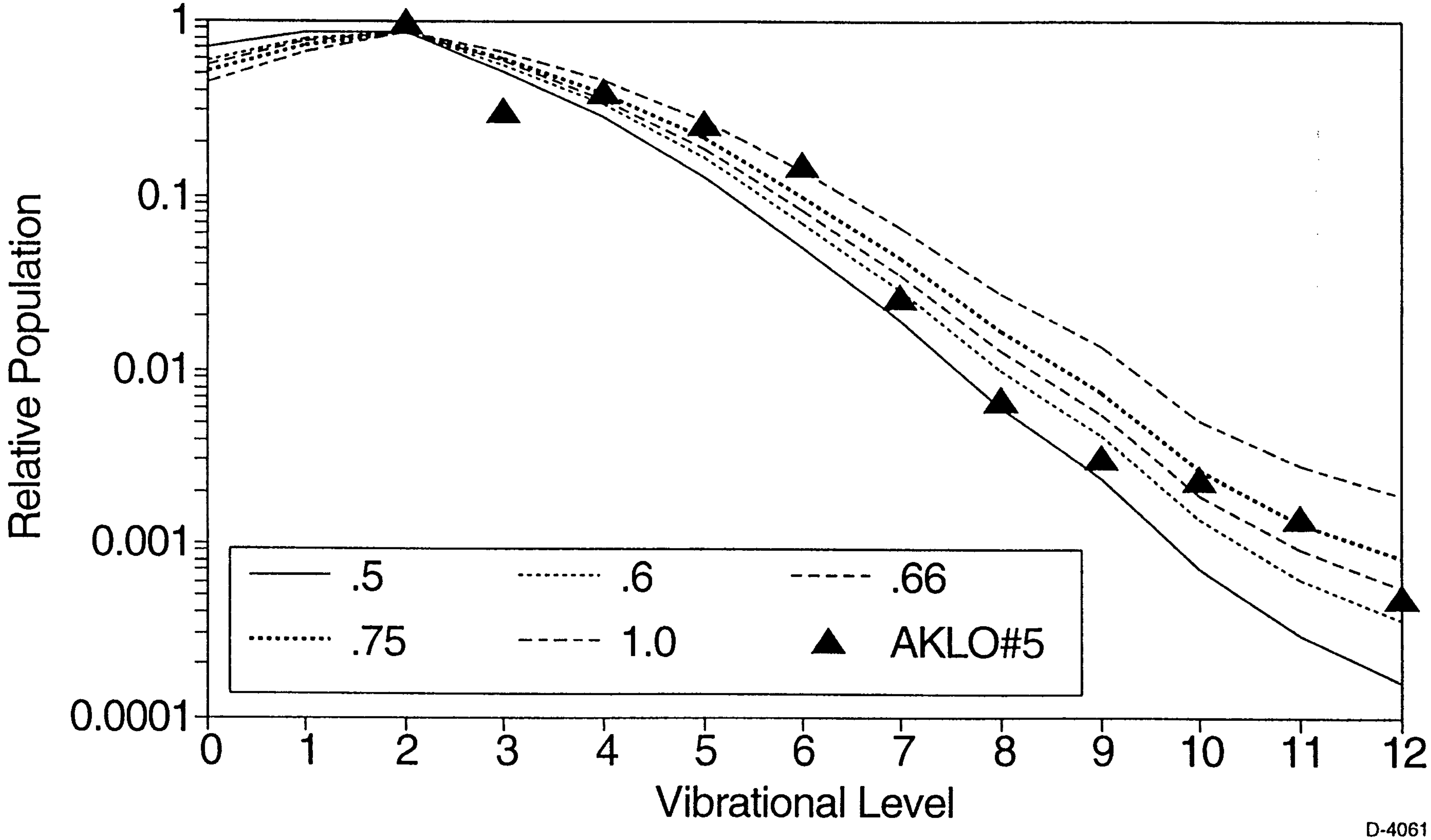

D-4061

Conclusions

- Spectrally resolved emissions from sprites exhibit excellent dynamic range and spectral reproducibility
- Atmospheric transmission correction is problematic
- Spectral distributions exhibit excellent dynamic range and are very reproducible
- Molecular internal populations extracted from emissions exhibit unique B-state distribution
- No N_2^+ A → X emissions observed
- Excitation levels provide insight into exciting electron energy distribution
- "Cold" N_2, B,v>6 distributions: no electrons > 10 eV energies

APPENDIX 14

Spectral and Kinetic Analysis

VG97-50

Spectral and Kinetic Analyses

1995 Campaign
$N_2(v) \rightleftharpoons CO_2\,(v)$

W.T. Rawlins, M.E. Fraser, and B.D. Green
Physical Sciences Inc.
20 New England Business Center
Andover, MA 01810

Sprites Meeting
14 April 1997

Laboratory Microwave Discharge - Pure N_2

Typical E = 30 V/cm

Typical [e] = 10^{11} to 10^{12} cm^{-3}

Druyvesteyn electron energy distribution

P (Torr)	"Altitude" (km)	E/N (V cm^2)	<E> (eV)
0.09	70	2×10^{-14}	> 10 (?)
1.0	55	2×10^{-15}	4
2.0	45	9×10^{-16}	2

Characteristic Electron Energies - Pure N_2 Discharge

96-4022a

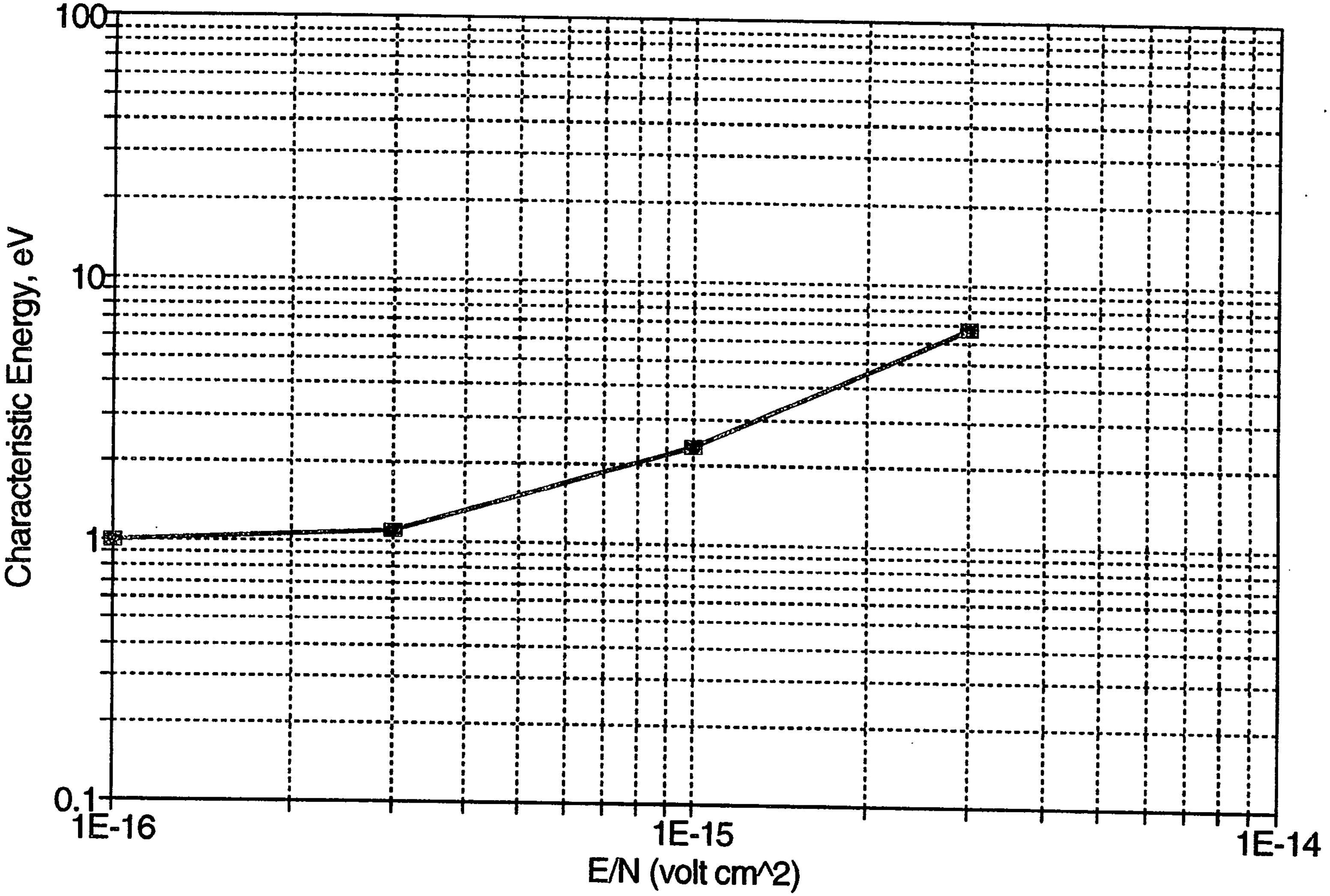

Laboratory 40 W Microwave Discharge Emission Spectra at 1 Torr (Piper)

N_2(B-A): v=0-12; N_2(A-X): v=2-5; 600 K

96-4024a

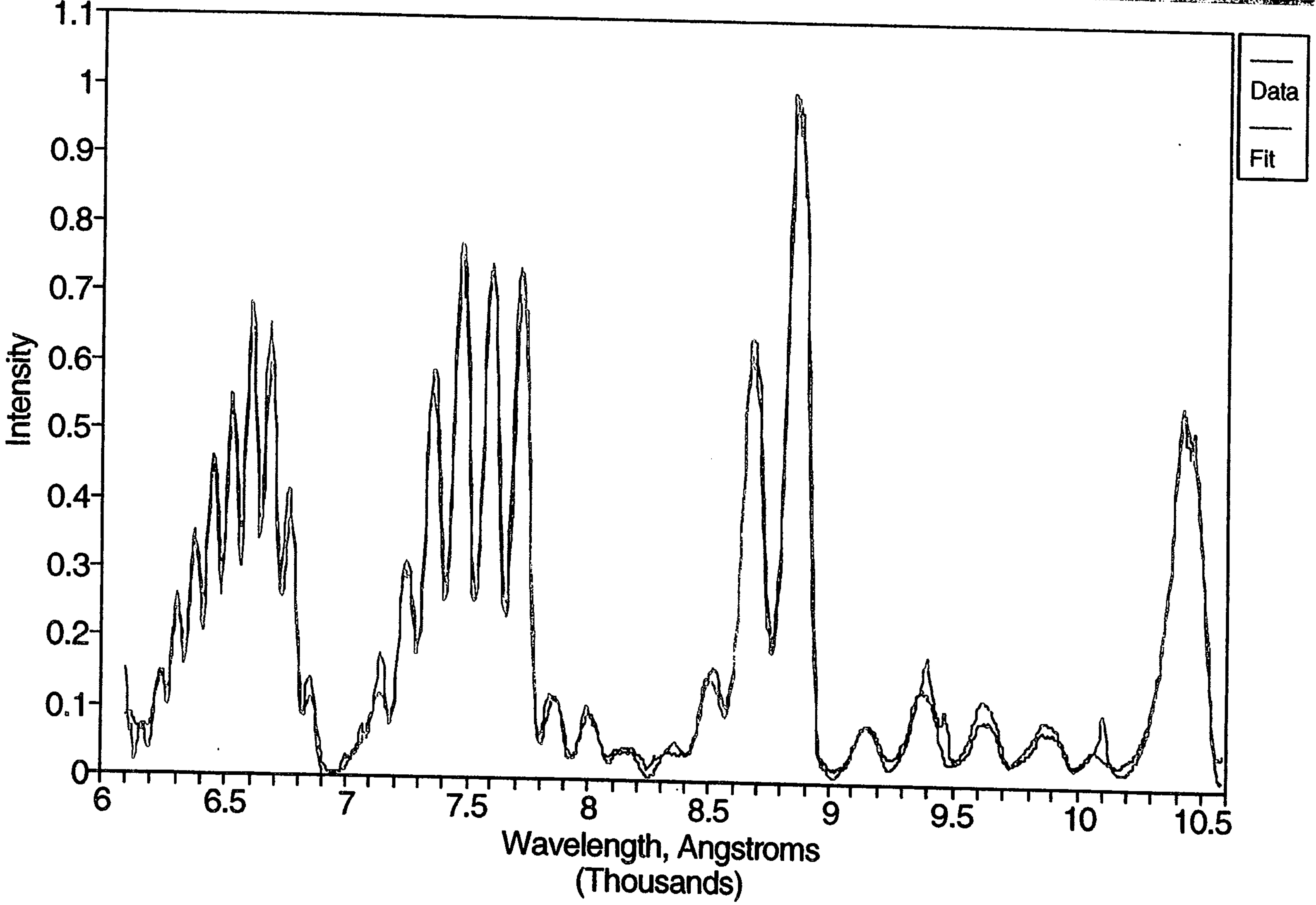

Atmospheric Transmission Through Plant Path to Sprite

96-4019a

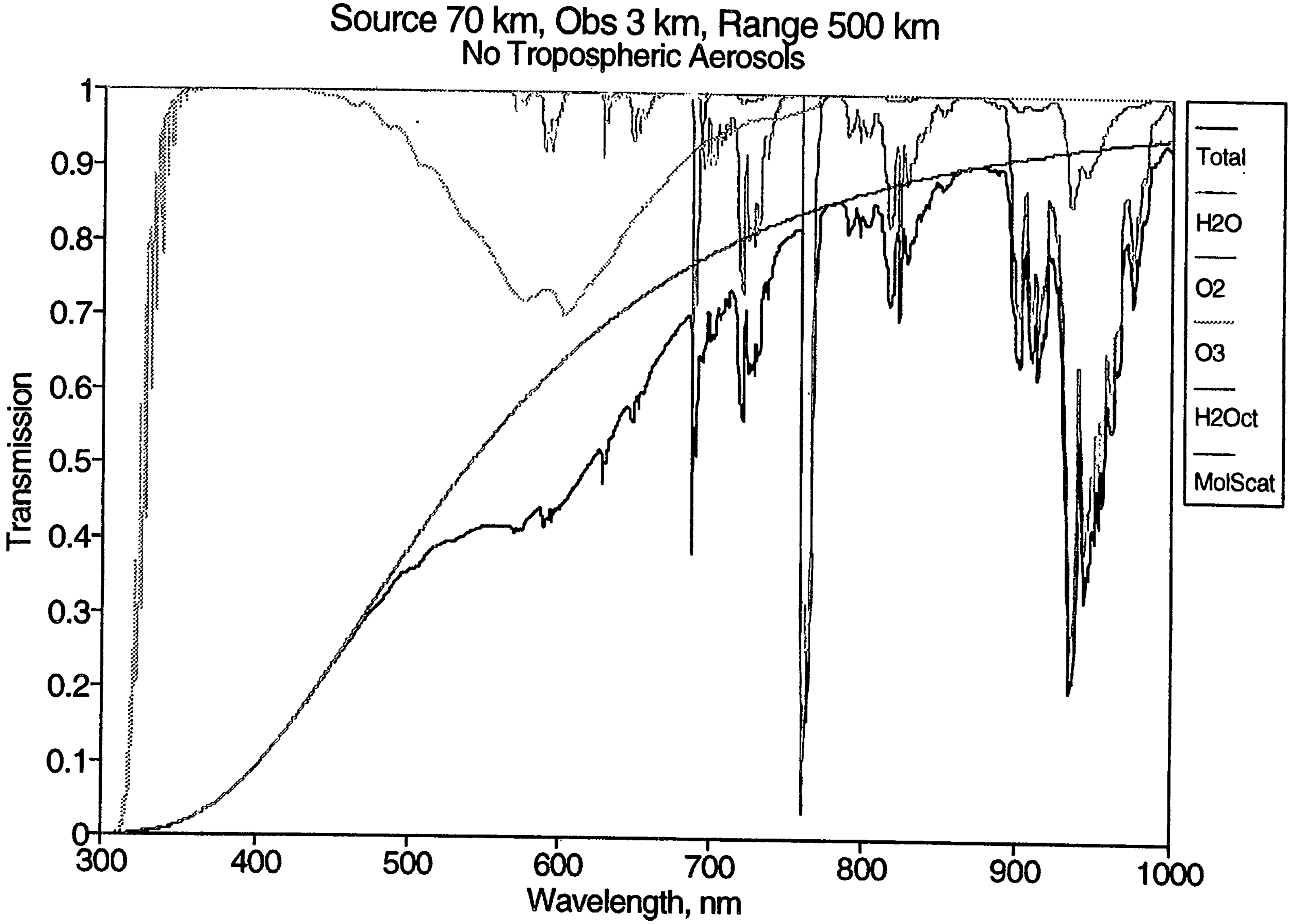

Source 70 km, Obs 3 km, Range 500 km
No Tropospheric Aerosols

N_2 1 + (M&B) 80 KM) and N_2 + A-X (LBC)

1 nm resolution, T_{rot} = 250 K

97-1134

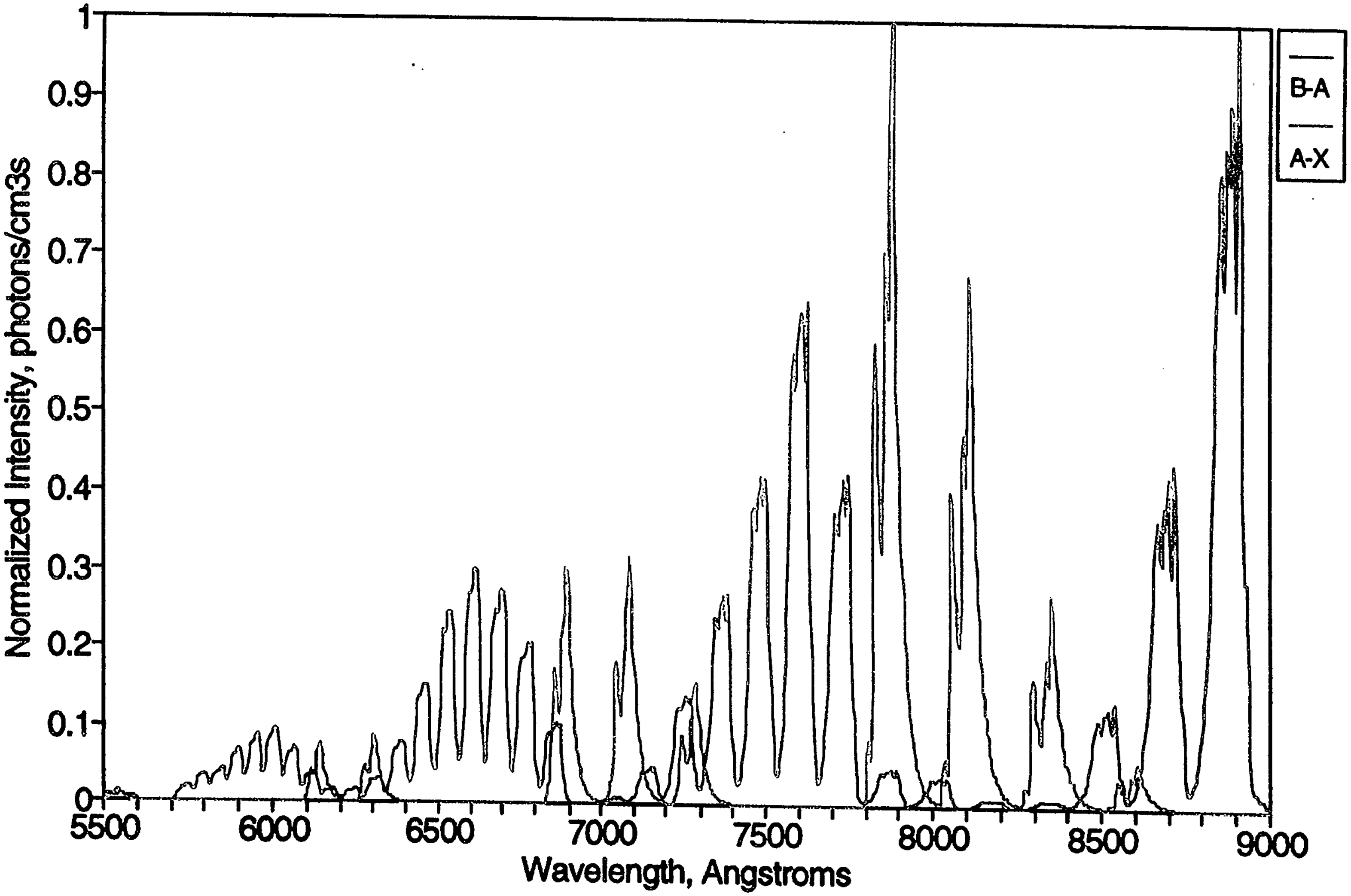

Source 70 km, Obs 3 km, Range 500 km
No Tropospheric Aerosols

97-1135

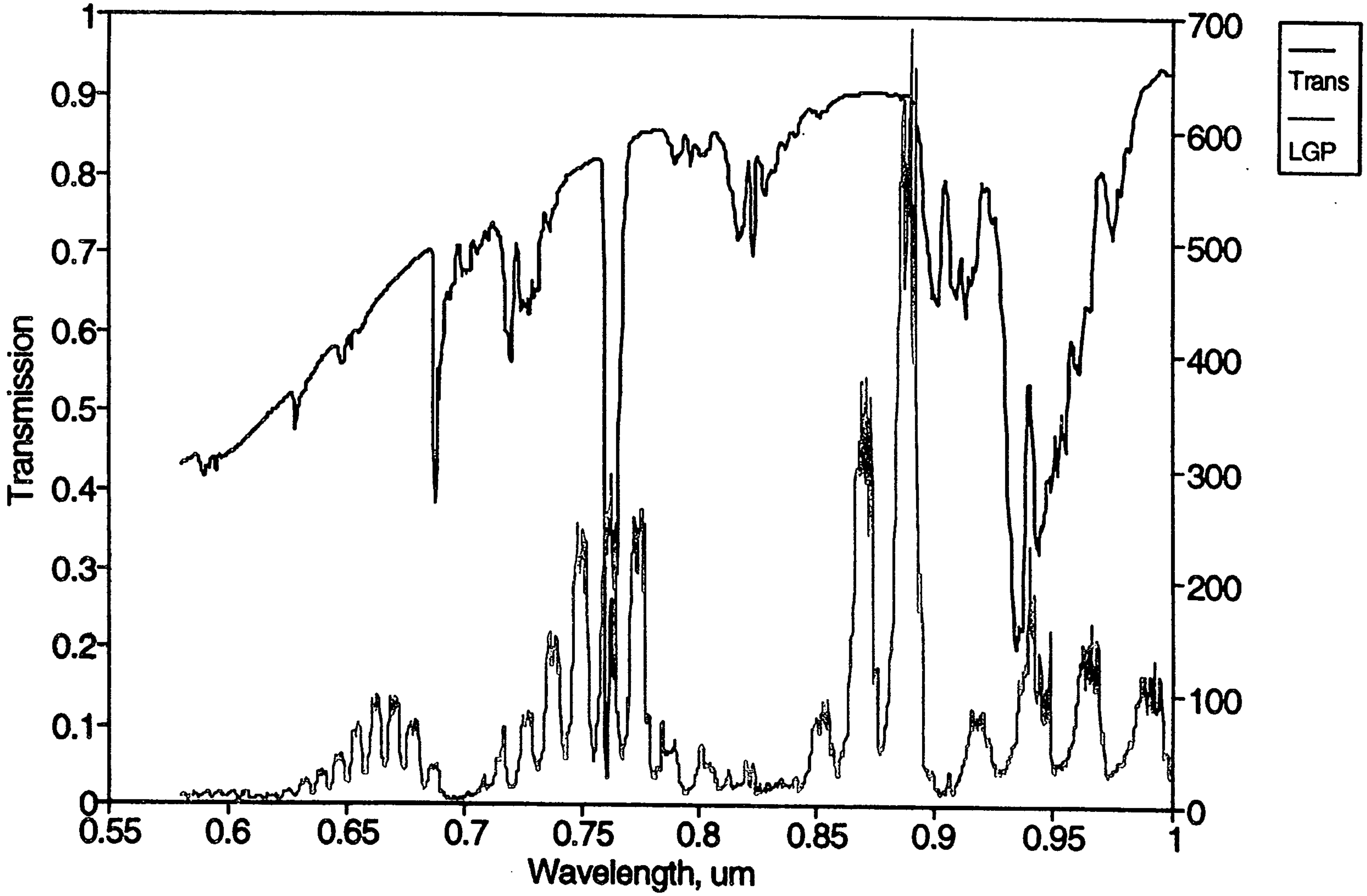

Sprite Spectra:
Log Scale

96-4020a

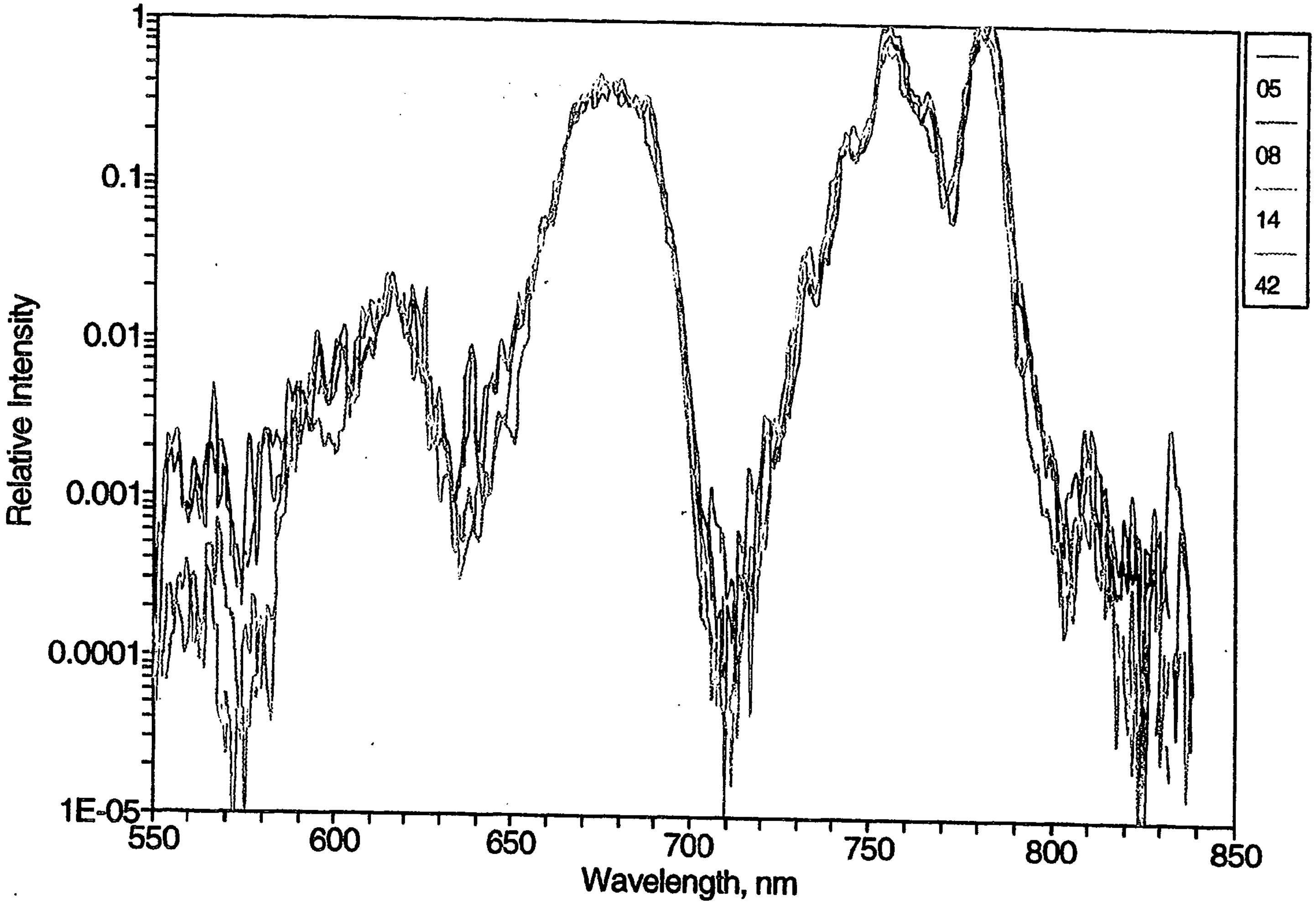

- Large dynamic range in Sprite data
- Very reproducible, little variability between Sprite spectral distributions

Compare AK Sprite and N_2 Discharge

Discharge: 90 W, 0.11 Torr

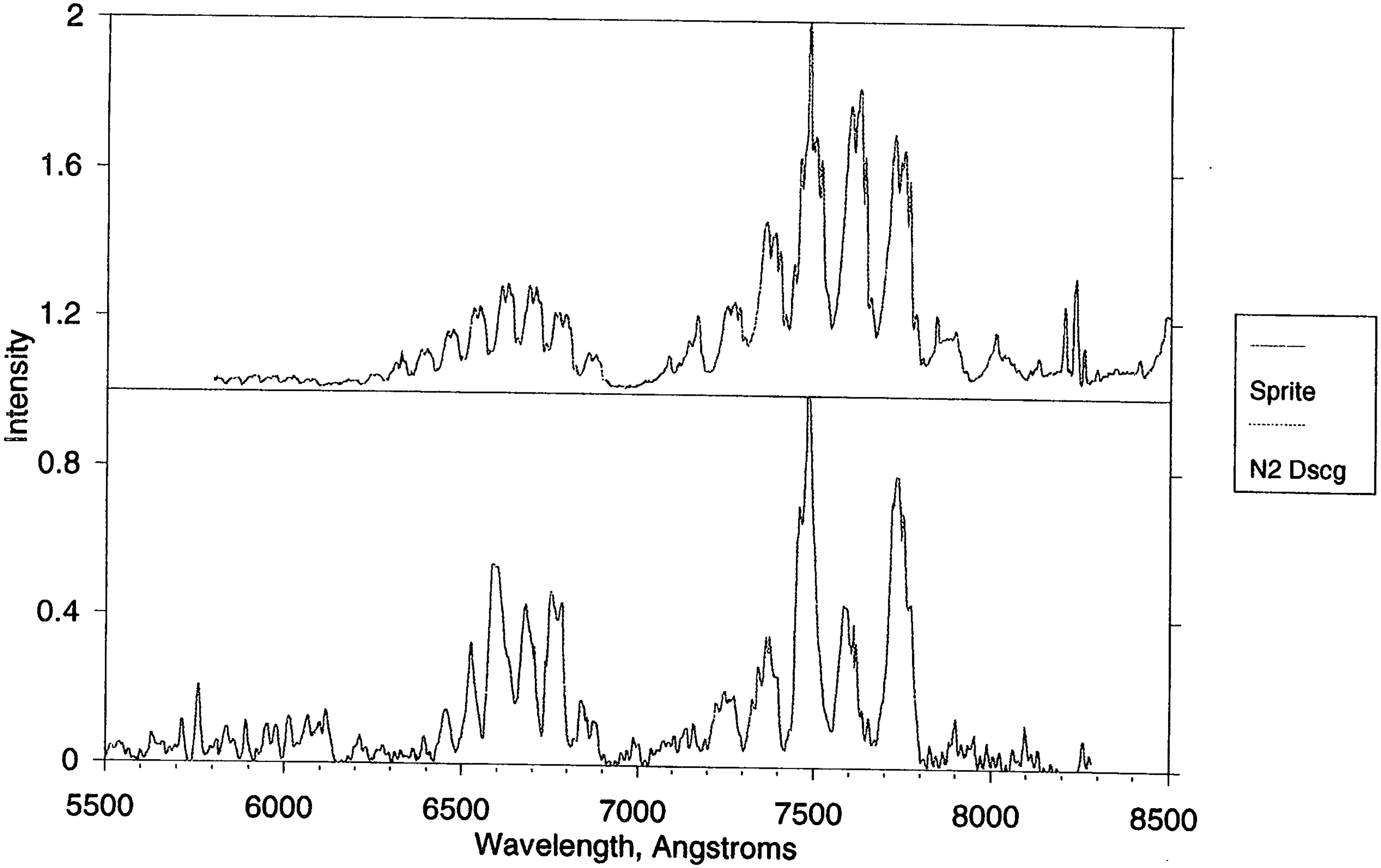

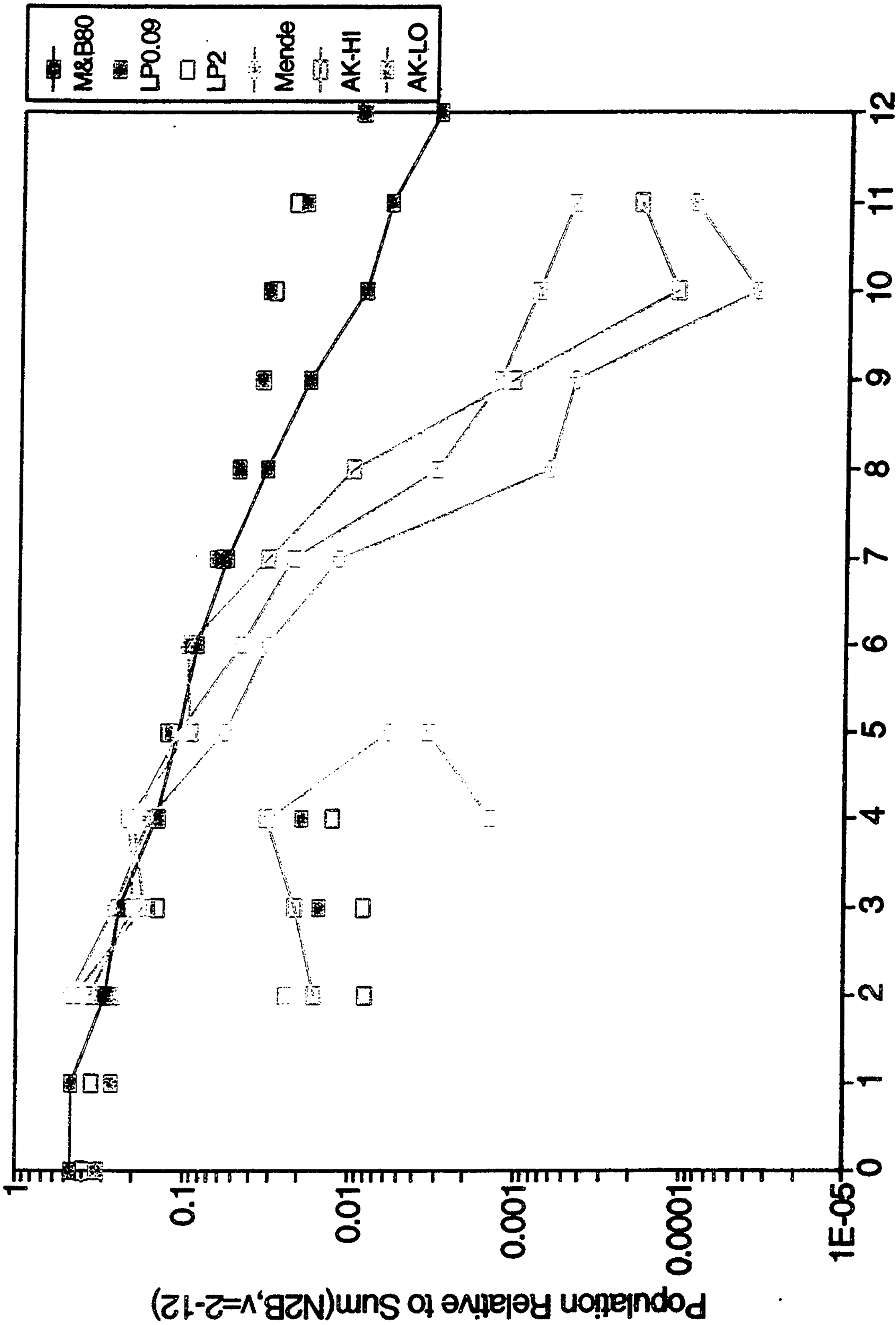
M&B80
LP0.09
LP2
Mende
AK-HI
AK-LO
Population Relative to Sum(N2B,v=2-12)
1
0.1
0.01
0.001
0.0001
1E-05
N2(B) and N2+(A) v' Level
0
1
2
3
4
5
6
7
8
9
10
11
12

Sprite Spectra: "A"

97-1137

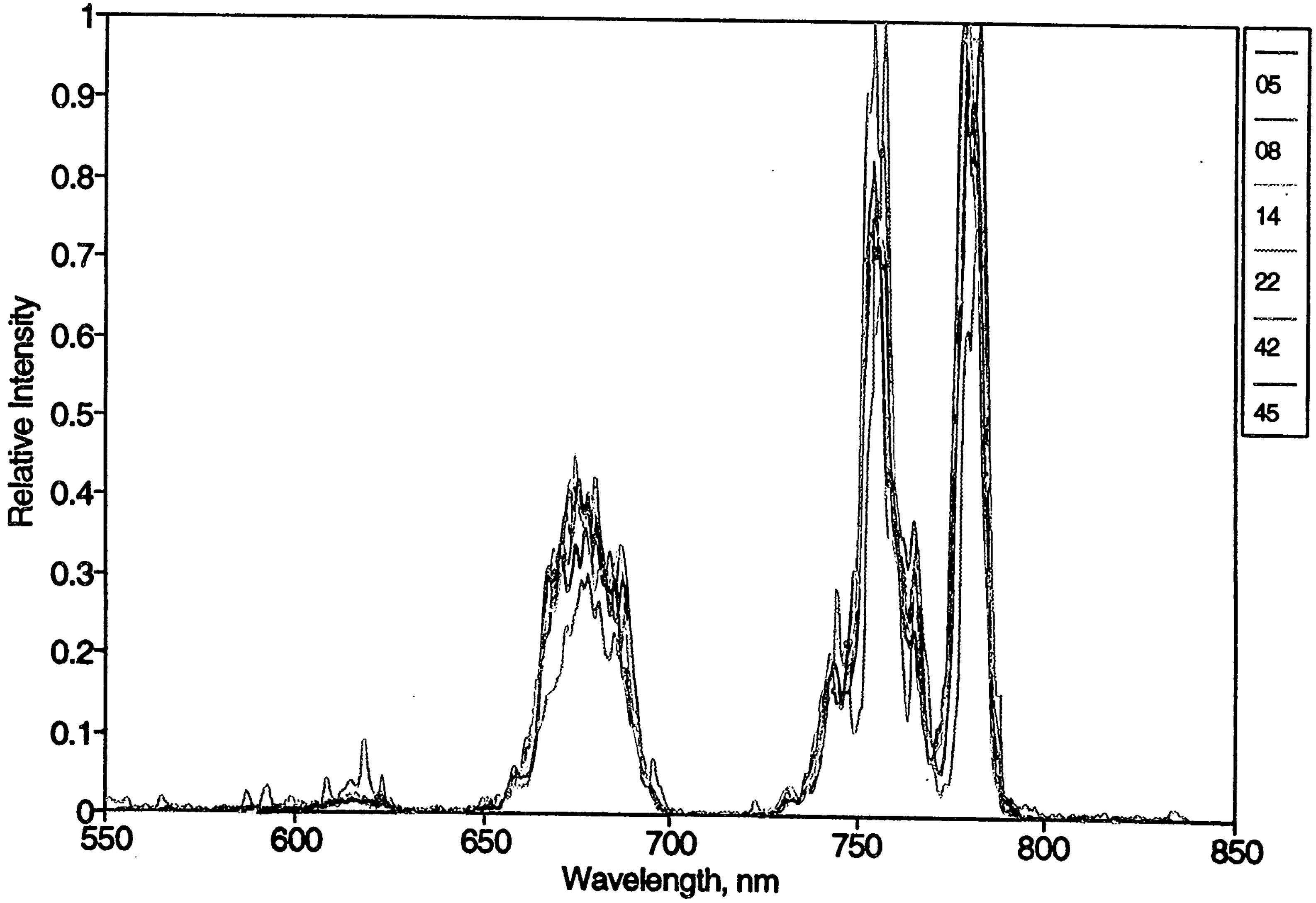

Sprite Spectra: "A-"

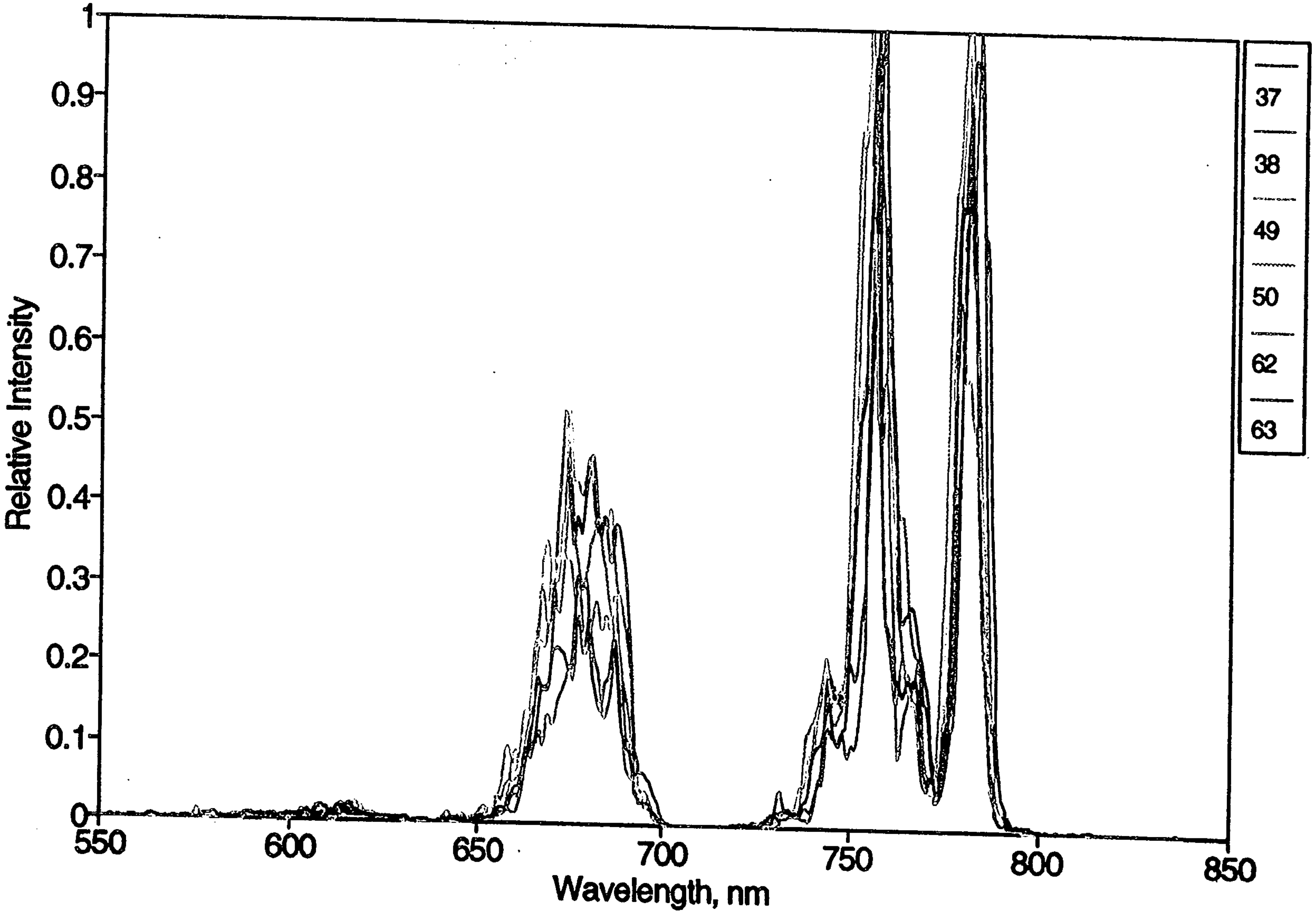

Sprite Spectra: "B"

97-1139

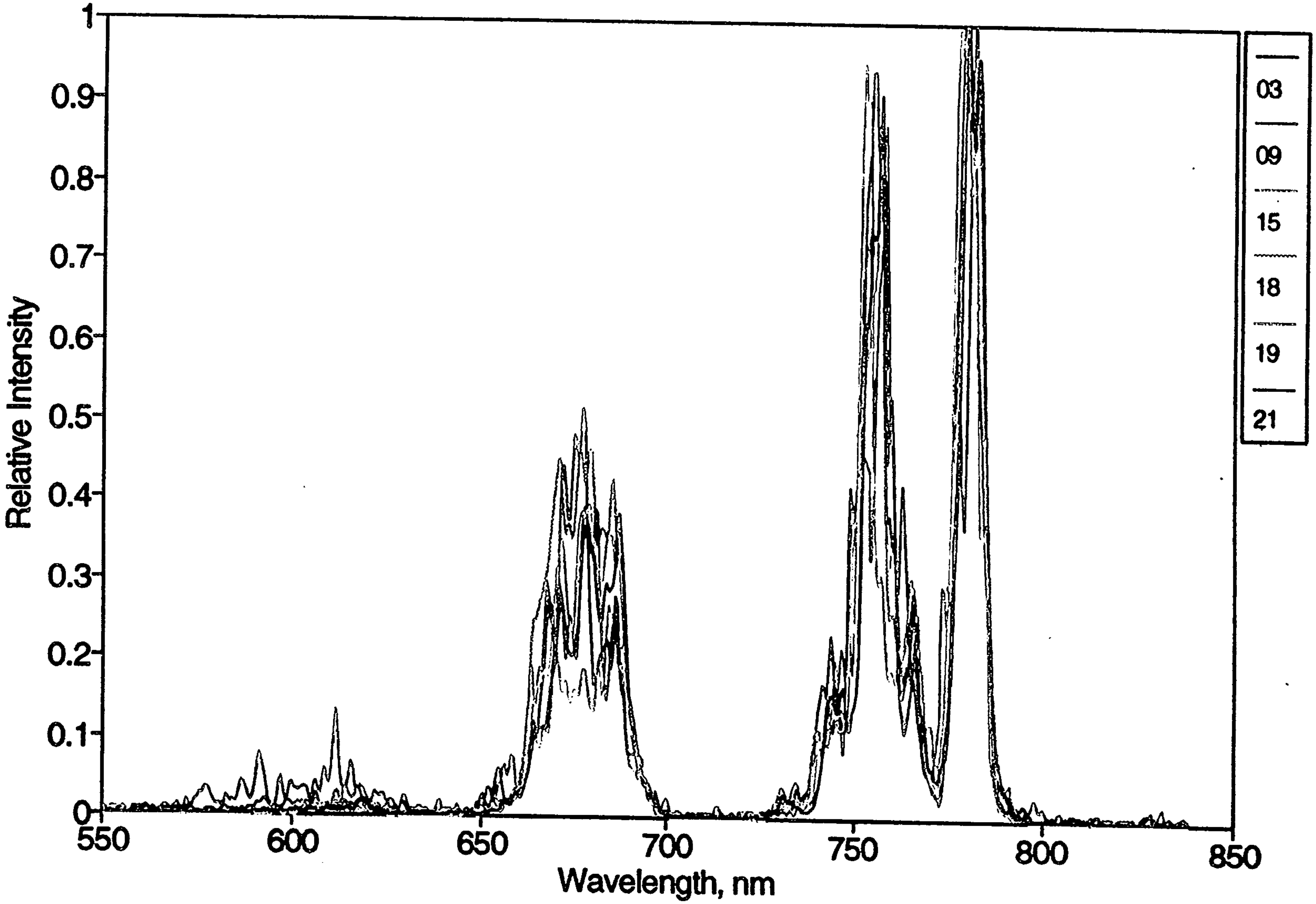

Sprite Spectra: "C"

97-1140

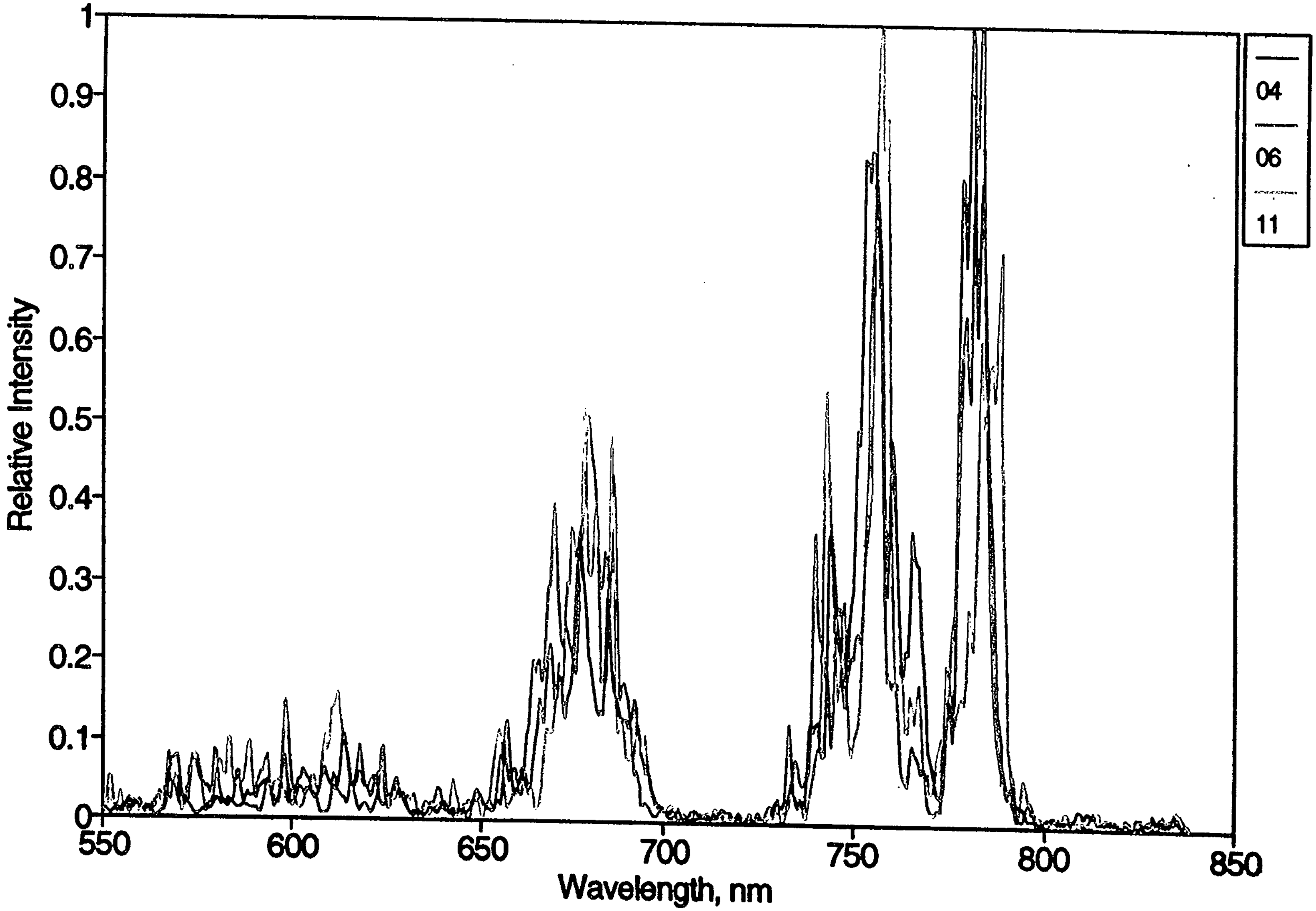

Sprite Spectra: "D"

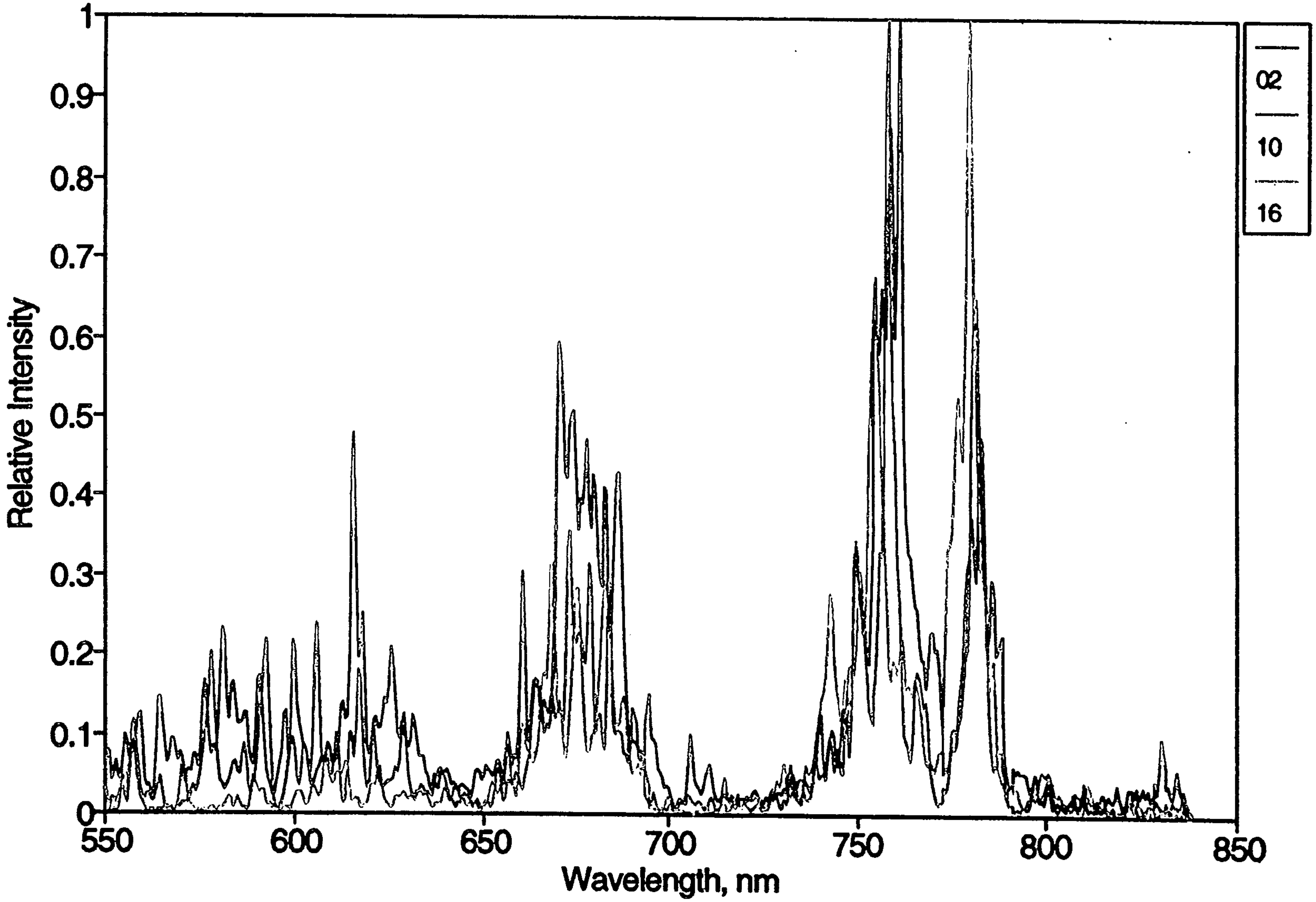

Spectral Fitting Procedure

96-4021a

- Generate spectral basis functions: 250 K, 60 Å
- Flat response, fit dv=2 for wavelength correction
- Atm transmission correction:
  - MODTRAN, US Std Atm, minimum aerosols
  - slant path parameters: 3→70 km @ 500 km
  - pass 60 Å slit function
- Fit dv=2 for v′=2,4-7 populations
- Fit dv=3 for v′=3-10 populations
- Combine populations to determine N_v/Sum(N_v)

Hampton et al. at 2 mm Resolution (AK-HI)

96-294b

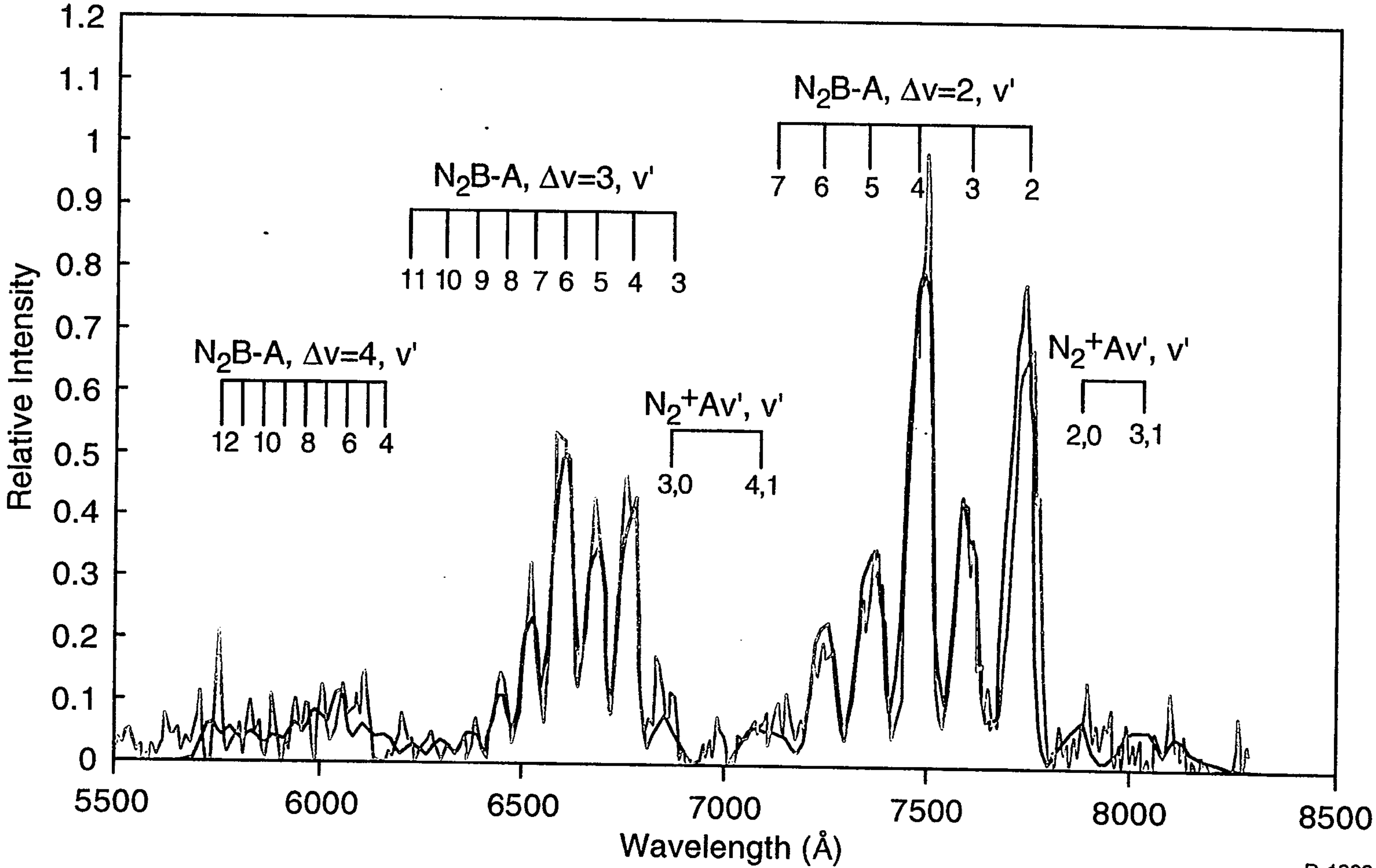

D-1266

N_2 1+, N_2+ Meinel Fit: 250 K, 6 nm

Sprite 05.dat + Trans 70-75A

97-1142

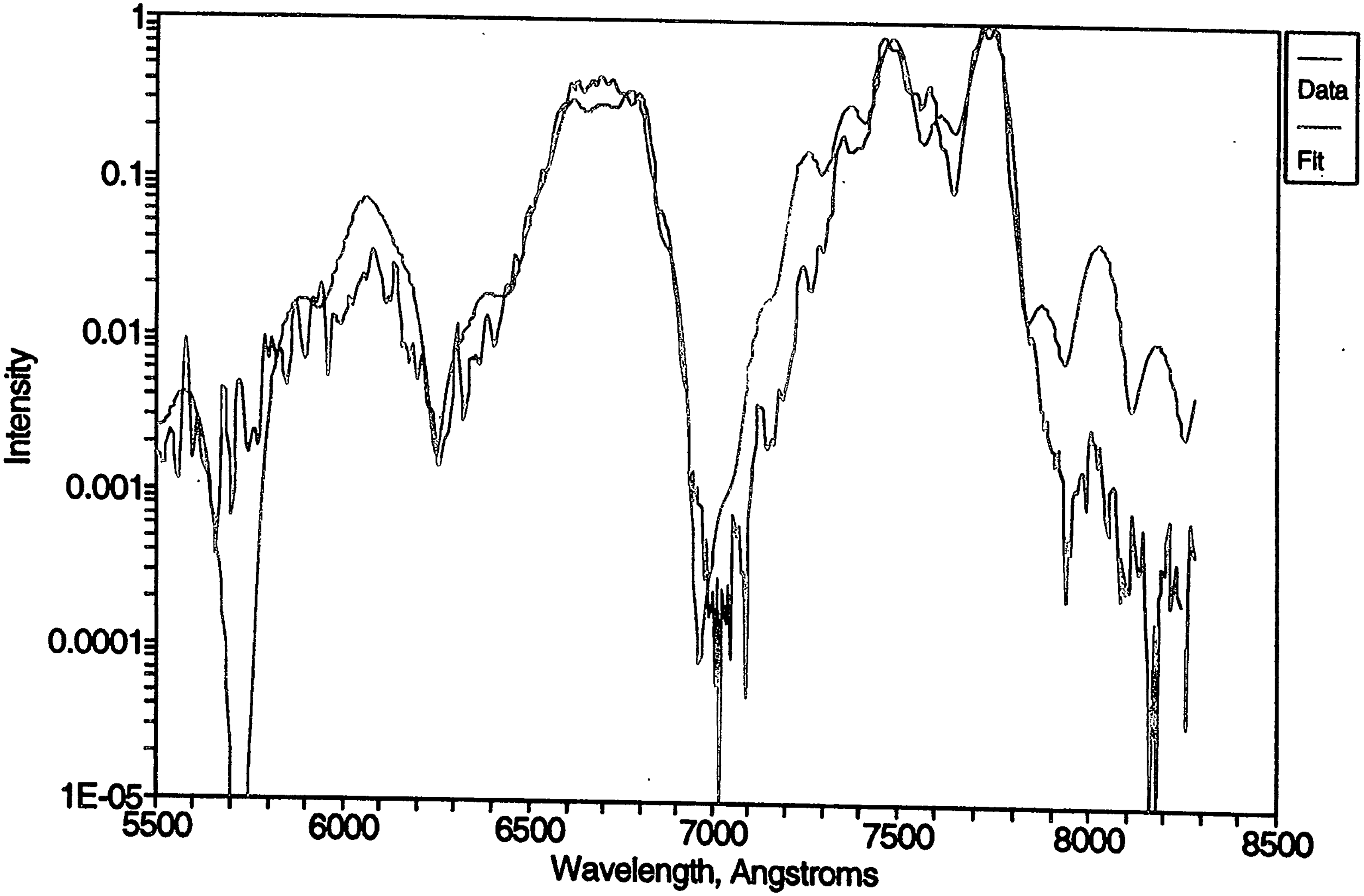

N_2 1+, N_2+ Meinel Fit: 250 K, 6 nm
Sprite 05.dat + Trans 70-75A

97-1143

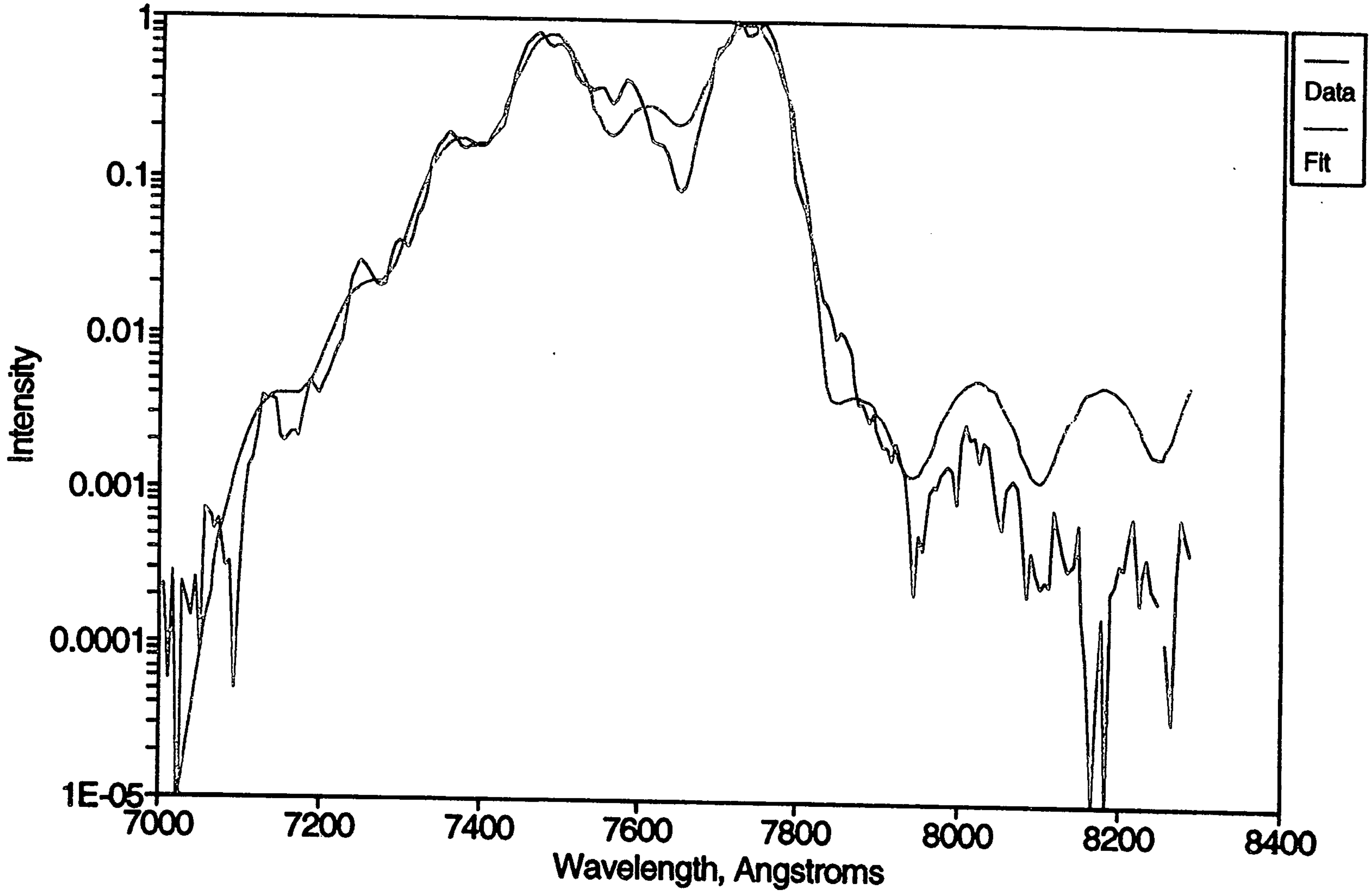

N_2 1+ Fit: 250 K, 6 nm, v=3-10

Sprite 05.dat + Trans 70-75A; dV=3 only

97-1144

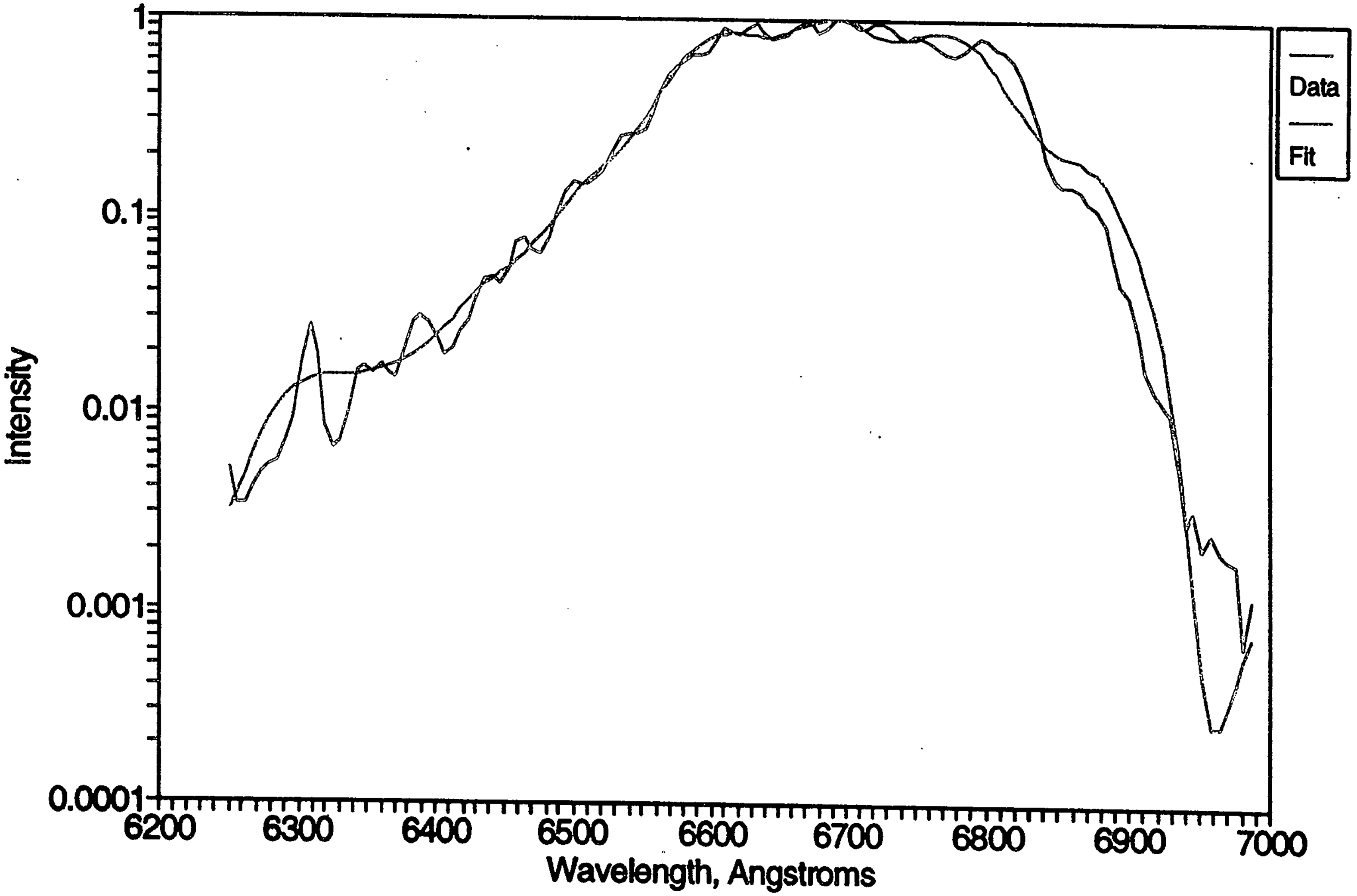

N_2 1+, N_2+ Meinel Fit
250 K, 6 nm

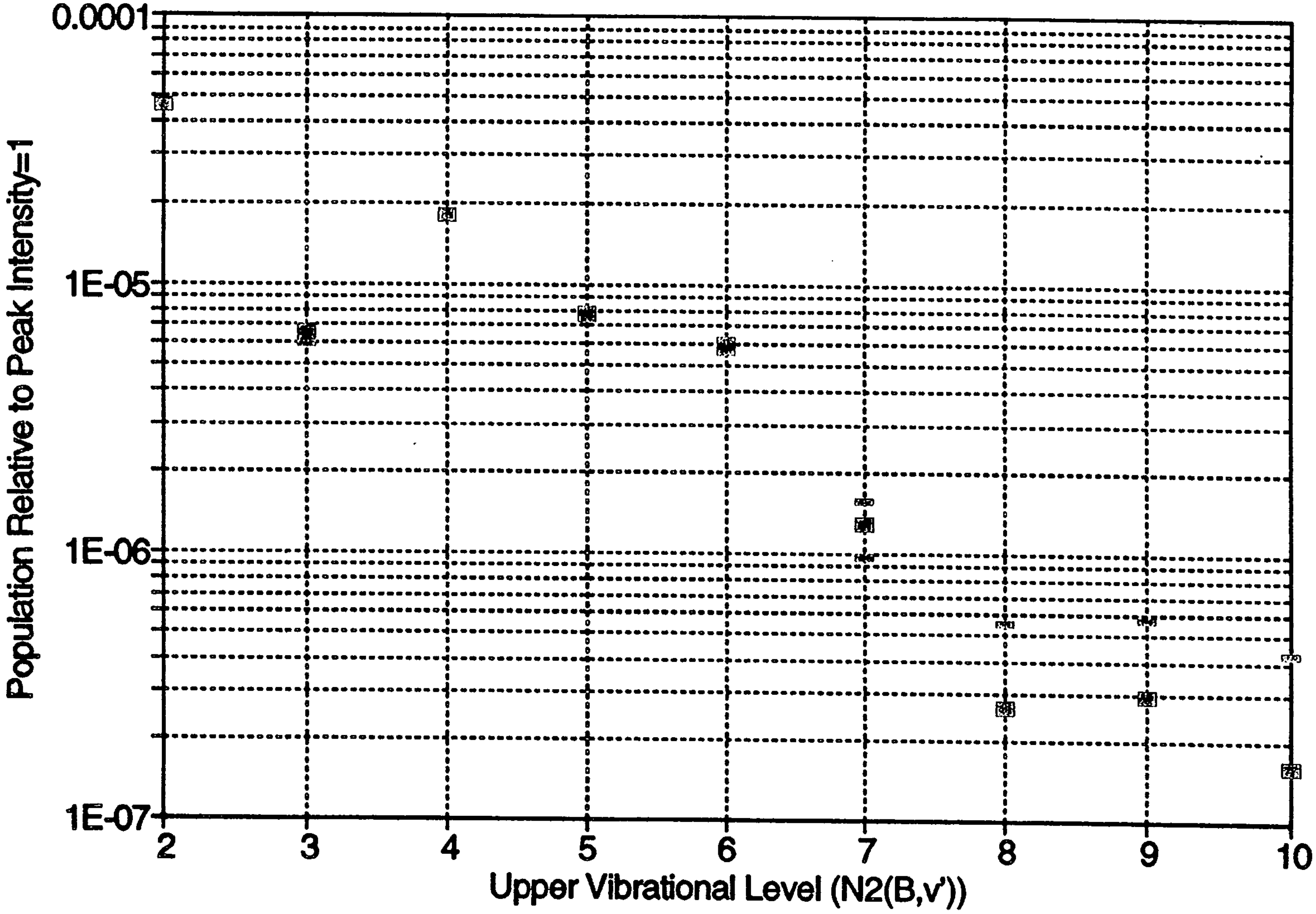

Nitrogen B-State Vibrational Population Distributions

96-3965a

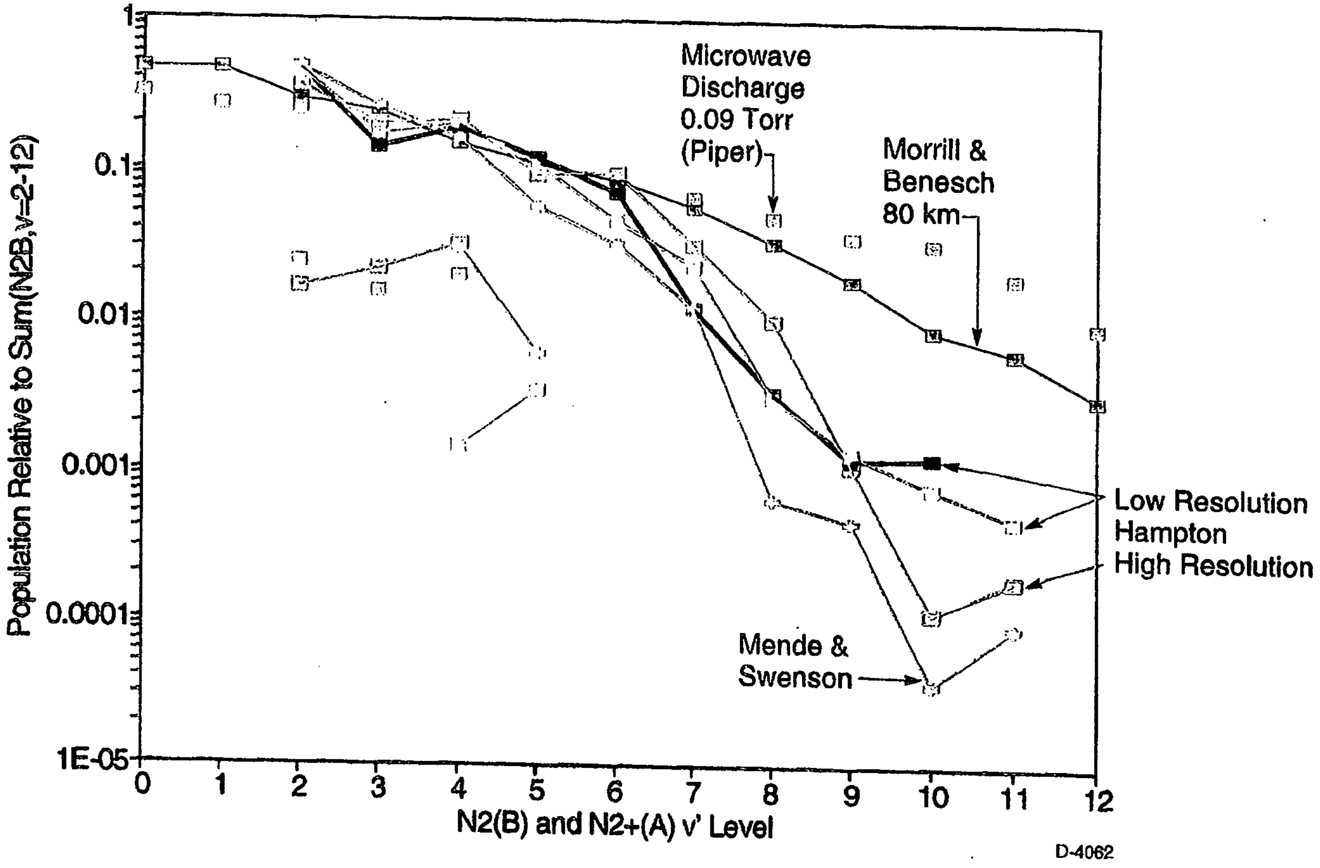

- Distributions similar (within error bars)
- Instrumental baseline signals and atmospheric transmission
- Derived populations clearly "colder" than auroral-like (MB) and microwave discharge (P) distributions

Vibrational Distributions

96-297b

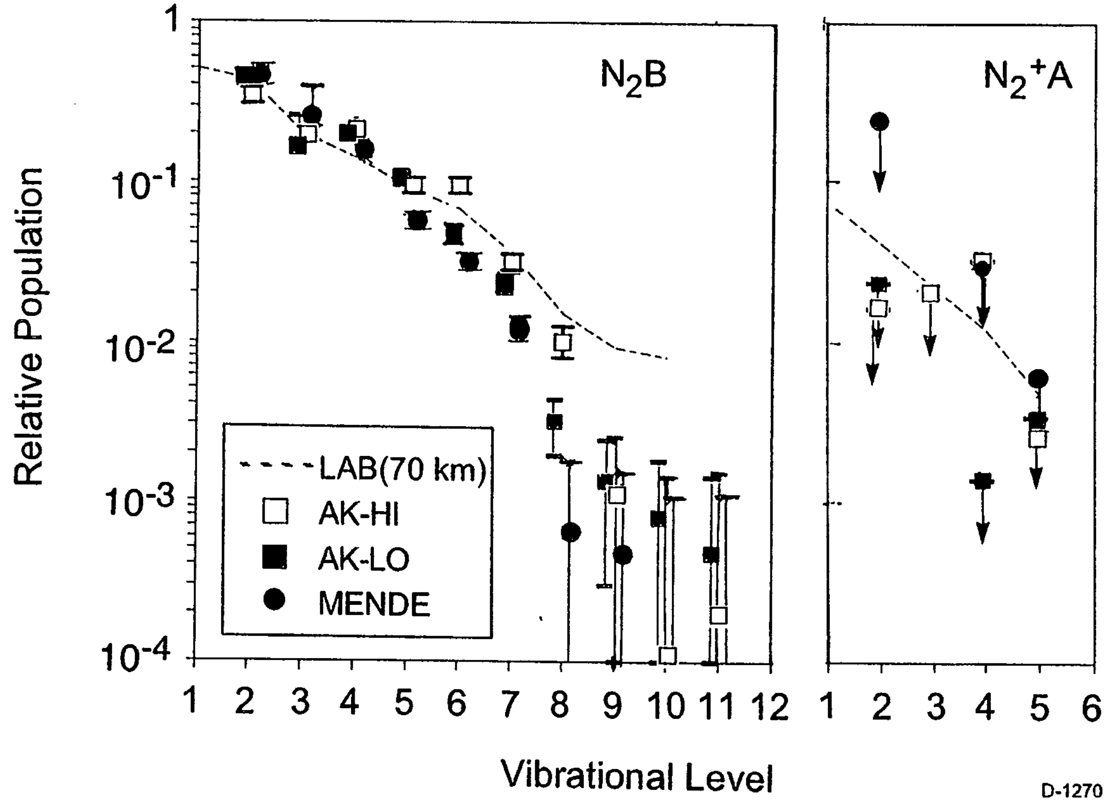

D-1270

From GRL 23(16), 2161 (1996)

What Happened to $N_2(B, v' > 6)$?

96-4028a

○ Transmission (response) function <7000 Å
- ozone
- aerosols

○ Quenching or W↔B intersystem collisional transfer (ICT)
- quenching unlikely
- ICT has only subtle effect on v distribution

○ High v′ not produced: not enough electrons > 10 eV

Boltzmann Electron Model

96-300b

- Boltzmann electron energy distribution
  - — convolve with excitation cross sections
  - — correct for quenching
  - — compare predicted and observed population distributions

- Best match: 1 eV electron "temperature"
  - — lower bound
  - — Druyvesteyn <E> probably 2 to 3 eV
  - — $T_e > 10$ eV required to produce observable $N_2^+(A)$

- Monoenergetic electron model
  - — 9 to 10 eV electrons must be present (N_2B, $v \geq 8$)
  - — > 23 eV electrons not present (no $N_2^+(A)$)

Boltzmann Electron Model

96-298b

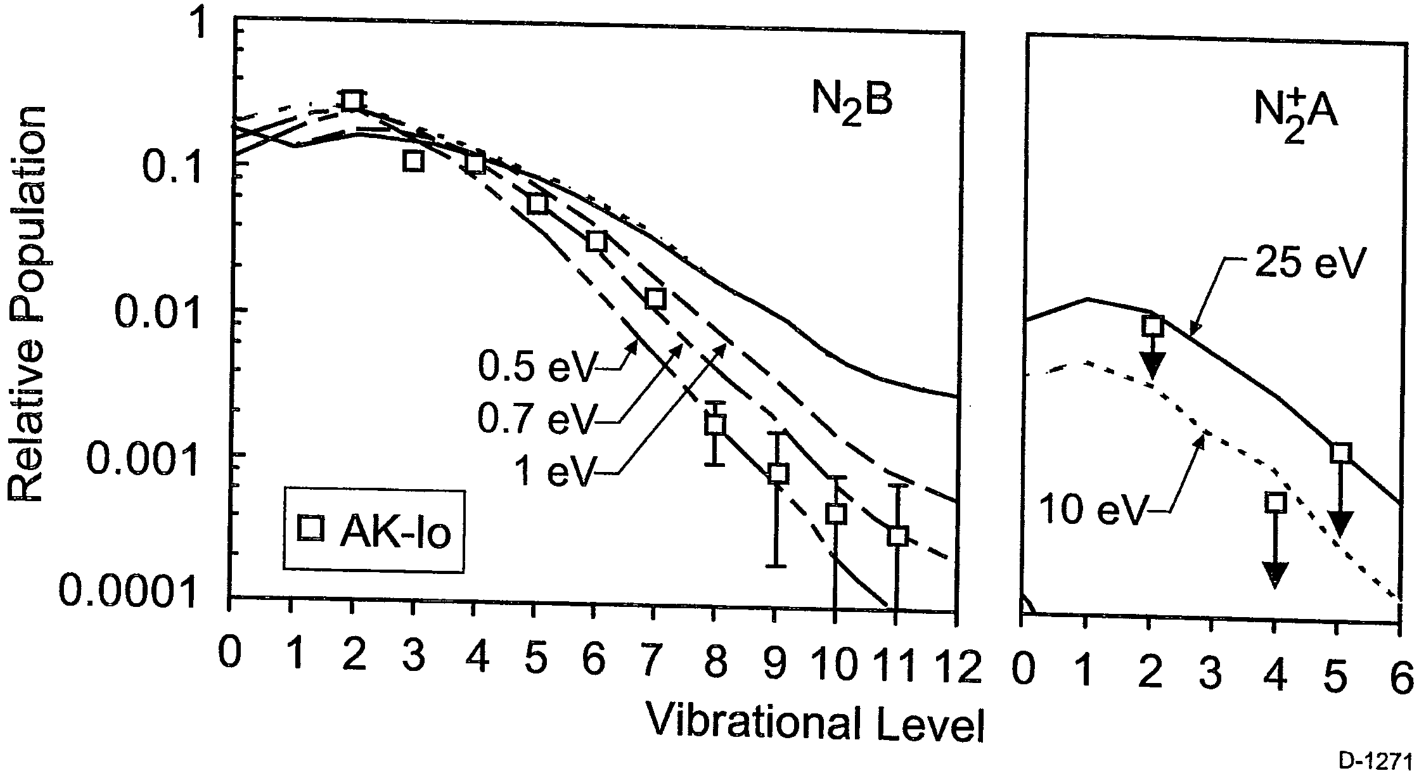

Monoenergetic Electron Model

96-299b

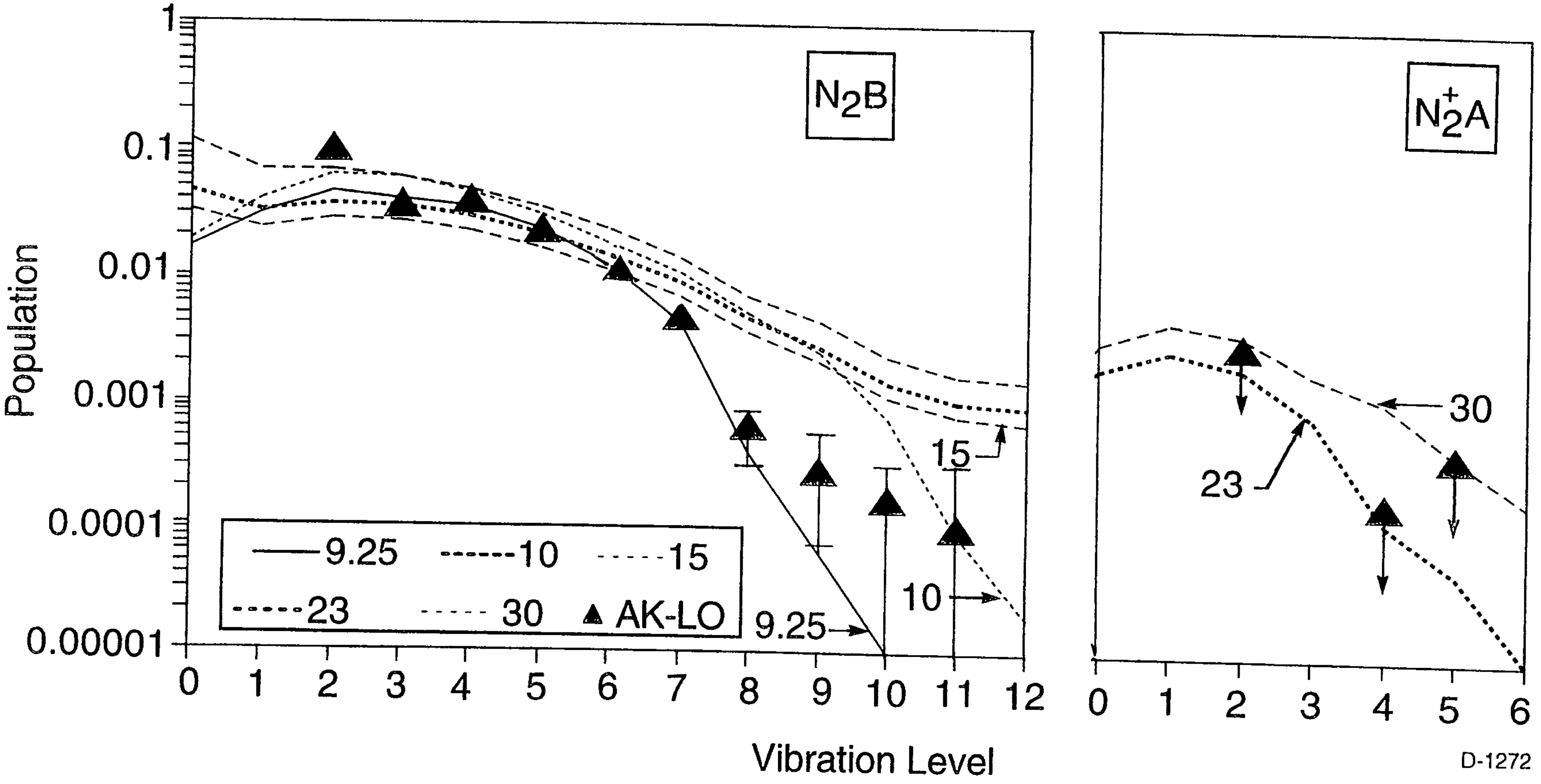

Normalized Vibrational Distribution

96-4027a

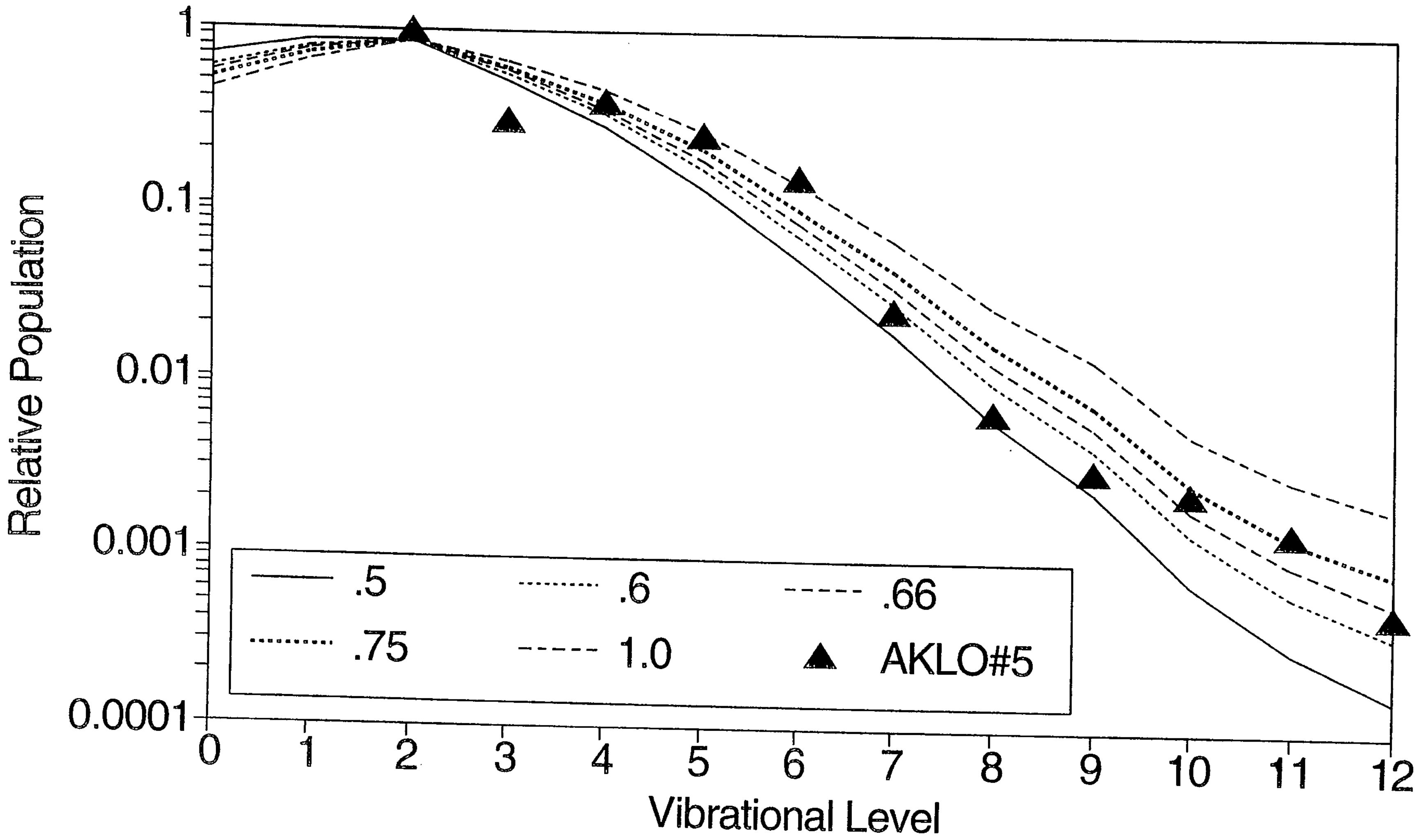

D-4061

Conclusions

- Spectrally resolved emissions from sprites exhibit excellent dynamic range and spectral reproducibility
- Atmospheric transmission correction is problematic
- Spectral distributions exhibit excellent dynamic range and are very reproducible
- Molecular internal populations extracted from emissions exhibit unique B-state distribution
- No N_2^+ A → X emissions observed
- Excitation levels provide insight into exciting electron energy distribution
- "Cold" N_2, B,v>6 distributions: no electrons > 10 eV energies

Questions on AK 95 Data

- Absolute intensities
- Altitude estimates
- Sprite viewing factors
  - temporal
  - spatial
- Star check on response correction
- ‘96 spectral data

Vibraluminescence

97-1124

$$e + N_2 \rightarrow N_2(v) + e$$

$$N_2(v) + CO_2 \rightleftharpoons CO_2(v) + N_2$$

$$CO_2\ (v) \rightleftharpoons CO_2 + h\nu$$

$$\left[\begin{array}{c} N_2(v) + \begin{pmatrix} N_2 & O \\ O_2 & H_2O \end{pmatrix} \rightarrow \text{quenched} \\ CO_2(v) + \begin{pmatrix} O_2 & O \\ CO_2 & H_2O \end{pmatrix} \rightarrow \text{quenched} \\ e + CO_2 \rightarrow CO_2(v) + e \end{array}\right] \text{negligible}$$

$N_2(v=1)$ Collisional Deactivation
CIAP 1974

97-1130

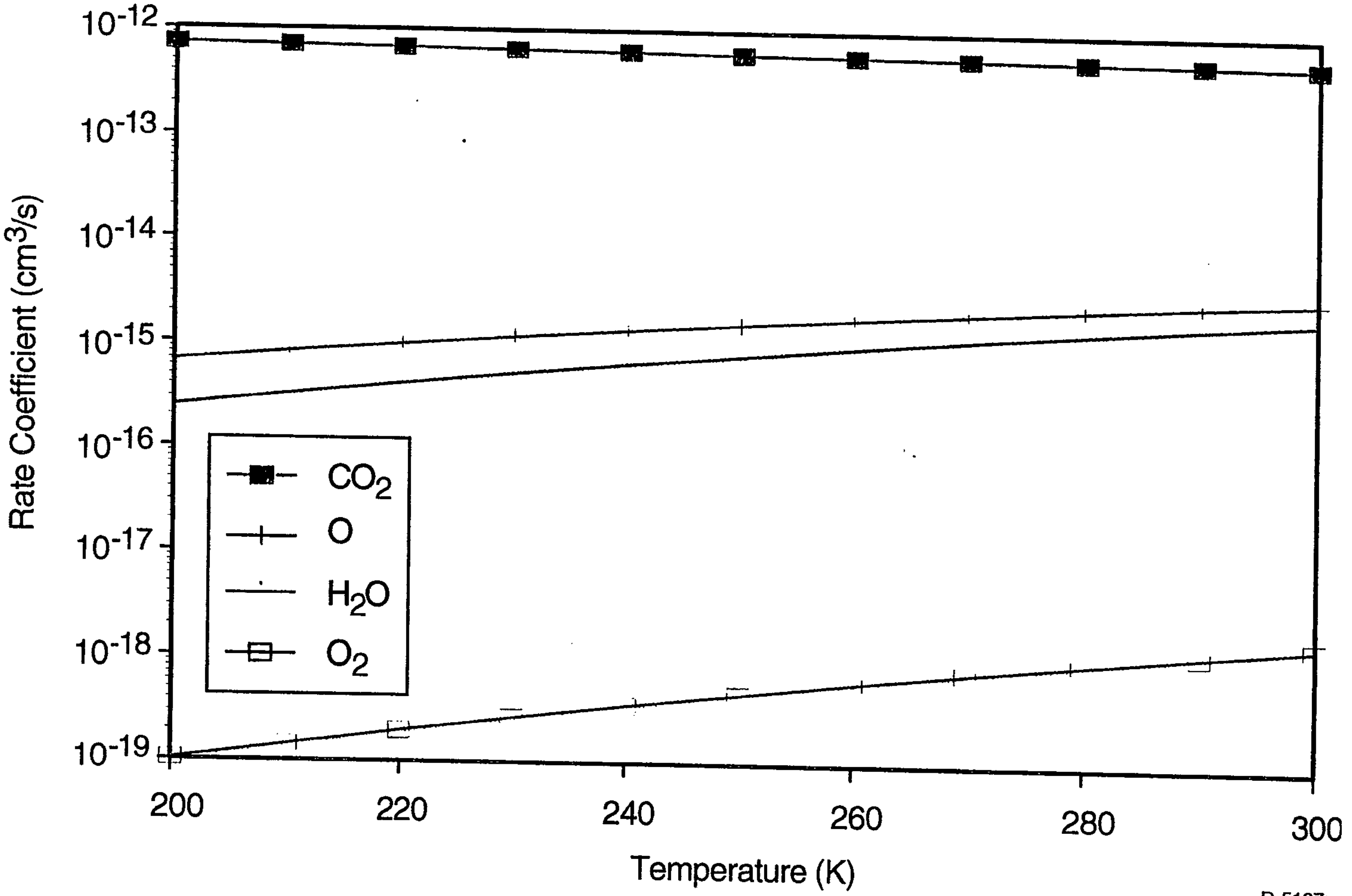

D-5127z

CO_2(001) Collisional Deactivation
CIAP 1974

97-1129

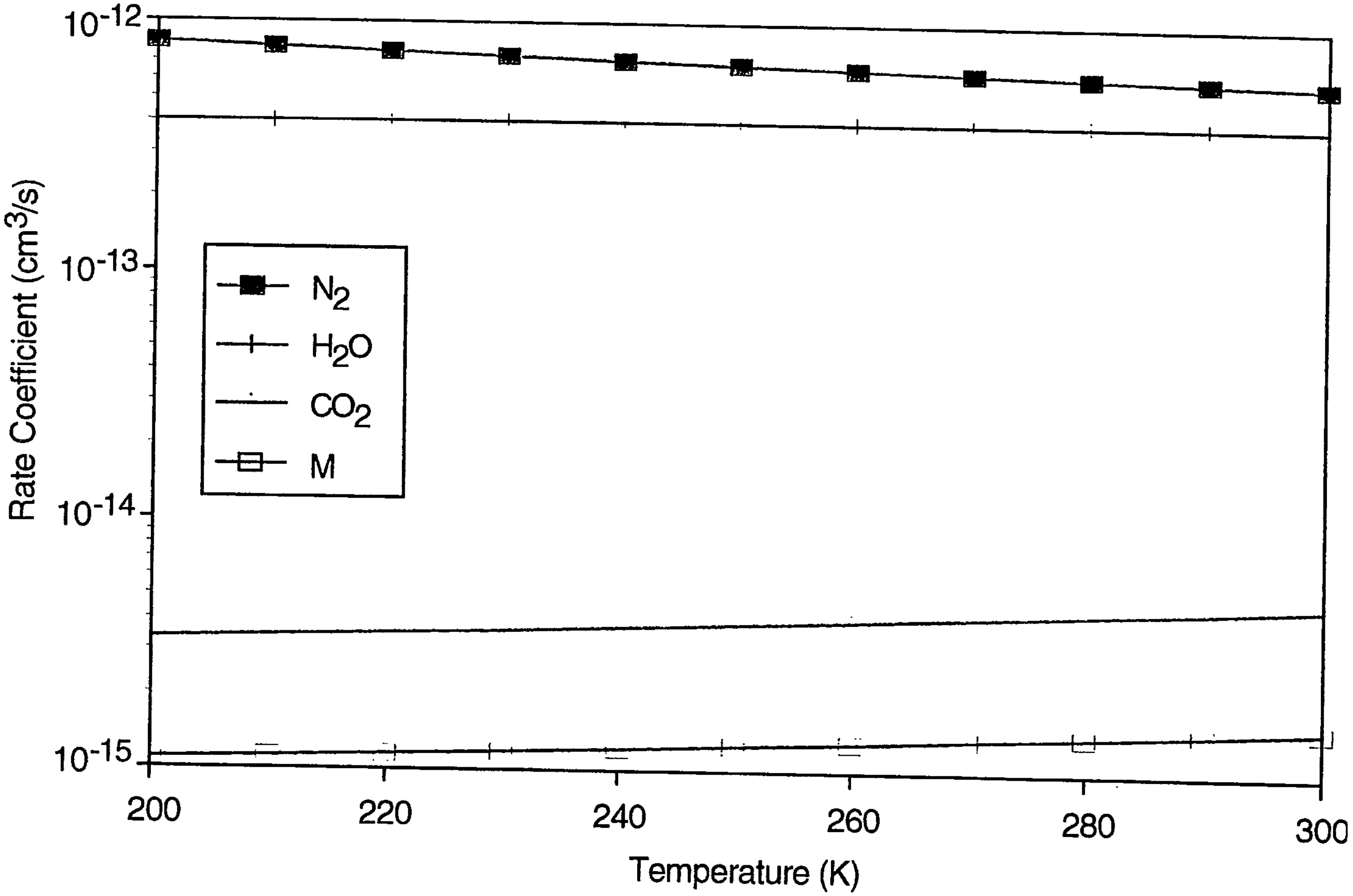

D-5126z

CO_2(001) Collisional Deactivation Rates

CIAP 1974, US Std Atm 1976

97-1132

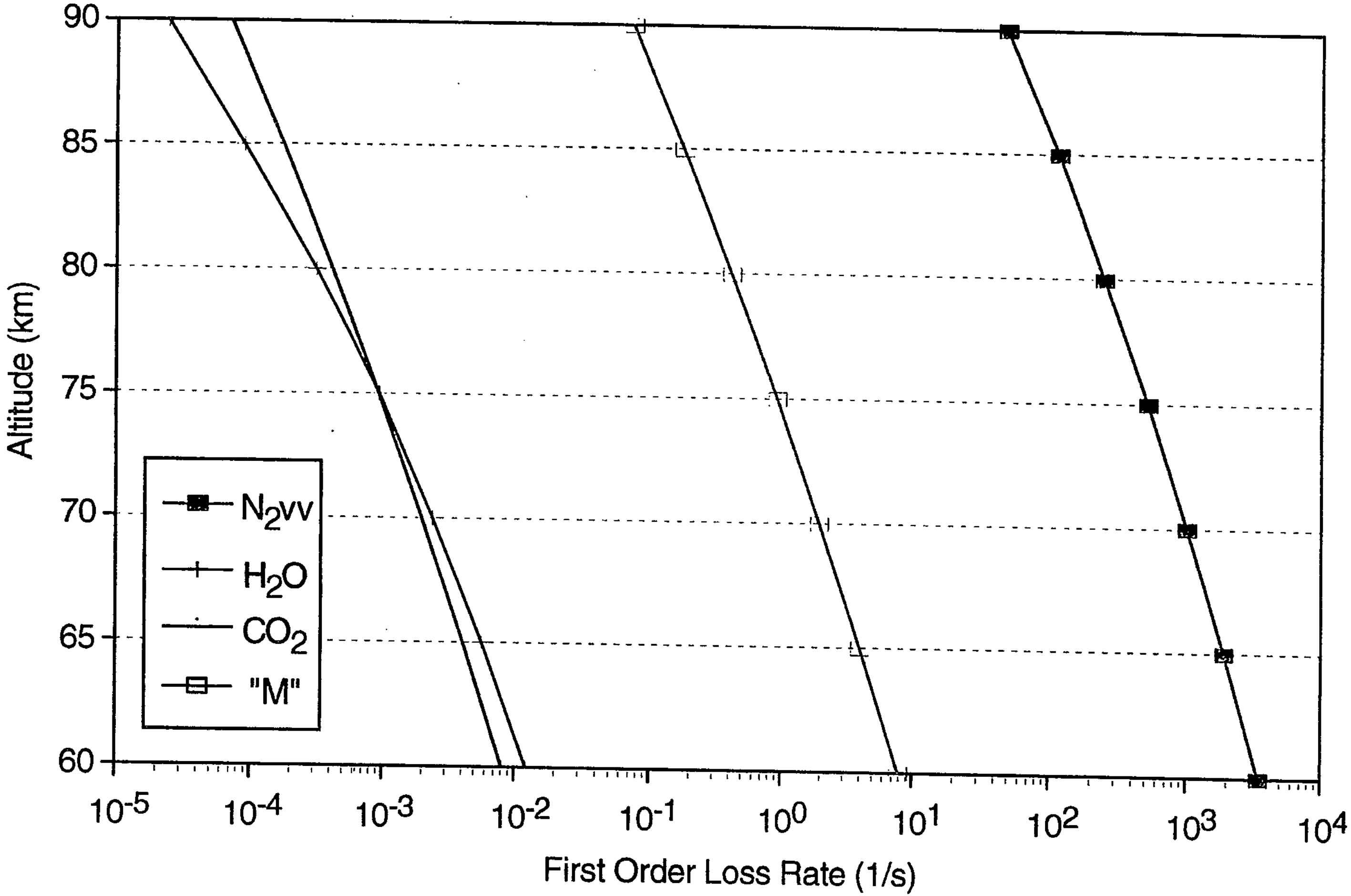

D-5124z

$N_2(v=1)$ Collisional Deactivation Rates

CIAP 1974, US Std Atm 1976

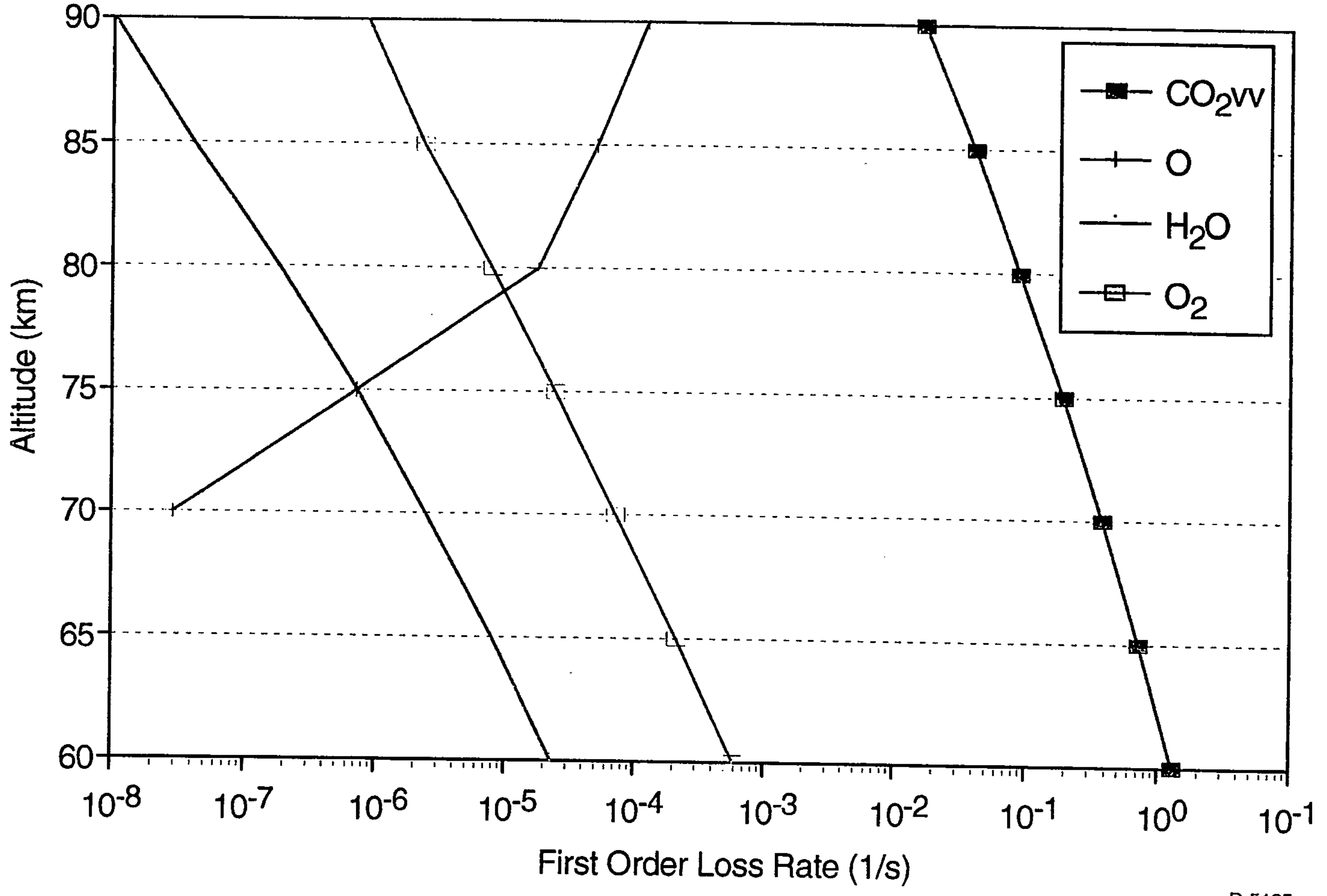

D-5125z

Vibraluminescence

Kumer EFA → $N_2(v)$ time constant
(~ 500 s at 80 km)

$$P_{N_2}(v) = k_1 \, [e] \, [N_2], \quad k_1 \sim 10^{-8} \text{ cm}^3 \text{ s}^{-1}$$

$$P_{CO_2}(v) = \frac{k_2}{k_{-2}} \frac{[CO_2]}{[N_2]} \, P_{N_2}(v)$$

Every $N_2(v)$ decay → 4.3 μm photon

$$I(z) = \frac{k_1[e] \, [N_2] \, t}{\tau_{EFA}}$$

$$R = \frac{1}{2\pi} \int_{z_2}^{z_1} I(z) dz$$

$N_2(v) + CO_2(v)$ Excitation in Sprites

80 km, [e] = 1 x 10^3 for 0.1 s, Kumer EFA

97-1131

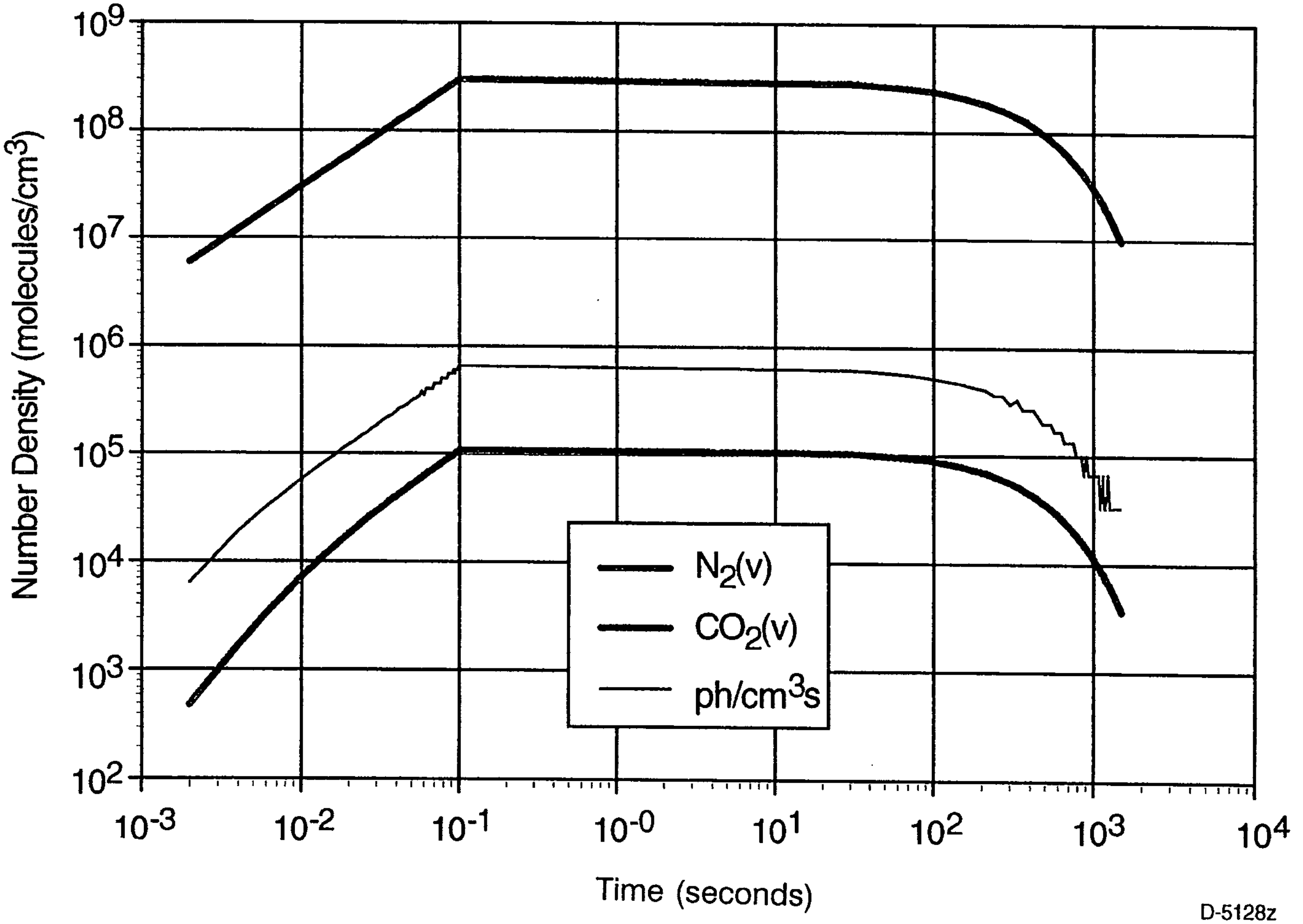

D-5128z

Vibraluminescence

For [e] = 10^3 cm^{-3}
t = 100 ms
60 to 90 km

upwelling R = 1.7 x 10^{-7} W/cm^2 sr

vs nadir earth ~ 10^{-6} W/cm^2 sr

10% effect discernible downloading?

If [e] → 10^4, 10^5 cm^{-3}

=> then have linearly increased effect

On-Going Kinetics

- Collaborating with R. Armstrong to create code inputs
- k for O_2 + e dissociation attachment
- Model excitation of N_2 (E, v) states
  - compare to spectral results
  - estimate UV and IR components
- $N_2(v)$ - $CO_2(v)$ magnitude and persistence

APPENDIX 15

Spectroscopy and Chemical Kinetics of Sprites

Spectroscopy and Chemical Kinetics of Sprites

W.T. Rawlins, B.D. Green, and M.E. Fraser
Physical Sciences Inc.
Andover, MA 01810

R.A. Armstrong
Mission Research Corp.
Nashua, NH

June 1998

Introduction

- Sprites exhibit characteristic, short-lived visible and UV emissions at 60 to 90 km

- Development of physical models requires delineation of time scales and energetics of optical emissions

- Potential for observable IR emissions is unknown

- Optical diagnostics
  - spectral: electron energetics, field strength
  - temporal: time scales for ionization, neutral electronic state excitation
  - intensities: electron densities

Hampton et al. at 2 nm Resolution (AK-HI)

96-294c

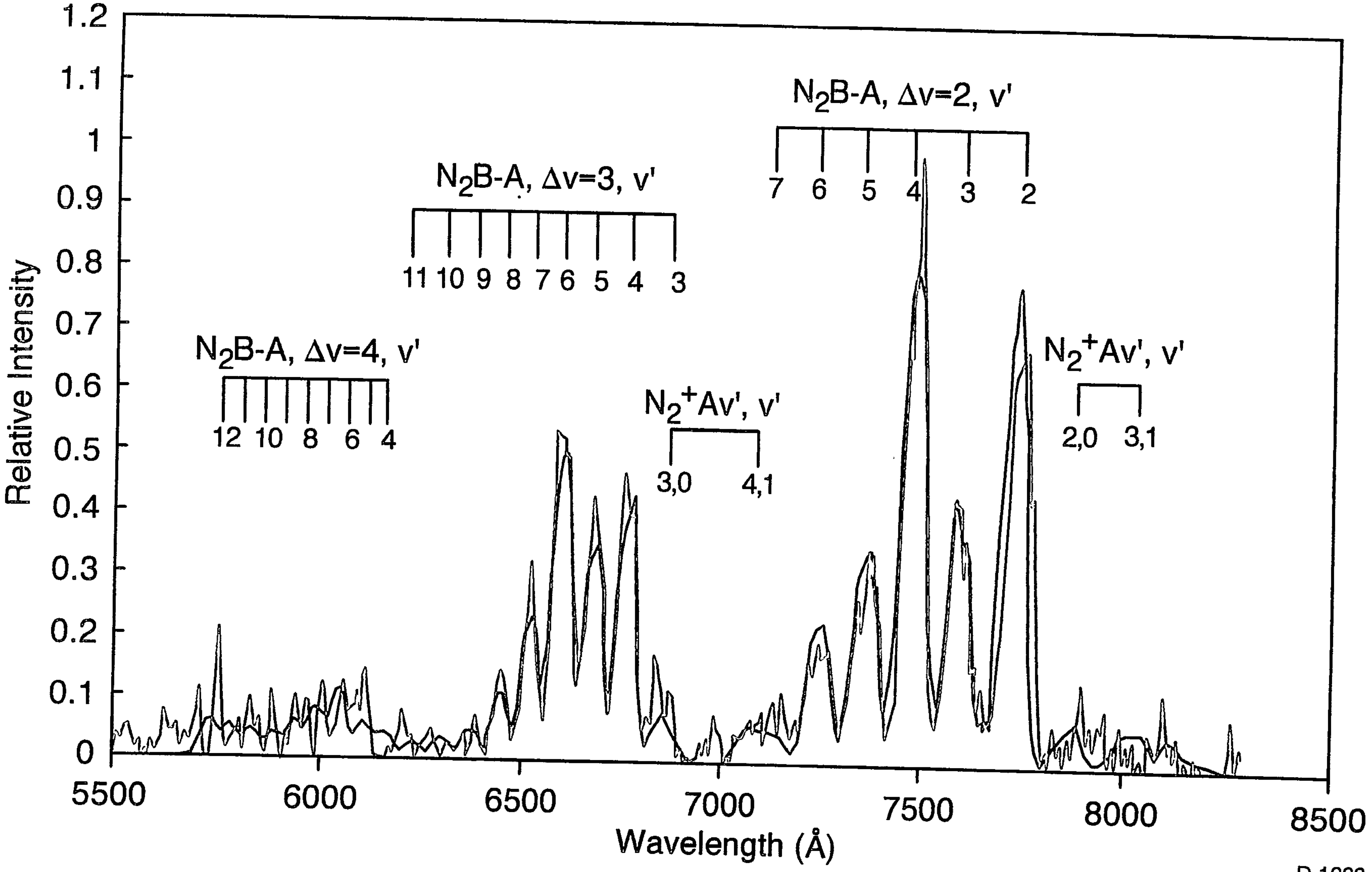

D-1266

Potential Energy Curves for N_2 and N_2^+

96-4018

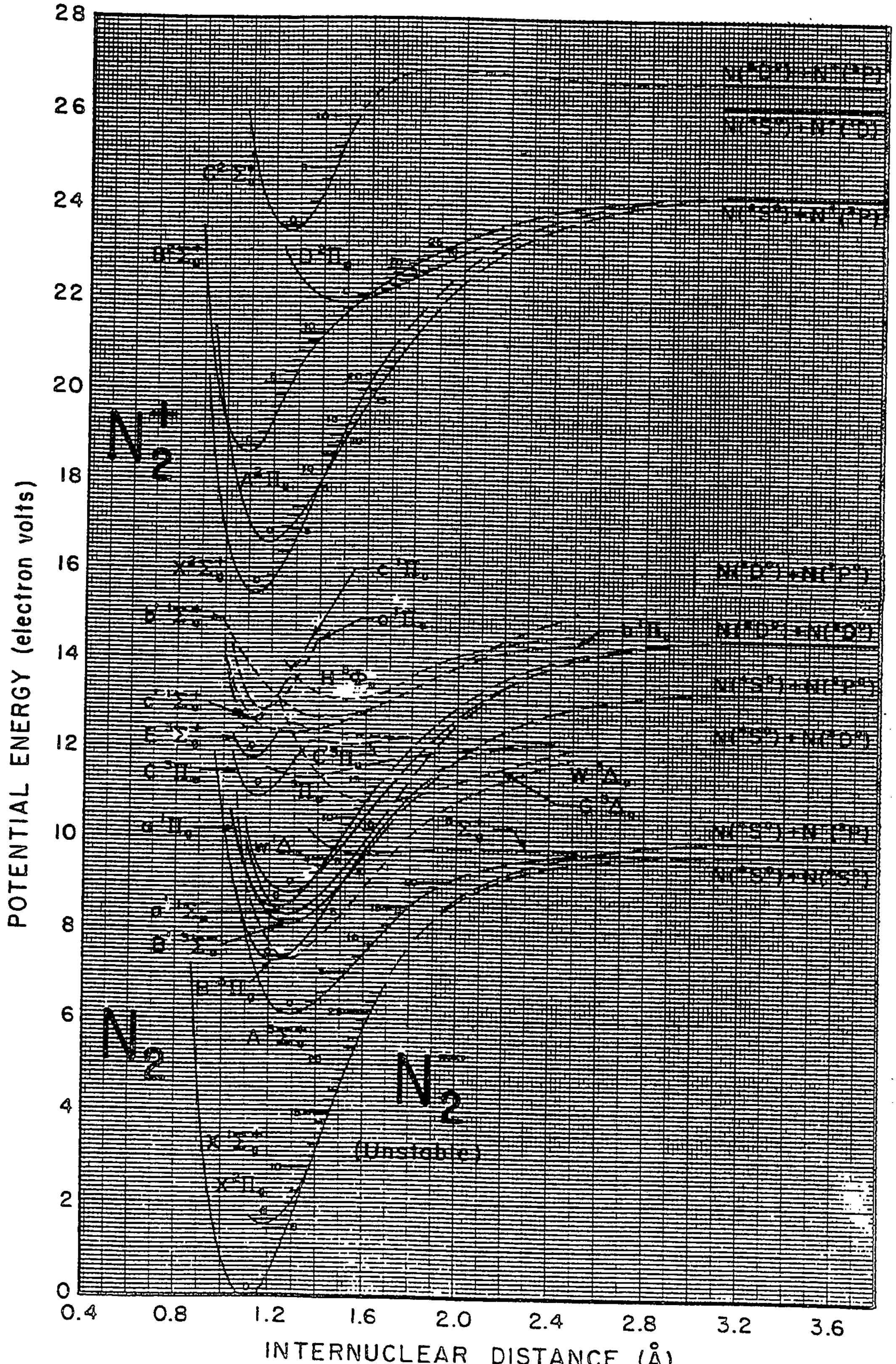

D-4059

N_2 1 + (M&B 80 KM) and N_2 + A-X (LBC)

- 1 nm resolution, T_{rot} = 250 K -

97-1134a

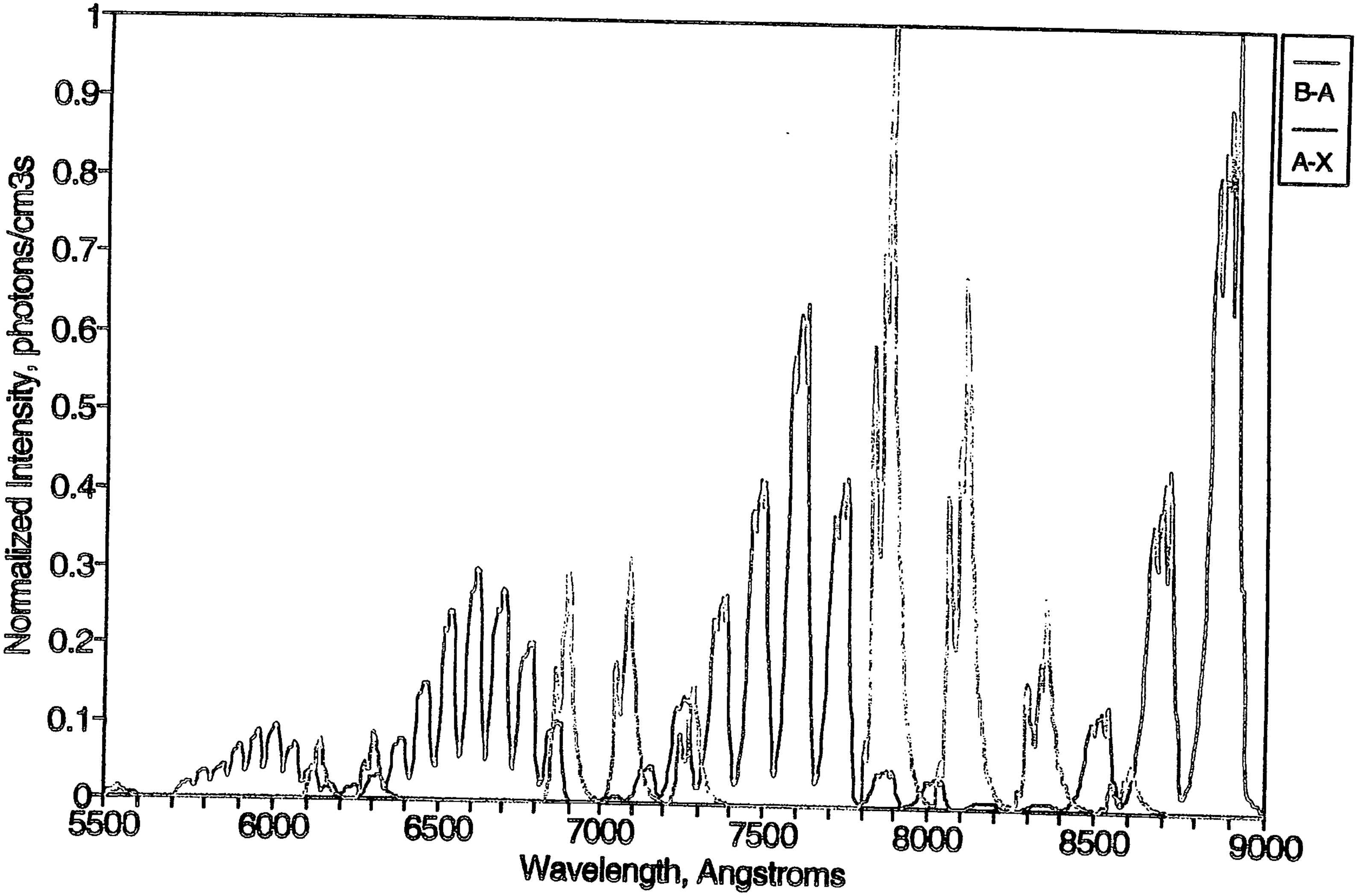

Compare AK Sprite and N_2 Discharge

- Discharge: 90 W, 0.11 Torr -

97-1146a

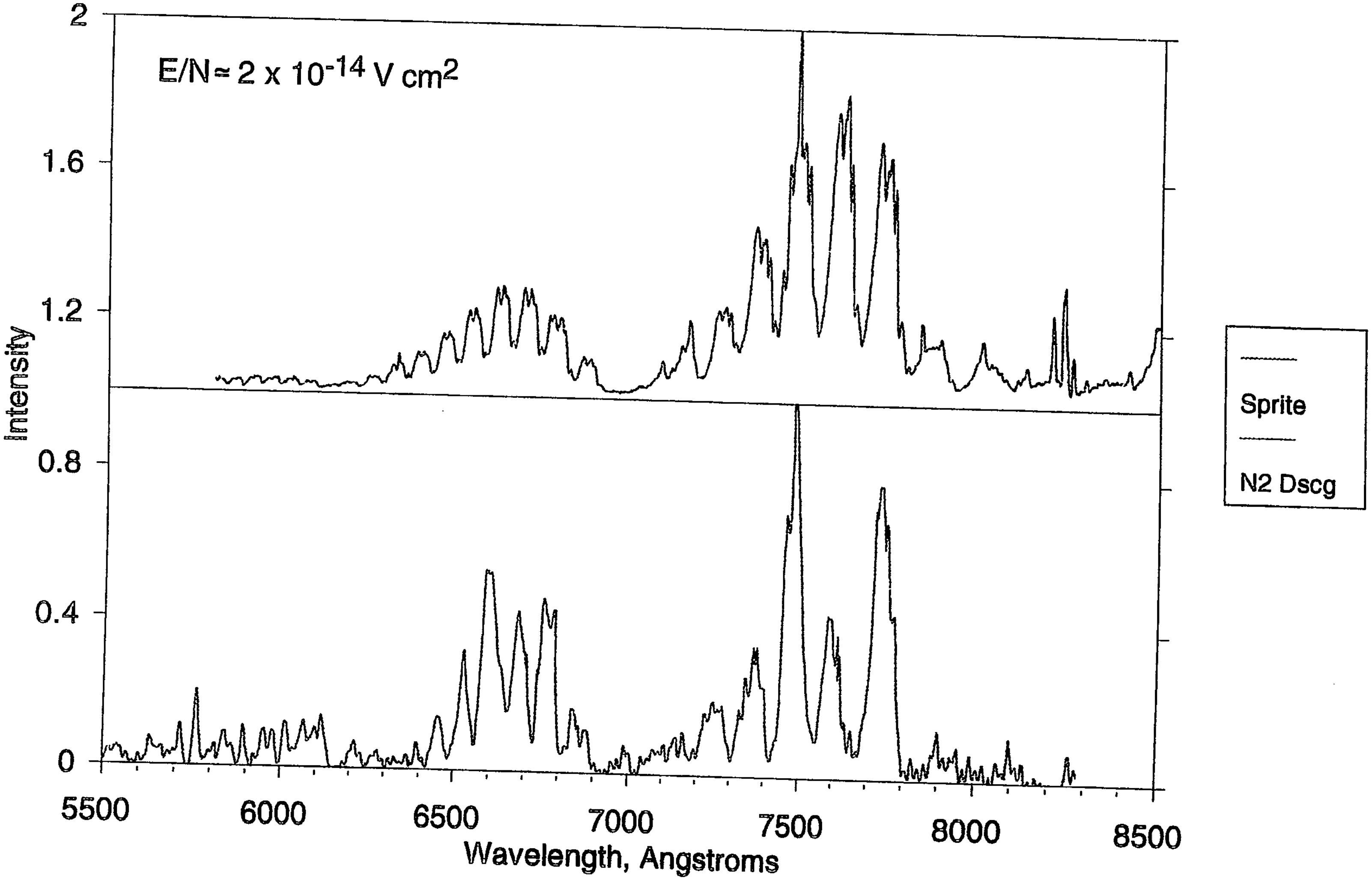

Laboratory 40 W Microwave Discharge Emission Spectra at 1 Torr (Piper)

$N_2(B\text{-}A)$: v=0-12; $N_2(A\text{-}X)$: v=2-5; 600 K

96-4024

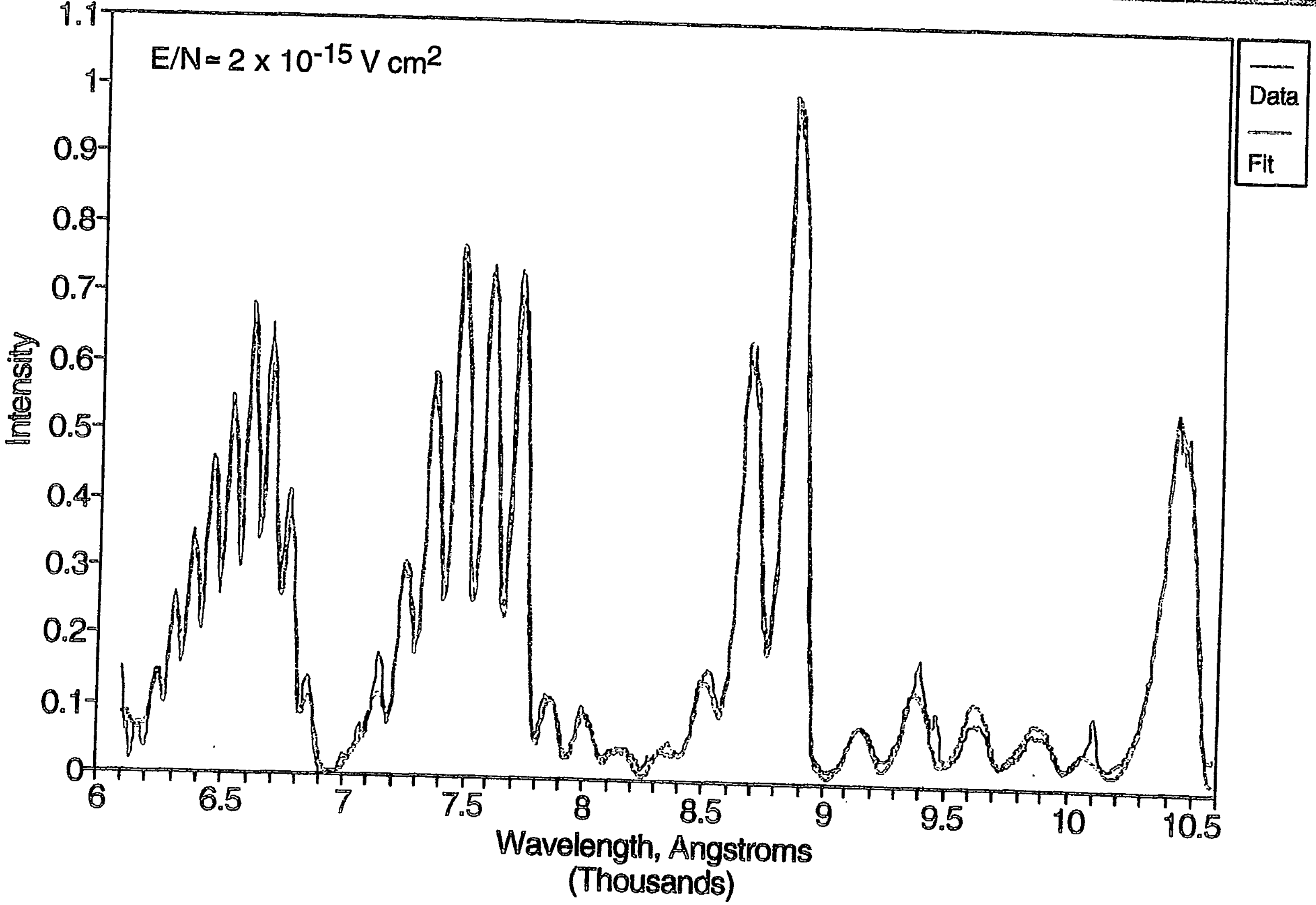

Atmospheric Transmission through Slant Path to Sprite

96-4019

Source 70 km, Obs 3 km, Range 500 km
No Tropospheric Aerosols

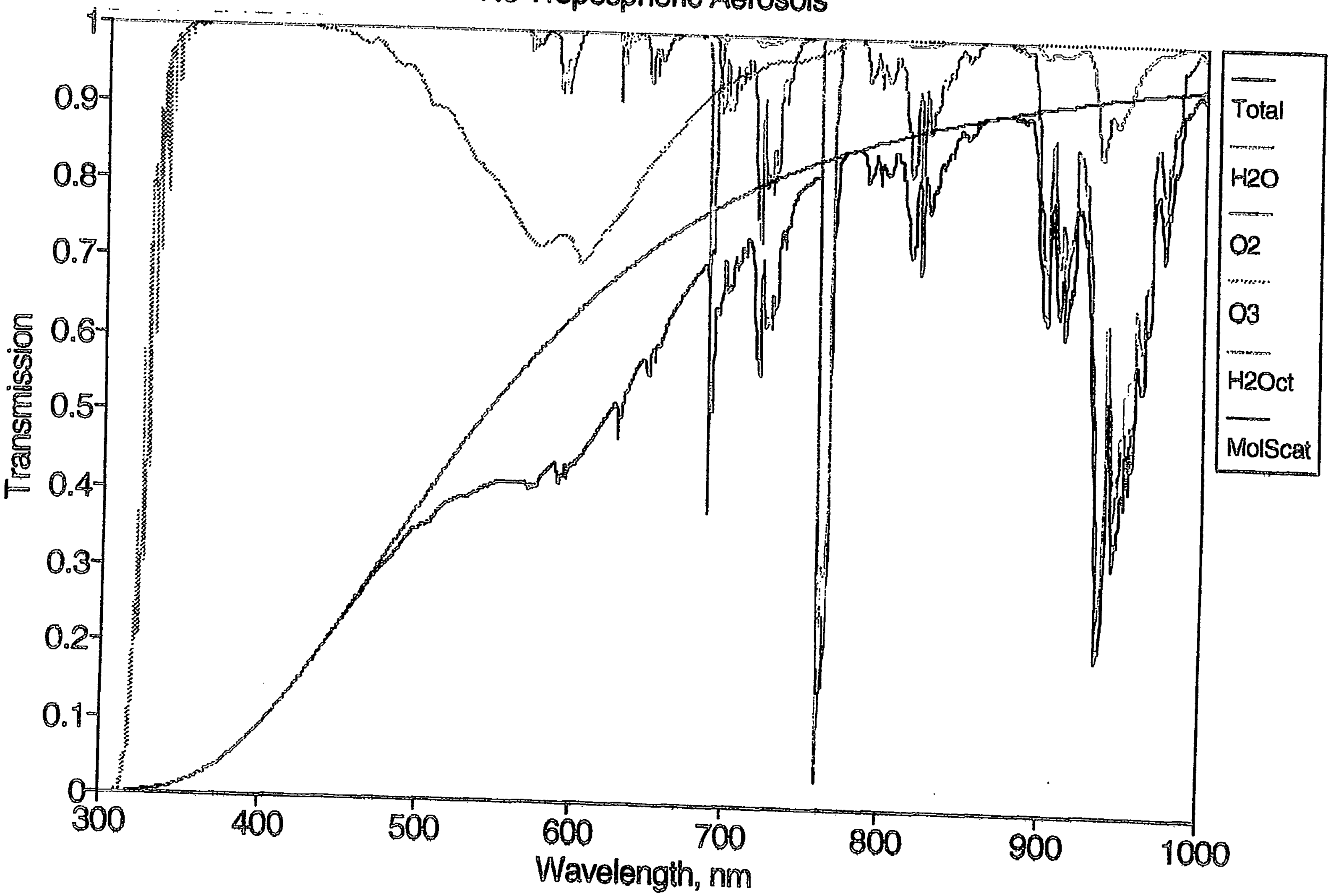

Source 70 km, Obs 3 km, Range 500 km

- No Tropospheric Aerosols -

97-1135a

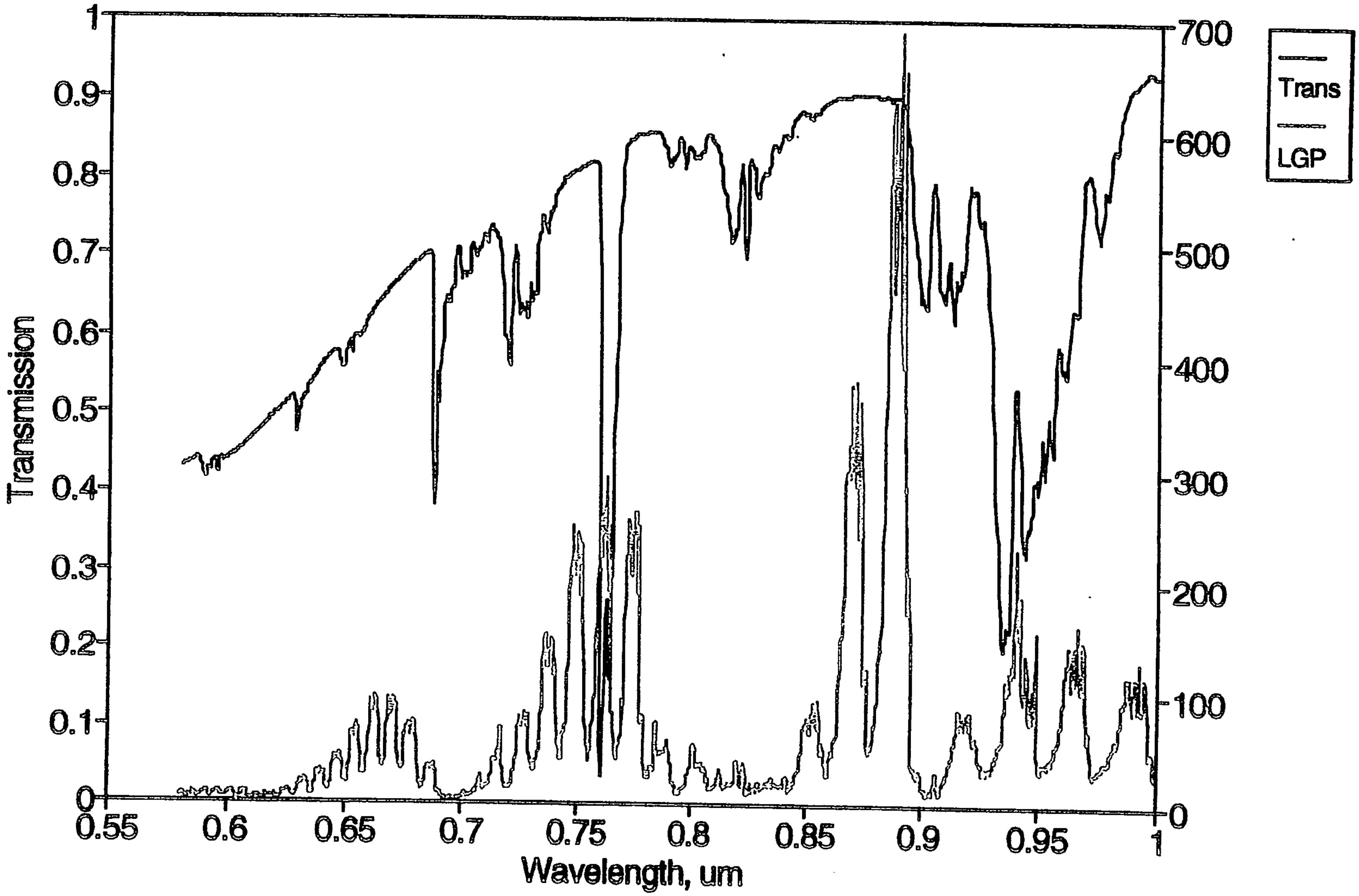

Sprite Spectra: Log Scale

- Spectra From Heavner et al., University of Alaska -

98-2040

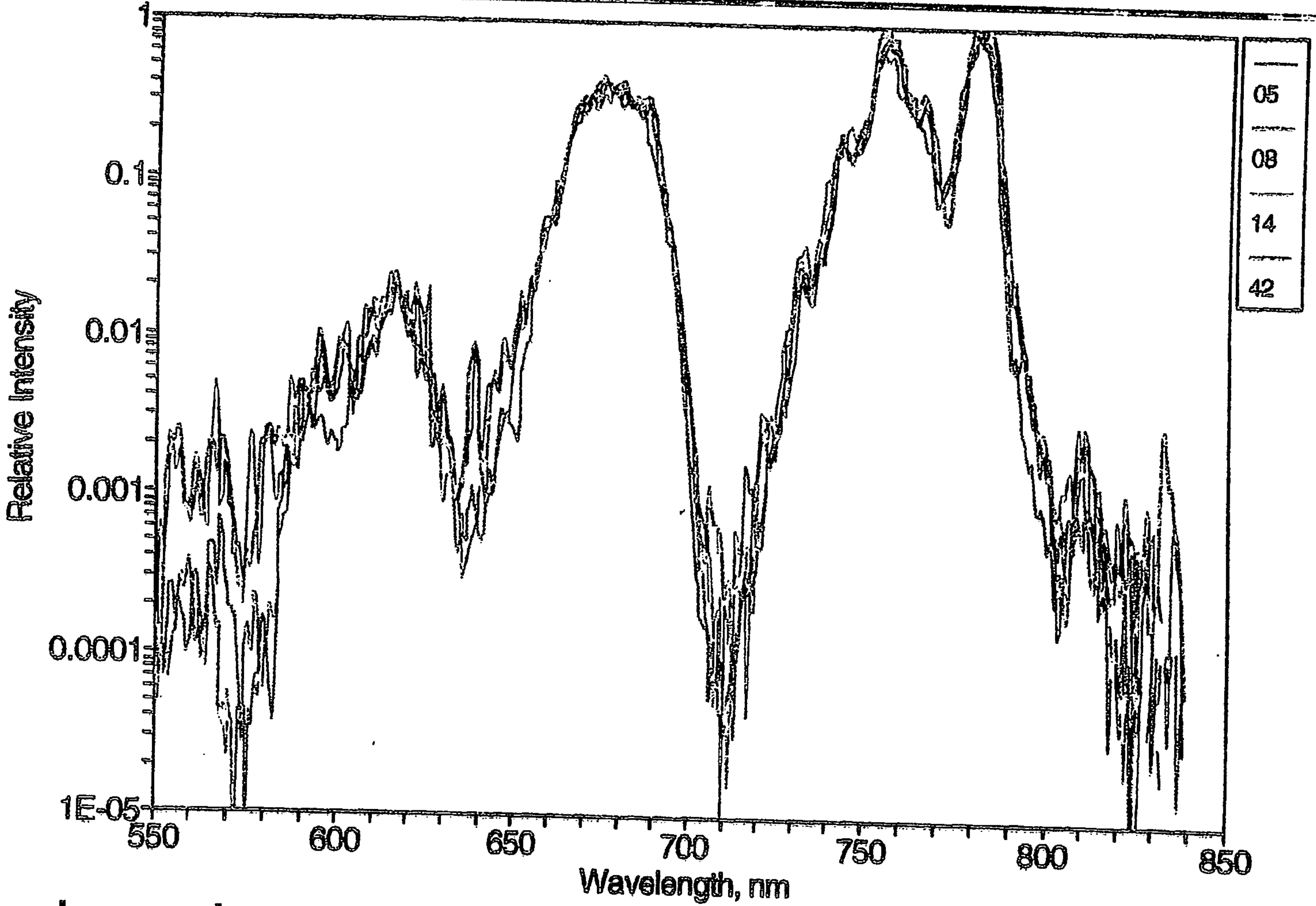

- Large dynamic range in sprite data
- Very reproducible, little variability between sprite spectral distributions

Spectral Fit, 250 K, 6 nm

- $\Delta v = 2$ bands of N_2 ($B \rightarrow A$) and N_2^+ ($A \rightarrow X$) -

98-2041

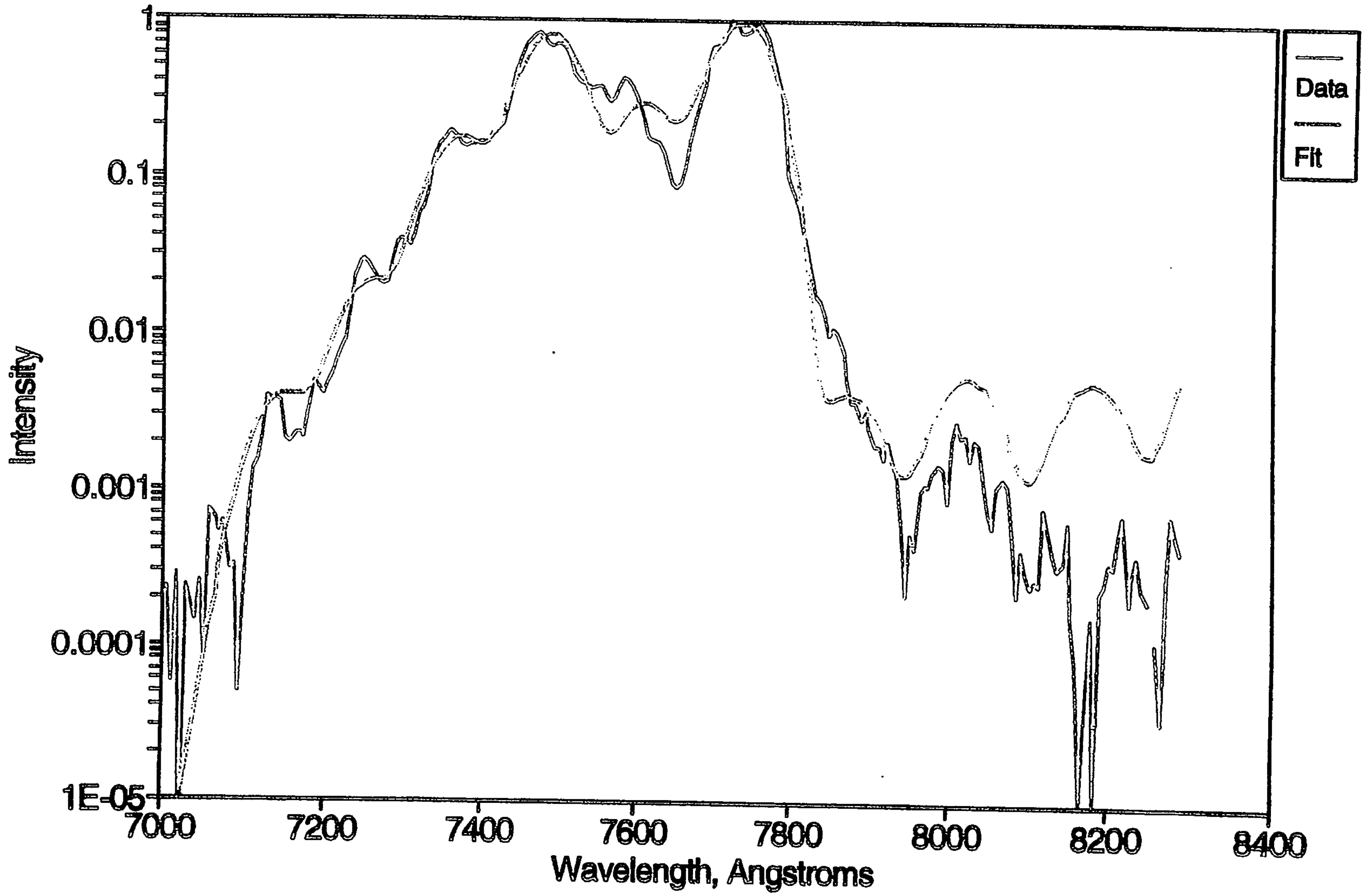

Spectral Fit, 250 K, 6 nm

- Δv = 3 bands of N_2 ($B \rightarrow A$), v' = 3-10 -

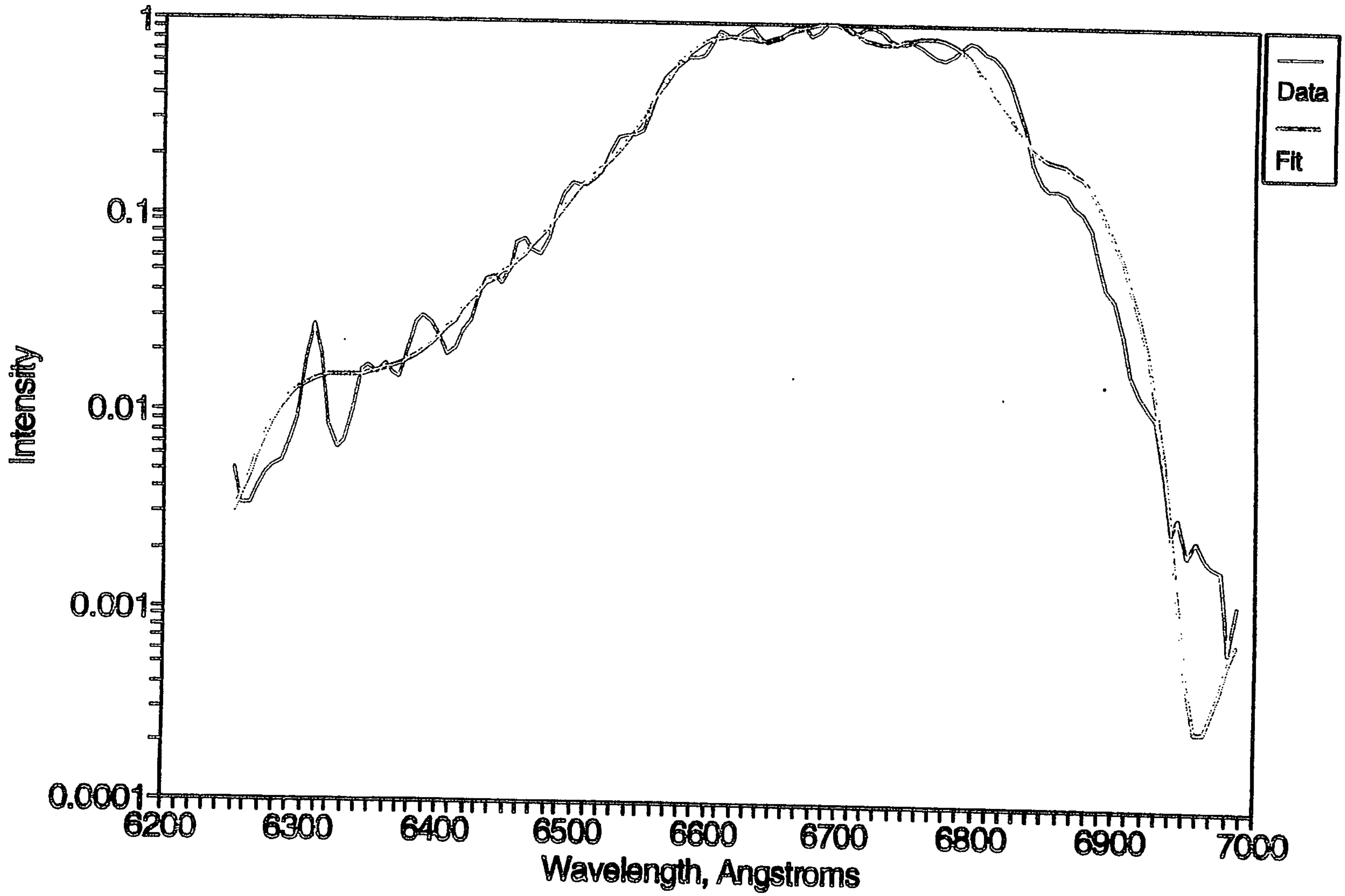

Nitrogen B-State Vibrational Population Distributions

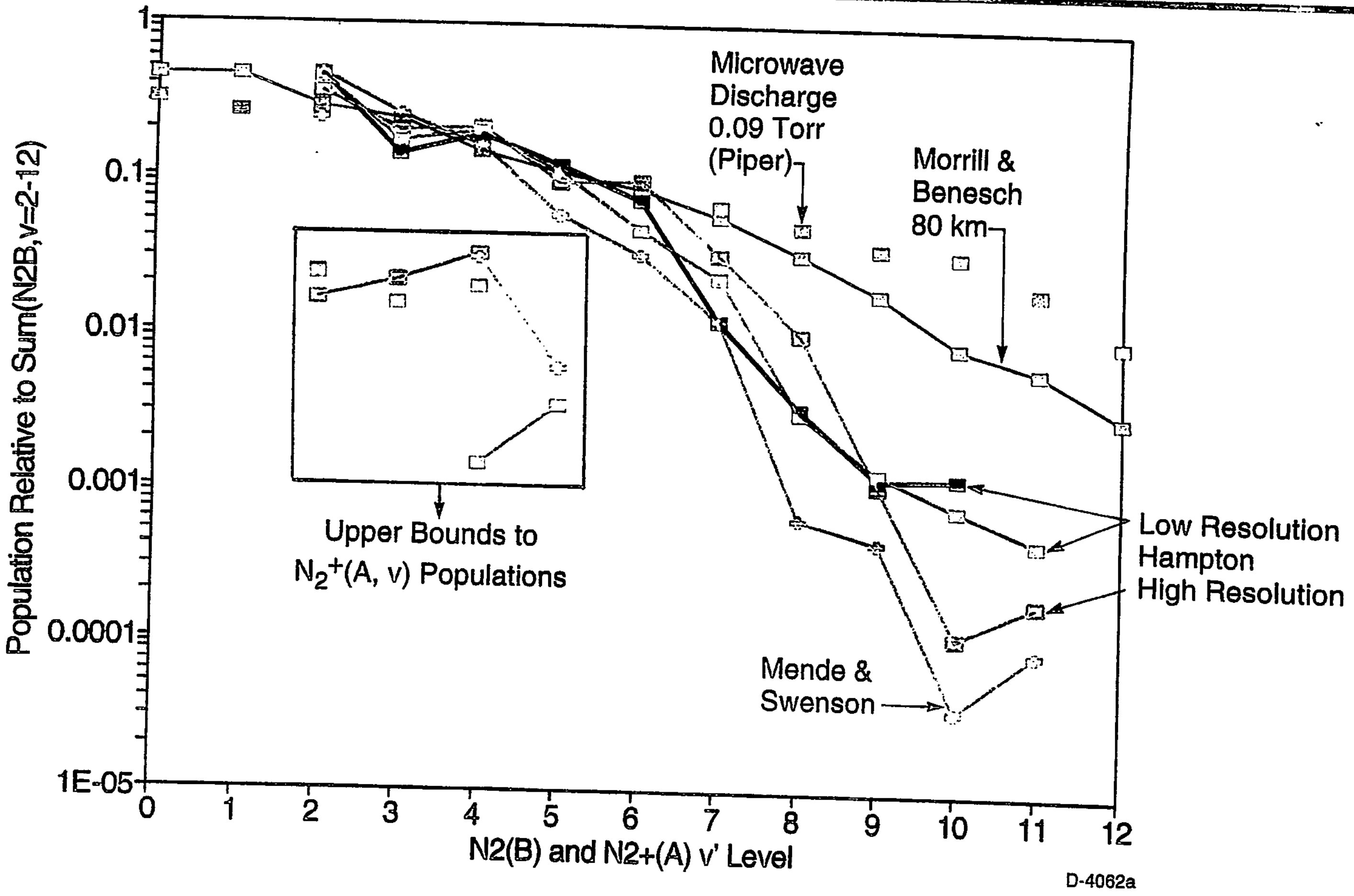

- Distributions similar (within error bars)
- Instrumental baseline signals and atmospheric transmission
- Derived populations clearly "colder" than auroral-like (MB) and microwave discharge (P) distributions

Boltzmann Transport Equation

- ELENDIF code: Morgan and Penetrante, 1989

- Input electron impact cross sections
  - ionization, attachment
  - dissociation
  - electronic and vibrational excitation

- Compute quantities vs E/N (field/density)
  - electron energy distribution, characteristic energy
  - excitation rate coefficients

$$k = \left(\frac{2e}{m} \right)^{1/2} \int_{0}^{\infty} \sigma(\epsilon) \; f(\epsilon)\epsilon \; d\epsilon$$

Electron Excitation of N_2 Electronic States

98-2034

- Absolute cross sections for each vibrational level as a function of electron energy:
  - $N_2\ B^3\Pi_g$, $N_2^+\ {}^2\Sigma_u$, $N_2^+\ {}^2\Pi_u$
    - Stanton and St. John, J.O.S.A. 59, 252 (1969)
  - $N_2\ C^3\Pi_u$ and B-state cascade
    - Shemansky and Broadfoot, J.Q.S.R.T. 11, 1401 (1971)
- Current: tabulate cross section for each (E,v) state at 0.25 eV intervals
- Relaxation due to radiative decay, collisional relaxation by N_2 and O_2
- Radiative lifetimes for each vibrational level of N_2 B, N_2^+ A:
  - Piper, Holtzclaw, Green, Blumberg, J.C.P. 90, 5337 (1989)
- Quenching of each vibrational level:
  - N_2^+ A: Piper, Green, Blumberg, Wolnik, J.C.P. 82, 3139 (1985)
  - N_2B: Piper, J.C.P. 97, 270 (1992)
- Previously: input Boltzmann electron distributions to match spectral distributions observed in Sprites by University of Alaska group
  - 1 eV electron "temperature" best reproduces data
- This effort: use detailed Boltzmann equation solutions to predict excitation rates vs E/N

Electron Excitation Cross-Sections

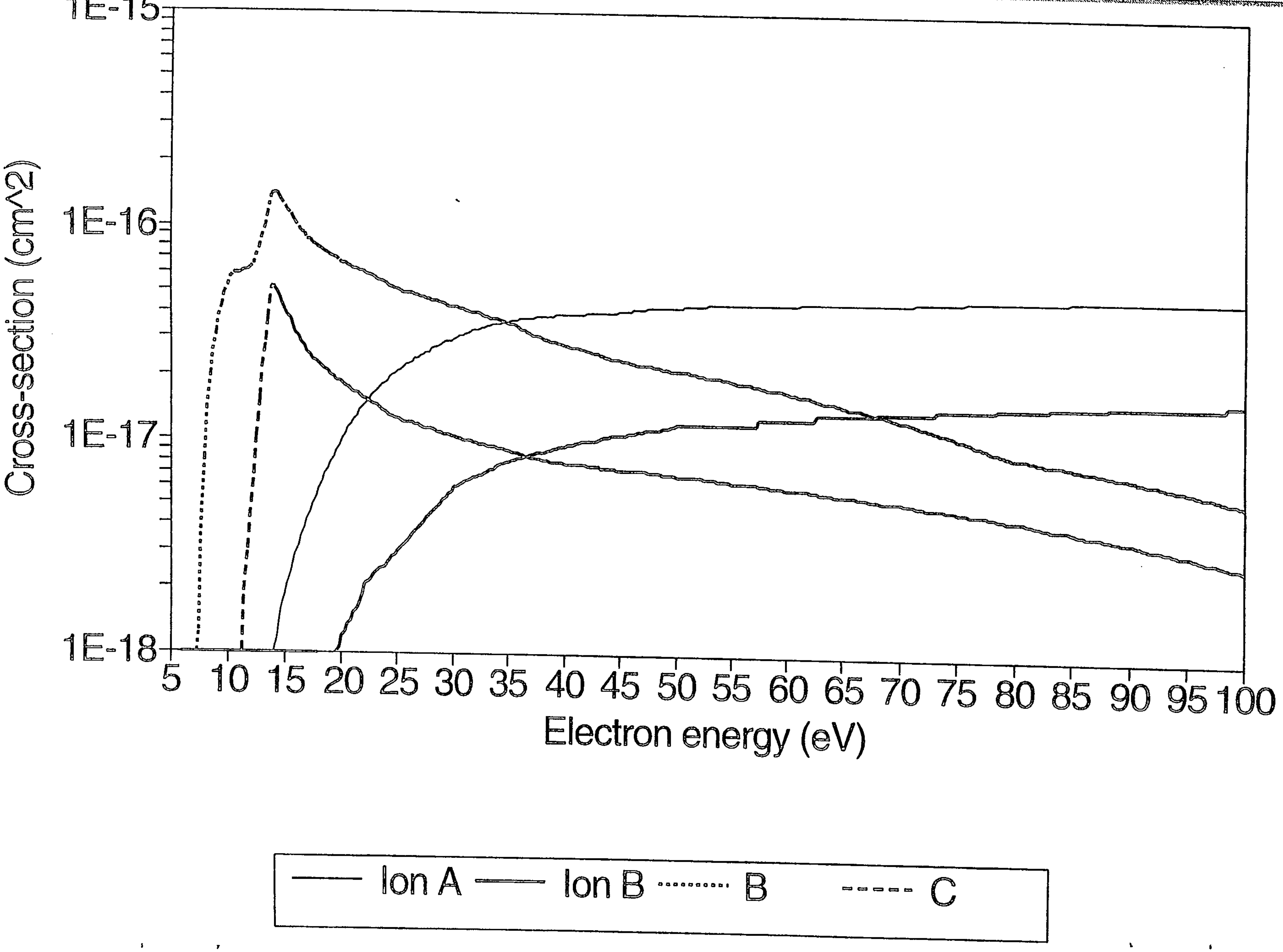

98-2024

B-State Excitation Cross-Section

98-2026

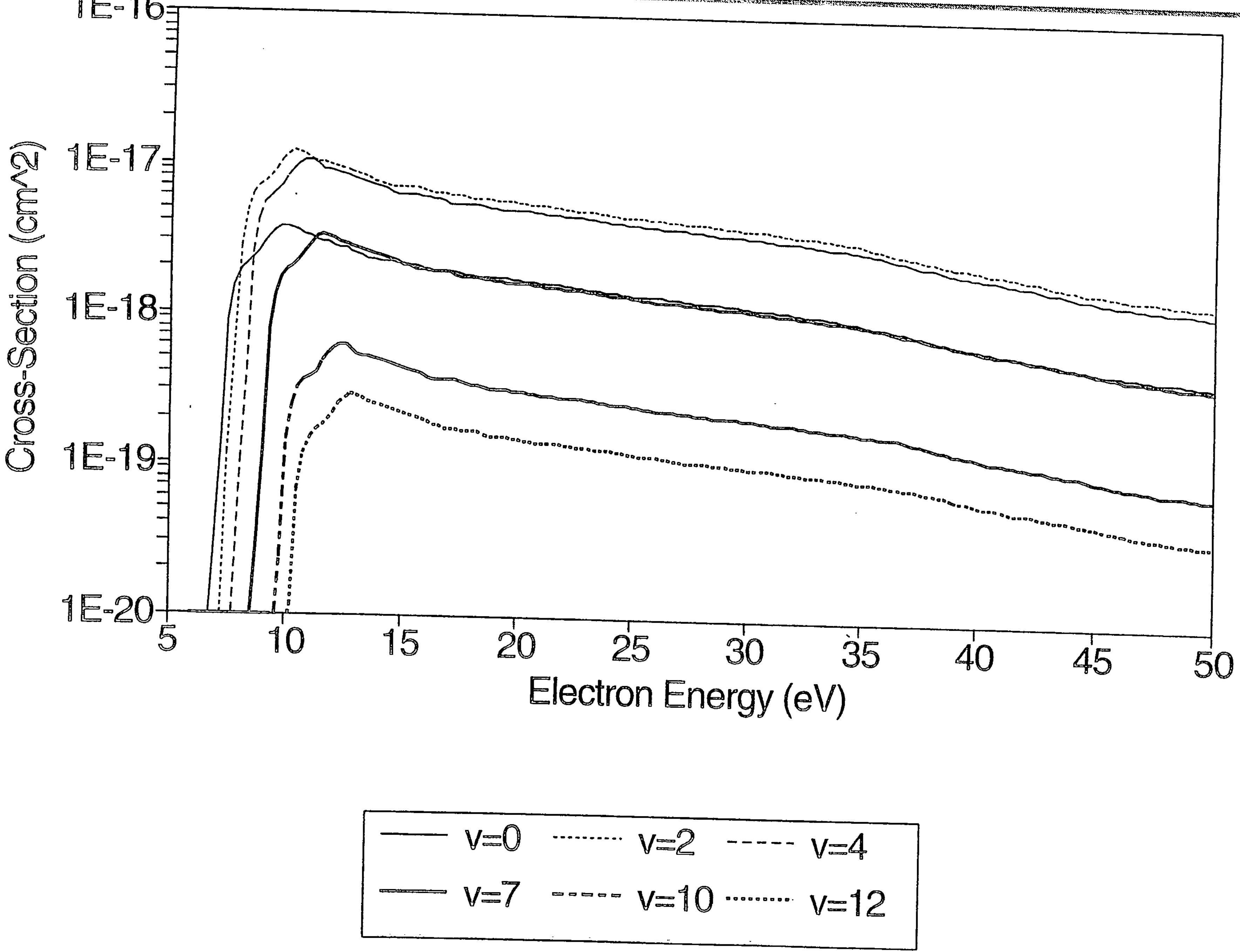

Electron Energy Distributions

- Dependence on E/N (V cm^2) -

98-2044

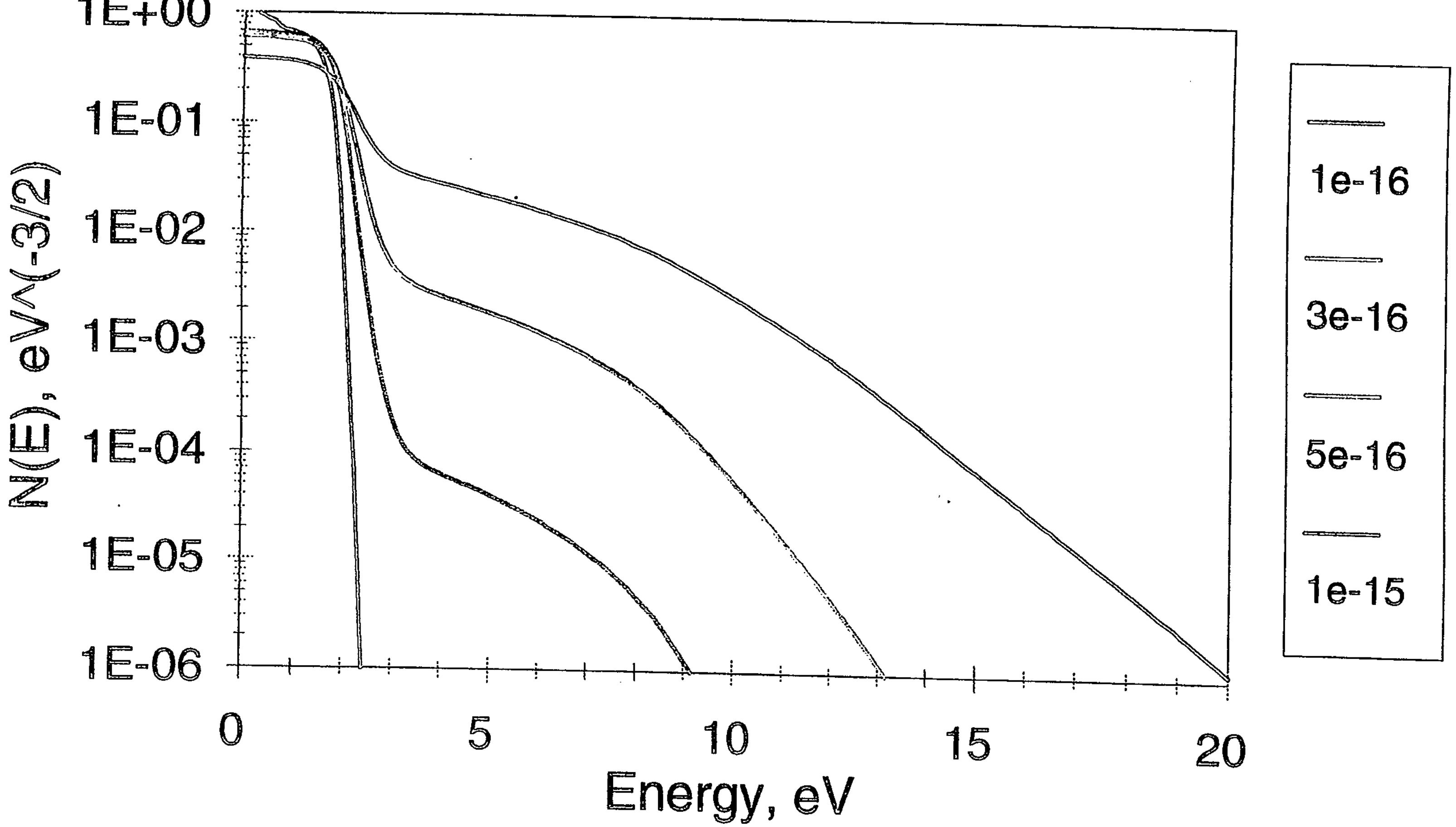

Characteristic Electron Energy

98-2046

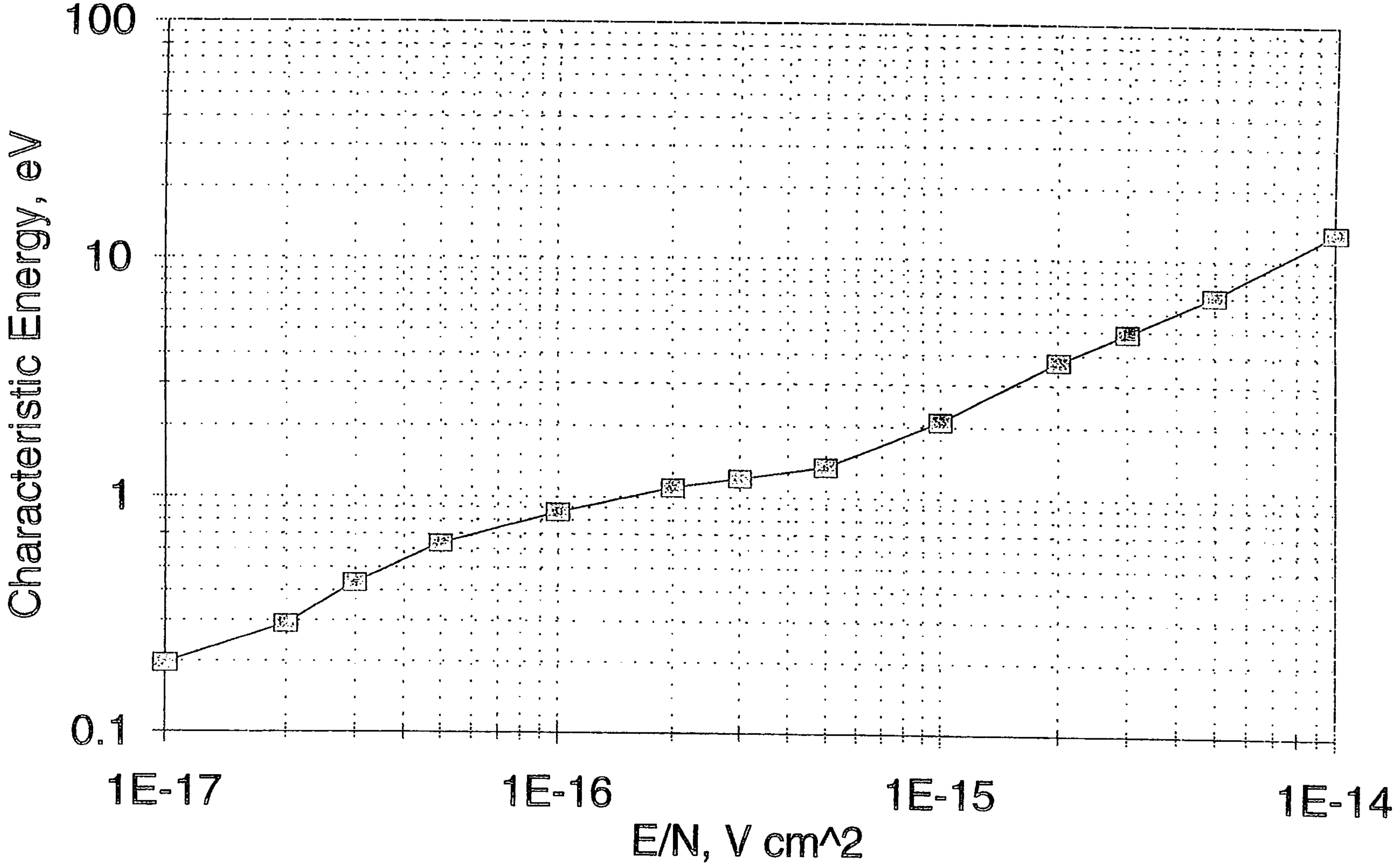

N_2 and N_2^+ Excitation

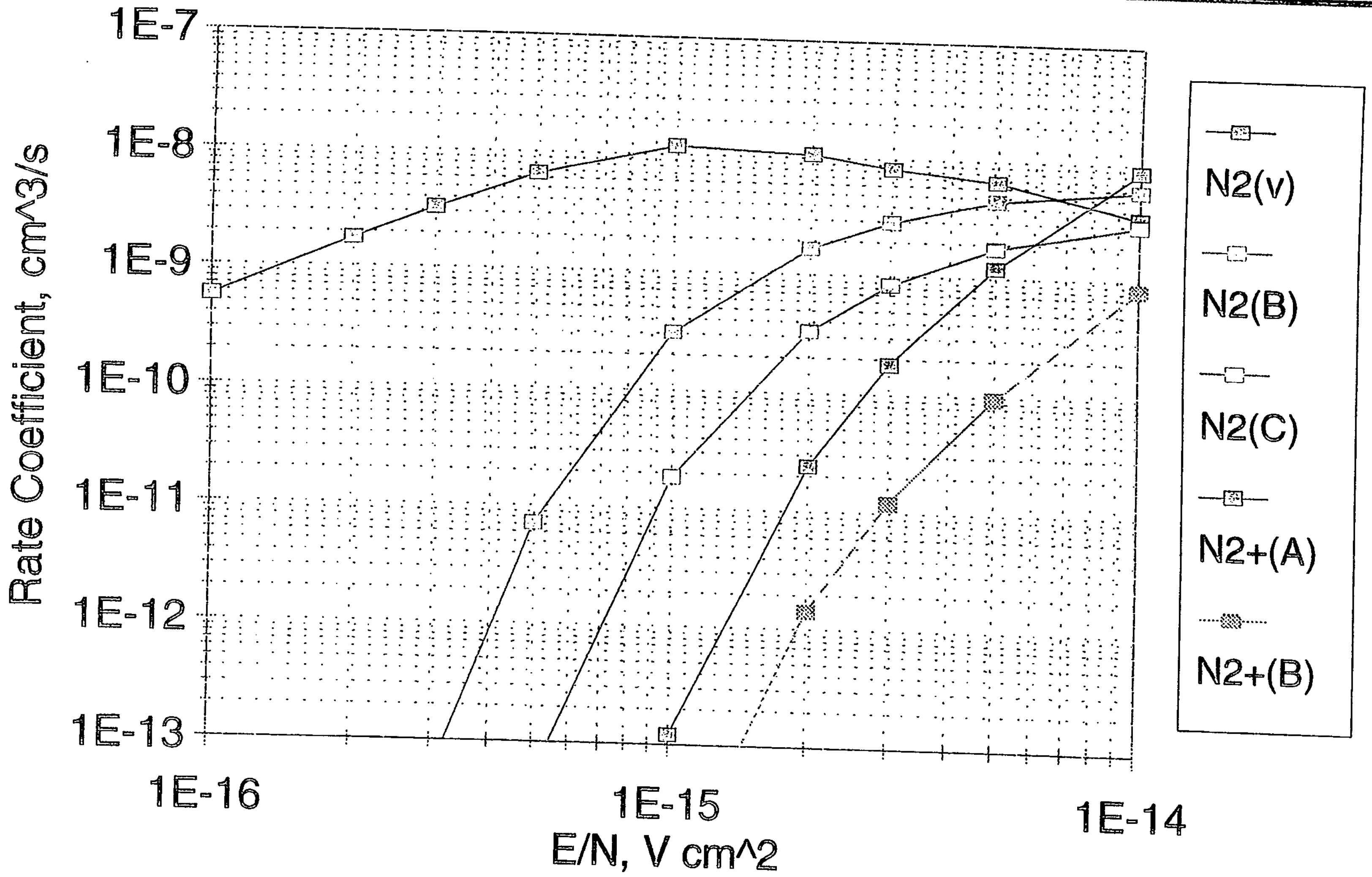

$N_2(B,v)$ Excitation

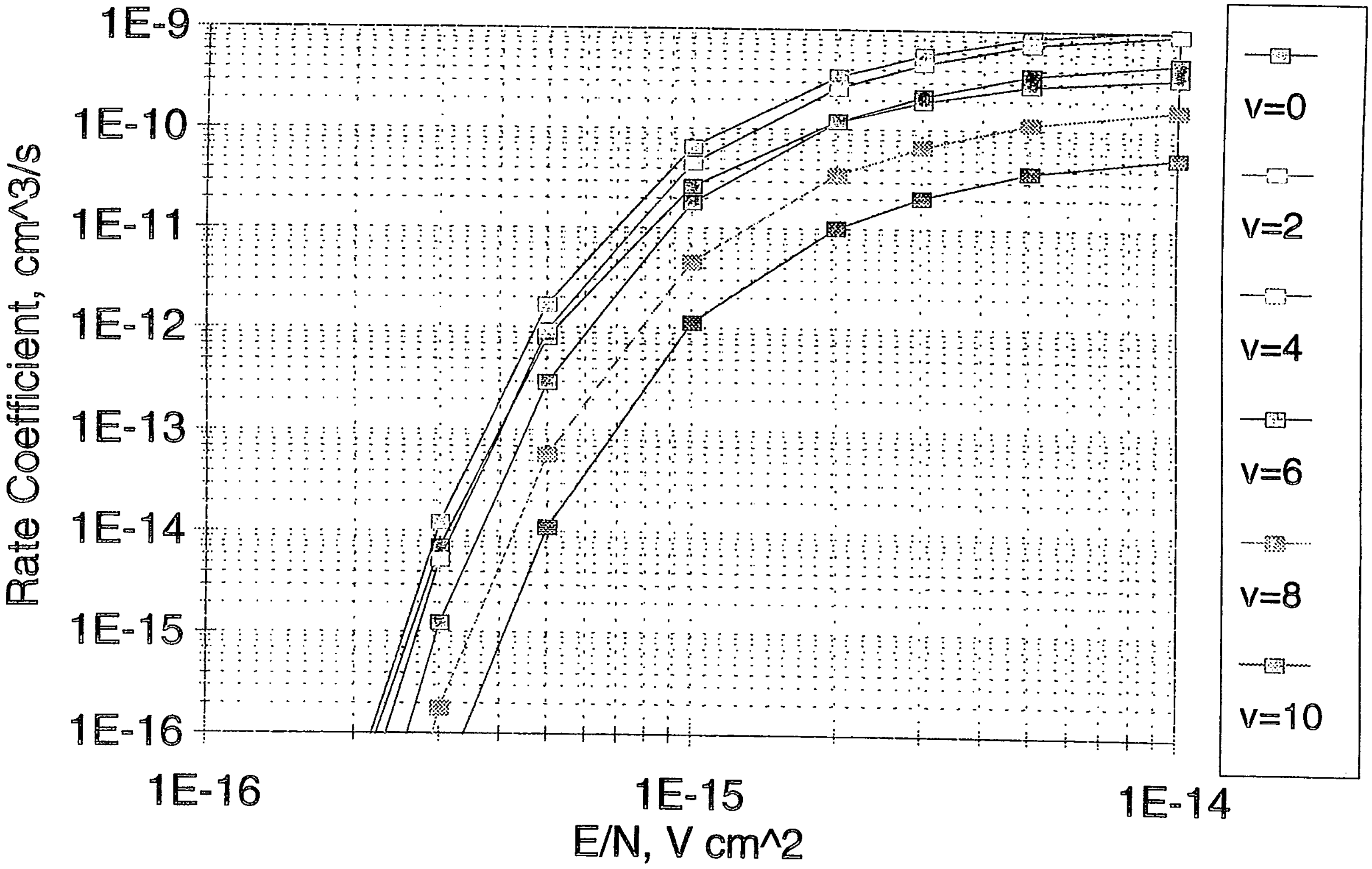

Vibrational Excitation

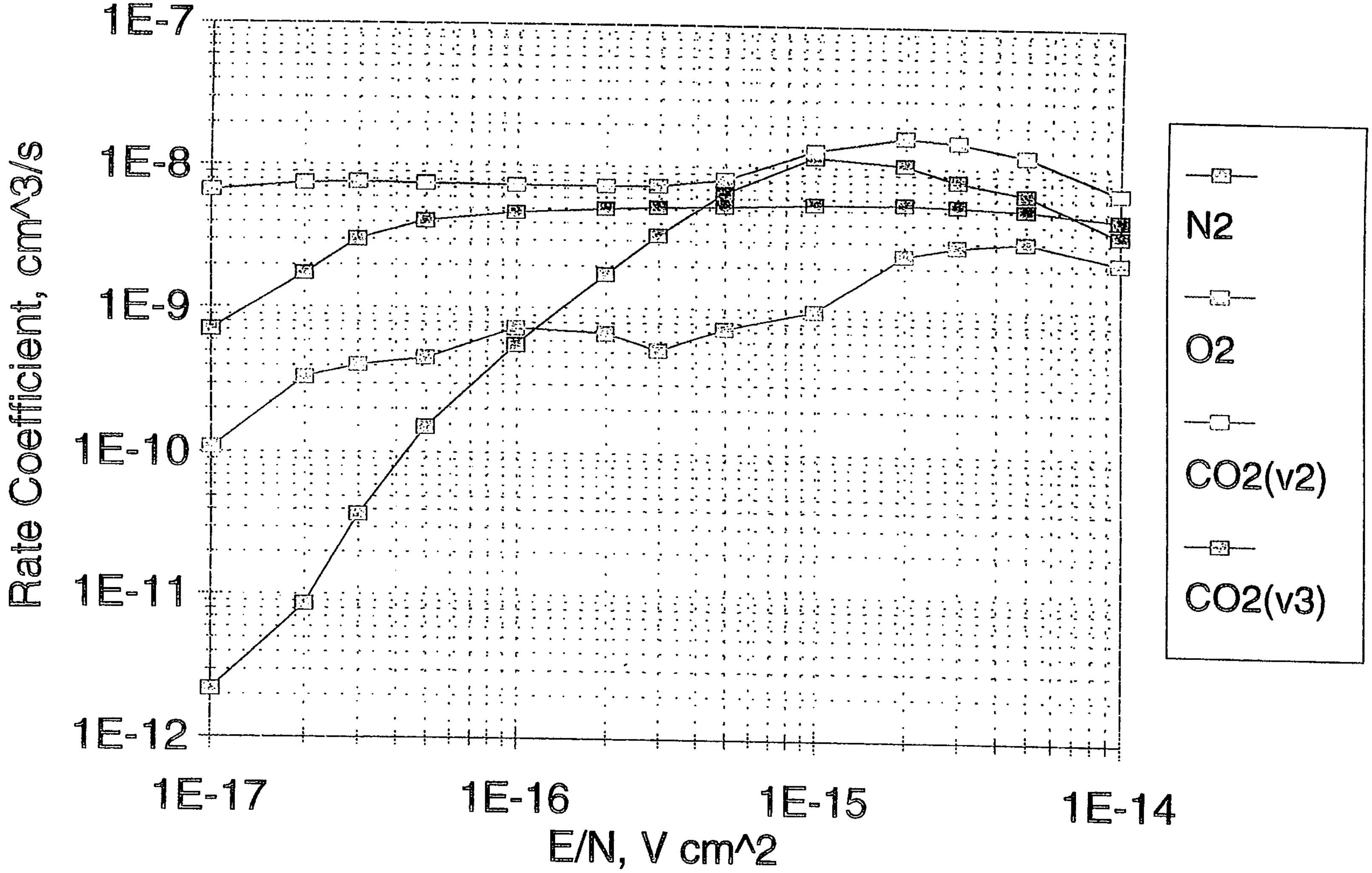

Relative N_2 (B,v) Distributions for Several E/N

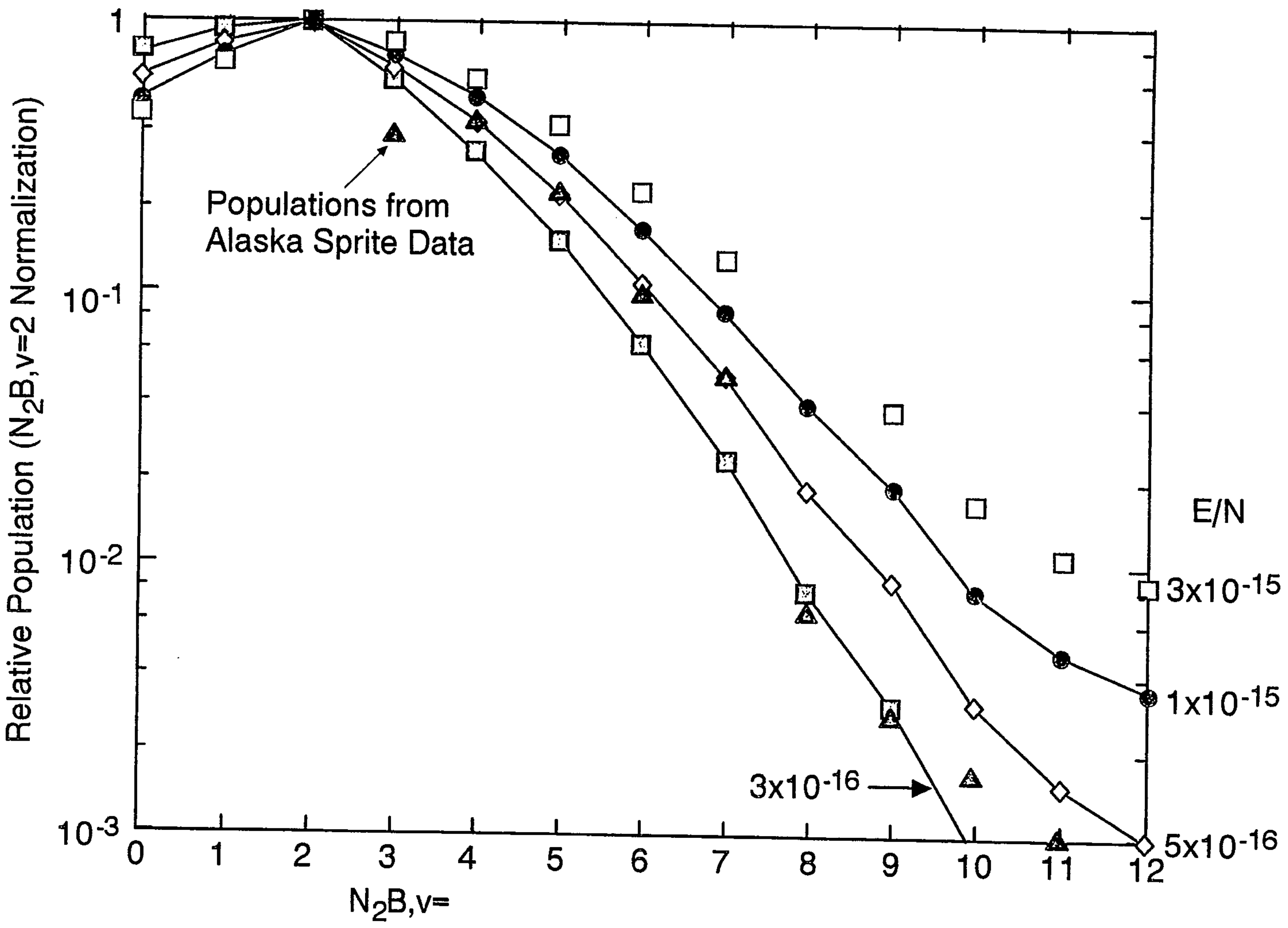

D-8925z

○ Sprite distribution agrees welll with E/N ~ 3 to 5 x 10^{-16} V cm^2

Relative N_2^* State Vibrational Distributions (normalized to $N_2(B, v=2)$)

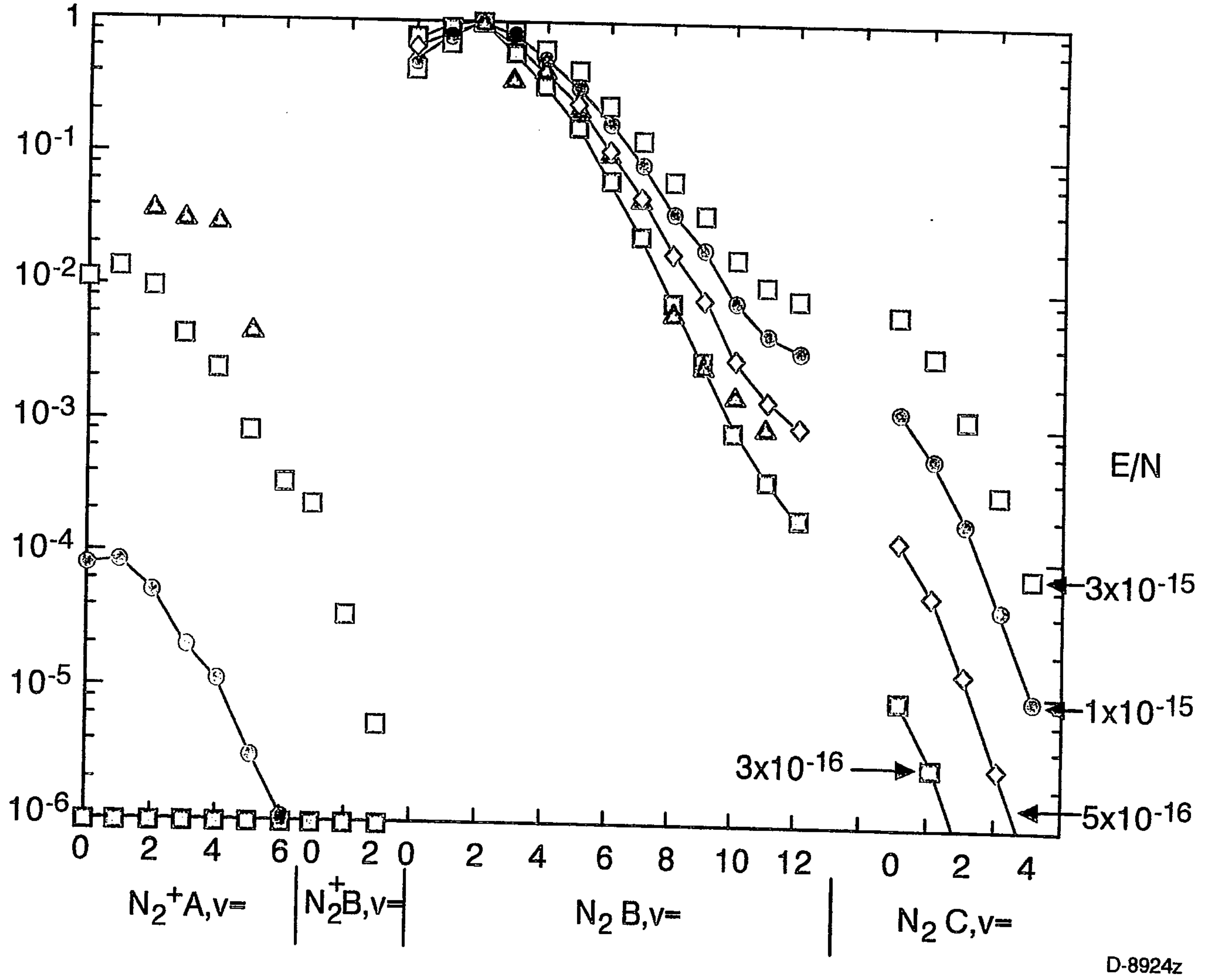

*Negligible ion state production for $E/N < 10^{-15}$

e/cc to Create 600 kR (1 km) Visible N21P

98-2035

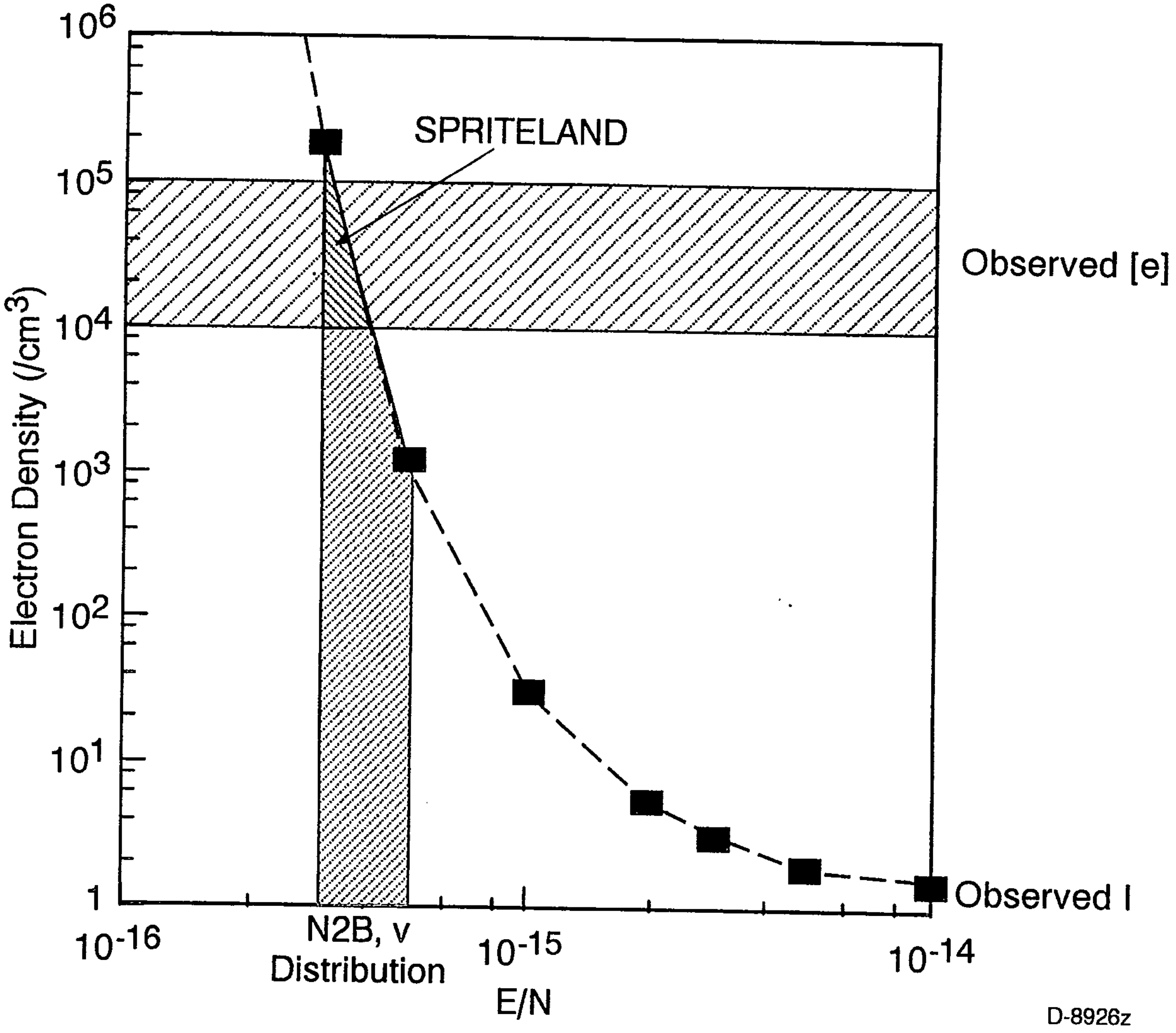

- Red Sprite exists only in narrow region bounded by [e], I, N_2Bv data

Sprites Persist and Can Exhibit "Re-Brightening"

Visible (video) Sprite persisted for over 180 mS (note: images are individual fields - time stamp is at end of first field and beginning of second). Images courtesy W.A. Lyons)

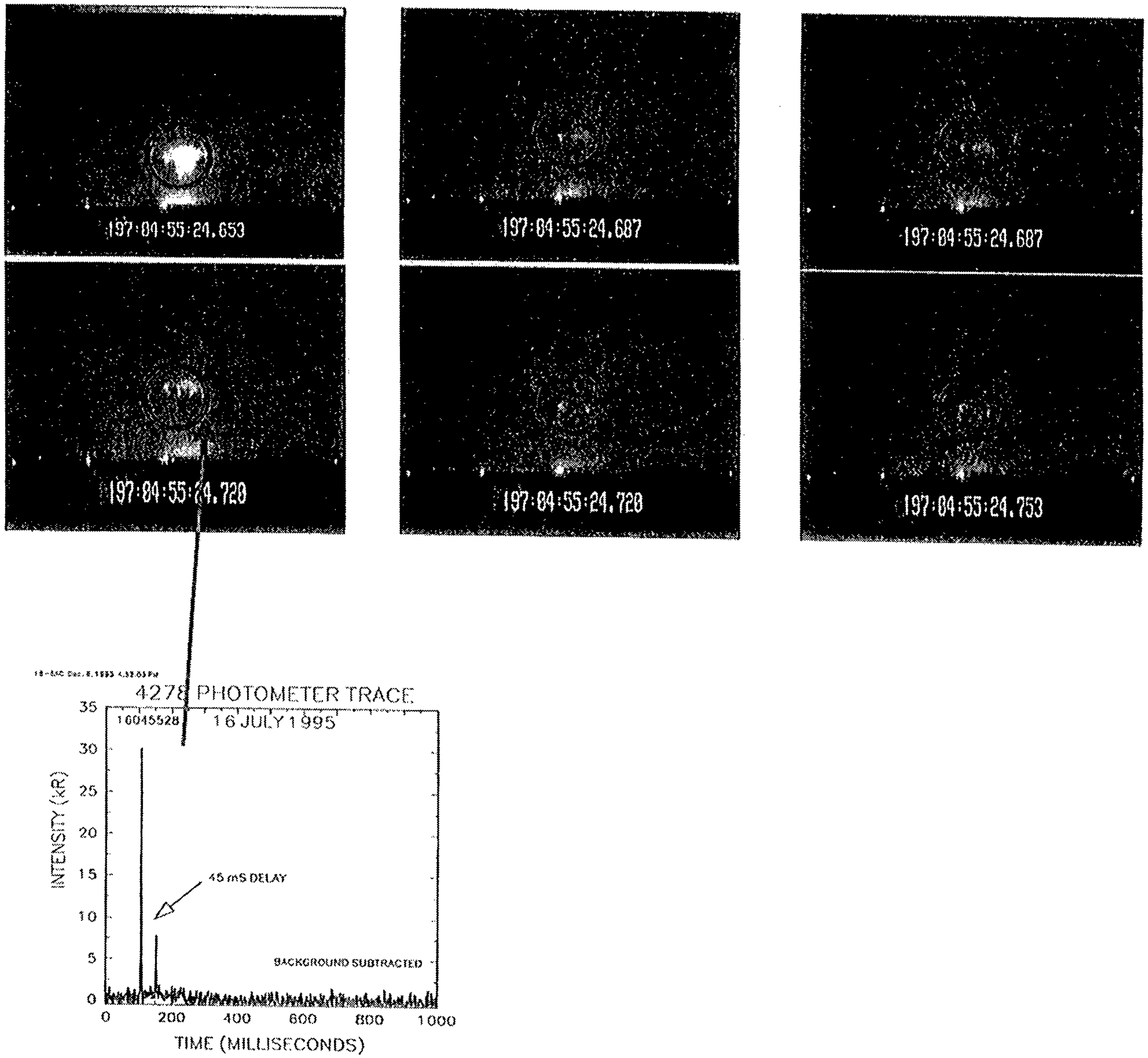

Results - 08/27/97 - *Elve with Sprite*

- visible Sprite (video) persisted for >50 mS -

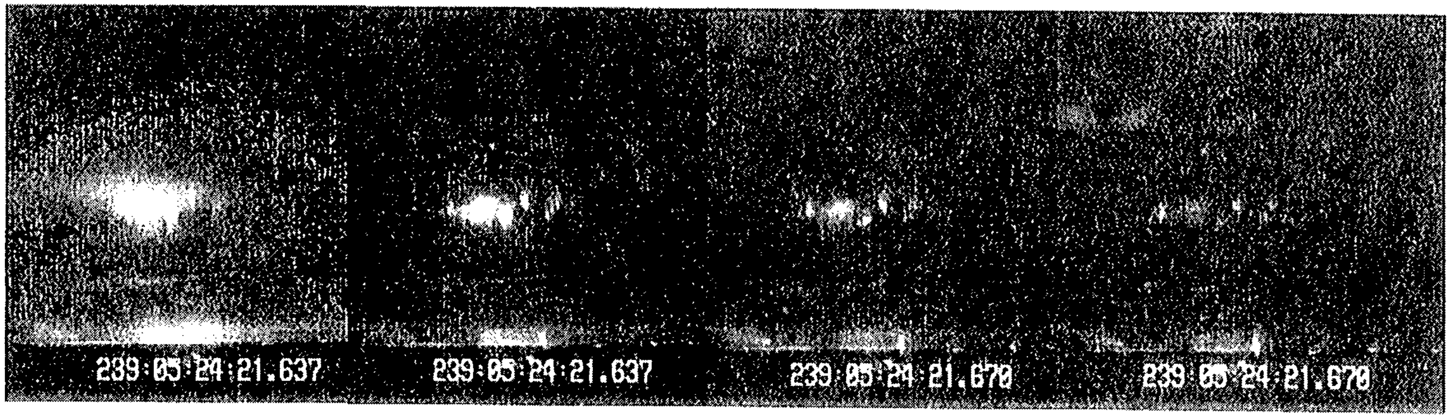

WIDE FOV XYBION CAMERA

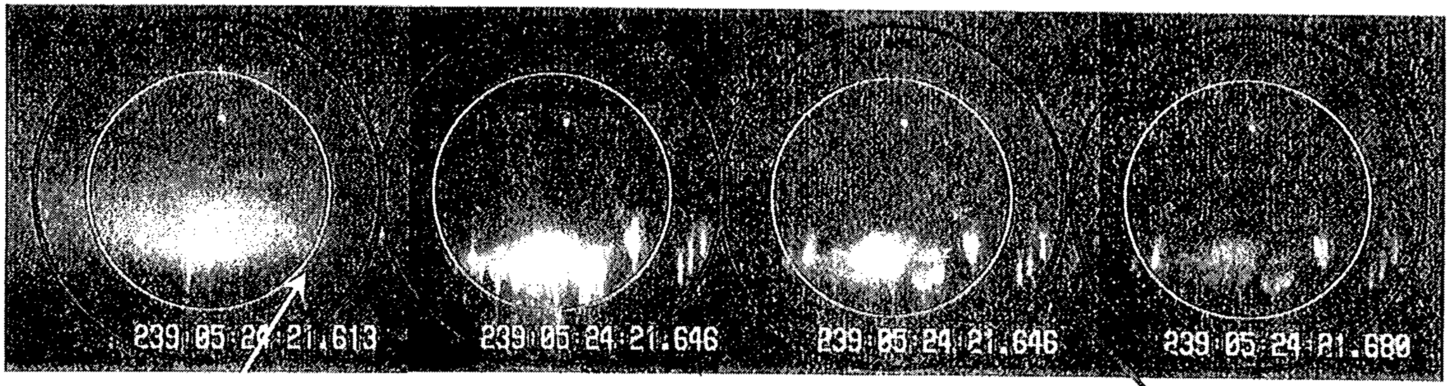

APPROXIMATE FOV
427.8 nm & 399.8 nm

NARROW FOV XYBION CAMERA

APPROXIMATE FOV
WINKLER (RED)

Photometer Trace

- 399.8 nm, 427.8 nm, Winkler (Red LP), VLF -

98-2101

Preliminary data on time-resolved 399.8 nm/427.8 nm ratio. Note ratio is unity for ~ 300 μS at Sprite initiation, implying very "hot" electron energy distribution

08-27-phot-A Dec. 3, 1997 3:14:35 PM

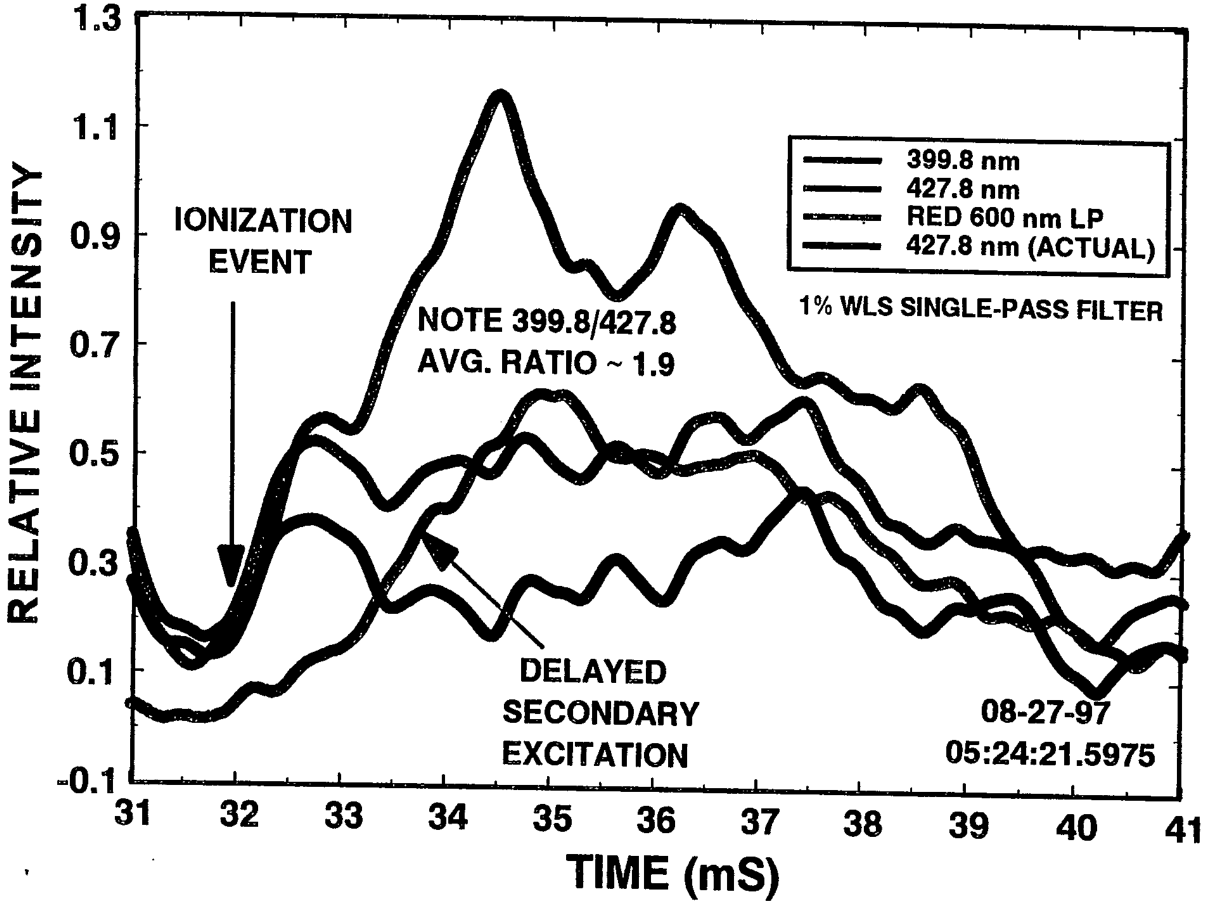

Archon Sprite Calculation

- Electron density very sensitive to electron temperature profile

- Electron temperature profile based on early-time (<300 μs) 399.8 nm/ 427.8 nm ratio and later time derived from N_2 first positive spectrum

- EDEP derived from 427.8 nm time profile

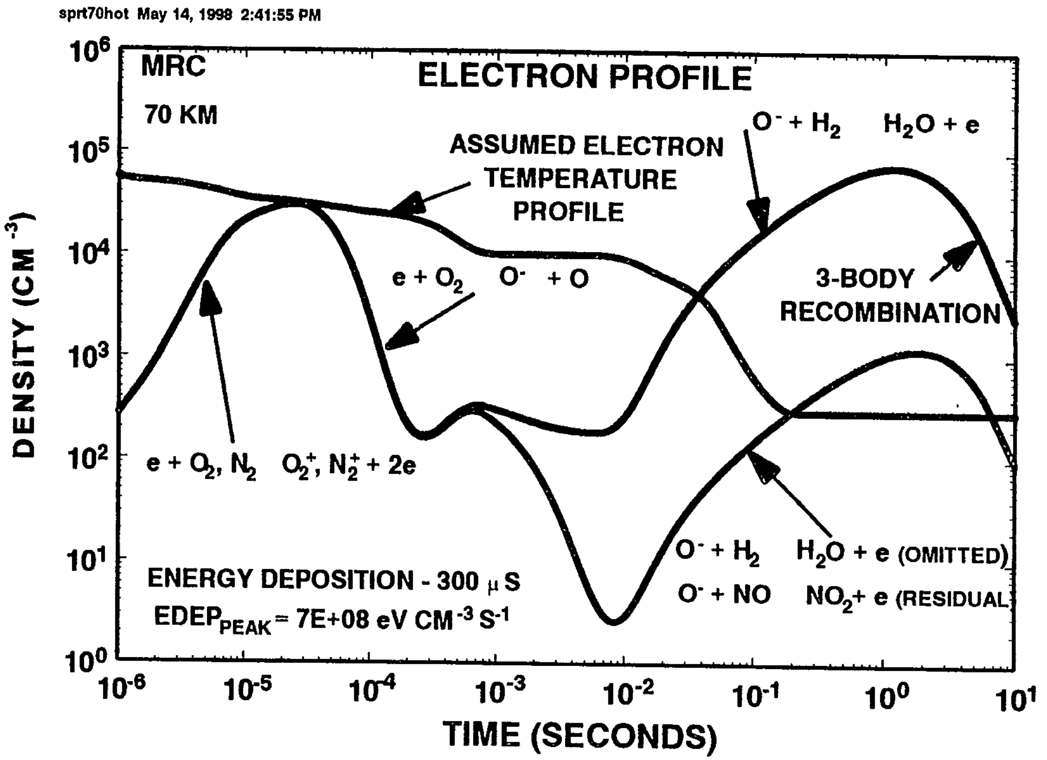

- Analysis of 427.8 nm data suggests 10^4 cm^{-3} <[e] <10^5 cm^{-3}

- Dowden derives [e] > 10^4 cm^{-3} from independent RF data

Sprite IR Radiators

- N_2 ($W^3\Delta \rightarrow B^3\Pi$), 2 to 5 μm
  - expect $\mathcal{O}$ (1 kR) concurrent with $N_2(B)$ excitation

- NO ($\Delta v = 1,2$), 2.7 μm, 5 to 6 μm
  - $N^* + O_2$ reaction
  - expect very little NO formation at low E/N

- CO_2 (ν_2, ν_3), 4 to 5 μm, 9 to 10 μm, 15 μm
  - energy transfer from $N_2(v)$
  - optically trapped, radiates to space
  - expect long duration enhancements above 4.3 μm background

CO_2 (ν_3) Vibraluminescence

$e^- + N_2 \rightarrow N_2(v) + e^-$ (fast)

$N_2(v) + CO_2 \leftrightarrows N_2 + CO_2(v)$

$CO_2(v) \rightleftarrows CO_2 + h\nu$ (4.3 μm)

Other collisional processes are negligible
- every $N_2(v) \rightarrow$ 4.3 μm photon

Emission is optically trapped: ~ 500 s at 80 km
- long duration compared to sprite

Radiance to space exceeds quiescent background for dosing rate $[e^-]\,\tau > 100\ \mathrm{cm^{-3}\,s^{-1}}$
- analysis of visible data indicates $[e^-]\,\tau \geq 1000\ \mathrm{cm^{-3}\,s^{-1}}$

Vibraluminescence

97-1124a

$$e + N_2 \rightarrow N_2(v) + e$$

$$N_2(v) + CO_2 \rightleftharpoons CO_2(v) + N_2$$

$$CO_2\,(v) \rightleftharpoons CO_2 + h\nu$$

$$\left[\begin{array}{c} N_2(v) + \begin{pmatrix} N_2 & O \\ O_2 & H_2O \end{pmatrix} \rightarrow \text{quenched} \\[2ex] CO_2(v) + \begin{pmatrix} O_2 & O \\ CO_2 & H_2O \end{pmatrix} \rightarrow \text{quenched} \\[2ex] e + CO_2 \rightarrow CO_2(v) + e \end{array}\right] \quad \text{negligible}$$

$N_2(v)$ + $CO_2(v)$ *Excitation in Sprites*

- 80 km, [e] = 1 x 10^3 for 0.1 s, Kumer EFA -

97-1131a

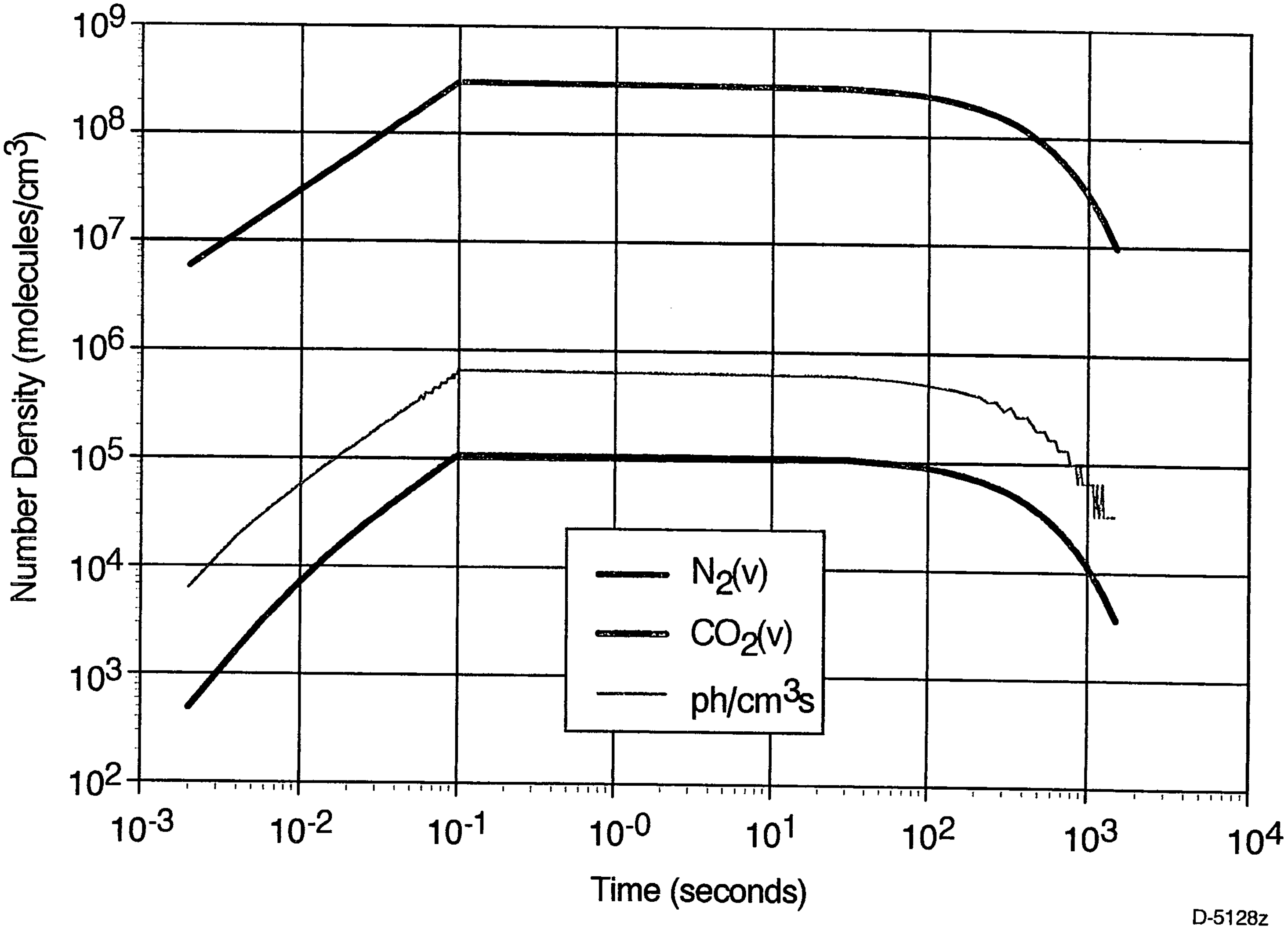

D-5128z

Conclusions

- Optical spectral and temporal data bound sprite dynamics
- Initial short ionization pulse
  - ~ 300 µs
  - $N_2(C)$, $N_2^+(B)$ UV emissions
  - initial [e] = 10^4 to 10^5 cm^{-3}, keV level
- Long-lived glow discharge (“red sprite”)
  - ≥ 100 ms
  - $N_2(B)$ visible/near IR emissions
  - $E/N = (3 \text{ to } 5) \times 10^{-16}$ V cm^2, ~ 70 km
  - $[e^-] = 10^4$ to 10^5 cm^{-3}, $\epsilon_{char} = 1$ eV
- Conditions favor vibrational excitation and vibraluminescence
  - expect significant, long-lived enhancements in $CO_2(v)$ emission to space

APPENDIX 16

Electron Distributions Responsible for Red Sprites

Electron Distributions Responsible for Red Sprites

B. D. Green, W. T. Rawlins, and M. E. Fraser
Physical Sciences Inc.
Andover MA

1. Introduction

Recent observation campaigns of red sprites, blue jets and elves are attempting to characterize their occurrence and identify their role in the global electricity circuit bridging altitudes between the tropopause and the bottom of the ionosphere. Red sprites represent the best characterized member of this family with quantified temporal and spectral (Hampton et al., 1994; Sentman et al., 1993,1995) behavior. Sprite formation seems to occur via a rapid ($< 300\ \mu s$) initiation pulse followed by a long lived (3 to 100 ms) red sprite which dominates the optical signature (Yukhimuk et al., 1997). We will make use of the spectral data to derive electron energetics and field strengths in the sprite volume; temporal (radiometer) data to determine time scales for ionization and electronic state excitation; and radiometer/spectrometer intensities to derive electron densities. We report here on the analysis of the energetics and time scales of optical emissions to derive field strengths and electron densities that can guide the development of physical models of red sprites. Optical diagnostics can provide significant insight to sprite chemistry and kinetics: spectral analyses yield electron energetics and field strength; temporal histories provide time scales for molecular excitation and ionization; intensities permit derivation of electron densities.

We have previously reported analyses of the red sprite data to extract molecular excitation levels (Green et al., 1996). The excited N_2 electronic state vibration distributions were related to the electrons producing the excitation assuming an approximate Boltzmann treatment. For the present paper, we have computed electron-impact rate coefficients and characteristic electron energies vs E/N (field/density - V/cm^2) using electronic-vibrational level specific excitation cross-sections and a more exact steady-state treatment. The comparison shows that red sprites consistently are observed in regions with E/N of 3 to $5 \times 10^{-16}\ V/cm^2$. The electron excitation rates at these E/N are consistent with the observed intensity (600 kR) (Sentman et al., 1995) and electron densities ($10^{4-5}\ e/cm^3$, Armstrong et al., 1998). Thus we believe the observations closely bound the electron distribution producing red sprites and should provide insight into atmospheric mechanisms. Moreover the electron distributions responsible for the red sprites can be used make UV and visible intensity predictions for other N_2 molecular neutral ($C\ ^3\pi$) and ion ($A\ ^2\pi$ and $B\ ^2\Sigma$) states excitation levels. Based on these electron excitation cross-sections, the intensity of IR emissions in red sprites is also estimated for N_2 electronic states, nitrogen metastable produced chemiluminescence and N_2 - $CO_2 \nu_3$ vibraluminescence.

2. Data Analysis

We have previously reported our analysis of the early spectral observations of sprites by the Alaska group (Hampton et al., 1993). Although emission from N_2B-state vibrational levels v=2-11 were observed, emission from N_2^+ A-state levels was not detectable above the noise levels in the data. This bounded the effective electron energy distribution. For the present effort, we undertook systematic spectral fitting to analyze data from the 1995 campaign to determine spectral variability. Spectral data of several sprites collected during the 1995 campaign (Heavner et al., 1996) is presented in Figure 1. Wavelength and intensity calibrations were performed at the Alaska Geophysical Institute. We applied an atmospheric transmission correction and compensated for instrumental baseline intensity variations across the spectrum. Although plotted here on an arbitrary intensity scale, the data exhibits excellent signal to noise of at least 1000:1 providing a wide dynamic range and the ability to search for weak emissions. Also note that the spectral distribution is very reproducible - there is little variability in the level of internal molecular excitation between sprites observed at different times and nights. This indicates that sprites may be produced in a relatively narrow set of atmospheric conditions (see below). Spectral fitting of over a dozen spectra yielded N_2 B-state distributions indistinguishable from our earlier analysis.

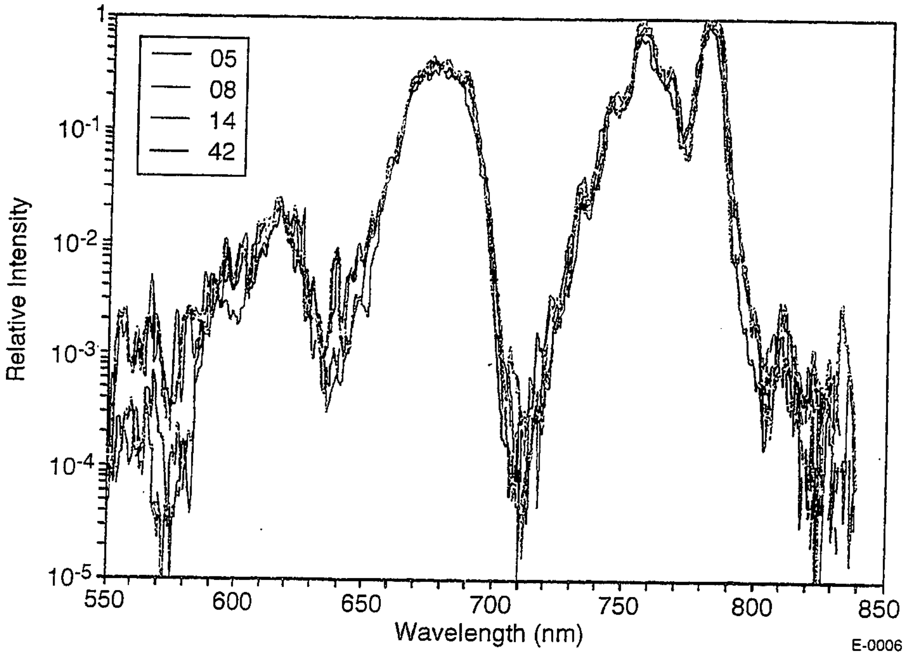

Figure 1. Sprite spectra: log scale.

The technique used for extracting vibrational populations from spectrally resolved radiant intensities has been described in general previously (Fraser et al., 1988) and as applied to the analysis of atmospheric emissions from red sprites (Green et al., 1996). Due to uncertainties in the response correction, we fit the Δv=2,3, and 4 vibrational sequences separately. Typical spectra are shown in Figure 2. Note that the dynamic range in the data is well over three orders of magnitude, permitting spectral contributions from weakly populated high vibrational levels to be distinguished above the noise level in the observational data. The N_2 B-state vibrational distributions derived from this analysis of the emissions from several sprites (acquired at

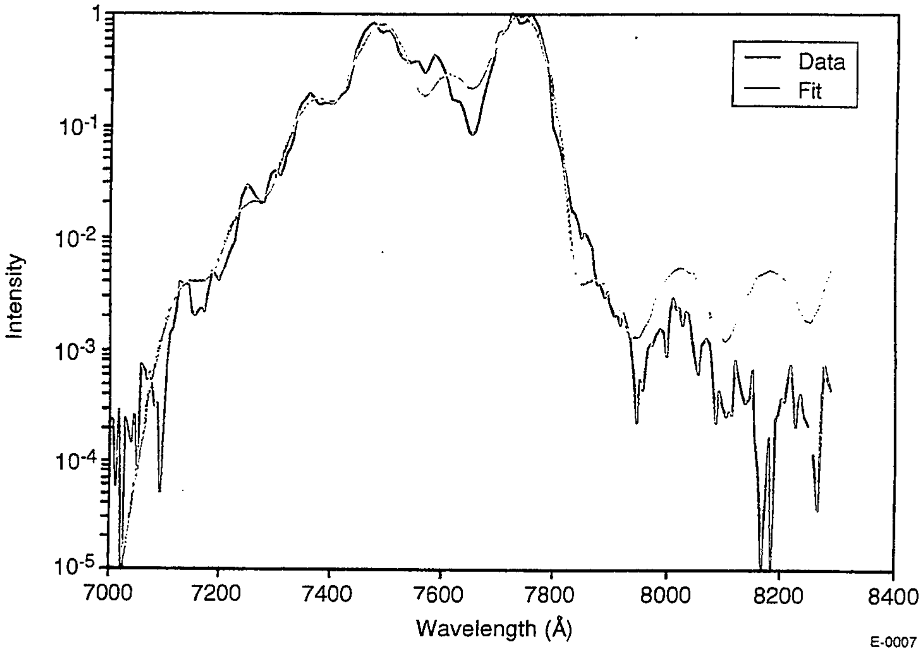

(a) Δv = 2 bands of N_2 (B → A) and N_2^+ (A → X)

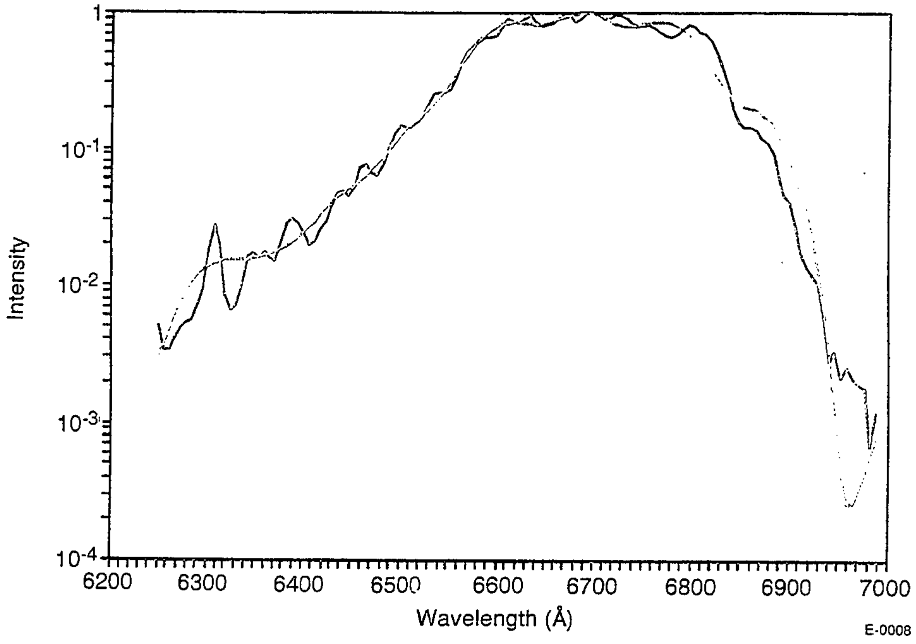

(b) Δv = 3 bands of N_2 (B → A), v′ = 3-10

Figure 2. Spectral fit, 250 K, 6 nm.

different times and on different days) are all quite similar. Their vibrational distribution is plotted in Figure 3 along with the distribution derived from our earlier work. The distributions are quite similar within their error bars. Once again emissions from N_2^+ A,v were not detectable in the spectrum. Only upper bounds on the populations of these levels could be set based on the noise (and statistical fitting uncertainty) level in the sprite data. These upper bounds are also shown in Figure 3.

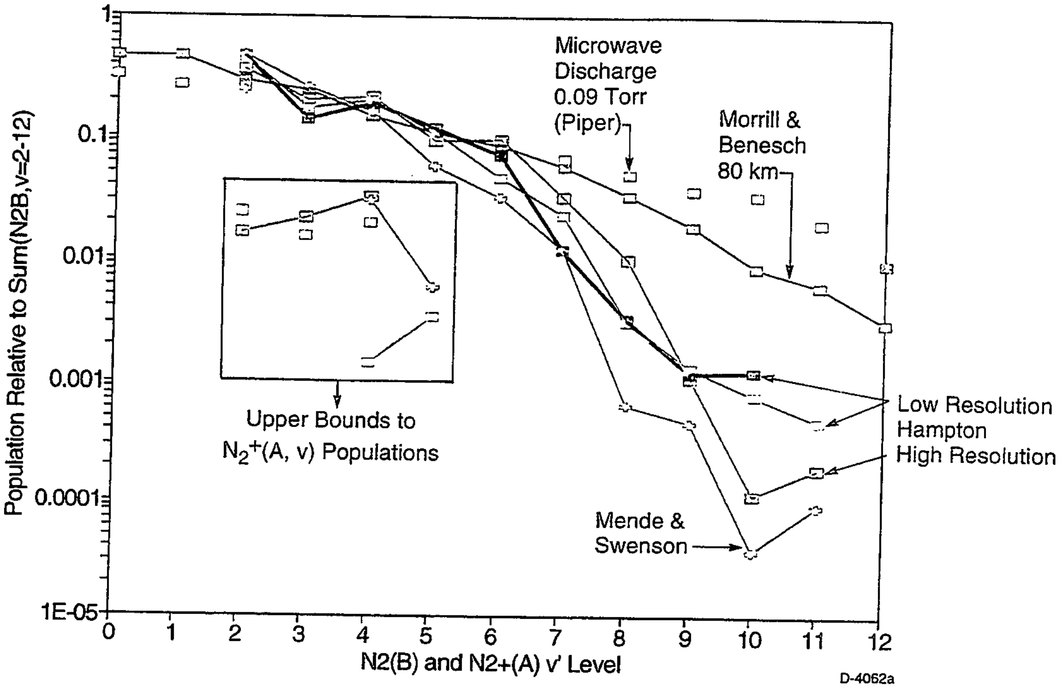

Figure 3. Nitrogen B-state vibrational population distributions.

One of the objectives of the current analysis is to extract electron energy distributions responsible for the observed red sprite emissions. Previously, we compared the sprite emissions to electron irradiated an atmospheric mixture of gases at pressures representative of 80 km altitudes. The 4 keV excitation electron energy produced a N_2 B-state vibrational distribution with significantly greater excitation in the highest levels than observed in sprites. As part of the current spectral analysis effort, we analyzed laboratory emissions from low pressure laboratory flowing discharge experiments with a well characterized electron excitation distributions. The spectrum obtained from the laboratory (Piper, 1997) and a red sprite are presented in Figure 4. The 90W laboratory discharge at 15 Pa representing a field strength per density (E/N) of 2 x 10^{-14} V cm^2 exhibits substantially more vibrational excitation than the red sprite. This is reflected in the derived N_2 B-state vibrational distribution also plotted in Figure 3. The vibrational distribution present in the laboratory discharge is "hotter" with significantly greater excitation in the highest vibrational levels. Laboratory spectra were analyzed at several values of E/N between 1 x 10^{-14} to 5 x 10^{-16} V cm^2. With these data as a basis, we undertook detailed electron distribution (Boltzmann transport) modeling to derive the characteristic distributions producing the observed sprite emissions.

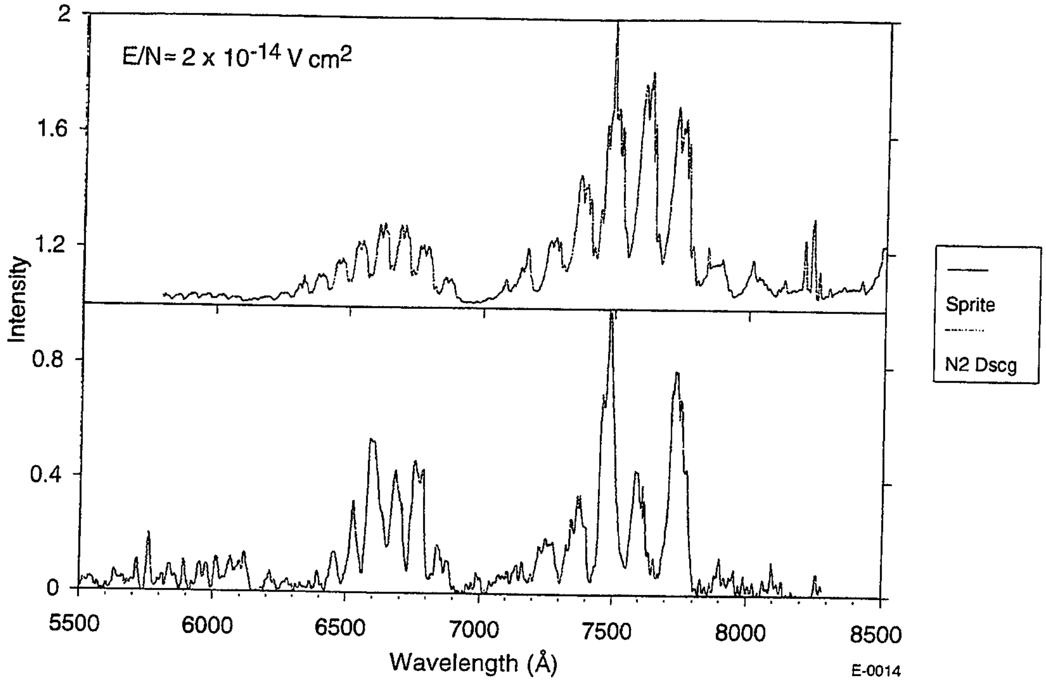

Figure 4. Compare AK Sprite and N_2 discharge. Discharge: 90 W, 0.11 Torr.

3. Electron Modeling

The analysis was performed using the ELENDIF code developed by Morgan and Penetrante (1989). The code accepts as input electron impact cross-sections for ionization, attachment, dissociation, and state specific electronic and vibrational excitation. Using the Boltzmann transport equation, the code calculates the electron energy distribution, characteristic energy, and electron-impact excitation rate coefficients (k) as a function of E/N (field/density) from the equation:

$$k = (2e/m)^{1/2} \int_{0}^{\infty} \sigma(\epsilon) f(\epsilon) \epsilon \, d\epsilon \quad .$$

Many of the cross-sections were obtained from the compilation by Phelps (1997). We augmented the Phelps compilation with absolute cross-sections for each vibrational level as a function of electron energy for the following states: N_2 $B^3\pi_g$, N_2^+ B $^2\Sigma_u$ and A $^2\pi_u$ using the data of Stanton and St. John (1969); and N_2 $C^3\pi_u$ and B-state cascade using the experimental data of Shemansky and Broadfoot (1971), preferring these total optical excitation cross-section measurements to the integrated differential scattering cross-section data of Cartwright et al. The total cross-sections used in our calculations for the four states of most interest (neutral B and C-states, and ion A and B-states) are plotted in Figure 5 as a function of electron energy. The relative excitation in to the four states vary greatly with energy. In particular, the differences in threshold

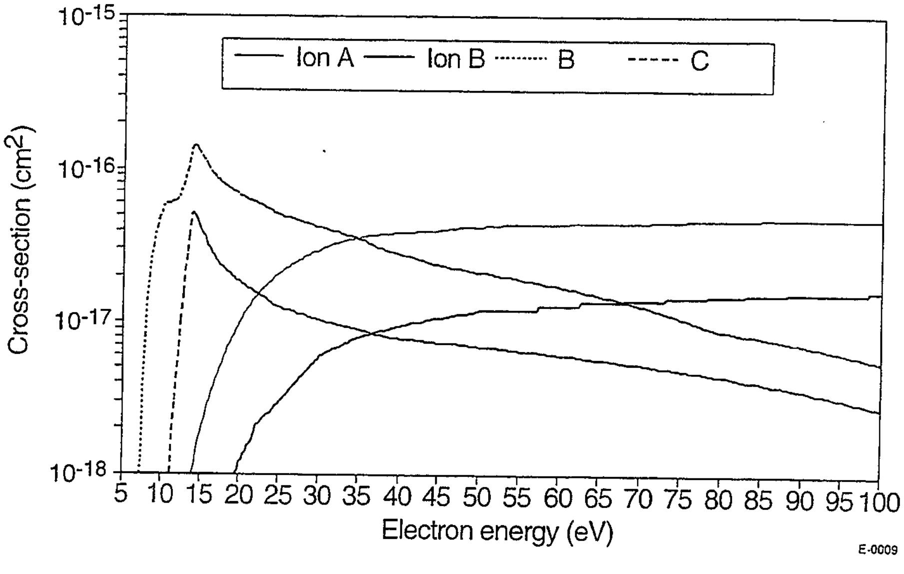

Figure 5. Electron excitation cross sections.

energies indicates that relative state populations will be a sensitive indicator of the fraction of the electron populations with energies between 8 and 20 eV. The cross-section for vibrational levels within the neutral B-state are shown in Figure 6. Note again that the vibrational distribution within the B-state will vary greatly depending upon the electron energy distribution between 8 and 14 eV.

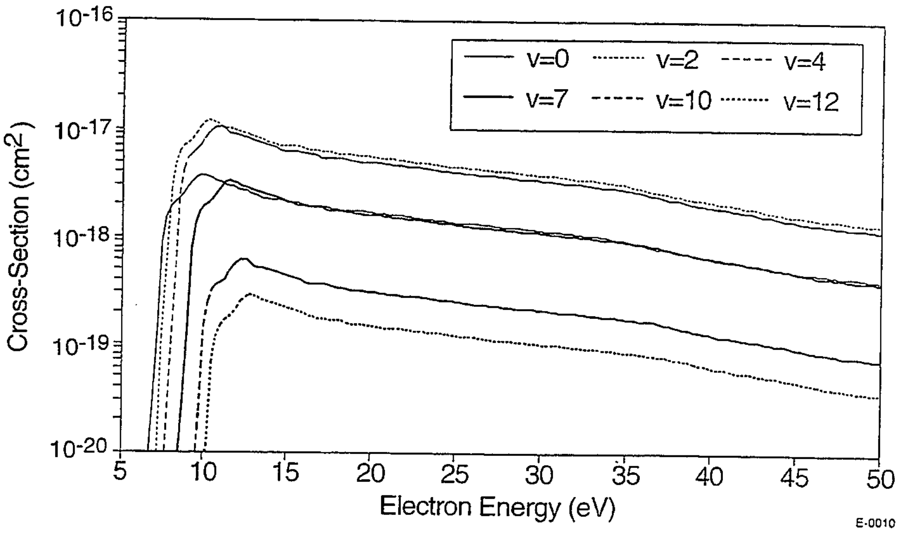

Figure 6. B-state excitation cross section.

Both radiative and collisional quenching of the molecular states must be included to correlate electron excitation rates with atmospheric radiances. Radiative lifetimes of Piper et al. (1989), and collisional quenching by N_2 and O_2 of the N_2^+ A (Piper et al., 1985) and N_2 B (Piper, 1992) were used to relax the distribution derived from Boltzmann transport modeling.

The electron energy distributions predicted for the ELENDIF code for a nitrogen/oxygen mixture as a function of E/N is shown in Figure 7. Increasing the E/N by only a factor of three produces a 10,000-fold increase in electrons possessing energy in the critical 10 eV region. The characteristic electron energy as a function of E/N is plotted in Figure 8. The characteristic energy is between 1 and 2 eV for E/N between 10^{-16} and 10^{-15} V cm^2.

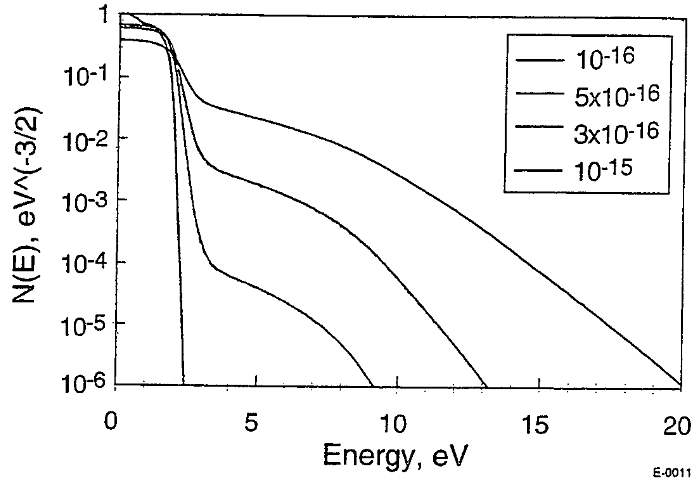

Figure 7. Electron energy distributions. Dependence of E/N (Vcm^2).

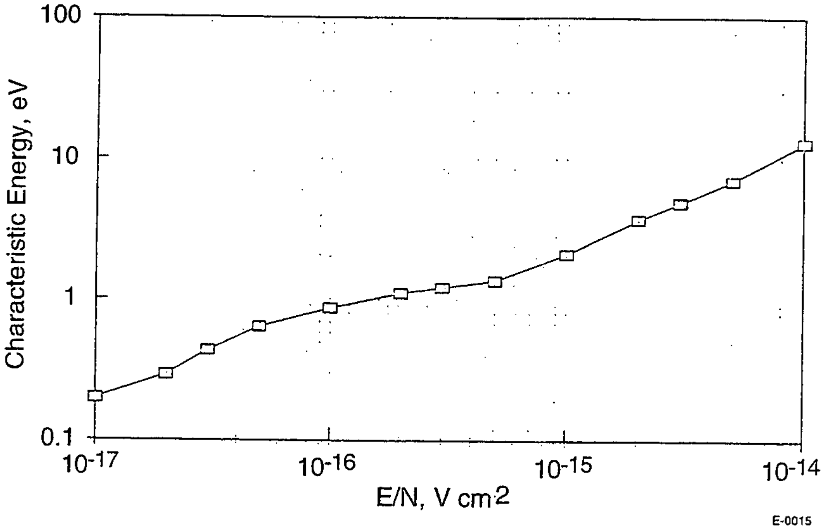

Figure 8. Characteristic electron energy.

The electron-impact excitation rate coefficients for several nitrogen states is shown as a function of E/N in Figure 9. Vibrational excitation of nitrogen is by the most efficient process. Excitation rates follow the threshold energy sequence with neutral B having a larger rate coefficient than the C-state, with ion A and B states having sequentially smaller rates. At values above 8 x 10^{-15} V cm^2, the ion A rate coefficient surpasses all the neutral rates. However, at E/N = 10^{-15} V cm^2, the ion A-state rate coefficient requires about a factor larger E/N to have a

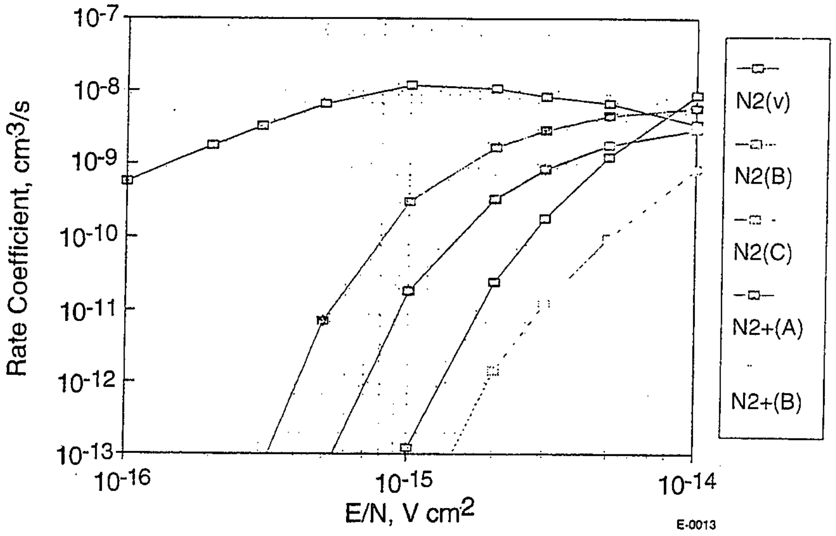

Figure 9. N_2 and N_2^+ excitation.

comparable rate coefficient to the neutral B-state. Thus, the relative abundance of molecules in the ion A-state should be a sensitive indicator of the electron excitation distribution. The magnitude of the neutral B-state rate coefficients for several vibrational states is shown in Figure 10 to be an even more sensitive indicator than the vibrational distribution - increasing by 100,000 between 3 x 10^{-16} and 1 x 10^{-15} V cm^2.

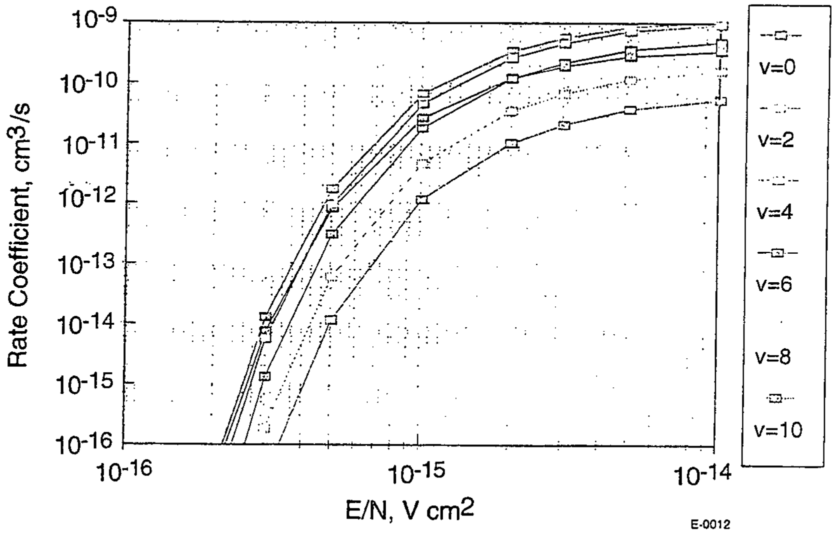

Figure 10. $N_2(B,v)$ excitation.

4. Model Comparison

The vibrational population distribution within the N_2 B-state changes significantly with E/N. Thus the B-state distribution derived from the red sprite observations provide a remote probe of the electron distribution within the sprite emission volume. The modeled B-state distributions for several E/N between 3 x 10^{-16} and 3 x 10^{-15} V cm^2, normalized to v=2, are plotted in Figure 11. Greater than an order of magnitude enhancements in population are observed for $v \geq 8$. Also shown in Figure 11 is the observed B-state sprite distribution (from Figure 3). The observed distribution closely follow a distribution arising from an excitation volume with E/N = 3 to 5 x 10^{-16} V cm^2, and differs significantly from lower or higher E/N distributions.

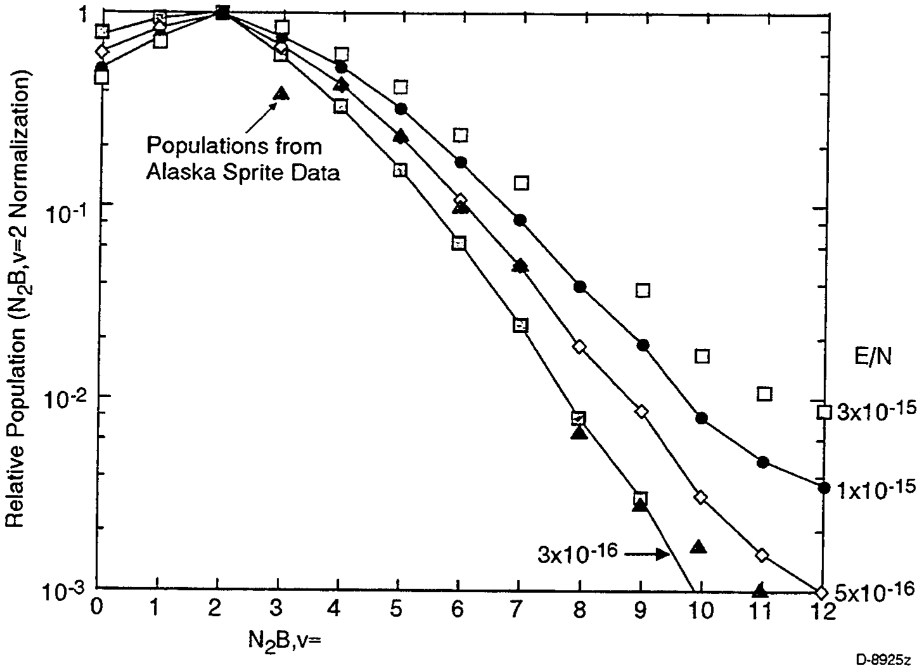

Figure 11. Relative N_2 (B,v) distributions for several E/N.

Absolute excitation rate coefficients permit the local conditions producing the sprite visible emission radiance to be estimated. The electron density required to produce 600 kR column radiance (Sentman et al., 1995) in a 1 km column as a function of E/N is plotted as the broken curve in Figure 12. The excitation rate coefficient is a very sensitive function of E/N as shown in Figure 10. The electron density required to match the observed radiance thus increases dramatically as E/N increases. (If the observed intensity is lower, the broken curve moves linearly downward. If the sprite visible emission column line-of-sight path is smaller, the curve moves linearly upward).

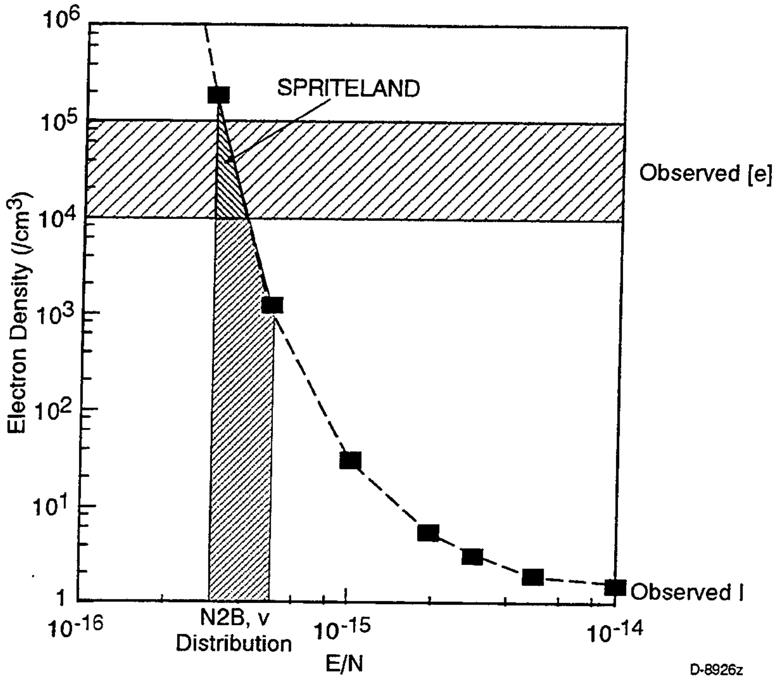

Figure 12. e/cc to create 600 kR (1 km) visible N21P.

The red sprite intensity is not the only observable - the spectral distribution and electron density place further constraints on the local conditions within red sprites. The spectral analysis and electron transport modeling bound E/N as 3 to 5 x 10^{-16} V cm^2 - indicated as a vertical band shaded region in Figure 12. Observations of electron density in the sprite volume (Armstrong et al., 1998) indicate local electron concentrations enhanced above ambient, but only with 10^4 to 10^5 e/cm^3. These electron concentrations are also indicated as the horizontal band shaded region on Figure 12. While neither the absolute intensity nor incoherent scatter radar measurements of electron density are simultaneous with the spectral measurements, they were acquired during the same campaign and indicate consistent enhancements to this level.

Only a small (solid shaded) physical region of Figure 12 satisfies all the observational constraints of intensity, electron density and spectral distribution. We suggest that red sprites emission is observed only when the local atmospheric conditions fall within these bounds. Future observations of red sprite intensity, spatial extent and local electron density should be used to better define this existence region. Similarly, red sprite production mechanisms should be similarly constrained and produce local conditions (intensity, electron density, column width, and E/N) matching the field observations and analysis.

The runaway upward propagating discharge mechanism proposed by Roussel-Dupre and Gurevich (1996) requires atmospheric electric field strengths of 100 keV/m magnitude such that electron acceleration by the field is greater than energy loss by inelastic scattering at all altitudes along the upward path. Secondary electron energies in the 1.5 eV range with local electron densities around 10^3 e/cm^3 are predicted. The EMP model predicts sprites originating from the bottom of the ionosphere and propagating downward (Bell et al., 1995, Taranenko et al., 1993a,b). Atmospheric field strengths of 20 V/m are predicted with characteristic electron temperatures between 4 and 20 eV and requires only a few percent enhancement above ambient electron density.

The current analysis assuming a 70 km sprite emission volume derives characteristic electron temperatures about 1 eV - closer to the runaway model; and field strengths of 50 to 90 V/m - intermediate between the two models, but closer to the EMP prediction. Future modeling incorporating these additional observational constraints may provide a clearer picture of the phenomenon producing red sprite emissions.

The two mechanisms differ on several other significant points: the runaway model favors sprite formation following a large (>100 Coulomb) positive cloud to ground stroke, with emission peaking below 65 km. The EMP model predicts sprite formation after multiple negative cloud to ground strokes with the peak of the emission occurring in the 85 to 95 km region. Both models predict bright UV and N_2 First Positive (B-A) emission of 10 M Rayleigh (10^{13} photons cm^{-2} s^{-1}) brightnesses. Our electron modeling permits us to address state's relative emission brightnesses.

The ELENDIF Boltzmann transport and quenching modeling was used to predict excitation rate coefficients as a function of E/N for the other visible/ultraviolet emitting states: the ion N_2^+ B $^2\Sigma_u$ and A $^2\pi_u$ states and the neutral N_2 $C^3\pi_u$ state. Within the sprite emission volume during the period when the observed red emission is occurring, the E/N distribution drives the emission from all N_2 states. The E/N distribution best matching the neutral B-state observations (3-5 x 10^{-16} V cm^2) predicts very small relative populations in the other states - with the C-state having populations 10^4 to 10^5 lower concentrations (10^3 times lower intensity), and the ion states would have concentrations lower than the B-state by more than a factor of 10^6. Thus our conclusion from our spectral fitting analysis that N_2^+ A-state emissions were not observable, and was required to be present at relative populations of ≤ 0.04 of the B,v=2 population are consistent with this modeling. The modeling suggests that the ion A-state is present at very low concentrations during the red sprite. Our predictions based on the observed red sprite distributions leads us to conclude that any ion state emission, if observed, must arise from a different part of the sprite such as a precursor/initiation phase or a different process than that producing the red sprite.

Modeling of red sprite excitation using the quasi-electrostatic heating approach coupled to time dependent nitrogen vibrational populations has been preformed by Morrill and co-workers (1998). They also conclude that electron energies in the 1 to 2 eV range are required to produce the observed distributions. However, their spectral analysis indicates that N_2^+ A state is just detectable in the emission sprite spectra, and the presence of that state may suggest that runaway electrons are producing the sprite excitation.

Given the E/N derived from the B-state distribution, we can estimate processes giving rise to IR emission as direct electron impact excitation and impact induced chemical reactions. Nitrogen W ($^3\Delta$ - B $^3\pi$) electronic state will occur concurrent with the (B-A) First Positive emission, with intensities on the order of 1 kR predicted based on 600 kR visible emission.

Electron impact will dissociate excite nitrogen atoms. Modeling using the ACCUCHEM package to estimate NO production from the $N^* + O_2$ reaction (Kennealy et al., 1978) indicated that little NO was formed at these low E/N values. As shown in Figure 9, vibrational excitation of nitrogen is the most efficient process at low E/N. Although vibrationally excited nitrogen does not emit in the IR, it efficiently transfers its excitation to another atmospheric species, CO_2 in a near-resonant process. This transfer and decay of the optically trapped CO_2 (v_3) emission has been treated previously (Kumer, 1977). Because all other collisional processes are negligible at sprite altitudes, every nitrogen vibration is transformed into a 4.3 μm CO_2 photon. However, the 4.3 μm emission is optically thick and multiple emissions/absorptions are required before the photon can escape (to space).

At 80 km, using the escape function from Kumer (1977), over 10^3 absorptions/emissions are required, giving a characteristic lifetime of the excitation of 500 seconds. The densities of nitrogen vibration, CO_2 (v_3), and volumetric photon emission rate are given in Figure 13 in response to a 10^3 e/cm^3 excitation pulse 0.1 second in duration The CO_2 vibraluminescence is seen to persist at elevated levels for nearly 1000 seconds. The effects at other wavelengths and trace emitters will be considered in future efforts.

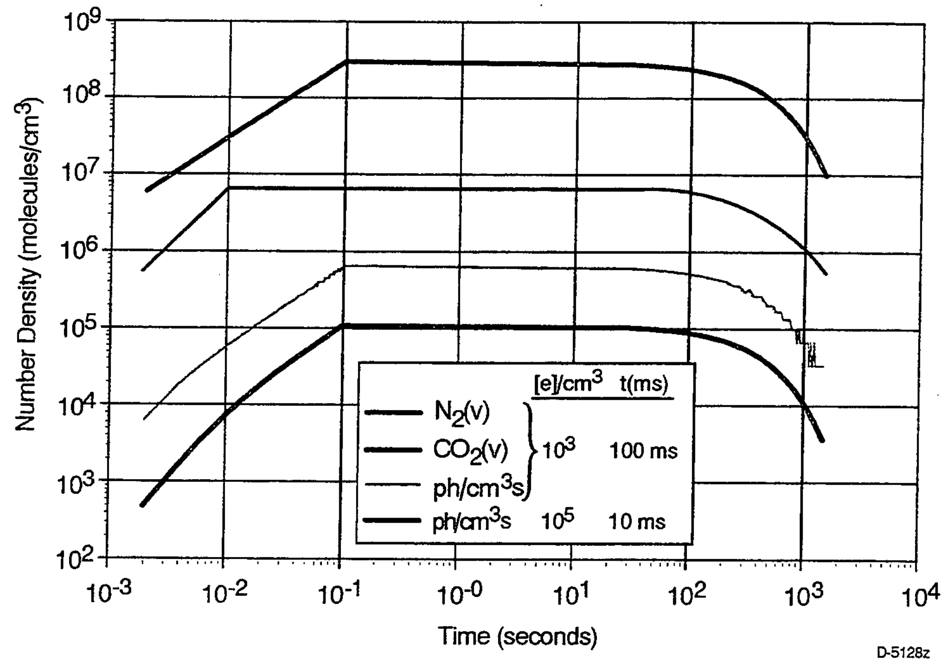

Figure 13. $N_2(v) + CO_2(v)$ excitation in Sprites.

5. Summary and Key Issues for Future Measurements

We present here an analysis using spectrally-resolved data from red sprites to remotely probe local conditions in the excitation volume. Detailed comparison of theoretical spectra with high dynamic range observational data permitted the highly excited vibrational levels of the N_2 B-state to be extracted. Modeling of electron Boltzmann transport and molecular quenching permitted vibrational state distributions to be predicted as a function of E/N. The observed B-state vibrational distributions in red sprites very closely follows the distribution from a region with an E/N of 3 to 5 x 10^{-16} V cm^2, representing a characteristic electron energy of approximately 1 eV. At these E/N levels, emissions from the ion A-state is predicted to be completely not observable (consistent with our spectral analysis), and UV emissions from neutral C-state within the same volume down by three orders of magnitude during the red sprite. UV emission from molecules in the ion B-state should be completely negligible during the red sprite.

We observe that the observed intensity and electron concentrations within sprites when coupled with our electron kinetic modeling and the observed B-state vibrational distribution define a narrow physical regime in atmospheric field strength and electron density where red sprites are observed, and perhaps can only exist. Observed red sprite spectral distributions exhibit little variability, but are sensitive to electron energy distribution. This supports our hypothesis that this regime is sharply defined. Definition of the boundaries of this regime is the challenge of future field observational campaigns.

Acknowledgments

We gratefully acknowledge the assistance at PSI of Mark Fraser with spectral fitting, John Cronin in performing the ELENDIF calculations, and Larry Piper by making microwave spectra available. We also acknowledge many stimulating discussions on sprite signatures, mechanisms and timescales with Russ Armstrong of Mission Research Corporation and Laila Jeong of the Air Force Research Laboratory. This research was sponsored by the Air Force Office of Scientific Research.

References

Armstrong, R.A., et al., special edition, J. Solar Terrestrial Physics (1998).

Bell, T. F., V.P. Pasco, and U. S. Inan,"Runaway Electrons as a Source of Red Sprites in the Mesosphere," Geophysics Research Letters **22**, 2127-2130 (1995).

Cartwright, D. C., S. Trajmar, A. Chutjian, and W. Williams,"Electron Impact Excitation of the Electronic States of N_2. II. Integral Cross Sections at Incident Energies from 10 to 50 eV," Physical Review A **16**(3), 1041-1051 (1977).

Fraser M. E., W. T. Rawlins, and S. M. Miller, "Infrared (2 to 8 μm) flourescence of the W $^3\Delta_u$ -> $B^3\Pi_g$ and w $^1\Delta_u$ -> $a^1\Pi_g$ systems of nitrogen," J. Chem. Phys. **88**, 538 (1988).

Green B. D., M. E. Fraser, W. T. Rawlins, L. Jeong, W.A.M. Blumberg, S. B. Mende, G. R. Swenson, D.L. Hampton, E. M. Wescott, and D. D. Sentman," Molecular Excitation in Sprites," Geophysics Research Letters **23** (16), 2161 (1996).

Hampton, D. L., M.. J. Heavner, E. M. Wescott, D. D. Sentman,"Optical Spectral Characteristics of Sprites," Geophysics Research Letters **21**, 875 (1994).

Heavner, M. J., D. R. Moudry, D. D. Sentman, E. M. Wescott, J. T. Desroschers, Spectral Observations of Sprites," Paper A71B-06, 1996 Fall Meeting AGU.

Kennealy, J. P., F. P. Del Greco, G. E. Caledonia, B. D. Green,"Nitric Oxide Chemiexcitation Occurring in the Reaction Between Metastable Nitrogen Atoms and Oxygen Molecules," J. Chem. Phys. **69**(4), 1574 (1978).

Kumer, J. B.," Atmospheric CO_2 and N_2 Vibrational Temperatures at 40- to 140-km Altitude," J. Geophysical Research **82**(16), 2195-2202 (1977).

Morgan, W. L. and B. M. Penetrante, "ELENDIF: A Time-Dependent Boltzmann Solver for Partially Ionized Plasmas," Lawrence Livermore National Laboratory UCRL-100820, April 1989.

Morrill, J. S., E. J. Bucsela, V. P. Pasco, S. L. Berg, W. M. Benesch, E. M. Wescott, and M. J. Heavner,"Time resolved N_2 Triplet State Vibrational Populations and Emissions Associated with Red Sprites," accepted J. Atmospheric and Solar-Terrestrial Physics (1997).

Phelps, A. private communication 1997. Database available at jilawww.colorado.edu

Piper, L. G. Private communication 1997.

Piper, L. G. "Energy transfer Studies on N_2 (X,v) and N_2 (B)," J. Chemical Physics **97**, 270 (1992).

Piper, L. G., B.D. Green, W.A.M. Blumberg, S.J. Wolnik,"Electron Impact Excitation of the N_2^+ Meinel Band," J. Chemical Physics **82**, 3139 (1985).

Piper, L. G., K.W. Holtzclaw, B.D. Green, W.A.M. Blumberg,"Experimental Determination of the Einstein Coefficients for the N_2 (B-A) Transition," J. Chemical Physics **90**, 5337 (1989).

Roussel-Dupre R. and A.V. Gurevich,"On Runaway Breakdown and Upward Propagating Discharges," J. Geophysical Research **101**(A2), 2297-2311 (1996).

Sentman, D. D. and E. M. Wescott,"Observations of Upper Atmospheric Optical Flashes Recorded from a n Aircraft," Geophysics Research Letters **20**(24), 2857-2860 (1993).

Sentman, D. D., E. M. Wescott, D. L. Osborne, D. L. Hampton, M. J. Heavner,"Preliminary Results from the Sprites94 Aircraft Campaign: 1. Red Sprites," Geophysical Research Letters **22**(19), 1205-1208 (1995).

Shemansky, D. E. and L.A. Broadfoot,"Excitation of N_2 and N_2^+ Systems by Electrons - II Excitation Cross Sections and N_2 1PG Low Pressure Afterglow," J. Quant. Spectros. Radiat. Transfer **11**, 1401 (1971).

Stanton and St. John,"Electron Excitation of the First Positive Bands of N_2 and of the First Negative and Meinel Bands of N_2^+," J.Opt.Soc.Amer. **59,** 252-260 (1969).

Taranenko, Y. N., U. S. Inan, and T. F. Bell,"The Interaction with the Lower Ionosphere of Electromagnetic Pulses from Lightning: Heating, Attachment, and Ionization," Geophysics Research Letters **20**(15), 1539-1542 (1993).

Taranenko, Y. N., U. S. Inan, and T. F. Bell,"The Interaction with the Lower Ionosphere of Electromagnetic Pulses from Lightning: Excitation of Optical Emissions," Geophysics Research Letters **20**(23), 2675-2678 (1993).

Yukhimuk, V., R. Roussel-Dupre, E. Symbalisty, Y. Taranenko,"Optical, Radio, and Gamma-Ray Characteristics of Blue Jets Produced by Runaway Air Breakdown," Paper A22C-12 AGU 1997 Fall Meeting.

APPENDIX 17

Diurnal Variability of Infrared Atmospheric Emissions Diagnostic of Odd Oxygen as Observed in the Delta 181 Mission

Diurnal Variability of Infrared Atmospheric Emissions Diagnostic of Odd Oxygen as Observed in the Delta 181 Mission

Lawrence G. Piper and. B. David Green
Physical Sciences Inc
20 New England Business Center
Andover, MA, 01810

and

Randall E. Murphy
Research Sciences Corporation
Sandwich, MA

INTRODUCTION

High altitude or orbital measurements of various radiating features provide the capability for true global observations of the composition and structure of the upper atmosphere. Our knowledge increases as a cycle of observation and modeling continues. That is, observations are compared to model calculations. The latter are revised as needed, and then further verified by additional observations. Many observations sample only few spectral features and cover a limited period of time. Some orbital missions, however, have been able to observe a host of spectral features over a complete diurnal cycle. Such measurements, then, provide the most rigorous tests for atmospheric models. We report here a set of observations of several spectral features, which are all diagnostic of the local atomic oxygen and ozone concentrations near 85 km. These observations come from the Delta 181 orbital mission and cover a complete diurnal cycle. We compare the observations to a comprehensive photochemical model.

The Delta 181 orbital mission observed the quiescent atmospheric earth limb radiance at several local times. The 300 km altitude, 28 degree latitude trajectory permitted low latitude and equatorial observations around equinox. Data were acquired at local noon, dusk, dawn, and midnight over two orbits. Hence substantially different spatial regions were sampled. Some of the observed variability, therefore, may be due to the geographic variations in addition to solar diurnal changes. Never the less, the Delta 181 mission provided a significant new data base of infrared earth-limb observations.

The flight instrument had two circular variable filter (CVF) spectrometers. One was liquid-nitrogen cooled and provided spectral coverage from 0.7 to 5.0 μm. The other, a liquid helium temperature instrument, covered the spectral region from 4.6 to 22 μm. These spectrometers had a spectral resolution of 2.5 to 3% of wavelength. The noise equivalent spectral radiance (NESR) of the instrument on orbit was about 1.2 x 10^{-13} W cm^{-2} sr^{-1} μm^{-1}, and was dominated by non rejected earth radiance (NRER)

The earth limb data were acquired by pitching the sensor through a 19 degree path which moved the center of the field-of-view of the instrument through tangent heights from 300 to -90 km (hard earth). Approximately 10 limb scans were completed in each observation sequence. Dawn and dusk scans were centered around the terminator crossing, looking perpendicular to the orbital velocity vector. A number of atmospheric emissions were observed including emissions from the hydroxyl night glow layer, $O_2(a\ ^1\Delta_g)$, ozone, NO, and CO_2.

The rapid scan rate through the limb compromised the data. Each spectral scan took 3 seconds while the field-of-view centerline swept up through the atmosphere at 10 km s^{-1}. Thus, each spectrum contained emission from several different scale heights. Correspondingly, the data base is sparse because a particular emission feature is monitored at 30 km height intervals. The field-of-view of the CVF was also quite large — roughly 50 km (full width tenth maximum) at the tangent point. Thus, emission from several scale heights was observed simultaneously and information on horizontal and vertical structure lacks detail. Finally, the rejection ability of the telescope was only moderate. However, by piecing together observations from a number of scans, a relatively comprehensive data base was constructed.

In this work we focus on how three of the observed features, all ultimately related to the concentrations of atmospheric oxygen atoms and ozone, vary as a function of local time. These three features are the singlet oxygen emission at 1.27 µm, $O_2(a\ ^1\Delta_g — X\ ^3\Sigma_g^-)$, the hydroxyl overtone emission bands around 1.6 µm, and the ozone ν_3 emission at 9.6 µm. The O_2(a-X) emission drops rapidly at sunset, drops somewhat more slowly throughout the night, then increases quite rapidly at sunrise. The OH(v) and $O_3(\nu_3)$ emissions, on the other hand, increase fairly rapidly at sunset. They continue to increase, but more slowly, up to about midnight, at which time they begin to decrease slowly until sunrise. At sunrise, these emissions decrease rapidly. The behavior of all these spectral features are linked to the chemistry of odd oxygen in the upper atmosphere, primarily the chemistry of atomic oxygen and its recombination product, ozone.

These trends are illustrated in Figures 1 through 3 where we have plotted the Delta 181 observations centered at 85 km altitude as a function of local time for ozone, hydroxyl, and singlet oxygen, respectively. The figures also show a comparison between observations and the comprehensive photochemical model of Rodrigo, et al.,[1] which we shall discuss shortly. We first describe the major chemical processes we can invoke to rationalize our observations. Then we will discuss the comparison between Delta 181 observations, the Rodrigo et al. model as well as several other models[2,3] and less-comprehensive sets of upper atmospheric observations.[4-6]

The ozone emission observed at 9.6 µm is excited primarily by earth-shine pumping of the ν_3=1 band of ozone.[2] Higher vibrational levels are also excited in the process of recombination of atomic and molecular oxygen, but our observations focus on the ν_3=1 band for which the earth-shine pumping is the primary excitation mechanism both during the day and at

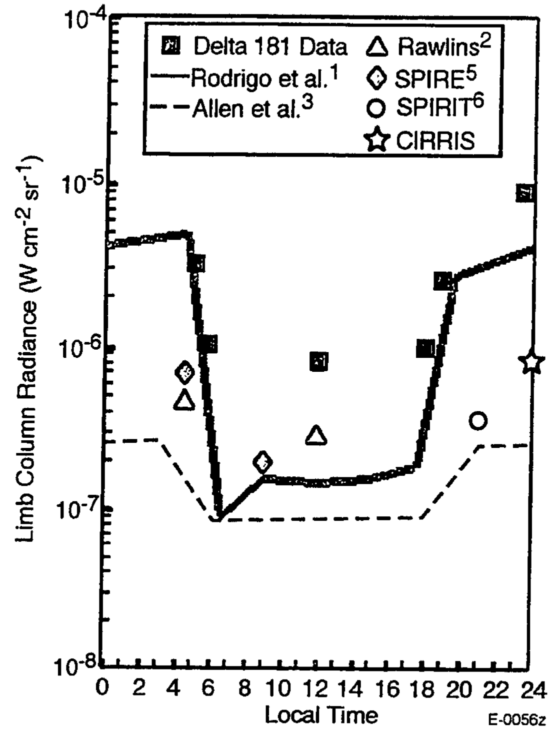

Figure 1. Variation in O_3 (v_3=1) emission near 85 km as a function of local time as observed in the Delta 181 mission, as modeled by Rodrigo et al.,[1] Rawlins,[2] and Allen et al.,[3] and as observed in several other sets of field measurements.[5, 6]

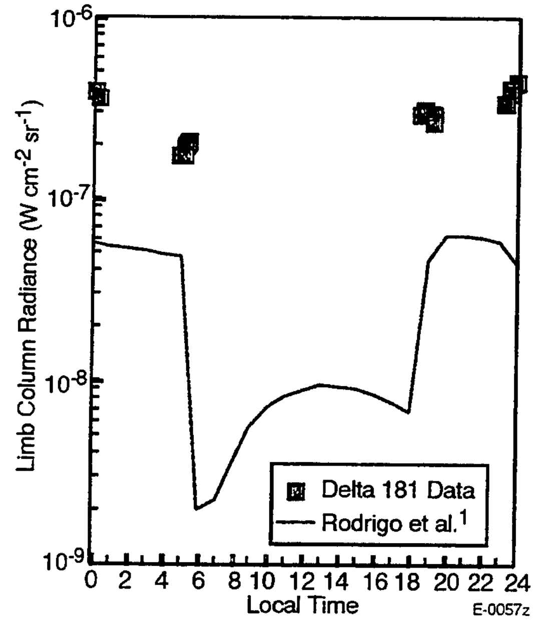

Figure 2. Variation in hydroxyl overtone emission near 85 km as a function of local time as observed in the Delta 181 mission and as modeled by Rodrigo et al.[1]

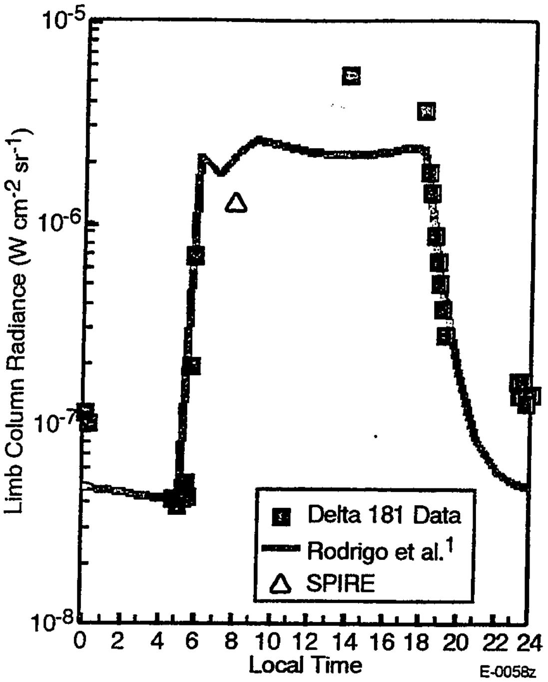

Figure 3. Variation in O_2 (a $^1\Delta_g$) emission near 85 km as a function of local time as observed in the Delta 181 mission and the SPIRE mission[4] and as modeled by Rodrigo et al.[1]

night. As such, the intensity of the observed emission is directly proportional to the local ozone concentration.

Ozone itself is generated by the recombination of oxygen atoms and molecules,

$$O + O_2 + M \rightarrow O_3 + M \,, \tag{1}$$

where, M stands for a third body, either O_2 or N_2. During the day solar photolysis is the primary mechanism for ozone depletion, while nighttime ozone destruction occurs primarily through reaction with atomic hydrogen and atomic oxygen:

$$H + O_3 \rightarrow OH(v) + O_2 \,, \tag{2}$$

and

$$O + O_3 \rightarrow 2O_2 \,. \tag{3}$$

During the daytime, then, the steady-state number density of ozone is given by

$$[O_3]_{ss} = k_1[O][O_2][M]/J_S \, , \tag{4}$$

where J_S is the rate of solar photolysis. Equation (4) shows clearly that the ozone number density varies in proportion to the O-atom number density. Knowing the ozone number density, therefore, allows one to back out the atomic oxygen number density given that the other important quantities in Eq. (4) are known.

At night, the steady-state ozone number density is given by

$$[O_3]_{ss} = k_1[O][O_2][M]/(k_2[H] + k_3[O]) \, . \tag{5}$$

Below about 100 km, the reaction with H dominates ozone removal, thus making ozone, once again, a tracer of atomic oxygen.

Just after sunset, the number density of ozone begins to increase because the major loss process for ozone, solar photolysis, terminates. A new steady-state number density, that given by Eq. (5), is established during the hours after sunset. Because nighttime loss rates are smaller than those during the day, this new steady-state number density is somewhat larger than that which obtains during the day at comparable O-atom number densities. Later in the night, the ozone number density begins to drop because the atomic-oxygen number density decreases during the night.

The 10 μm band data mirror these trends. The solid squares in Figure 1 represent emission from v=1 of the ν_3 band of ozone. As mentioned, this band is excited primarily by earth-shine pumping, and its intensity, therefore, is directly proportional to the ozone number density. The intensity increases roughly a factor of three immediately upon sunset, and another factor of three between sunset and midnight. It then decreases roughly a factor of two between midnight and sunrise. At sunrise, the ozone emission decreases more rapidly, falling a factor of 3 between 5:30 and 6:00 a.m. local time. This is, of course, because solar photolysis begins to be an important ozone loss mechanism at sunrise.

The primary mechanism for generating vibrational emission from OH is through reaction between H atoms and O_3, reaction 2. The OH is then lost via radiation, quenching, and reaction with atomic oxygen,

$$O + OH \rightarrow H + O_2 \, . \tag{6}$$

Reaction 6 is not vibrational-level specific, so serves as a sink for non-radiating OH as well. Its effect is to release the atomic hydrogen that is lost through reaction 2, thereby helping to maintain a reasonably constant H-atom number density throughout the night. The intensity of the

OH(v) emission, therefore, will be proportional to the number density of ozone, and indirectly, then to that of atomic oxygen. Between sundown and midnight (please see Figure 2), the ozone increases, and with it the OH(v) emission rate. This increase is roughly a factor of three, the same as that observed for the 10 μm ozone data. After midnight, the OH(v) emission decreases in proportion to the observed decrease in O_3. Just as the sun begins to rise, the OH(v) intensity declines at a more rapid rate than it did between midnight and dawn. This again is in keeping with the observed changes in O_3.

We consider finally the $O_2(a\ {}^1\Delta_g — X\ {}^3\Sigma_g^-)$ at 1.27 μm. During the day time, O_2(a) is generated primarily by the solar photolysis of ozone. It is lost via radiation and quenching, principally by molecular oxygen. Thus, the intensity of the O_2(a-X) emission essentially is proportional to the product of the solar flux and the local ozone number density. As the sun begins to set, around 6 p.m. local time, the solar flux drops off and the 1.27 μm emission intensity decreases rapidly. For the data in Figure 3, the emission decays with a time constant of about 26 minutes. In all, the O_2(a) emission intensity drops by some one and a half orders of magnitude.

The decay in the O_2(a) intensity between midnight and dawn is much slower than that observed during the two hours after sunset. This is because during the night, the O_2(a) is produced by the three-body recombination of atomic oxygen,

$$O + O + M \rightarrow O_2(a) + M \ . \tag{7}$$

In actuality, the mechanism is somewhat more complex than is shown by reaction 7,[7] but reaction 7 is correct schematically. Recombination reactions of atomic oxygen deplete the O-atom number density and generate O_2(a). The O_2(a) emission intensity should vary approximately as the square of the O-atom number density. The O_2(a) emission intensity, therefore, should decrease between midnight and dawn at a rate somewhat faster than the decreases observed for O_3 and OH(v). The observed decrease in the O_2(a) emission intensity between midnight and dawn is a factor of three. This is indeed much larger than the factor of two observed for the decreases in O_3 and OH(v) emissions, although not quite the squared dependence predicted by the different O-atom number density dependancies between the two sets of emissions. Just at dawn, approximately 5:30 a.m. local time, the O_2(a) intensity jumps rapidly. This is, or course, because solar photolysis of O_3 again becomes the primary mechanism for generating O_2(a).

The behavior of these various species have been modeled by a number of workers.[1,2,4] In particular Rodrigo et al.[1] have proposed a unified photochemical model which includes all important species related to oxygen and hydrogen in the upper atmosphere. Their model is a non-steady model of the atmosphere between 60 and 220 km, includes dynamical as well as photochemical effects, and is appropriate to middle latitudes, equinox conditions and moderate solar activity. The model atmosphere they propose is quite similar to others including Jacchia and MSIS, although they do note some deviations between their model and MSIS 86 at higher altitudes. These differences don't concern us since our observations center around 85 km.

Figures 1 through 3 compare their model results with our observations for ozone, hydroxyl, and singlet oxygen, respectively.

Rodrigo et al. provide column emission rates for $O_2(a)$ as a function of local time integrated between 60 and 100 km. Their calculations on OH(v) provide column concentrations for individual vibrational levels 2 through 6 over the same altitude range also as a function of local time. Finally, for ozone, they provide local ozone concentrations as a function of time at several altitudes between 60 and 100 km. Since our measurements were all of limb radiances, we had to convert Rodrigo et al.'s results to units consistent with the observations. This primarily consisted of determining an appropriate conversion factor between column radiances and limb radiances given the rather large foot print in the present observations. We found a factor of about 30 was appropriate for the OH(v) and $O_2(a)$ radiators. We had first to convert the OH(v) column concentrations to column radiances by multiplying the model concentrations by thermally averaged Einstein coefficients for OH(v) calculated by Holtzclaw et al.[8] Their values are consistent with those proposed by Nelson et al.,[9] but are somewhat more comprehensive. We then summed over all vibrational levels since our observations comprised the whole of the OH(v) first overtone emission.

For ozone, we used Rodrigo et al.'s calculated local concentrations and the procedures outlined by Rawlins[2] to calculate local band photon-emission rates from the model concentrations and known earth-shine pumping, radiative decay and quenching rates. We then converted to these local emission rates to limb radiances having a suitably wide foot print, using the procedure outlined by Green et al.[5]

As seen in Figures 1 and 3, the Delta 181 observations are about a factor of two to three larger than the model calculations of Rodrigo, et al. In relative terms, however, the diurnal trends indicated by the data and the model agree rather well. The discrepancy in the absolute values could result from calibration errors in the data or might indicate differences between local atomic oxygen concentrations extant during the observations compared to the concentrations chosen by Rodrigo et al. for their model atmosphere. The important point is the good relative agreement between the observations of two different features, both of which can be taken as diagnostic of odd oxygen concentrations in the mesosphere.

The absolute agreement between the model and the observed data for the hydroxyl emissions (please see Figure 2) is considerably larger than was the case for the other two observed features. Here again, however, the comparison between observation and model of the relative diurnal trends is good. We think the added discrepancy in the absolute intensities may well result from differences in the atomic hydrogen concentrations extant in the atmosphere during the observation period compared to that chosen by Rodrigo et al. as input to their model.

Analyzing the diurnal variations in the emissions observed in the Delta 181 flight gives us insight into the diurnal variations of important chemical species in the upper atmosphere. We have shown how this analysis displays the trends in the number densities of both odd oxygen and odd hydrogen species. Such detailed information on the composition of the upper atmosphere and how it changes can provide invaluable input to improved models of the radiation signatures of the upper atmosphere.

Acknowledgments

The authors acknowledge many insightful comments by Terry Rawlins of PSI. This work was supported in part by the Strategic Defense Initiative Office. We also appreciate partial financial support from the Air Force Office of Scientific Research (Task 2310G4) and Defense Nuclear Agency (Project SA, Task SA/SDI, work unit 00175) from a contract with the Phillips Laboratory/Geophysics Directorate under contract no. F19628-88-C-00173.

References

1. Rodrigo, R., López-González, M.J., and López-Moreno, J.J., "Variability of the Neutral Mesospheric and Lower Thermospheric Composition in the Diurnal cycle," Planet. Space Sci. 39, 803 (1991).
2. Rawlins, W.T., "Chemistry of Vibrationally Excited Ozone in the Upper Atmosphere," J. Geophys. Res. 90, 12,283 (1985).
3. Allen, M., Lunine, J.I., and Yung, Y.L., "The Vertical Distribution of Ozone in the Mesosphere and Lower Thermosphere," J. Geophys. Res. 89, 4841 (1984).
4. Winick, J.R., Picard, R.H., Sharma, R.D., and Nadile, R.M., "Oxygen Singlet Delta 1.58-Micrometer (0-1) Limb Radiance in the Upper Stratosphere and Lower Mesosphere," J. Geophys. Res. 90, 9804 (1985).
5. Green, B.D., Rawlins, W.T., and Nadile, R.M., "Diurnal Variability of Vibrationally Excited Mesospheric Ozone as Observed During the SPIRE Mission," J. Geophys. Res. 91, 311 (1986).
6. Rawlins, W.T., Woodward, A.M., and Smith, D.R., "Aeronomy of Infrared Ozone Fluorescence Measured During an Aurora by the SPIRIT 1 Rocket-Borne Interferometer," J. Geophys. Res. 98, 3677 (1993).
7. Ali, A.A., Ogryzlo, E.A., Shen, Y.Q., and Wassell, P.T., "The Formation of O_2 (a $^1\Delta_g$) in Homogeneous and Heterogeneous Atom Recombination," Can. J. Phys. 64, 1614 (1986).
8. Holtzclaw, K.W., Person, J.C., and Green, B.D., "Einstein Coefficients for Emission from High Rotational States of the OH(X $^2\Pi$) Radical," J. Quant. Spectrosc. Radiat. Transfer 49, 223 (1993).
9. Nelson, Jr., D.D., Schiffman, A., Nesbitt, D.J., Orlando, J.J., and Burkholder, J.B., "H + O_3 Fourier-transform Infrared Emission and Laser Absorption Studies of OH(X $^2\Pi$) Radical: An Experimental Dipole Moment Function and State-to-state Einstein A Coefficients," J. Chem. Phys. 93, 7003 (1990).

APPENDIX 18

Midcourse Space Experiment (MSX):

The Aurora of 10 November 1996 Observed Over Scandinavia

Midcourse Space Experiment (MSX):

The Aurora of 10 November 1996 Observed Over Scandinavia

M. Fraser, W. Gallery, T. Opar, G. Romick, D. Anderson, D. Morrison, M. Kendra, R. Hegblom, H. Gardiner, and R. O'Neil

Spring AGU Conference

May 1997

EL1505000030101

- 10 November 1996, 17:31 to 17:50 UT
- Constant tangent height of 105 km
- Nighttime observation of an aurora over Scandinavia
- Boresight azimuth change provided second observation
- Instrument complement:

  SPIII Radiometer (mirror scan on)

    Band A 6-11 um, B 4.3 um, C 11-13 um, D 14-16 um, E 17-26 um

  UVISI (IUN, IUW, IVN, IVW at 2 frames per second)

  SBV (1 frame per second)

Simulation of EL1505000030101
10 Nov 1996

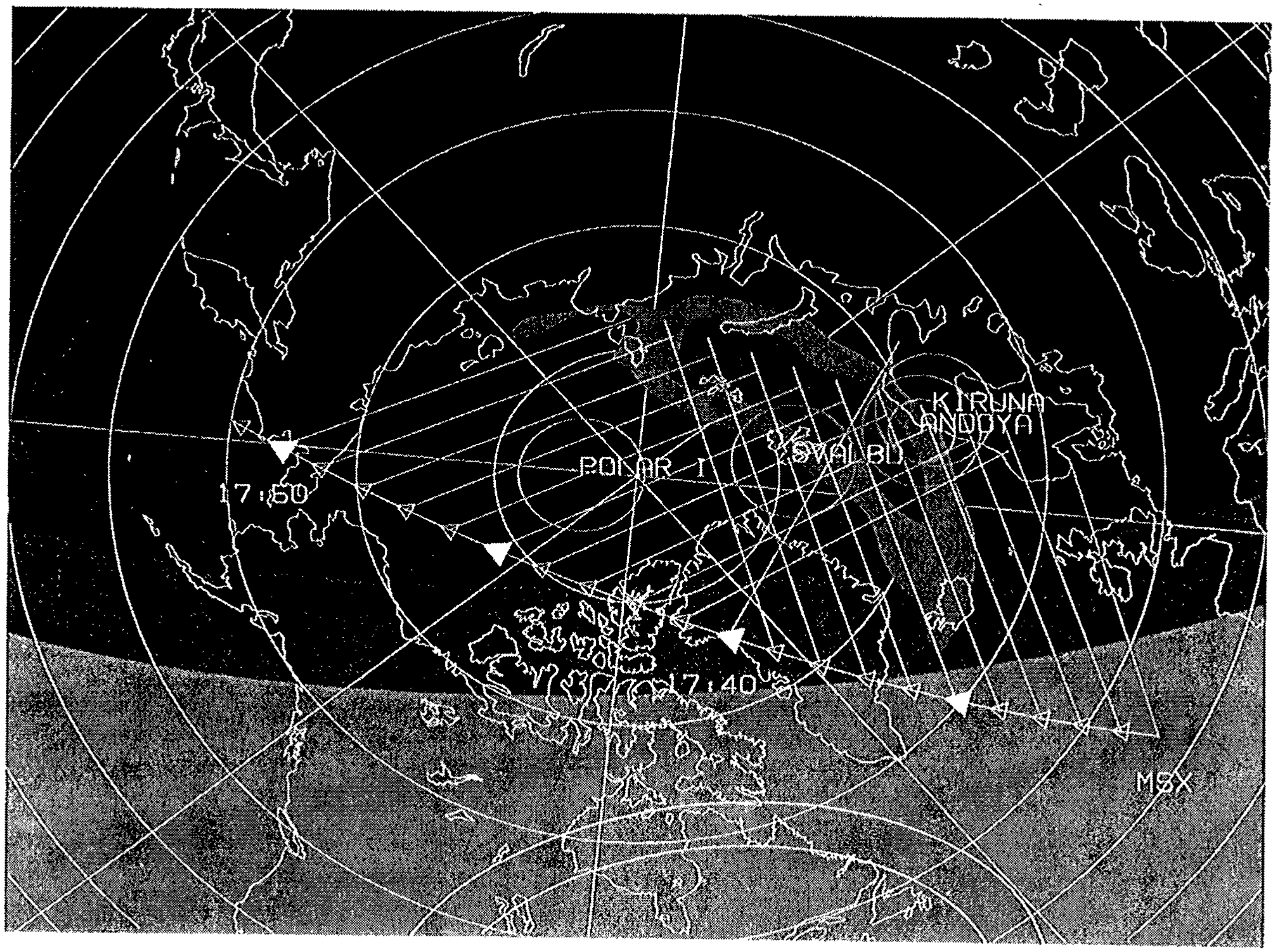

Offtrack Angle, Nadir Angle and Tangent Height

EL15 BEGINNING ON 1996 315 (11-10-96) AT 17:29:17.400
USING UL_EL15050000301_01_0104A.256

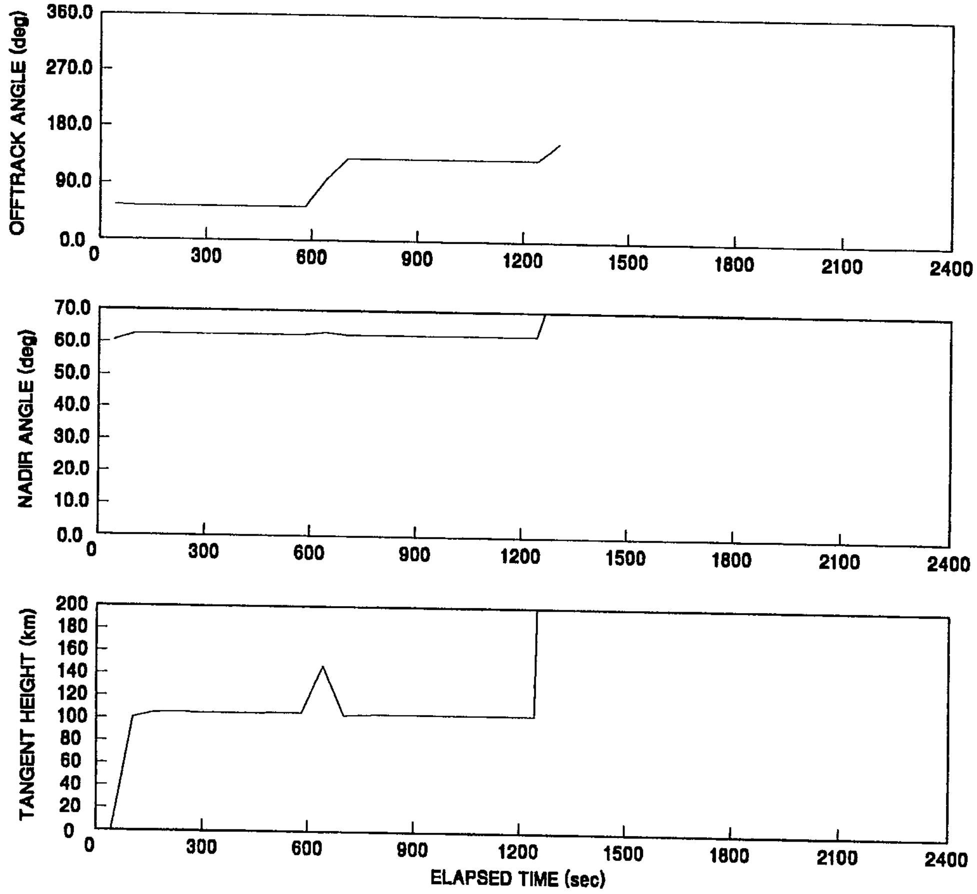

OFFTRACK ANGLE + RIGHT FOLLOWING ANSI/AIAA STANDARD R-004-1992

MSX BORESIGHT – NOT A CERTIFIED PRODUCT

PLH/GPD/RADEX
03/18/97

Target Point

EL15 BEGINNING ON 1996 315 (11-10-96) AT 17:29:17.400
USING UL_EL15050000301_01_0104A.256

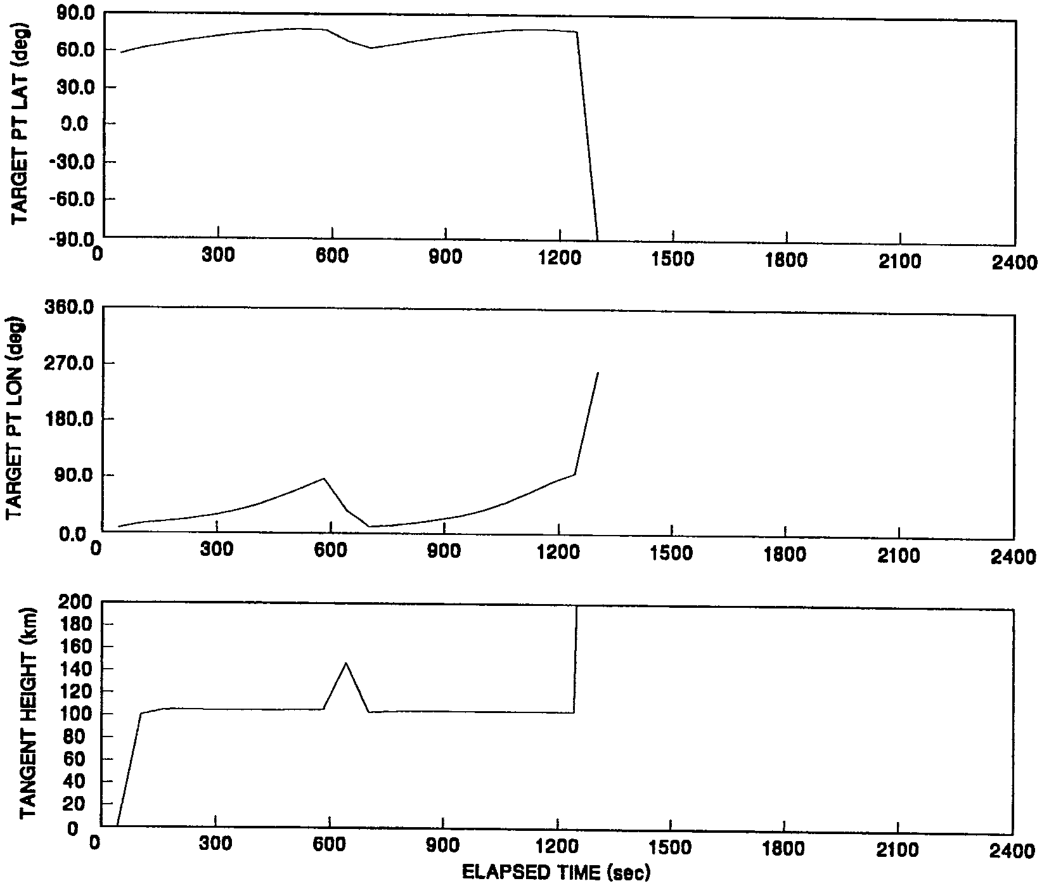

OFFTRACK ANGLE + RIGHT FOLLOWING ANSI/AIAA STANDARD R-004-1992

MSX BORESIGHT – NOT A CERTIFIED PRODUCT

PLH/GPD/RADEX
03/18/97

Instrument FOR's

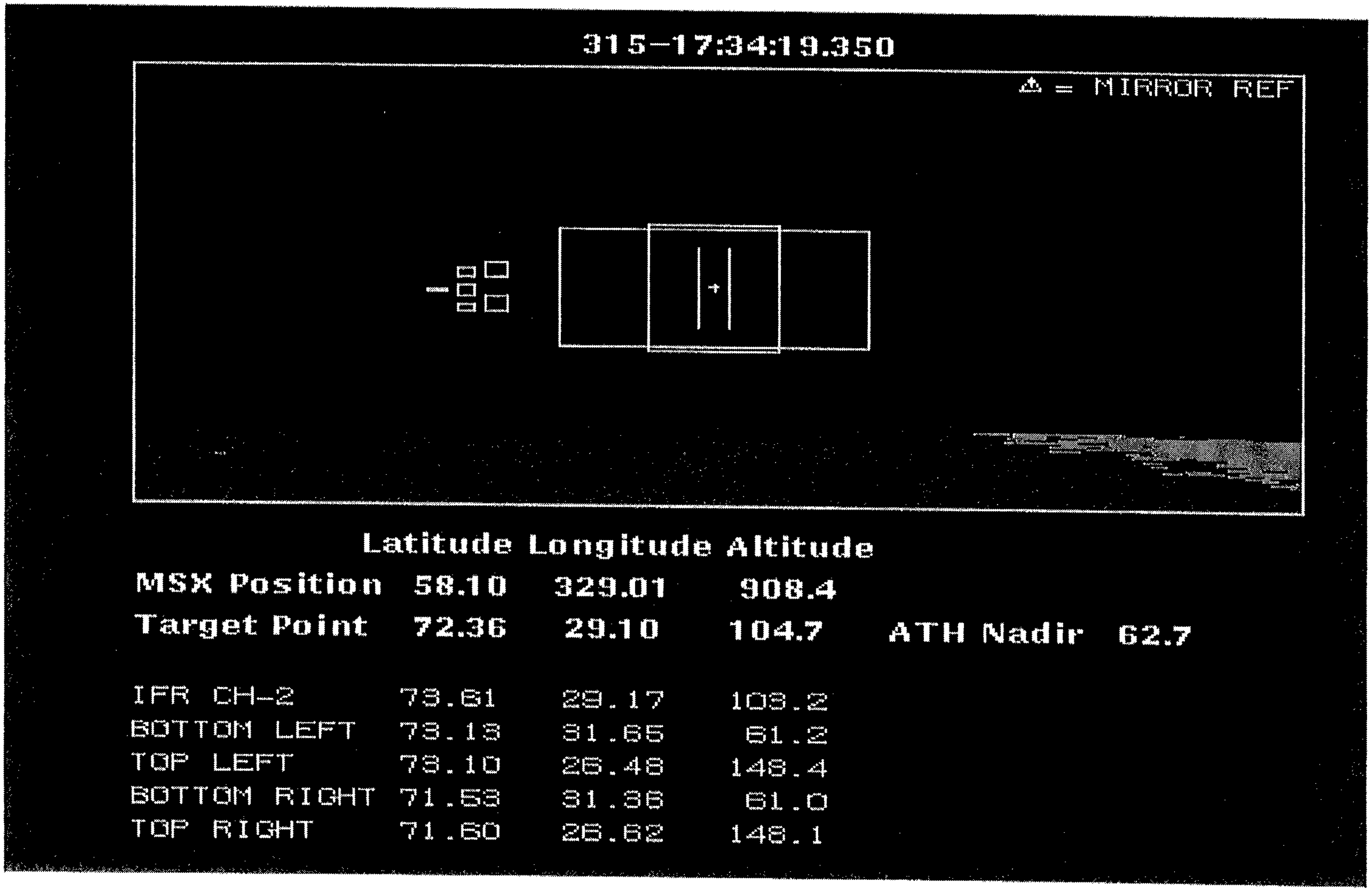

```
315-17:34:19.350
                                        ⚠ = MIRROR REF

               Latitude Longitude Altitude
MSX Position   58.10     329.01    908.4
Target Point   72.36      29.10    104.7    ATH Nadir  62.7

IFR CH-2       73.61      29.17    103.2
BOTTOM LEFT    73.13      31.65     61.2
TOP LEFT       73.10      26.48    148.4
BOTTOM RIGHT   71.53      31.36     61.0
TOP RIGHT      71.60      26.62    148.1
```

Automated Data Products

- Geographic database
  - Pointing and instrument FOR's
- Images
  - Temporal and spatial for all IR bands
  - Spatial UVISI images
  - Spatial SBV images
- Spectra
  - UVISI SPIM's
- Time Series
  - All IR bands
- Radiance profiles
  - IR bands with template predictions

UVISI Images - 17:34:18.150 UT

IUW

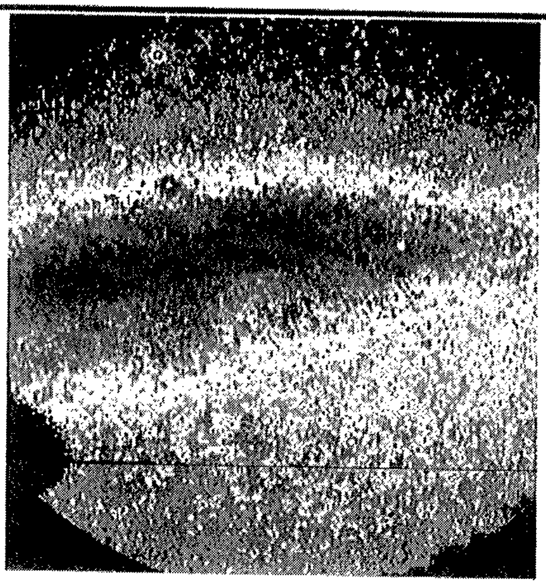

IVW

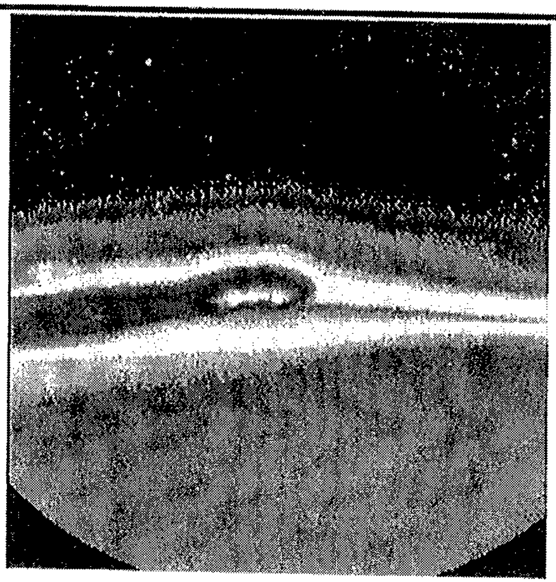

IUN

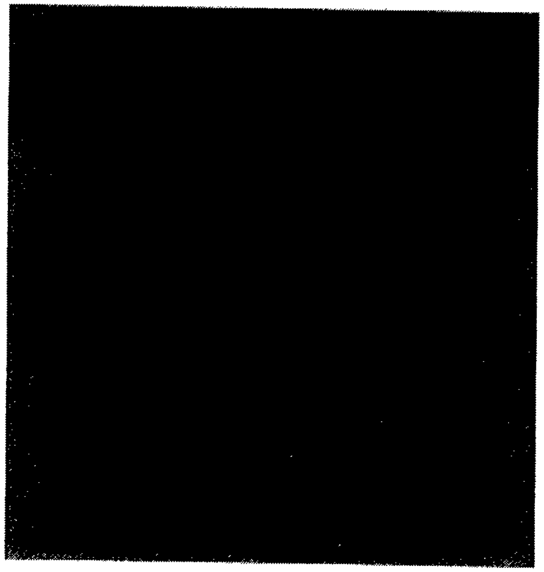

IVN

Band B Spatial Image

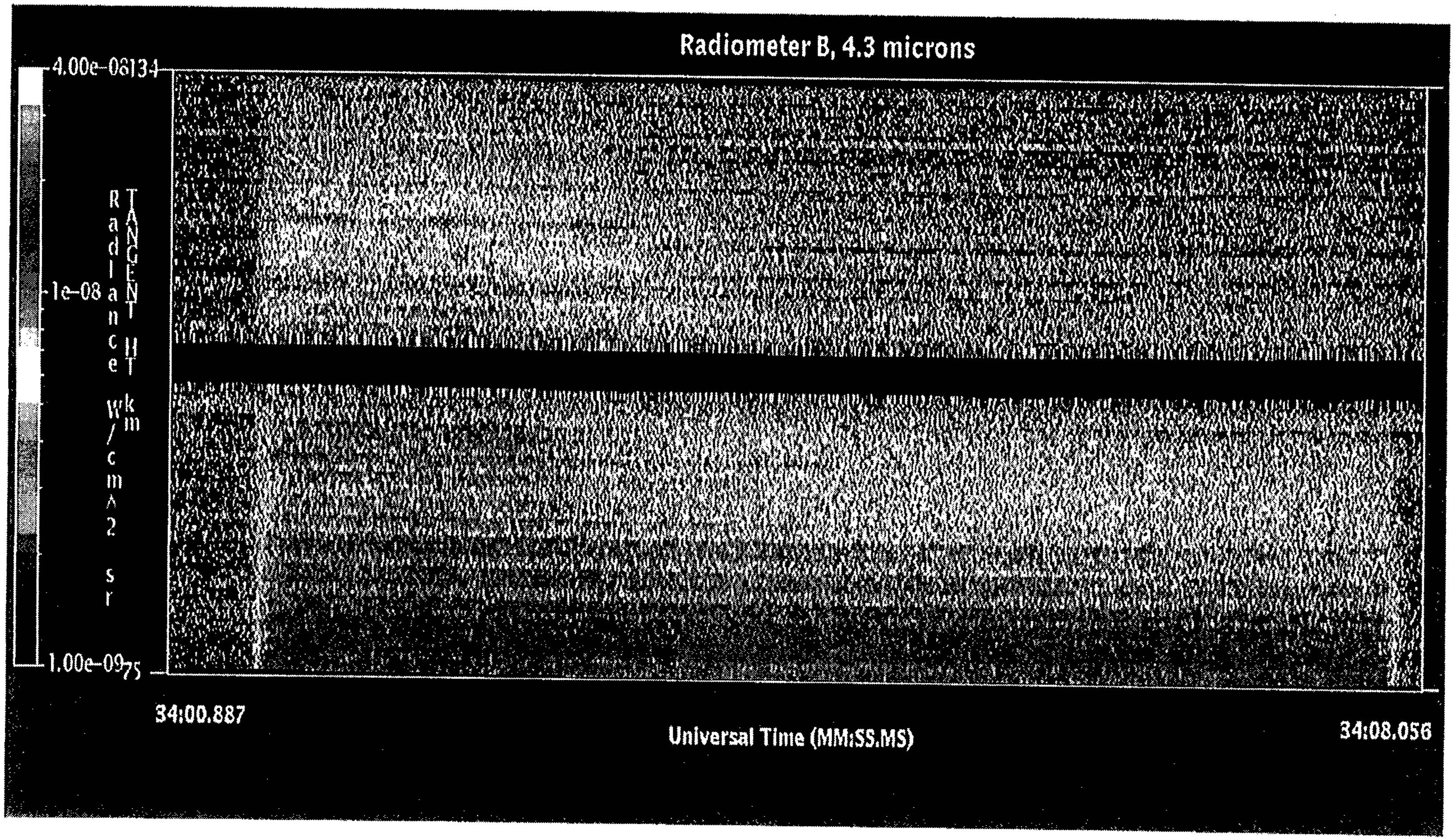

Band B Enhancement

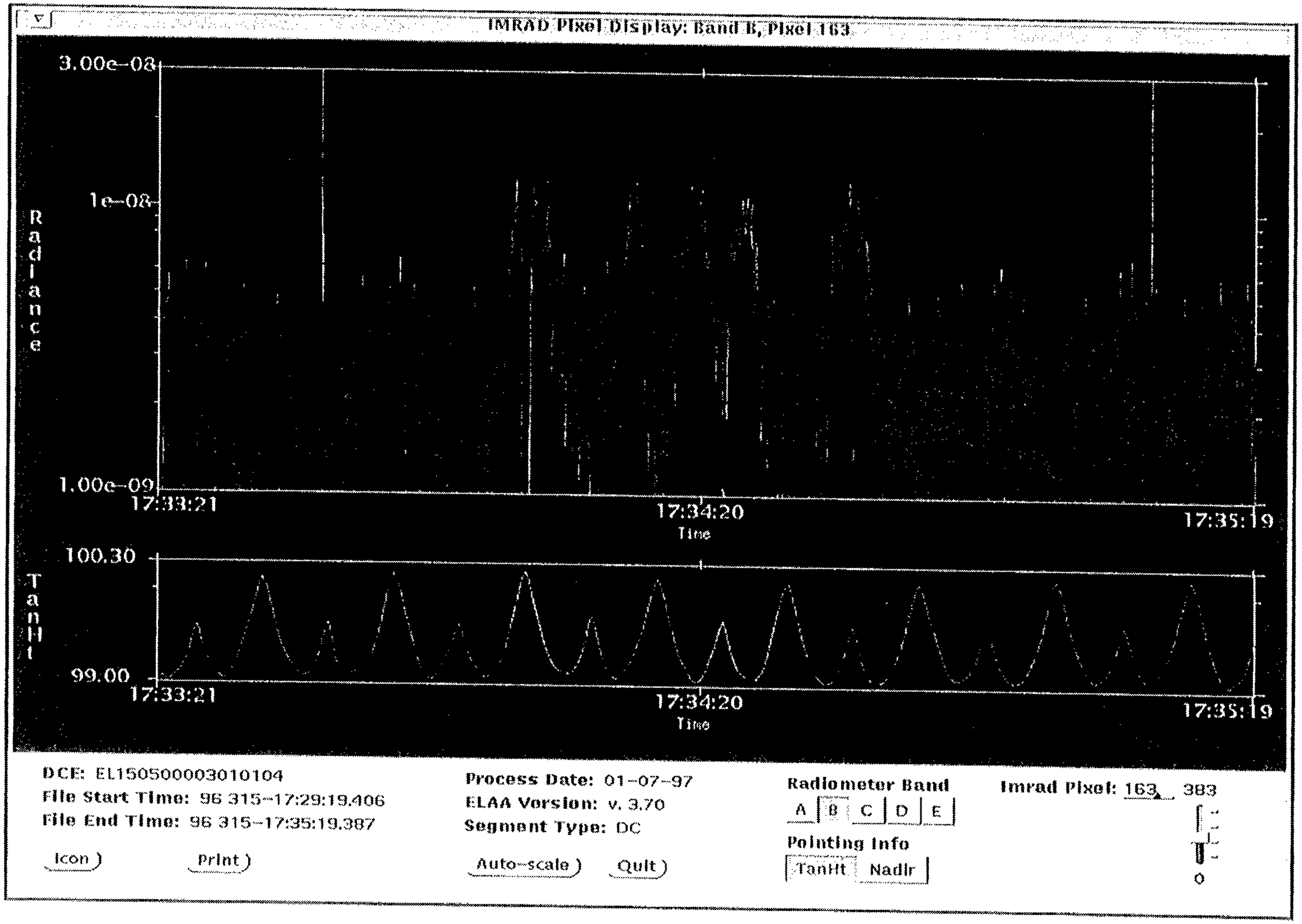

DCE: EL150500003010104
File Start Time: 96 315-17:29:19.406
File End Time: 96 315-17:35:19.387

Process Date: 01-07-97
ELAA Version: v. 3.70
Segment Type: DC

Imrad Pixel: 163 383

Band D

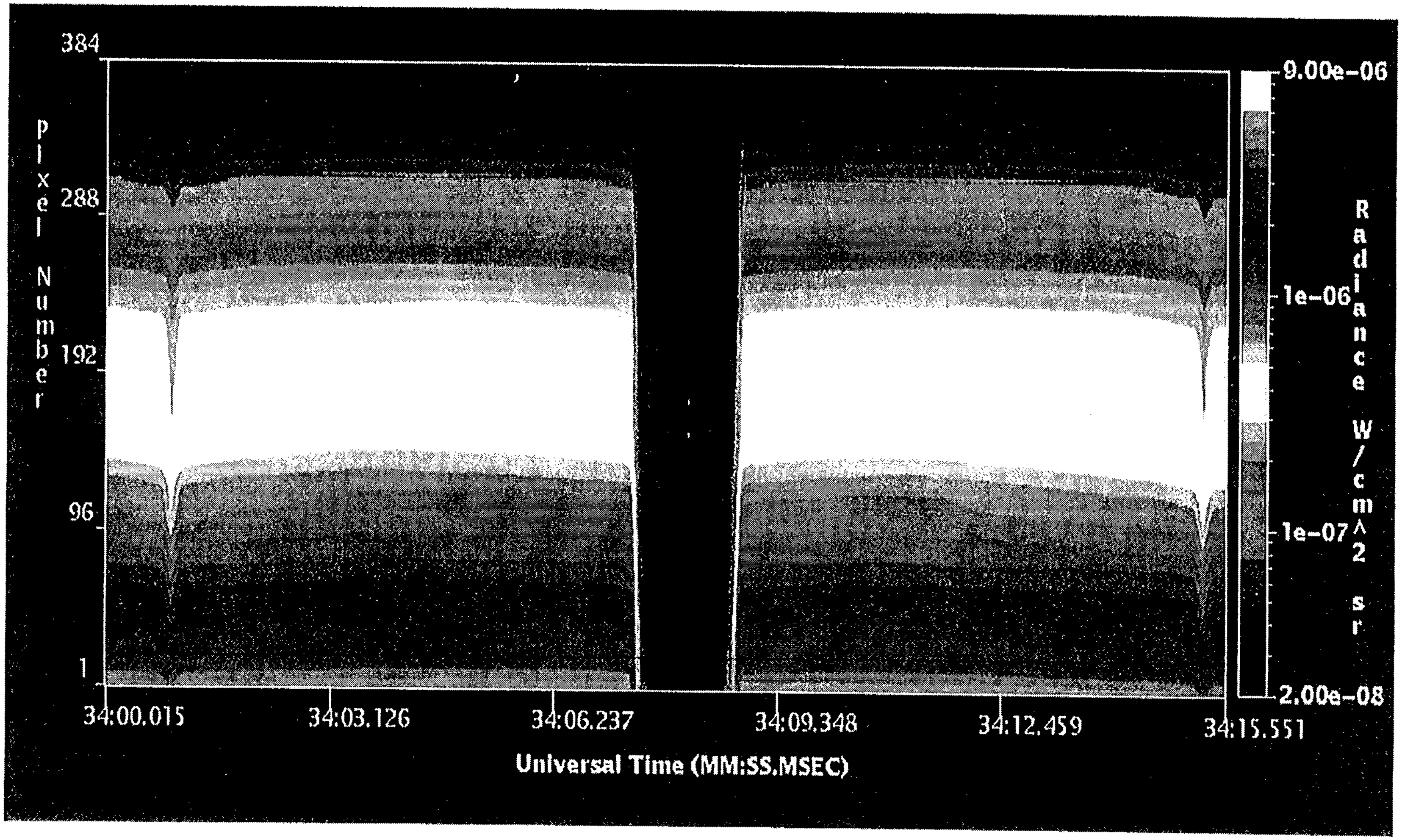
384
288
192
96
1
Pixel Number
34:00.015
34:03.126
34:06.237
34:09.348
34:12.459
34:15.551
Universal Time (MM:SS.MSEC)
9.00e-06
1e-06
1e-07
2.00e-08
Radiance W/cm^2 sr

Band D

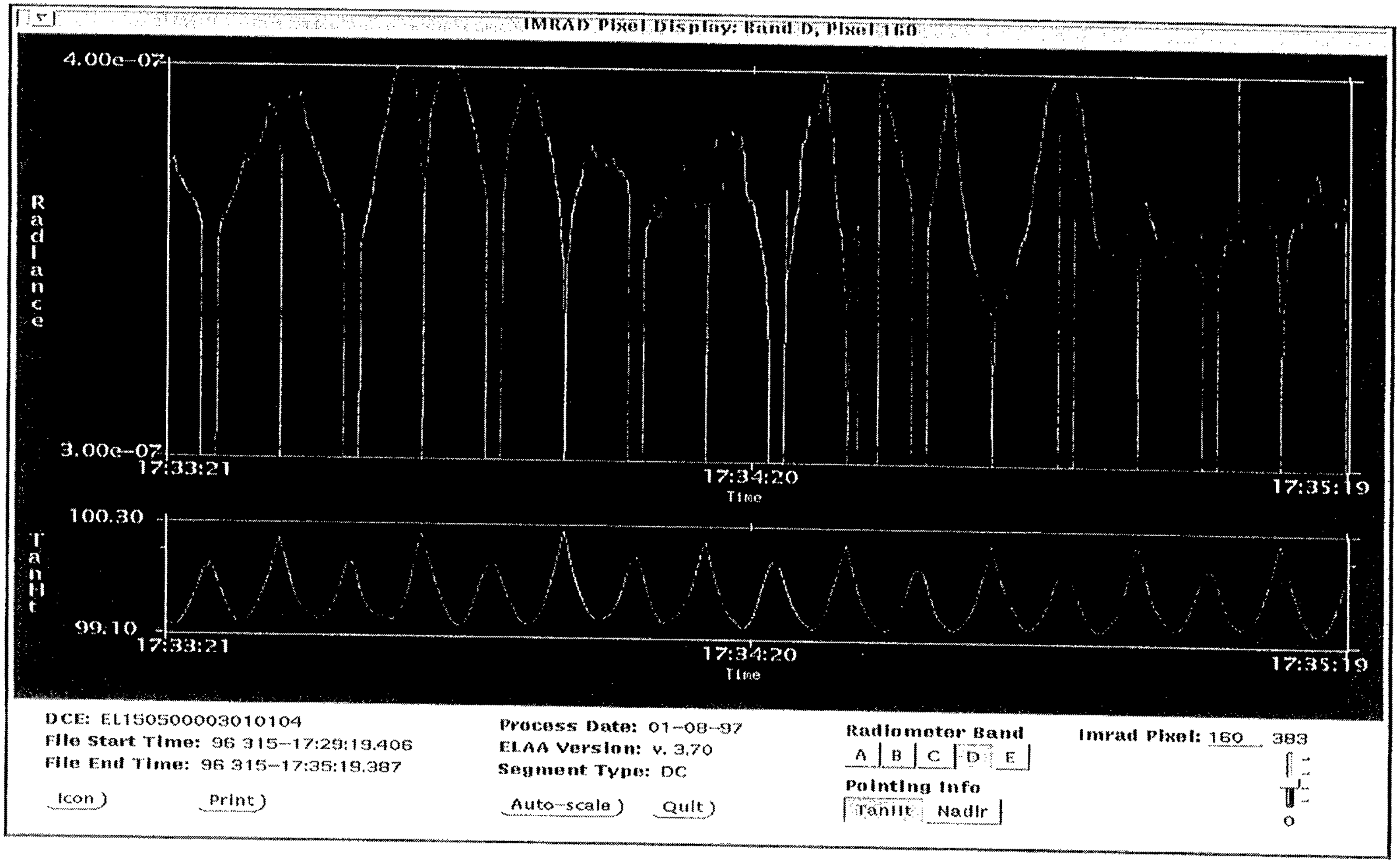

DCE: EL150500003010104
File Start Time: 96 315–17:29:19.406
File End Time: 96 315–17:35:19.387

Process Date: 01–08–97
ELAA Version: v. 3.70
Segment Type: DC

Radiometer Band D

Pointing Info Tanlit

Imrad Pixel: 160

UVISI Images - 17:41:40.400 UT

IUW

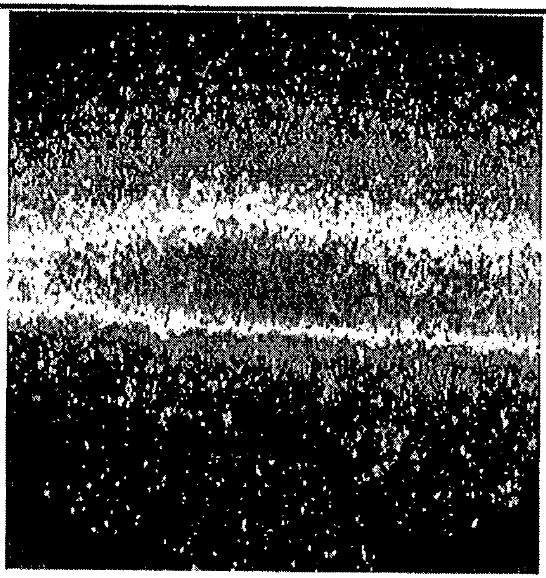

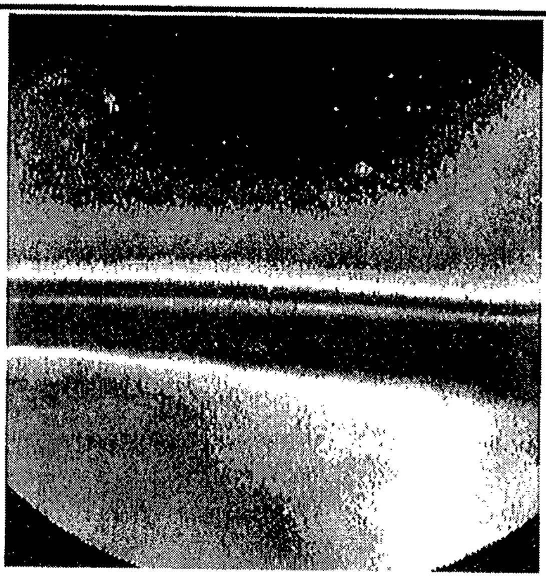

IVW

IUN

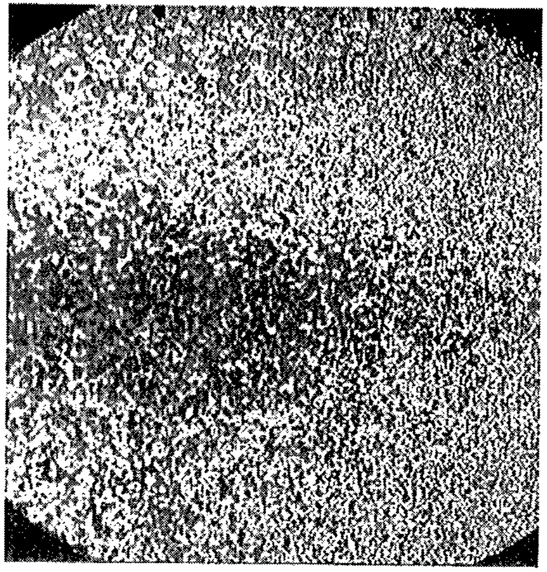

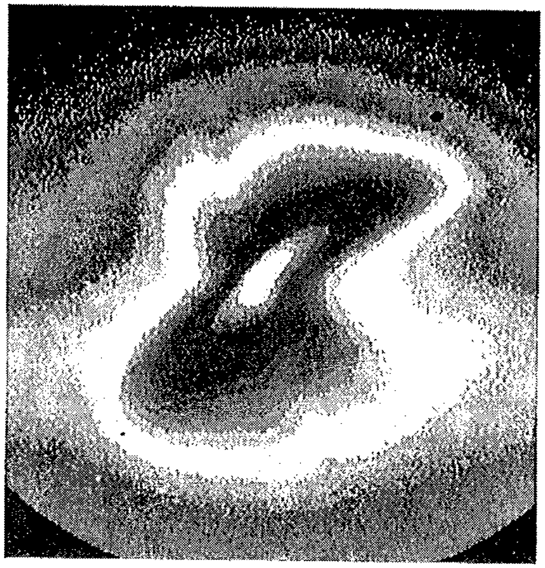

IVN

Band A Temporal Image

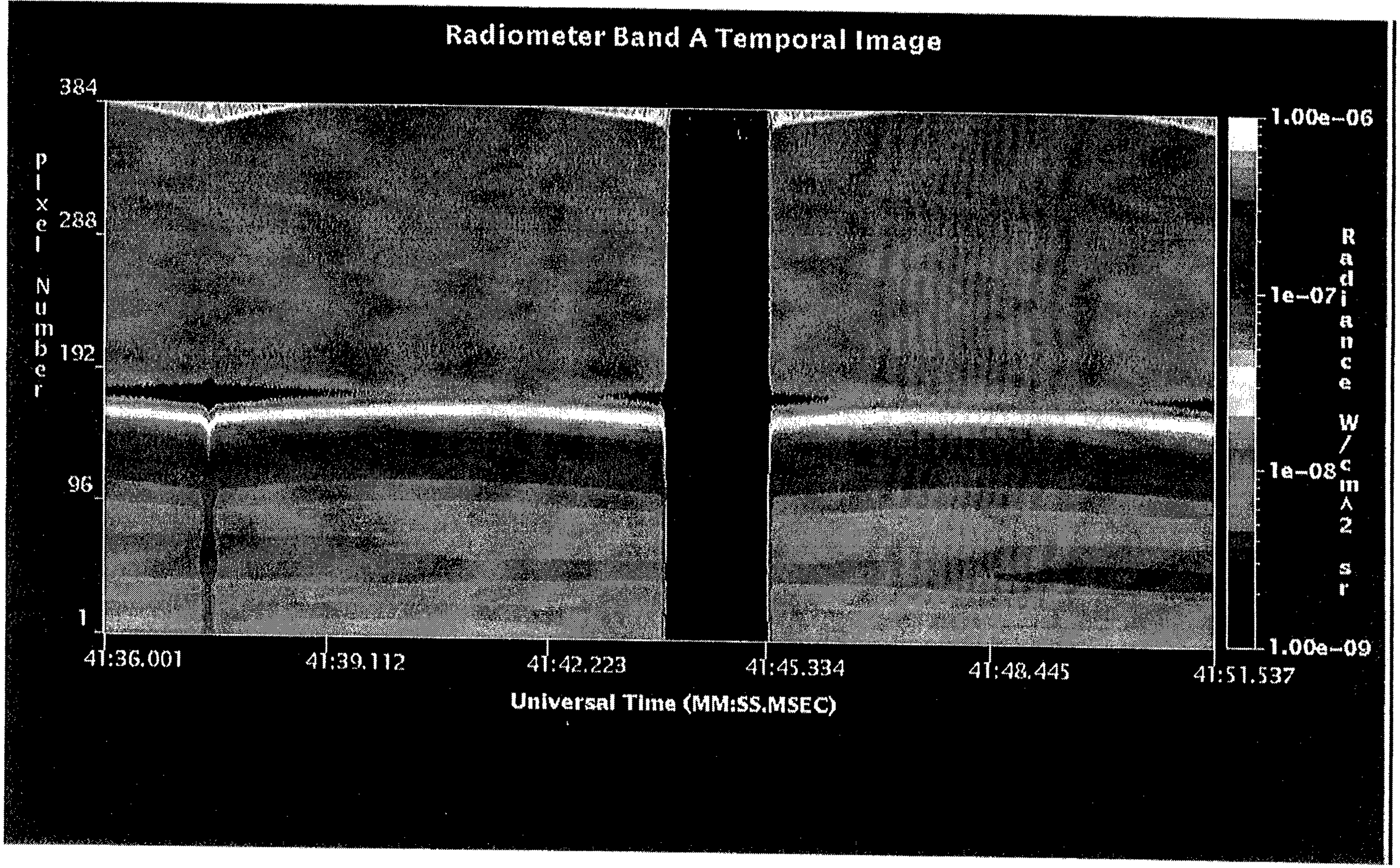

Conclusions

- Substantial auroral enhancements in UV and Visible wavelengths
- Modest but definite enhancement in Band B (4.3 um CO_2)
- Less pronounced effects in other radiometer bands
- Modeling and further data analysis will yield:
  - Dosing and ionization rates
  - CO_2 enhancement mechanism
  - Effects in other IR bands

APPENDIX 19

Midcourse Space Experiment (MSX):

Auroral MWIR and LWIR Backgrounds, Observations, and Analysis

Midcourse Space Experiment (MSX):

Auroral MWIR and LWIR Backgrounds, Observations and Analysis

M. Fraser, W. Gallery, T. Opar, M. Kendra, P. Wintersteiner,
J. Winick, R. Picard, R. Sharma, H. Gardiner, and R. O'Neil

Poster Paper Number PC-5

1997 Meeting of the MSX Interim Results Review (IRR)

2-3 June 1997

Abstract

MSX observed a bright aurora over northern Scandinavia in the period from 17:31 to 17:50 UT on 10 November 1996. The event was documented by the extensive suite of co-aligned ultraviolet, visible and infrared sensors on the MSX satellite. The UVISI ultraviolet and visible imagers acquired both narrow and wide-field data at a rate of two frames per second. Spirit III acquired data in all five IR bands with the mirror scan on creating 3 degree images.

This paper presents a preliminary analysis of the data with interpretation of possible systems impact. The analysis so far shows the UV, visible, and IR data to be self-consistent and well correlated. The 3914 line provides information on total dosing and dosing rate. Bands A (6-11 um) and B (4.3 um) observed strong enhancements at specific altitudes. These observations have been evaluated by current models employing known chemistry and excitation mechanisms.

EL1505000030101

- 10 November 1996, 17:31 to 17:50 UT
- Constant tangent height of 105 km
- Nighttime observation of an aurora over Scandinavia
- Boresight azimuth change provided second observation
- Instrument complement:

SPIII Radiometer (mirror scan on)

Band A 6-10.9 um, B 4.3 um, C 11.1-13.2 um, D 13.5-16 um, E 18.1-26 um

UVISI imagers (IUN, IUW, IVN, IVW at 2 frames/s)

UVISI spectrographic imagers (SPIMs, all five)

SBV (1 frame per second)

Simulation of EL1505000030101
10 Nov 1996

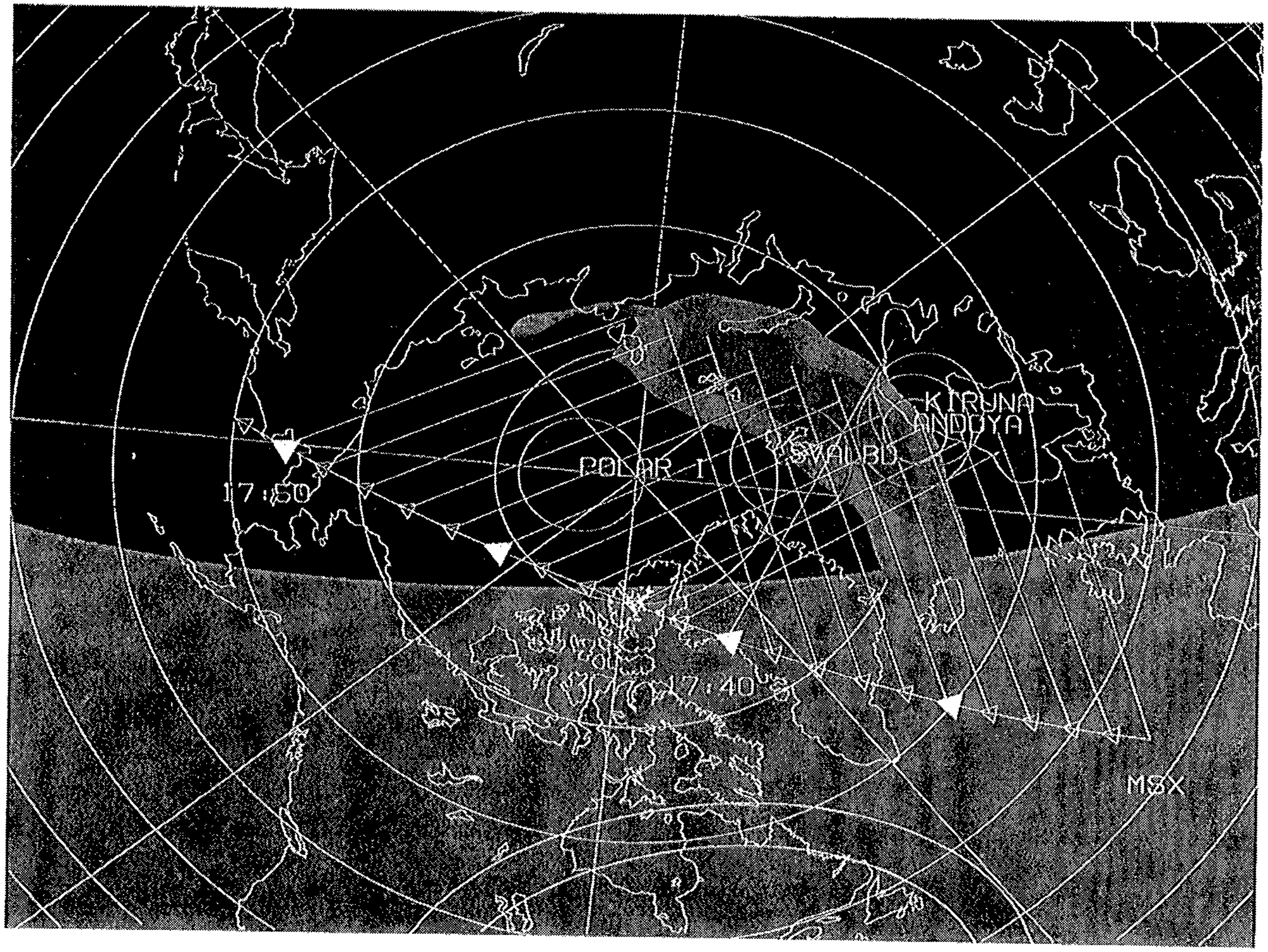

- MSX position shown in one min. intervals
- Modeled auroral oval shown; predictions compare well with observations
- Shaded areas show terminator at 0, 110, and 900 km altitude

Instrument FOR's

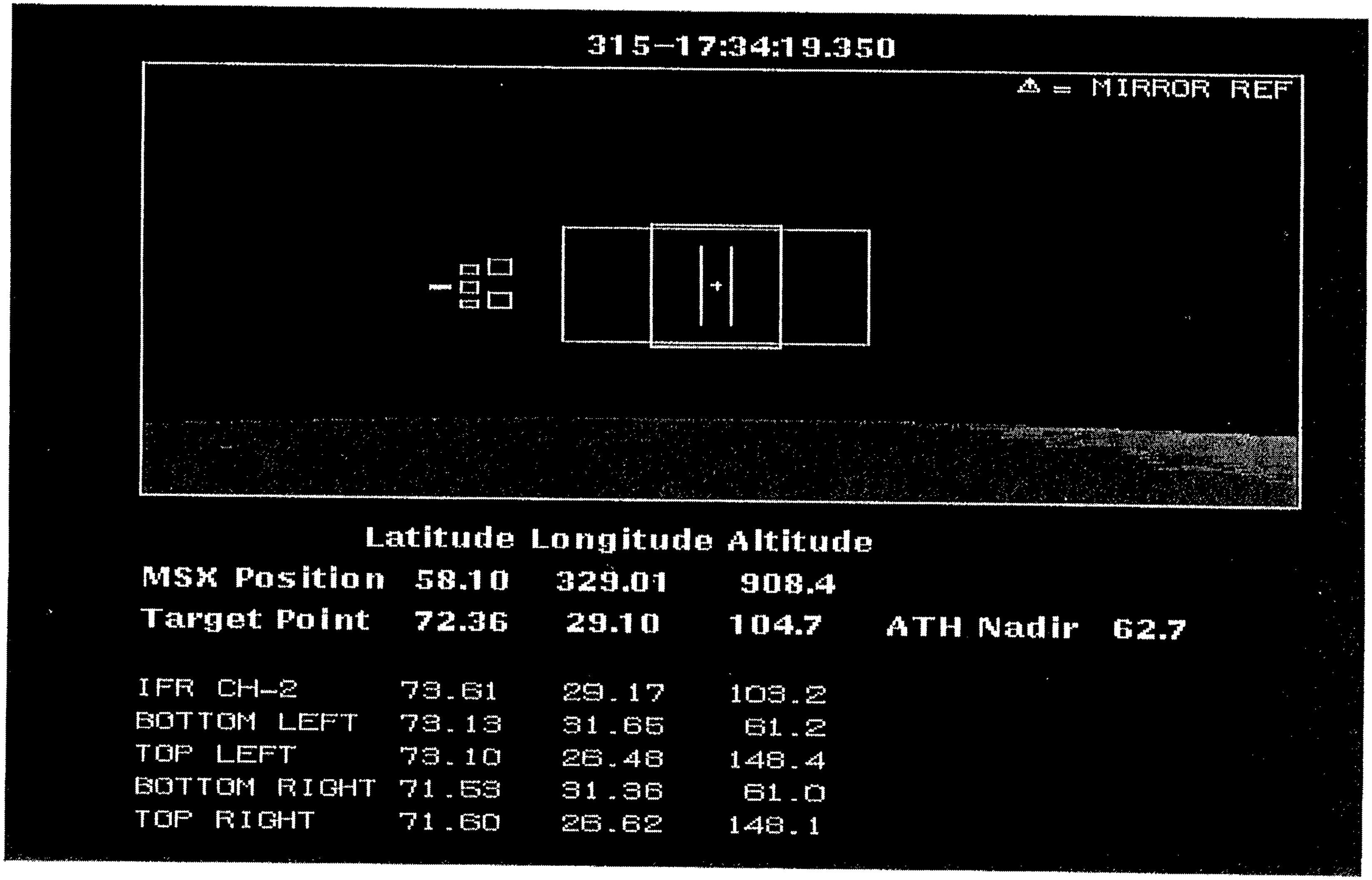

315−17:34:19.350

	Latitude	Longitude	Altitude	
MSX Position	**58.10**	**329.01**	**908.4**	
Target Point	**72.36**	**29.10**	**104.7**	**ATH Nadir 62.7**
IFR CH−2	73.61	29.17	103.2	
BOTTOM LEFT	73.13	31.65	61.2	
TOP LEFT	73.10	26.48	148.4	
BOTTOM RIGHT	71.53	31.36	61.0	
TOP RIGHT	71.60	26.62	148.1	

Visible Wide (380-900 nm) with Visible Narrow (300-900 nm) FOV

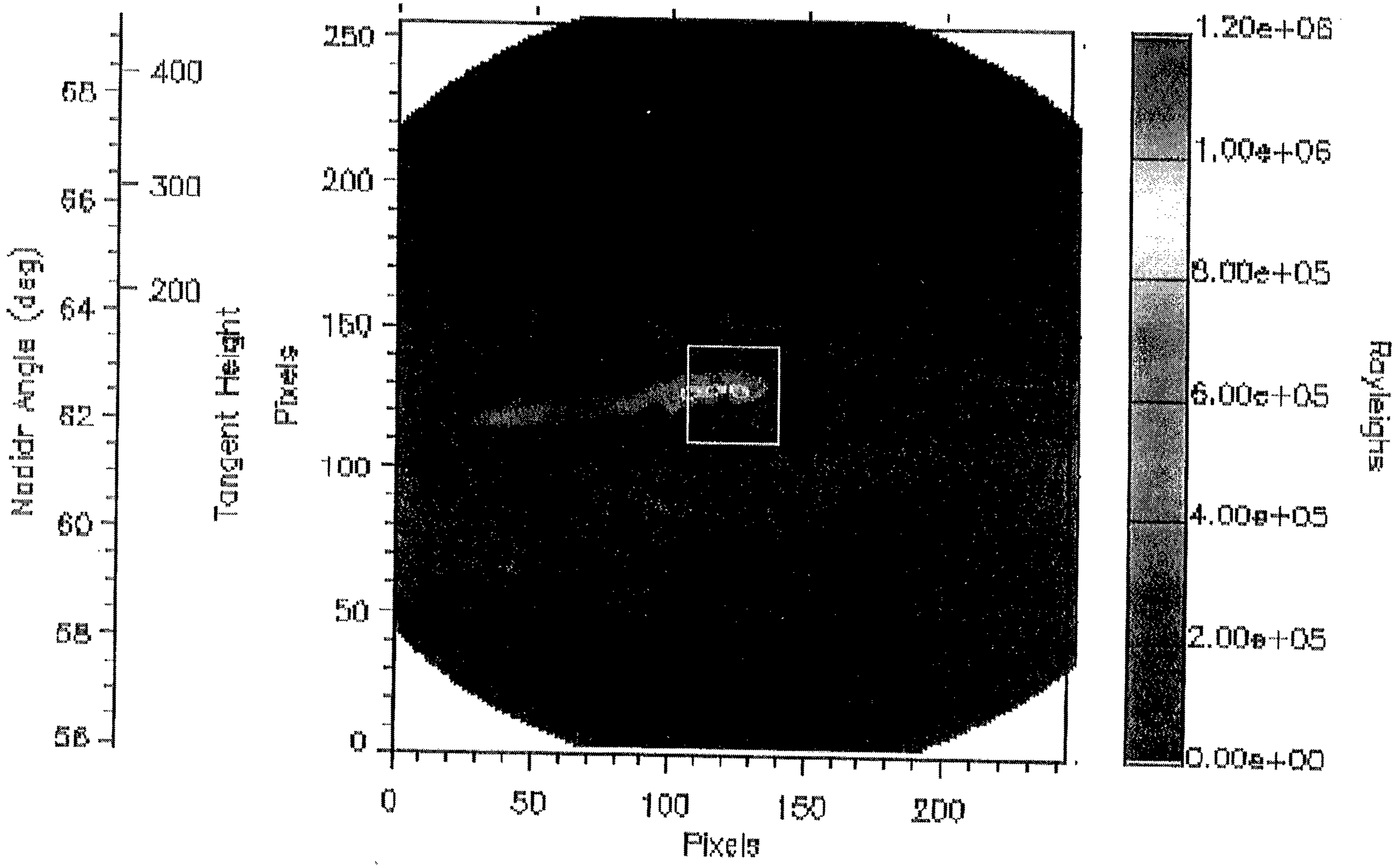

UVISI Narrow and Band B Images

Instrument FOR's

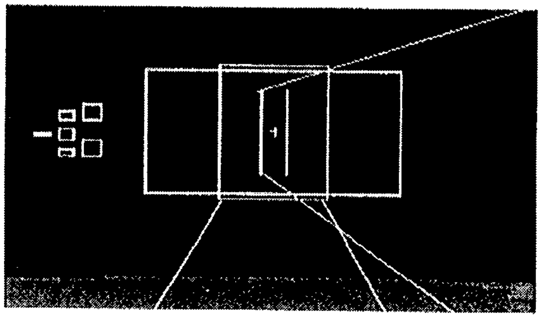

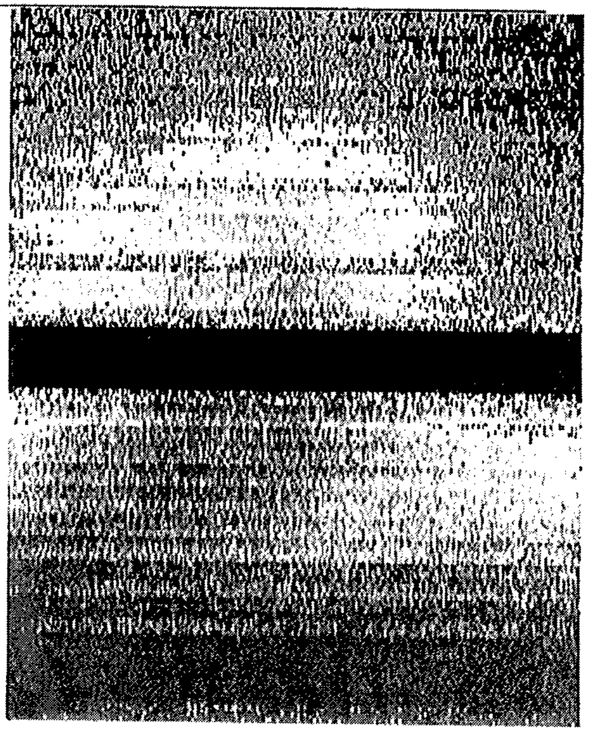

Band B (4.3 um)
1 x 2 deg.

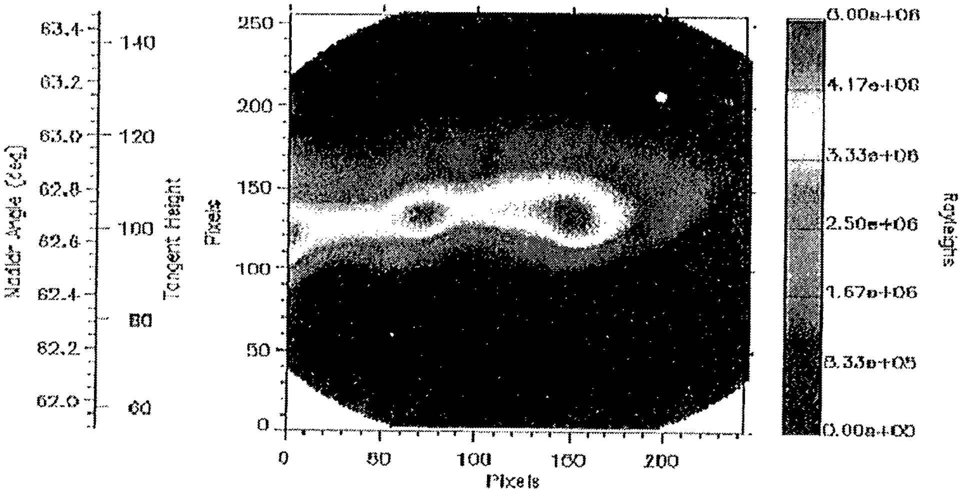

IVN
300-900 nm
1.59 x 1.28 deg.

3914 A SPIM Image and Profile

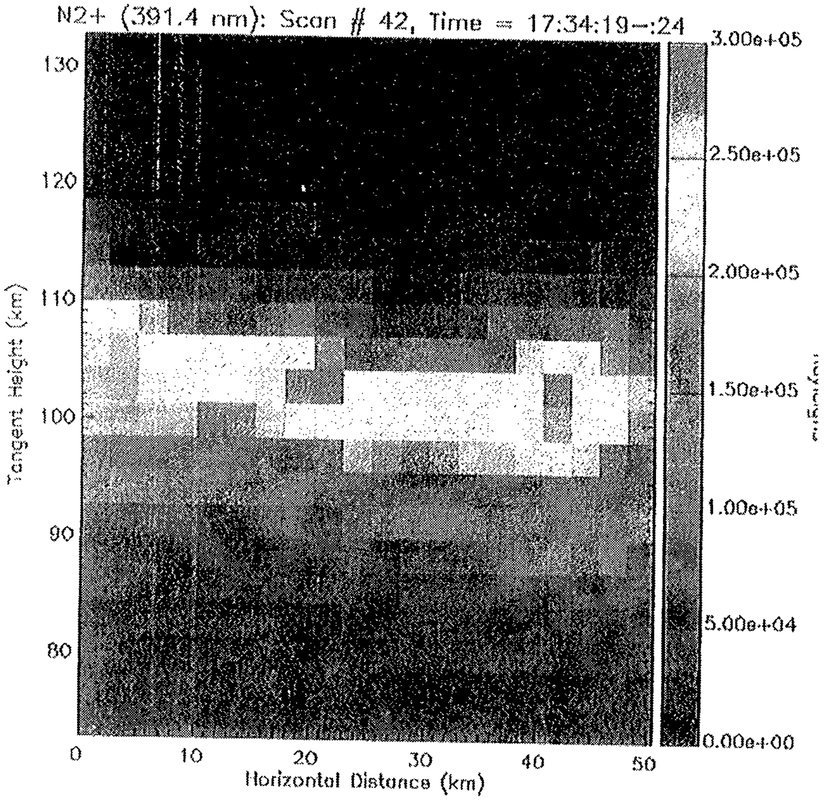

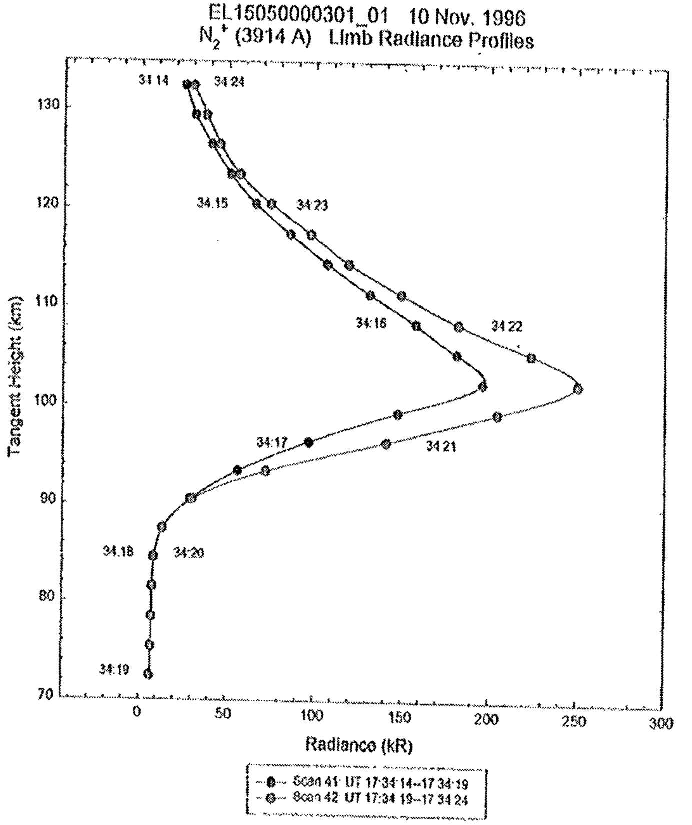

- Image corresponds closely to IVN and IR Band B data
- Profiles show max dosing at 105 km

Band A Auroral Enhancement

- 6-11 um
- Color scale chosen to highlight higher altitude enhancement

Auroral Radiative Processes

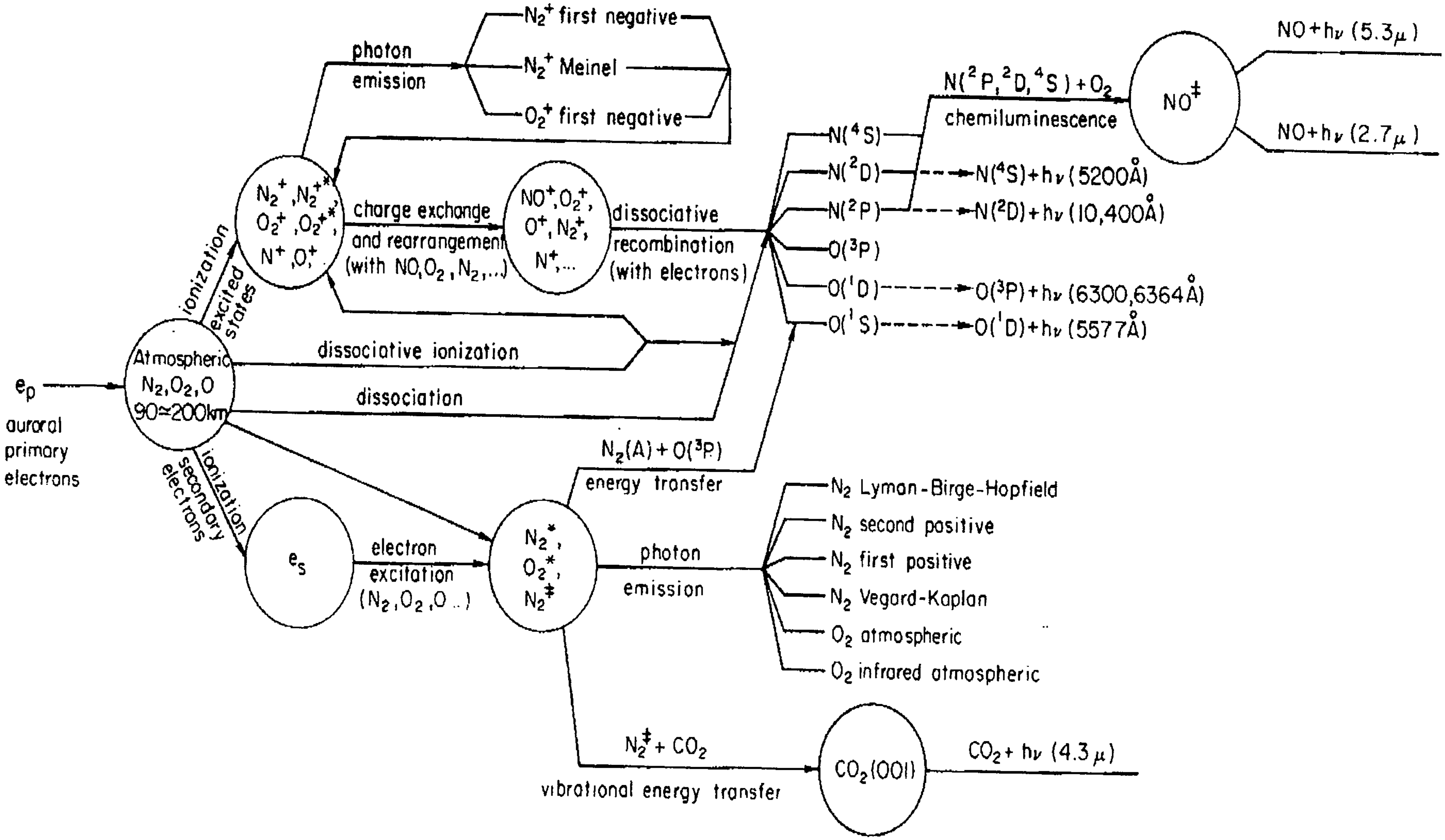

Summary of Observations

- Substantial auroral enhancements in UV and Visible wavelengths
- Auroral effects observed in three Spirit III radiometer bands
- Spirit III observed strong 4.3 um enhancement of 10-20x over ambient background above 100 km, smaller enhancements below (4x at 95 km, 2x at 90 km)
- Strongest dosing regions in UV and IR appear to coincide
- Detailed examination and cross-correlation of temporal and spatial UV, Visible and IR database in progress

Preliminary Modeling Evaluation

- Strong CO_2 enhancements at lower altitudes requires 300-500 s pre-dosing; confirmed in late time observations
- Preliminary AARC model comparisons produce a consistent altitude profile with enhanced CO_2 data
- Simulation of 4.3 um behavior consistent with known sources and excitation mechanisms:

$CO_2 + N_2\,(v=1) \leftrightarrow CO_2\,(v_3) + N_2\,(v=0)$ v-v transfer

$CO_2 + hv \leftrightarrow CO_2\,(v_3)$ radiative loss and transfer

and NO^+ emissions from ion-molecule reactions,

$N^+ + O_2 \rightarrow NO^+\,(v<12) + O$

$N_2^+ + O \rightarrow NO^+\,(v<2) + N(^2D)$

$N_2^+ + O \rightarrow NO^+(v>10) + N(^4S)$

Conclusions and Systems Impact

- 3914 A intensity exceeded 200 kR
  - bright aurora
- 4.3 um enhancement approximately 10^{-8} W/sr-cm^2-um
- Known chemistry can account for 4.3 um enhancement
- Band A enhancement due to NO radiance produced from $N(^2D) + O_2$
- Observed IR enhancements are dynamic
  - rapid temporal variations
  - strong gradients